
UCLouvain

Institute of Condensed
Matter and Nanosciences

Institute for Information
and Communication
Technologies, Electronics and
Applied Mathematics

Dearest of friends, at your earnest request, I will now make known to you, in an unpolished narrative, the undoubted though hidden virtue of the magnetic stone, concerning which philosophers up to the present time give us no information, because it is characteristic of good things to be hidden in darkness until they are brought to light by application to public utility.

Out of affection for you, I will write in a simple style about things entirely unknown to the ordinary individual. Nevertheless I will speak only of the manifest properties of this stone, because this tract will form part of a work on the construction of philosophical instruments.

The disclosing of the hidden properties of this stone is like the art of the stone sculptor. Although I may call the matters about which you inquire evident and of inestimable value, they are considered by common folk to be illusions and mere creations of the imagination. But the things that are hidden from the multitude will become clear to astrologers and students of nature, and will constitute their delight, and for experienced travelers it will be a significant help.

Translation by Brother Arnold, M.Sc.
The letter of Petrus Peregrinus on the magnet, A.D. 1269.
Mc. Graw Publishing Company,
New York: United States of America. 1904. 76 pp.

Amicorum intime, quandam magnetis lapidis occultam virtutem, a te interpellatus, rudi narratione tibi reserabo utcumque. Nihil enim, apud philosophos, absque noticie principio est iucundum ; et in tenebris orbitat, et obfuscatur bonorum natura, donee in communis deductionis radium erigatur.

Amore ergo tui conseribam, sermone piano, que vulgo studentium penitus sunt ignota ; attamen nonnisi de manifestis huius lapidis in hac epistola trademus scientiam, eo quod, hoc tradito, pars erit tractatus in qua docebimus philosophica componere instrumenta.

De occultis huius lapidis tractare, spectat ad artem lapidis sculpture. Et, licet opera, de quibus quesivisti appellem manifesta, erunt tamen inextimabilia, et vulgo quasi illusiones et fantasmata. Et ideo quo ad vulgum secreta sunt, astrologis autem et naturalibus satis erunt manifesta, et ipsis erunt solatium, et provectis viatoribus non modici erunt iuvamenti.

Petrus Peregrinus de Maricourt (1269)
Epistola Petrus Peregrinus de Maricourt ad Sygerum de Foucaucourt, militem, de magnete

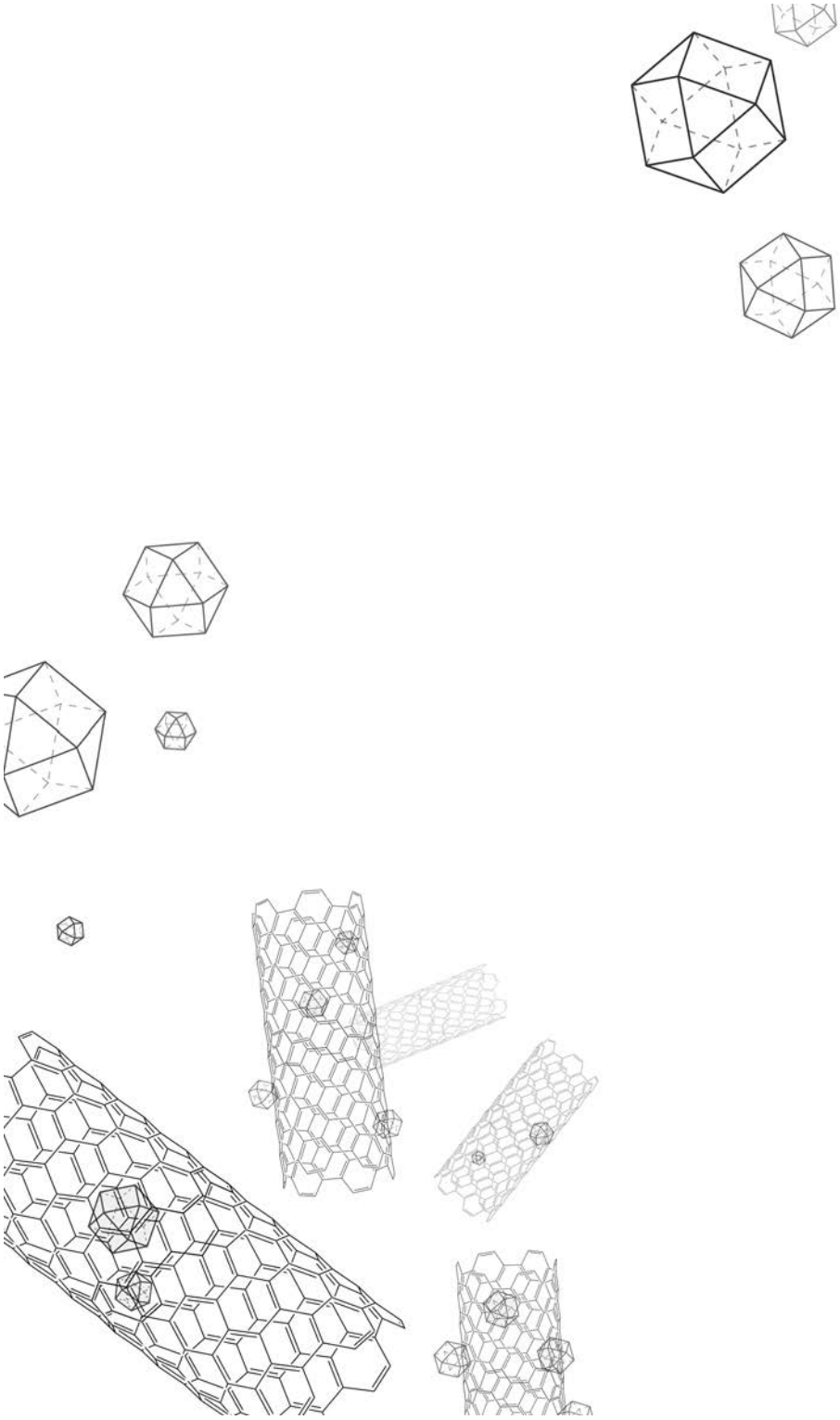

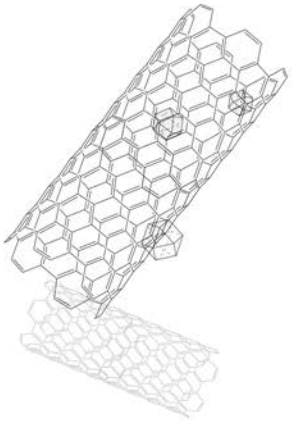

para ti, Sabina

que la maravilla sea en tu vida

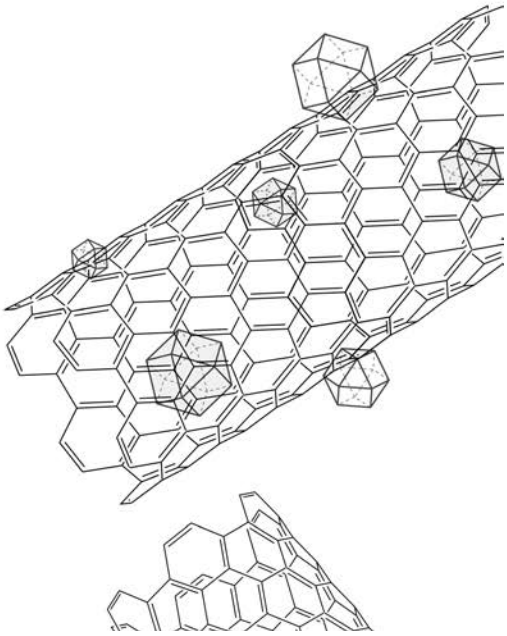


gratias

Je tiens à exprimer ma gratitude la plus sincère envers les Professeurs Sophie Hermans et Isabelle Huynen. Merci de votre accompagnement attentif, minutieux et rigoureux, de votre soutien, d'être un exemple de courage et de ténacité. Merci pour votre engagement, votre « don de soi » et votre amour passionné de la connaissance. Ce que j'ai partagé avec vous m'a permis de mieux chercher, d'ouvrir des nouveaux pans de ma conscience à cette réalité complexe et fascinante. C'est un don exceptionnel que vous m'avez offert et je vous en suis très reconnaissant.

I warmly thank the members of my jury, Prof. Carla Bittencourt, Prof. Arnaud Delcorte, Pof. Jacques Devaux, Prof. Véronique Dupuis and Prof. Jean-Pierre Raskin. Thank you for bringing in new perspectives into this research. I found inspiration in our exchanges and your thoughtful insights allowed improving the quality of this manuscript.

Merci aux Professeurs Arnaud Delcorte et Christian Bailly, membres de mon comité d'accompagnement, pour votre suivi attentif et bienveillant, pour ces nombreuses discussions scientifiques qui m'ont motivé et m'ont aidé à avancer.

Je remercie de façon très particulière Sébastien Depaifve, Julien Mahin, Arnaud Wolf et Yzaora Tchuitio Yagang. Merci pour votre travail, votre effort et votre ténacité. Ils sont une pierre angulaire de cet édifice. Merci aussi pour votre curiosité et votre créativité, pour vos échecs et vos doutes. Ils ont consolidé ce projet et lui ont donné des formes que je n'aurais pas su créer tout seul. Merci de tout cœur d'avoir été une source inépuisable de motivation, un moteur pour aller de l'avant jusqu'à la fin. Merci de votre amitié et votre soutien.

Merci querida Jacqueline Boniver et ¡gracias ! Jean-François Statsijns. Votre aide a facilité sans cesse mon travail au laboratoire ; votre soutien discret et inébranlable a fait la différence.

Merci aussi à mes collègues du laboratoire de Chimie Inorganique pour l'aide reçue tout au long de mes recherches ainsi que pour les moments de détente passés en votre compagnie. De façon plus particulière, je tiens à remercier Tommy « el Papi » Haynes et Anto Desmecht de m'avoir apporté une légèreté bienveillante pendant toutes ces années. Merci aussi d'avoir veillé sur l'activité virtuelle de mon ordinateur ! Merci Béatrice Vanhorenbeke pour ton écoute, ta présence et tes encouragements. Et merci Florence Pennetreau de m'avoir accueilli et accompagné lors des premières années comme tu l'as fait.

De même, je remercie vivement mes collègues du Projet « Nano4Waves », Yann Danlée et Rajkumar Jaiswar pour le travail réalisé ensemble, pour votre optimisme, curiosité et motivation contagieuses, vos idées et vos conseils.

A heartfelt 'thank you' to all-those-so-many fellow scientists and technicians who contributed to this research. Thank you for sharing your expertise, for making science with me: Prof. Benoit P. Pichon, Prof. Andrés Botello, Prof. Yaroslav Filinchuck, Prof. Yann Garcia, Pascale Lipnick, Laurence Ryelandt, Pierre Eloy, Koen Robeyns, Souley Djandjandi, Pascal Simon, David Spote, Claude Polenius, Anne Iserentant, Pascal Van Velthem, Aurélien Lherbier, Ester Tooten, Loïc van Oldeneel tot Oldenzeel, Victor Xhurdebise, Marinela M. Dîrtu, Nikolay Tumanov, Raphaël P. Hermann, Yinguo Xiao, Nathalie Mayer, Delphine Magnin, Nicolas De Crom, Nathalie Mager, David Spote, Victor Xhurdebise, Gäel Hamoir, Sergey Basov, Iurii Dovgaliuk, Jessica Campos, Henok Mesfin and Frederic Van Wonterghem.

Ce long camino a été fait avec vous. Et c'est à vous si nombreux que quiero también decir 'merci' :

A mis padres, José Mederos Silva y Madeleine Henry Grosjean. ¡Hasta aquí llegamos! Gracias por ser el alfa y durante tantos años, la base, el crisol y el motor. Por hoy ser quienes son y por quienes serán.

A mi hermana María Guadalupe Mederos-Henry, por mis primeras letras y calificaciones, por ser presencia y compañía en lo íntimo y la esencia. A ti Daniel Figueroa-Salinas. Y a mi sobrina, Sabina Figueroa-Mederos. Gracias por esta vida que nos une, por hacer sentido.

Tim Blaise, gracias por ser un barco, una granada, la menta. Por nuestros claroscuros y nuestras montañas, por ser hogar conmigo.

A mis otros hermanos
[Masashi Kikushima, Cristina Díaz, Tania Martínez, Ingrid Arriaga, Carlos Omar Heras, Enrique y Zamantha Rosas, Mariana Madrigal, Jessica Lewinsky, Gilda María Pasco (tu güero, mis sobrinos), Yanel de Moral, Gabriela González, Alberto Guillermo López.

A esta encarnación tuya, Ana Laura Camacho Puebla. Un uno de antes del principio, la luz en la sombra.

A ti Chuchis Geniets por la vida que pasa a través de tu mano y tu abrazo.

Por todo el émerveillement que comparto contigo Francisco Castro Miranda.

Et à Justine de Moriamé, pour ce qu'il y a de beau.

Y por la paciencia y confianza a las que hay que agregar la esperanza, Zoé Miratorres.

And, indeed, gracias Juani por tus relecturas.]

Et à tous ceux tan magníficos : Karen Bonne, Rafael Costa, Olivier Schmidt, Andrés Botello, Fréderic Rolland, Jasper de Smedt, Brecht DS, Grégory Hye, Kris Snick, Johan Maricq, Maëlle Toubert, Irina Carrillo, Sam Zarka, Terry Scott.

Merci Pascale Pillon. À toi Thijsje. A ustedes, Profesores Videa. Pour ces vastes espaces.

Merci Jana Sanyova pour ton soutien formidable.

Merci Marie Postec pour cette confiance créatrice. À vous, Sarah Benrubi et Estelle Van Geyts, pour votre accueil du cœur et vos mains tendues. Et à mes collègues de La Cambre et de l'IRPA-KIK, merci - heel hartelijk bedankt, pour ces partages enrichissants et votre bienveillance.

À mes étudiants, pour votre effort qui me motive, votre curiosité qui me fait apprendre, pour ce privilège de créer un des liens les plus signifiants qui puisse être établi.

Aux Henry. À vous Marc-Hubert et Géneviève, merci de votre empreinte lumineuse et votre puissance. À vous Anne et Willy de Roo, pour votre accueil attentionné, Nadia Grégoire, Francis Wilmart, merci de m'avoir ouvert vos portes et vos bras. Stéphane Depret, pour ce lien qui soutient. Merci à toute la troupe « Tinou », à la cheftaine Catherine. Merci Marie-Jeanne Brichard d'incarner ce que l'amour a de plus puissant.

Aux Gaumais, pour vos attentions chaleureuses. Virginie et Joël Blaise, Philippe Willemsen, Laurent, Géneviève et Lise Daniel-Stassain, Camille Lambert, Ingrid Delferière et Estelle Fischer.

À vous tous, con el corazón en la mano, je vous dis

'gracias'.

Decoration of nanocarbon supports with magnetic nanoparticles for the control of electromagnetic propagation

Submitted by

Francisco Jos Jorge MEDEROS HENRY

In partial fulfi lment of the requirements for the degree of

Doctor of Philosophy in Science

at the

Universit catholique de Louvain

Supervised by

Professors Sophie Hermans & Isabelle Huynen

Louvain la Neuve, Belgium

2019

doctoral commitee

supervisors

Prof. Sophie Hermans
UCLouvain/IMCN, Louvain-la-Neuve, Belgium

Prof. Isabelle Huynen
UCLouvain/ICTEAM, Louvain-la-Neuve, Belgium

president

Prof. Jacques Devaux
UCLouvain/IMCN, Louvain-la-Neuve, Belgium

secretary

Prof. Arnaud Delcorte
UCLouvain/IMCN, Louvain-la-Neuve, Belgium

members

Prof. Carla Bittencourt
UMons/Chimie des Int-ractions Plasma-Surface, Mons, Belgium

Prof. V-ronique Dupuis
Universit- Lyon 1 /Institut Lumi-re Mati-re, Villeurbanne , France

Prof. Jean-Pierre Raskin
UCLouvain/ICTEAM, Louvain-la-Neuve, Belgium

Acronym	Definition
A	Absorption
AC	Autoclave synthesis
AC-C	Autoclave synthesis using a complex metal precursor
AC-S	Autoclave synthesis using a salt metal precursor
AFM	Antiferromagnetic magnetic order
AP	Ambient pressure synthesis
APTES	(3-Aminopropyl)triethoxysilane
ARC	Action de recherches concertée
BCC	Body-centered cubic crystal structure
BCRC	Belgian Ceramic Research Center
BSMA	IMCN's Bio- and Soft Matter Pole
CA	Citric acid
CA	Circuit analogous
CNT	Carbon nanotube
CO	Carbon monoxide
COV	Covalent linkage synthesis
CPW	Coplanar waveguide
DC	Direct current
DCOP	Direct co-precipitation synthesis
DNG	Double negative materials
DPS	Double positive materials
DUT	Device under test
EB	Exchange Bias
EBG	Electromagnetic Bandgap Materials
EG	Ethylene glycol
EHS	Electromagnetic hypersensitivity disorder
ELEN	ICTEAM's Electrical Engineering Department
ELI	UCLouvain's Earth and Life Institute
ELIE	ELI's Environmental Sciences Department
EM	Electromagnetic
EMC	Electromagnetic compatibility
EMI	Electromagnetic interference
EMRA	Environment and Materials Research Association

EMWs	Electromagnetic waves
ENG	Epsilon-negative materials
ENZ	Epsilon-near-zero materials
EPR	Electron paramagnetic resonance
EU	European Union
FBW	Fractional Bandwidth
FCC	Face-centered cubic crystal structure
FiM	Ferrimagnetic magnetic order
FM	Ferromagnetic magnetic order
FMR	Ferromagnetic resonance
FSS	Frequency-selective surface
GHz	Gigahertz
GNPs	Graphene nanoplatelets
GO	Graphene oxide
GR	Green rusts
HCP	Hexagonal close packed crystal structure
HRTEM	High-resolution transmission electron microscopy
ICP-AES	Inductively coupled plasma atomic emission spectroscopy
ICTEAM	UCLouvain's Institute for Information and Communication Technologies Electronics and Applied Mathematics
IF	Intermediate frequency
IMAP	IMMC's Materials Process and Engineering pole
IMCN	UCLouvain's Institute of Condensed Matter and Nanosciences
IMMC	UCLouvain's Institute of Mechanics, Materials and Civil Engineering
IPCMS	Institut de Physique et Chimie des Matériaux de Strasbourg
JC	Jerusalem-cross
LHM	Left-handed materials
LR	Loading rate
M	Metal
MAM	Microwave absorbing material
MaNP	Magnetite nanoparticle
MD	Multimagnetic domain
MNG	Mu-negative materials
MNP	Magnetic nanoparticle

MNZ	Mu-near-zero materials
MOST	IMCN's Molecular Chemistry, Materials and Catalysis Pole
MS	Microstrip
MWCNT	Multi-walled carbon nanotube
NcS	Nanocarbon supports
NcP	Nanocomposite particle
NIM	Negative refraction index material
NiNP	Nickel nanoparticle
NMR	Nuclear magnetic resonance
NP	Nanoparticle
ox-MWCNT	Oxidized multi-walled carbon nanotube
PC	Polycarbonate
PEG	Polyethylene glycol
PTFE	Polytetrafluoroethylene
PVP	Polyvinylpyrrolidone
rGO	Reduced graphene oxide
RT	Relative thickness
SD	Single magnetic domain
SE	Shielding effectiveness
SEM-EDX	Scanning electron microscopy with coupled energy-dispersive X-ray spectroscopy
SHF	Microwave super high frequency band
SOLV	Solvothermal synthesis
SPL	Superparamagnetic limit
SPM	Superparamagnetic state
SQUID	Superconducting Quantum Interference Device magnetometer
SRR	Split ring resonators
SWCNT	Single-walled carbon nanotube
TEM	Transmission electron microscopy
TEOS	Tetraethoxysilane
TGA	Thermogravimetric analysis
THF	Tetrahydrofuran
TL	Transmission line
TMAOH	Tetramethylammonium hydroxide
TMAX	Maximum temperature

ToF-SIMS	Time of flight secondary ion mass spectrometry
TREG	Triethylene glycol
UNISTRA	Université de Strasbourg
USA	United States of America
UWB	Ultra-wideband absorber
VNA	Vector Network Analyzer
VSM	Vibrating sample magnetometer
XPS	X-Ray photoelectron spectroscopy
XRPD	Powder X-Ray diffraction
ZF	Field-cooled SQUID analysis
ZFC	Zero-field cooled SQUID analysis
ZVI	Zero-valent iron


intr
cti

odu
on

Electromagnetic waves (EMWs) consist of the synchronized oscillation of an electric (E) and a magnetic (H) field components of equal energy. EMWs are grouped into seven bands according to their wavelengths, corresponding photon energy ranges and applications, constituting what is known as the electromagnetic spectrum (see Figure 1).

Electronic systems and telecommunication devices based on low-power microwave EMWs, ranging from 2 to 40 GHz, have been massively developed in the last decades. This frequency window has been chosen for several reasons. On the one hand, it allows producing narrower EMW beams than radio waves, thus allowing frequency reuse [1, 2]. On the other hand, they provide higher data transfer rates and broader bandwidths [1]. Furthermore, earth's atmosphere is more or less transparent to microwaves below 40 GHz.

First used in 1958 to convey free-space power transmission [2], microwaves are nowadays employed in a myriad of applications that define our contemporary way of life. From point-to-point communication links to wireless networks, microwave radio relay networks, radar, satellite and spacecraft communication, collision avoidance systems, remote sensing, radio astronomy or even ovens for cooking and garage door openers, microwaves have become ubiquitous. Furthermore, the current communication apparatus must support multiple frequency bands. The mobile phone is so far the most common example with a tri-band, quad-band or penta-band embedded system [3]. This multiplication of narrow frequency bands products is extremely complex because of massive and entangled signal transmission and reception.

The extensive use of these media has contributed to the emergence of diverse electromagnetic interference (EMI) or pollution problems [4-6].

EMIs can be defined as conducted and/or radiated electromagnetic signals emitted by electrical circuits which, under operation, perturb proper operation of surrounding electrical devices or cause radiative damage to living/biological species [4].The interference issue can occur between different devices, amongst subcomponents of sensitive devices themselves or between the power microchips [7].

Furthermore, in the last decade, the so-called electromagnetic hypersensitivity (EHS) disorder has been attracting worldwide attention given its potential consequences on public health. Individuals affected by EHS report a range of non-specific symptoms (*e.g.* headaches, fatigue, subjective cognitive problems or sleep disturbances [8, 9]) that are triggered by exposure to EMWs such as those commonly used in current telecommunication systems (10 MHz-300 GHz). Even though no precise scientific basis has yet been given to this phenomenon [10, 11], efforts have been placed in establishing precise exposure limits for a wide diversity of appliances. Such is the case of the specific absorption rates (SAR) defined for radiofrequency-based devices. For instance, current 4G cellphones, operating between 2 and 8 GHz, have a maximum 1.6W/kg SAR. Considering such a SAR limit and the power involved during cellphone usage, an average person should not make use of such a device for more than 24 minutes per day [12]. However, these specific SAR limits were defined in 1996 and are thus growingly considered outdated and useless to evaluate real exposure risks in our current hyperconnected society. Consequently, the debate about the health risks posed by EMWs continues to rage and epidemiological studies with adequate statistical significance, based upon large numbers of participants with sufficient latency and intensity of exposure to specific EMW frequencies, are being demanded [13].

Considering the potential impact of such disruptive effects, EMI shielding has become a ubiquitous necessity and, in certain countries, a legal requirement. For instance, the European Union (EU) member states have adopted and thrice updated an electromagnetic compatibility (EMC) directive applying to any electronic equipment which is "liable to cause electromagnetic disturbance or the performance of which is liable to be affected by such disturbance" [14] in a frequency range comprised between 0 Hz to 150 KHz [15]. In order to achieve EMC conformity, all these electronic devices must now integrate EMI shielding materials in order to be sold and/or used in the EU territory.

Nowadays, broadband absorption is the unique convincing solution in various circumstances (*e.g.* dysfunction of microchips, disturbed signal transmission, EM pollution or EHS disorders) where the complete disappearance of the unwanted microwave is desired. However, new sophisticated devices require a smart management of absorption in specific bands. Indeed, multi-band telecommunications are already essential for many usual devices, as mentioned above. Where the bands are widely separated in frequency, parallel transmit and receive signal path circuits must be provided, which increase the cost, complexity and power demand of such multi-band devices [15, 17]. Therefore, an active quest for novel and effective EMI shielding materials animates current scientific research in this area.

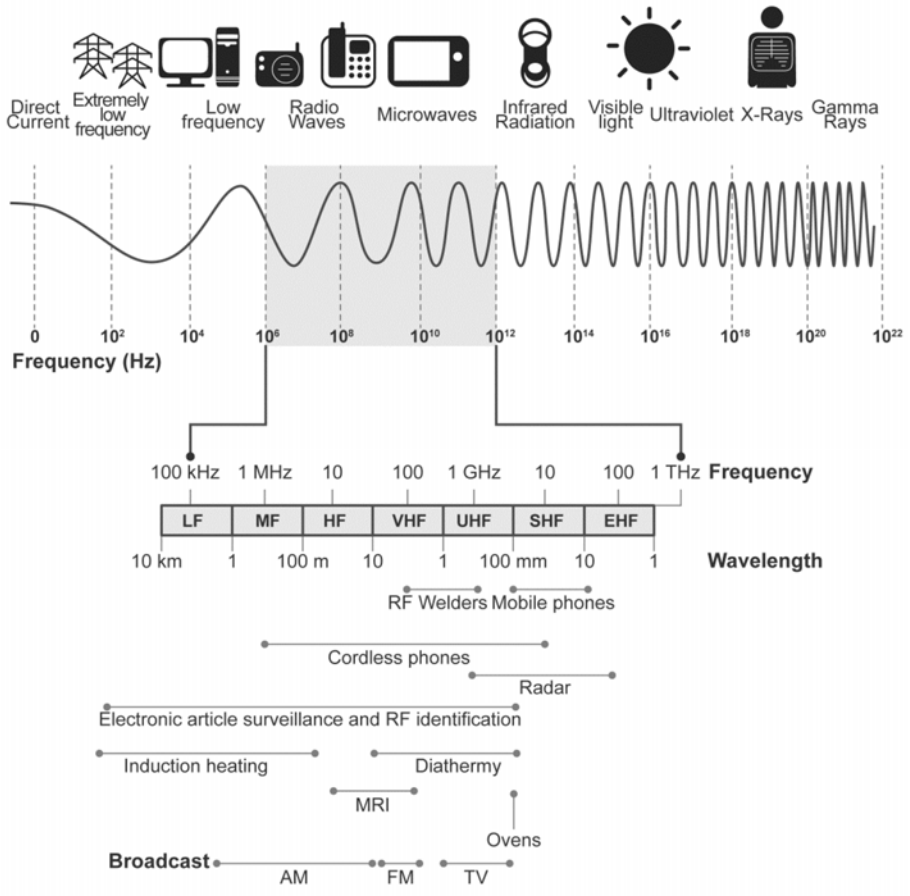

Figure 1 - Representation of the electromagnetic spectrum and its subdivisions. Particular emphasis is placed on the subdivisions of the radio and microwaves ranges as well as some of their applications in contemporary life. Adapted from [18].

1.1 Electromagnetic interference (EMI) shielding materials: physical principles and classification

EMI shielding can be achieved either through reflection, absorption or multiple reflections of the unwanted EMWs. The classical EMI shielding solution is based on EMW reflectors such as metal foils or coatings (*e.g.* Faraday cages) [19], operating from direct current (DC) to high frequency microwaves. However, EMW reflectors are usually heavy, expensive, voluminous and hardly shapeable EMI solutions. Also, given their metallic nature, they are often prone to corrosion and thus require constant maintenance. Novel, non-metallic or corrosion-resistant, highly conductive, composite materials have been recently proposed [20, 21] to overcome the above-stated drawbacks of classical EMW reflectors. However, in all cases, these methods are being increasingly considered unsatisfactory given that they simply deflect the unwanted electromagnetic signal, shifting the problem elsewhere.

Electromagnetic shielding by absorption is a much better option as it radically solves the problem by removing the disruptive EMW completely. If electromagnetic absorption is specifically situated in the microwave range, then these materials are called microwave absorbing materials or MAMs. In ideal conditions, optimal MAMs must minimize reflection while greatly reducing transmission of the incoming EMW. The physical principles underlying a MAMs ability to operate in such a particular manner will be briefly presented in the following section.

1.1.1 EMI shielding physical principles

When an electromagnetic wave encounters a given material, the latter can reflect, absorb or transmit the incoming EMW at different rates (see Figure 2). All three mechanisms participate in what is called electromagnetic attenuation, the exponential decrease with distance of

the intensity or power of an EMW as it passes through a particular material.

A given material's transmission (T), reflection (R) or absorption (A) ratios can be obtained by measuring the incoming (P_{in}), reflected (P_{ref}) and transmitted (P_{out}) EMW power [22, 23], as defined by the following equations:

$$T = \frac{P_{out}}{P_{in}} \qquad \textbf{Equation 1.1}$$

$$R = \frac{P_{ref}}{P_{in}} \qquad \textbf{Equation 1.2}$$

$$A = \frac{P_{abs}}{P_{in}} = \frac{P_{in} - P_{ref} - P_{out}}{P_{in}} = 1 - R - T \qquad \textbf{Equation 1.3}$$

The material's effective absorption, A_{eff}, can be known if the absorption rate is normalized by the remaining intensity of the EMW after primary reflection:

$$A_{eff} = \frac{1 - R - T}{1 - R} \qquad \textbf{Equation 1.4}$$

As can be deduced from Equation 1.4, an efficient MAM must minimize transmission while keeping a low reflection coefficient.

Such a material's ability to transmit or reflect an incoming EMW will mostly depend on two of its bulk physical properties: its electrical permittivity, ε, and magnetic permeability, μ [24]. The electrical permittivity describes a material's ability to be polarized as it is subjected to an applied electric field. This polarization originates from electronic, atomic, dipolar or ionic sources found in the material. Likewise, the magnetic permeability characterizes the ability of a material to support the formation of a magnetic field within itself. In other words, it represents the degree of magnetization that a material acquires as it is exposed to an applied magnetic field. It arises from the

presence of spin magnetic moments of elementary particles, mostly the electrons.

The relationship between transmission of an incoming EMW, *T*, and a given material ε and μ parameters is given by Equation 1.5:

$$T = e^{-i\omega t\sqrt{\epsilon\mu}} = e^{-\frac{i\omega t}{c}\sqrt{\varepsilon_r\mu_r}} \qquad \textbf{Equation 1.5}$$

Where *t* is the thickness of the material, ω is the frequency or pulsation of the incoming EMW, *c* is the speed of light in vacuum, *i* is the imaginary number and ε_r and μ_r are the relative permittivity and permeability.

Likewise, Equation 1.6 describes how reflection, *R*, at the interface of a given material interacting with an incoming EMW, depends on the relative permittivity and permeability values of the material:

$$R = \frac{\sqrt{\frac{\mu_r}{\varepsilon_r}} - 1}{\sqrt{\frac{\mu_r}{\varepsilon_r}} + 1} \qquad \textbf{Equation 1.6}$$

Both *T* and *R* vary as the frequency, ω, of the incoming EMW changes given that both ε and μ are also frequency-dependent. It is for this reason that both physical parameters are also commonly noted as $\varepsilon(\omega)$ and $\mu(\omega)$.

In Equation 1.6, the term $\sqrt{\mu_r/\varepsilon_r}$ is also known as the impedance, *Z*, of dielectric materials. Impedance is commonly used to describe and classify EMI shielding materials, as will be discussed in the following section.

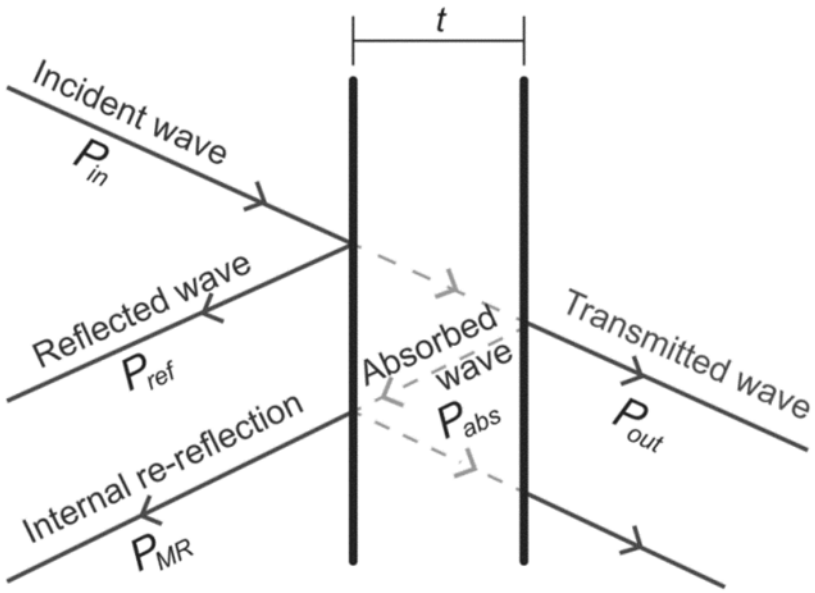

Figure 2 – Reflection, absorption and transmission phenomena occurring when an EMW encounters any given medium.

1.1.2 Classification of EMI shielding MAMs

As shown in the previous section, the dielectric properties of a MAM must be carefully selected in order to minimize reflection. Indeed, as the relative permittivity of the incident wave medium and that of the shielding material differ, an impedance mismatch is created. EMW reflection is proportional to the magnitude of such an impedance mismatch.

Thus, depending on their impedance values, MAMs can be grouped in two main categories: impedance matching and resonant absorbers [25]. In both cases, they are able to shield against a large range of frequencies and for such reason, they are considered as broadband shields. However, MAMs belonging to the former category show null or small differences of impedance with respect to the incident medium. Consequently, incoming wave reflection on their surface is greatly reduced. Several well-known designs belonging to this category are the pyramid, tapered loading or matching layer absorbers (see Figure 3, top row). Even though they provide excellent absorption performance, impedance matching absorbers are usually thick and fragile.

The second category includes materials that have different impedance values from that of the EMW incident medium. Therefore, these materials do not absorb all the incoming electromagnetic power. Indeed, part of the wave undergoes a first reflection on the surface of the material while the rest is transmitted to its interior. A thin metal coating found on their backside produces a second reflection. If the distance between the two reflection phenomena is equal to a multiple of half the incoming EMW wavelength ($\lambda/2$), the two reflected waves will destructively interfere. Some of the most common resonant absorber designs are the Dallenbach layers, the Salisbury screens and the Jaumann layers (see Figure 3, bottom row).

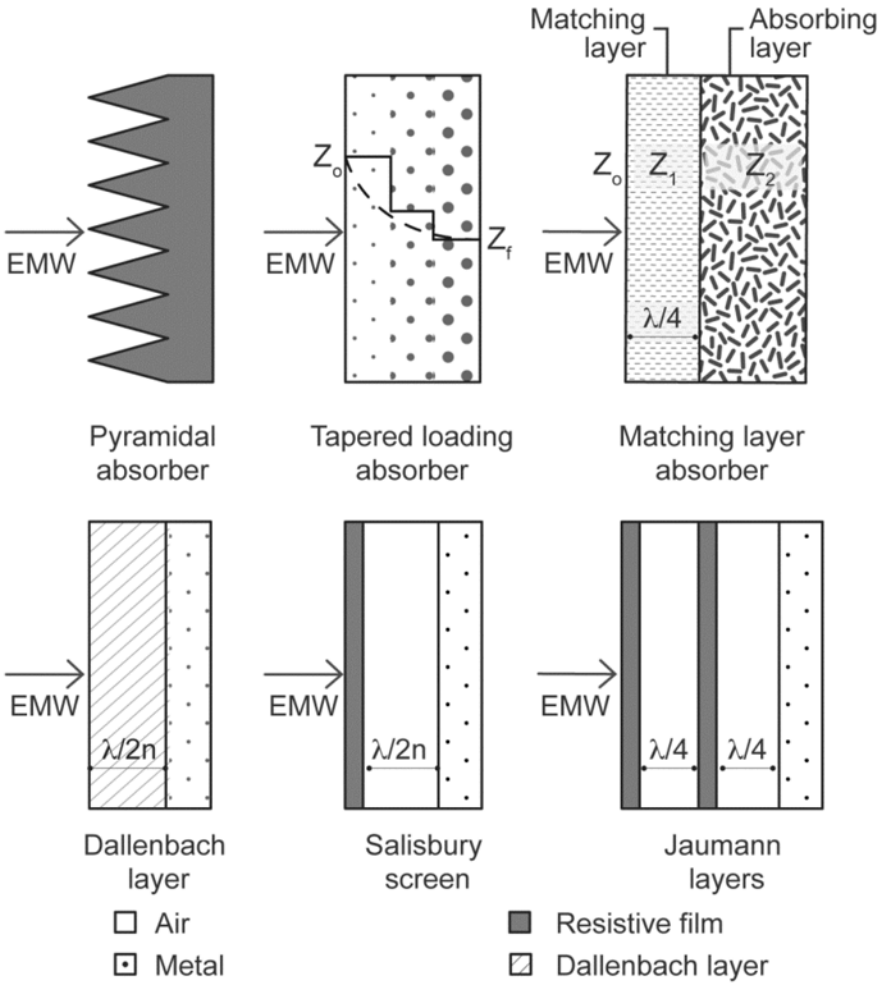

Figure 3 – Common designs for impedance matching (top row) and resonant (bottom row) absorbers. Adapted from [25].

1.2 Metamaterials: tailoring the electromagnetic properties of matter

Metamaterials are entirely man-made materials exhibiting electromagnetic properties that cannot be found in nature [26, 27]. Indeed, by engineering these materials electrical permittivity, ε, and magnetic permeability, μ, the scientific community has produced a new type of artificial materials that dramatically affect the propagation of EMWs in unprecedented ways [28, 30].

Strictly speaking, metamaterials are considered to be at the interface between a material and a device because they are able to implement some functions themselves and thus are more than a mere support used for device fabrication, as regular materials are [28]. For this reason and because of their tunable exceptional electromagnetic properties, metamaterials are considered a scientific and technological revolution that will provide a totally new set of exciting functionalities. From invisibility cloaks to high-resolution imaging systems, the scientific literature from the past decade is thus thriving with an ever-continuously growing number of suggested applications for this type of materials.

Up to this point, most of these applications have been designed for the microwave region of the electromagnetic spectrum [26, 28] and thus, in the years to come, metamaterials are expected to effectively play a key role in future electronic devices [29]. In fact, it has been proven that the main limitations of conventional microwave components can be overcome if they are appropriately loaded with some of the already-existing metamaterials, thus opening the door to a revolutionary ultracompact generation of devices with improved performances [28].

Given that a metamaterial uniqueness resides in its non-traditional electromagnetic properties, most of the classification systems that have been proposed for them are based on the values of their electric permittivity, ε, and magnetic permeability, μ, values, parameters that describe their electromagnetic behavior [27, 28]. Figure 4 shows a popular representation of one such classification, the Epsilon-Mu chart, in which the different categories correspond to particular combinations of permittivity and permeability values.

The right top quadrant of this chart corresponds to those materials with positive values for real parts of both ε and μ, being thus usually called *double positive materials* (DPS). Most conventional natural and artificial materials can be found in this quadrant.

On the other hand, in the down left quadrant, the so-called *double negative* (DNG) or *left-handed* (LHM) materials possess negative values for real parts of both ε and μ, a combination of constitutive parameters that is not found in nature. The first studies on the fundamental properties of LHMs are commonly credited to the Russian physicist Victor Veselago who theoretically postulated their existence in 1967 [30]. According to Veselago, one such material would possess a negative refraction index and exhibit unconventional electromagnetic properties such as the backward propagation of waves, where electromagnetic energy and phase-front (or phase-velocity) are transmitted in opposite directions even though the material is isotropic and homogeneous [30].

However, it is only within the last two decades that LHMs were finally produced. This important delay was partly due to the fact that, although it is well known how to obtain a material with $\varepsilon < 0$, the creation of a $\mu < 0$ material was particularly challenging given that there are no naturally occurring materials with negative μ [31]. This difficulty was experimentally overcome in the year 2000, when Smith *et al.* [32]

reported the first negative refraction index material (NIM) created by separately constructing and then combining two basic units: an array of wires, element yielding a $\varepsilon < 0$, and an array of split ring resonators (SRR), a design made of concentric metallic rings with gaps that exhibits a $\mu < 0$ regime around its magnetic resonance frequency [31].

The two other quadrants of the chart in Figure 4 correspond to materials having the product $\varepsilon\mu < 0$. These materials can be classified as either *Epsilon-negative* (ENG) or *Mu-negative* (MNG), depending on whether their ε or μ has a negative real value, respectively. Generally speaking, when such materials are exposed to a frequency range that implies a negative value for ε or μ, a stopband phenomenon is observed where pure attenuation of forward waves with no propagation occurs [26]. Nonetheless, it is important to notice that not all ENGs or MNGs are metamaterials, since there are natural materials that possess these properties. However, one such material is effectively considered a metamaterial when it exhibits such properties at frequencies where natural materials do not [30].

Other classes of metamaterials correspond to those materials possessing $-1 \leq \varepsilon, \mu \leq 1$ values. These "low-value" materials are classified as either *Epsilon-near-zero* (ENZ) or *Mu-near-zero* (MNZ) materials, while those materials exhibiting low values for both parameters are called *near-zero-index* or *zero-index* materials. On the other hand, materials with extremely high values of ε or μ are always considered metamaterials since no natural material exhibits these characteristics. Few examples of these so-called *Mu-very-large*, *Epsilon-very-large* or *very-large-index* materials exist [28].

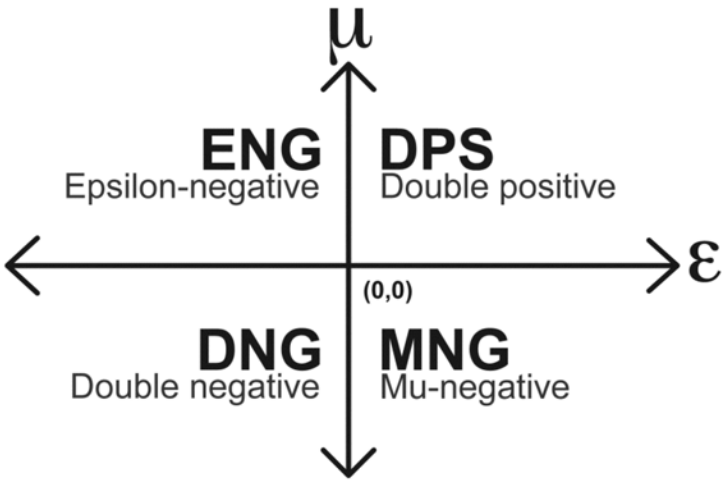

Figure 4 - Terminology and classification of metamaterials according to their ε and μ values. Adapted from [28].

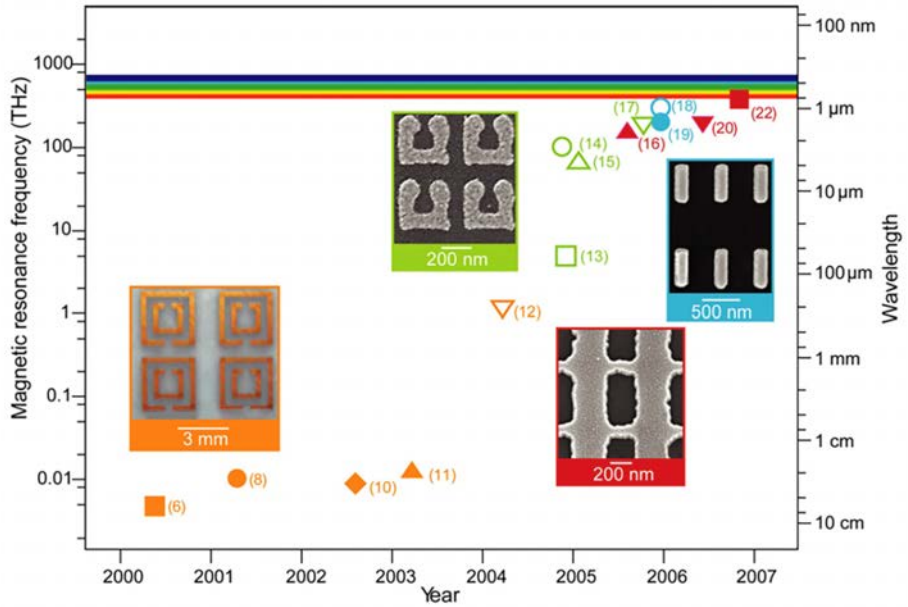

Figure 5 - The progress in the negative permeability, μ, and negative index, n, materials up to 2012. The solid symbols denote n<0 while the open symbols denote μ<0. The numbers in parenthesis correspond to the number of scientific publications published each year for each type of design. The different designs are represented by different colors: orange belongs to designs based on split-ring resonators (SRR); green corresponds to U-shaped SRR designs; blue denotes metallic cut-wire pairs while red stands for the fishnet designs. The actual appearance of each design can be appreciated in the four inset pictures. Taken from [31].

1.2.1 Metamaterials design parameters and production methods

As it can be noticed from the previous section, a wide range of different metamaterials can be produced if a rational design is skillfully translated into a large-scale assembly of electrically and magnetically responsive inclusions that allow for the precise control of ε or μ values.

Given the exceptional properties and enthusing potential applications of LHMs, this specific type of metamaterials has received the most attention. LHMs were thus the first ones to be produced experimentally and are actually the most studied and well-known class of metamaterials [31]. Whatsoever, it is supposed that if the basic logic underlying LHMs construction is followed, any type of metamaterial with particular values of ε and μ can be produced.

Most of the first LHMs were designed to be responsive in the GHz frequency region and were based on Smith *et al.* [32] first prototype. However, alternative designs such as the cut and continuous wires or the fishnet structure [31], were also explored to obtain negative refraction indexes at higher frequencies (*e.g.* visible frequency range), giving promising results.

Figure 5 represents the fast-paced evolution of these metamaterials' design and the consequent shift toward higher operation wavelengths. It also clearly shows that the size of the resonant inclusions is inversely correlated to the frequency of operation, noted λ by Soukolis *et al.* [31]. Thus, in order to reach higher operation frequencies, the designed inclusions have had to shrink from the millimeter to the nanoscale. However, besides having a direct influence on λ, the size of the inclusions is also of extreme importance since the relationship between λ and the unit cell size, a, has to be kept such that $a << \lambda/10$. If this requirement is not met, the metamaterial could barely be

considered as an effective continuous medium and thus homogenization techniques yielding mixing rules, essential for the design procedures given they can predict the metamaterial effective parameters, could no longer be used. Besides the size, Bilotti and Sevgi [28] have also underlined that the inclusions alignment, shape/geometry, abundance and spatial periodic or random distribution in a host material are also significant parameters for the control of both ε and μ.

Currently, the most common approach for the production of this first generation of metamaterials has been the so-called structural approach. This method creates the different inclusions with fabrication techniques used traditionally in the field of electronics for integrated circuit production [27]. Shadow mask/etching methods related to photolithography in the visible or ultraviolet range and electron/laser beam lithography techniques have been widely used to create a variety of millimetric to nanometric inclusions bearing the different patterns mentioned above.

However, the structural approach is clearly reaching its limits, especially when the downscaling of these inclusions to the nanometric range is concerned. These restrictions are drawn either because these techniques have relatively poor resolution limits or because it is practically impossible to use them in large-scale production. For example, in the case of electron beam lithography, the achievable practical resolution is in the range of 10-20 nm [33], the best that can be obtained with the set of techniques currently in use. Unfortunately, the instruments needed for this lithographic procedure are extremely costly and production times are lengthy.

An increasingly explored alternative to the structural methods are the chemical techniques, that can be considered bottom-up routes when

compared to the above-mentioned techniques that are top-down [27]. While being able to create nanoparticles and nanostructures that can easily comply with the dimensional constraint $a << \lambda/10$ described above, the chemical methods can also easily offset the resolution drawbacks presented by conventional lithographic techniques. Furthermore, producing larger amounts of the necessary inclusions is feasible, a requirement that must be met if the industrial production of metamaterials is to be sought.

The choice of the chemical methods employed to produce a metamaterial greatly depends on the application for which it has been designed. For instance, the spatial periodical arrangement of the electromagnetic-active inclusions is a strict requisite if the metamaterial is to be used in optical-frequency applications such as perfect lensing, magnifying sub-diffraction limited objects, or a visible-light invisibility cloak [26, 34]. Indeed, the presence of disordered areas in such a metamaterial is known to reduce and broaden their resonant response or cause a shift in their resonance frequency, also causing greater dispersivity and loss and thus reducing their overall-performance [27]. However, the latter characteristics specific to a disordered or non-periodical metamaterial are actually beneficial if it is intended to be used as a EMW absorber.

Consequently, the scientific community has extensively experimented by combining nanochemistry and self-assembly methods [35-39] to produce optical metamaterials possessing a regular pattern across a large area or volume. The proposed optical metamaterial structures are extraordinarily diverse but are mostly based on nanoparticles composed of noble metals (Ag or Au) [40-42], tightly packed around a dielectric core [40, 43, 44] or dispersed in it [45-47] and quite often presented as liquid crystals [43, 48, 49].

However, if the metamaterial is intended for applications that rely on wave absorption, as is the case of EMI shielding, randomized inclusions are tolerated as long as their sizes are maintained in the nanoscale. Indeed, if the diameters of the produced electromagnetic-active inclusions and the distance between them is much smaller than the intended operational wavelength, resonance phenomena related to wave diffraction on the lattice are not expected [50].

The metamaterial design paradigm, centered on the sophisticated, independent control of the material's ε and μ parameters, can be particularly useful to produce highly efficient microwave absorbing materials (MAMs) with low reflectivity. As explained in Section 1.1.1, the capacity of a material to absorb or reflect an incoming EMW is intimately linked to its ε and μ parameters. Therefore, a metamaterial approach to a MAM design would allow to independently control the values of both parameters so that, ultimately, absorption is favored over reflection. Furthermore, in order to promote absorption in these materials, the electromagnetic-active inclusions have to induce electrical and magnetic losses that contribute to dissipate the electromagnetic energy conveyed by the microwave.

Bearing this in mind, several metamaterial MAMs have been described in the scientific literature. Most of the proposed MAM solutions are multiphase composites, produced by mixing three different building blocks. The first component is an electrically conducting material, such as conducting polymers [51, 52], graphenic materials [53-56], carbon nanotubes (CNTs) [57-59] carbon fibers [60] or combinations of these [61]. The second is a magnetic material such as nanoparticles or microwires of ferromagnetic metals [62, 63] or ferrites [64, 65]. The third and last element is a dielectric material, mostly non-conductive polymers [53, 57, 59, 66].

1.3 Nanocarbon supports decorated with magnetic nanoparticles: a novel approach to metamaterial MAMs

Recently, Hermans, Huynen *et al.* [67] proposed to develop a new generation of MAM metamaterials using a *bottom-up* approach. *Via* an *Actions de Recherches Concertés* (ARC) project entitled "Nano4Waves", this team envisioned the synergic combination of three main building blocks: magnetic nanoparticles (MNPs), nanocarbon supports (NcS) and a dielectric polymeric matrix (see Figure 6).

These three basic units inherit the metamaterial MAM design logic described at the end of section 1.2.1. Nonetheless, one important difference opens the way towards a new type of MAM metamaterials: the control of ε and μ as to obtain Mu-negative materials is efficiently performed by a clever structuration of these three constituents, from the nano to the centimeter scale.

Indeed, by means of chemical assembly, the nanocarbon supports and the magnetic nanoparticles will produce a microwave-active MNP@NcS nanocomposite. Afterwards, these nanocomposites are to be dispersed in a dielectric polymeric matrix, allowing to control their abundance, spatial distribution and alignment, as well as the final material anisotropy, gradient and/or periodicity properties in one or two dimensions.

As will be discussed later, in section 1.4, the present thesis will develop the Nano4Waves design paradigm, focusing on the MNPs and NcS building blocks and their effect on the electromagnetic properties of the obtained materials. Therefore, the following two sections will review the physical mechanisms that can be exploited to control ε and μ *via* the NcS and the MNPs, respectively.

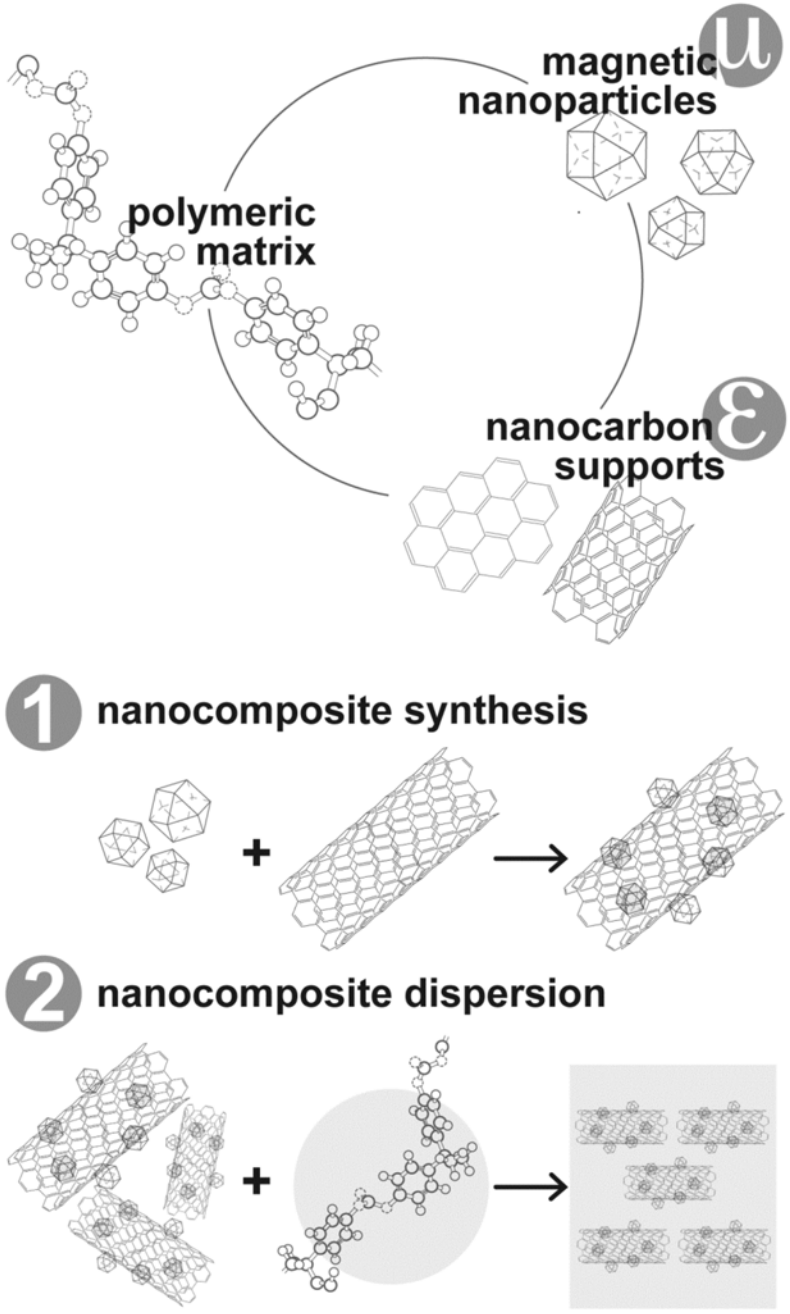

Figure 6 –The Nano4Waves paradigm: the chemical assembly of magnetic nanoparticles and nanocarbon supports produce novel nanocomposites that can later be dispersed in a host polymeric matrix to obtain novel MAMs.

1.3.1 The ε-control building block: graphene and carbon nanotubes as nanocarbon supports (NcS)

As mentioned in section 1.1.1, the electrical properties of a particular material can be defined through its electric permittivity, ε, which is intrinsically related to its conductivity, σ. Indeed, the electric permittivity indicates how a given medium responds when an electric field forms. As for conductivity, it is a measure of the material ability to allow the free motion of electrical charge carriers induced by an electrical field. Thus, it is defined as the inverse of electric resistivity and is linked to the electric permittivity by the following equation:

$$\varepsilon(f) = \varepsilon'(f) + i\varepsilon''(f) = \varepsilon_r\varepsilon_o(f) - i\frac{\sigma(f)}{2\pi f} \qquad \textbf{Equation 1.7}$$

The oscillating nature of an EMW implies that the value of ε varies with the frequency of the incoming EMW, *f*, due to a lag in response of materials to the external field [63]. Thus, the permittivity is written in terms of a real, ε', and an imaginary component, ε'', the latter being specifically related to dielectric losses. This two-term expression will be used to describe the electrical permittivity variations observed in the different systems that constitute this research project (*e.g.* the NcS, either pristine or decorated with MNPs, the composited obtained by the dispersion of the obtained nanocomposites in the polymeric matrix, etc.).

Dielectric losses, which dissipate the electric component of an incoming EMW, are mainly due to two mechanisms. The first one depends on the formation of electric currents within a given material. Indeed, energetic loss related to the conduction of electrical currents occurs by means of electrical resistance and heat generation. This

phenomenon is known as Ohmic conduction and is the principal source of dielectric loss [63, 68]. The second mechanism, contributing to a lesser extent to the dissipation of electrical energy, is called dielectric relaxation [69, 70]. It is related to polarization/relaxation of the permanent and induced molecular dipoles of the material hit by the incoming EMW.

The electrical properties of nanocarbons have been widely studied since Buckminsterfullerenes were introduced by Kroto in 1985 [71] and carbon nanotubes (CNTs) were presented to the scientific community by Ijima in 1991 [72]. Both fullerenes and carbon nanotubes are synthetic allotropes of carbon, made of sp^2 hybridized atoms similarly to graphite. However, while the former possess a spherical shape, the latter adopt a cylindrical, hollow cigar-like structure.

Fullerenes are classified according to the number of carbon atoms that make up their tridimensional structure, the archetypical member of this family being the Buckminsterfullerene made of 60 carbon atoms and thus also known as the C_{60} [71]. Likewise, carbon nanotubes are classified into two main categories depending on the number of coaxial cylindrical carbon tubes that compose them: single walled carbon nanotubes (SWCNTs) and multi walled carbon nanotubes (MWCNTs) [73].

As shown in Figure 7, all nanocarbons possess the same underlying structural element [73]. This building unit, called graphene, is a layer of one-atom-thick carbon sheet composed of fused aromatic hexagonal rings. Geim and Novoselov discovered graphene in 2004 [74], a discovery for which they were awarded the Nobel Prize in Physics in 2010 [75]. Ever since, this material has been in the spotlight

of international research efforts given its lightweight and exceptional mechanical, electrical and thermal properties [76, 77].

Given the difficulty to isolate a single layer of defect-free graphene, different types of closely related graphenic nanocarbons have also been described in the scientific literature. For instance, graphene nanoplatelets (GNPs) are obtained when not one but several atomic planes of graphene are isolated together. Also, if graphene, GNPs or graphite are treated using harsh oxidative conditions, such as the Hummers, Staudenmaier or Brodie's methods [78], an oxidized derivative, called graphene oxide (GO), is obtained. Finally, reduced graphene oxide (rGO) is most currently produced by submitting GO to either chemical, thermal, electrochemical or hydrothermal reduction processes [78].

Graphene and GNPs are poorly dispersible in solvents [76], a drawback that has been partially overcome by using graphene oxide instead. Indeed, GO, with its abundant oxygen-containing functionalities such as hydroxyl, epoxy and carboxyl groups (see Figure 7), is easily dispersible in water or polar organic solvents. It can also be chemically modified to present other functional groups on its surface, by reactions involving ester and amide bonds [79], being thus considered a more versatile precursor for a wider range of applications [78]. Furthermore, the introduced oxygenated groups are responsible for repulsive interactions between the graphene sheets, widening the interlayer spacing and preventing their agglomeration [79].

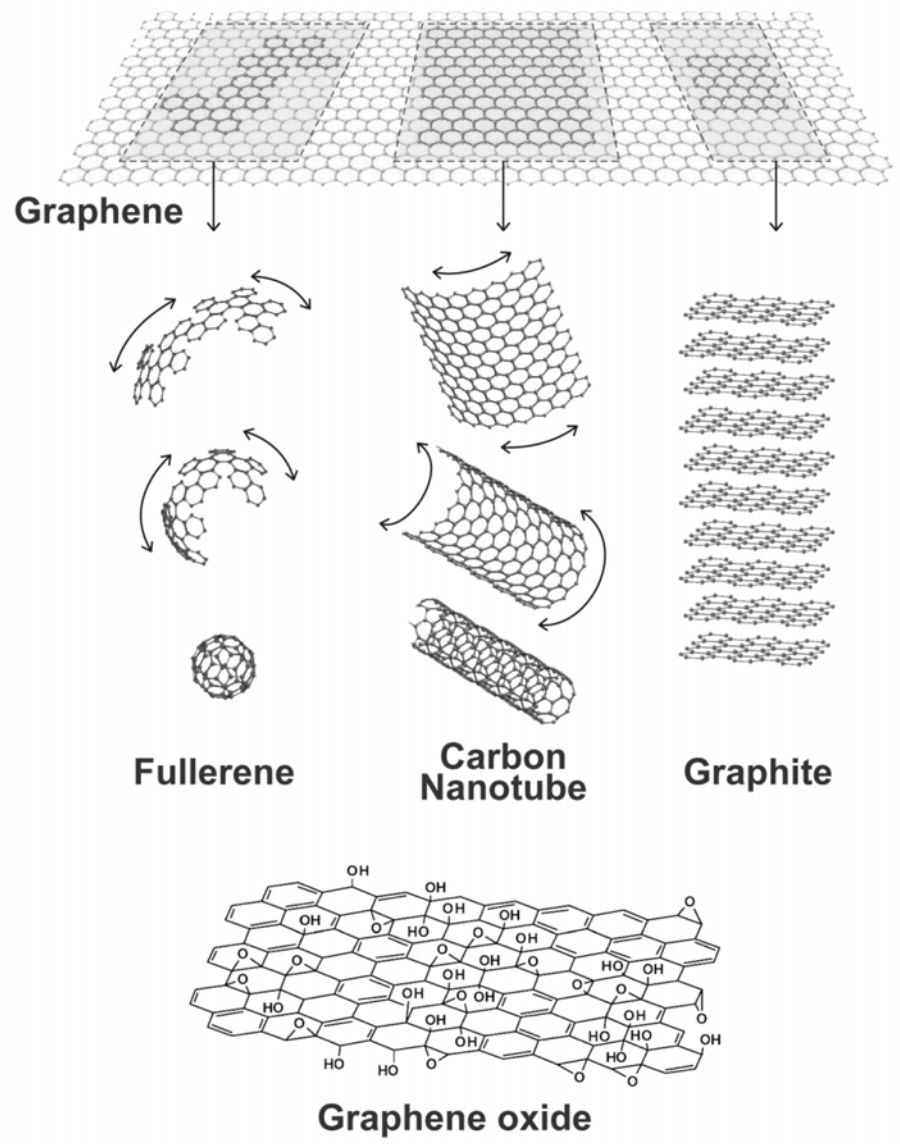

Figure 7 - Graphene is the 2D building material for nanocarbons of all other dimensionalities. It can be wrapped in a sphere to form a fullerene, rolled to yield a carbon nanotube and piled together to form graphite. If oxidized to create graphene oxide, different oxygen-containing functional groups are present. Adapted from [74, 79].

As mentioned above, each graphene layer is an extended aromatic network of sp^2 carbon atoms. Thus, it possesses a large number of highly mobile π electrons. Furthermore, given it has two atoms per unit cell, its valence and conduction bands are cone-shaped and meet at the K points of the Brillouin zone (80, 81). These particularities are responsible for single-layer, large-area, defect-free graphene to be a crystalline semimetal with zero bandgap [74, 80]. One of the most important consequences of such a zero bandgap, is the extremely high carrier mobility observed at room temperature. For instance, in the absence of charged impurities and ripples, mobilities of 200,000 cm^2/VS have been predicted (80). This property makes up for graphene's astonishing (theoretical) electrical conductivity, close to the conductivity quantum e^2/h per carrier type [74], where e is the elementary charge and h Planck constant. However, in practice, the direct current (DC) conductivity of graphene varies between 10^7 and 10^8 S/m [82], due to the difficulty of obtaining defectless, large-area, single sheets of graphene.

Defects in graphene can appear during its production or processing. They can also be deliberately induced by physical or chemical treatments [78, 83]. Such is the particular case of graphene oxide (GO) and reduced graphene oxide (rGO). In the case of the former, oxidation destroys the graphenic aromatic network to such an extent that most of the carbon atoms in this material are sp^3-hybridized [84, 85]. Consequently, the conductivity of GO is so low that it is considered an electrical insulator [79, 86]. As for rGO, the sp^2 network is partially restored by the reduction process [78]. Yan and Chou [84] have shown that rGO is constituted of ordered sp^2 domains scattered amongst highly disordered sp^3 domains with oxygen-containing functional groups and vacancies. These defects tend to scatter and/or trap charge carriers traveling through the sp^2 networks, limiting their mobility. The relative abundance and location of these defects depends on the

chosen reduction method, which thus greatly influences rGO's electrical properties [78]. Accordingly, DC conductivity values for rGO films reported in the scientific literature can vary from as low as 10 S/m [87] to as high as $6.3x10^5$ S/m [88].

The electrical properties of graphene nanoplatelets (GNPs) are poor when compared to those of an isolated graphene sheet [89]. Moreover, they can show an anisotropic behavior [91], similarly to graphite. Indeed, graphite, composed of a high number of stacked graphenic sheets held together by π-π interactions, shows a large anisotropy in its electrical conductivity. For instance, values reported in the scientific literature establish that the conductivity along the plane of the stacked sheets (indicated as $\sigma_{||}$) is between ten thousand [90] to a hundred thousand [92] times larger than normal to that plane (indicated $\sigma_{\perp}$). Interestingly, experimental data also show that the more oriented and parallel the graphene sheets are inside the graphitic crystal, the higher the anisotropy and the lower the $\sigma_{\perp}$ [92]. This is mostly due to the lack of coupling between the graphitic layers [93]. In the case of GNPs, differences between $\sigma_{||}$ and $\sigma_{\perp}$ have not been systematically explored. However, it is assumed that they would increase as the number of stacked graphenic sheets increases. In any case, typical in plane DC conductivity ($\sigma_{||}$) values reported in the scientific literature for GNP films vary between $\sigma \sim 10^4$ S/m [94] and $\sigma \sim 10^5$ S/m [95].

For carbon nanotubes, their electrical properties also vary significantly, from semiconducting to metallic. This unique feature depends on the nanotube structure (*e.g.* the orientation of the honeycomb lattice with respect to the tube axis) [96]. One way of apprehending how different CNT structures can be produced is to represent a carbon nanotube as a graphene sheet which has to be rolled up to form a cylinder (as shown in Figure 7). In such a case, graphene has to be rolled up so that a carbon atom from any given hexagon, for instance atom

labelled *O* in Figure 8, overlaps an equivalent carbon atom belonging to another ring, anywhere in the graphenic sheet (atom A in Figure 8).

The distance between *O* and *A* is called the helicity [97] or rolling vector [98], C_h, and represents the circumference of the as-created CNT. As shown in Figure 8, C_h can be decomposed into two vectors, parallel to the lattice vectors of graphene, a_1 and a_2. Hamada *et al.* (97) created a notation based on two helicity indexes *n* and *m* that allow to unambiguously describe each CNT structure. The values of *n* and *m* indicate the number of hexagons, from the graphene lattice, crossed by each of the vectors composing C_h. In the example shown in Figure 8, n=4 and m=2 so that the tube that would result from that rolling up action would be a (4, 2) SWCNT.

As also shown in Figure 8, the angle θ formed between C_h and the zigzag axis of the graphenic sheet is the helicity angle. Depending on the value of θ, CNTs can be classified into three categories: zigzag ($\theta = 0°$), armchair ($\theta = 30°$), or chiral ($0° < \theta < 30°$) (see Figure 9).

Due to their cylindrical shape, CNTs electrons are confined in one direction, along the nanotube axis. For this reason, electronic properties of CNTs strongly depend on their helicity and on their radii of curvature. For a radius of curvature above ~0.7 nm, all armchair SWCNTs exhibit a metallic conductivity behavior. Also, zigzag or chiral SWCNTs can be zero band gap semiconductors (and thus can be assimilated to a metal) if the difference between their *n* and *m* helicity indexes is equal to an integer multiple of 3 [99]. The rest of the SWCNTs are semiconductors. This means that, of the non-armchair SWCNTs, one third are metallic and two thirds are semiconducting.

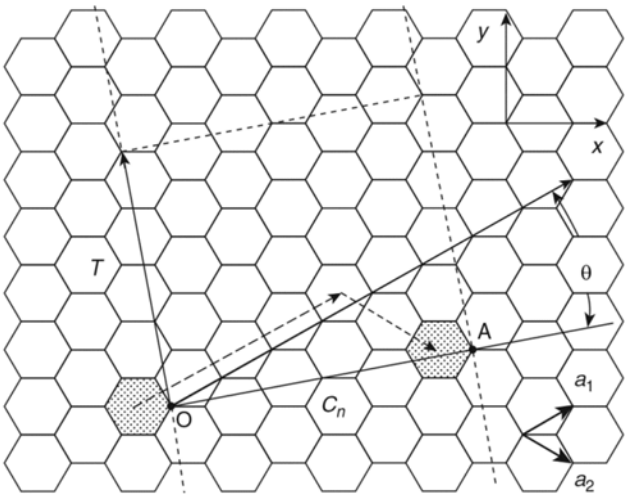

Figure 8 – Geometric rules allowing for the creation of any kind of SWCNT from rolling a flat graphene sheet into a cylinder. Taken from [96].

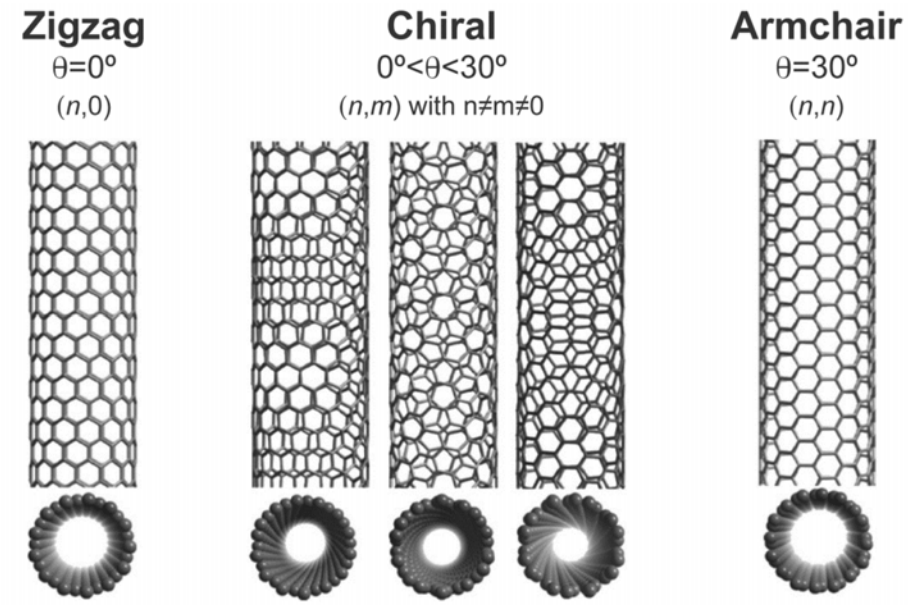

Figure 9 - Different types of SWCNTs as defined by their helicity angles and indices. Adapted from [96].

In their simplest configuration, MWCNTs can be considered as the concentric assembly of a series of equal SWCNTs of increasing diameter. In this case, it is considered that each of the SWCNTs tends to maintain its own electrical behavior. In any case, a metallic behavior is expected for all MWCNTs whose outer diameter is larger than 14 nm, no matter if the constitutive SWCNTs are of the metallic or semiconductor types [96]. Thus, typical electrical conductivities found for MWCNTs range between 10^6 and 10^7 S/m [82].

1.3.2 The μ-controlling building block: ferro and ferrimagnetic nanoparticles (MNPs)

As mentioned in section 1.1.1, the magnetic permeability, μ, is a measure of a material's ability to support the formation of a magnetic field within itself when submitted to an external magnetic field. Higher permeability materials are thus able to channel the external magnetic field by providing low resistance paths.

The channeled magnetic energy of an EMW can be dissipated by means of different loss mechanisms. These mechanisms are greatly dependent on a series of concepts related to nanoparticle magnetism which will be shortly reviewed hereafter.

1.3.2.1 Magnetism at the nanoscale: a short review of basic concepts

The fundamental source of material magnetism is the magnetic moments of electrons that make up the atomic electron shells. As a general rule, if the electron shell is not closed (meaning all electrons are not paired), the atom has a resulting nonzero magnetic moment [100, 101]. Magnetic moments are usually sketched out as magnetic dipoles (see Figure 10) and the dipole magnetic moment per unit volume is known as the magnetization, *M*, of the material. Spin coupling interactions amidst magnetic dipoles of neighboring atoms, in a molecule or a crystal for example, can induce a certain degree of ordering of the spins, also called the magnetic structure [102]. Materials can

thus be classified by their magnetic properties as either weakly (diamagnetic and paramagnetic) or strongly magnetic (ferromagnetic, FM, ferrimagnetic, FiM, or antiferromagnetic, AFM) [100].

According to its magnetic structure, a given material shows a particular behavior when an external magnetic field, *H*, is applied. For instance, diamagnetic and paramagnetic materials only display magnetic features if an external magnetic field is applied to them: a negative or a positive magnetization in the case of diamagnetic or paramagnetic materials, respectively [100]. However, in both cases, such magnetization will readily disappear upon removal of the applied field.

AFM materials exhibit zero global magnetization when no external magnetic field is applied. Indeed, they are composed of magnetic atoms, all bearing the same magnetic moment, separated in two groups or sublattices [101]. The magnetic structure is such that all moments within a given sublattice are parallel to each other and antiparallel to the moments within the other sublattice (see Figure 10). However, in the presence of a non-null *H*, the absolute value one of the sublattice magnetizations might differ from that of the other sublattice, resulting in a non-zero net magnetization.

On the contrary, FM and FiM materials, such as the ones that will be dealt with in this research project, exhibit stronger spontaneous magnetizations, independently of the external magnetic field. As shown in Figure 10, the magnetic structure of the former type of materials can be visualized as only one magnetic lattice composed of parallel dipoles. For the latter, two oppositely directed magnetic sublattices of different magnitude are superposed, producing a non-zero net magnetization [100].

It is important to mention that these three types of magnetic structures are only conserved below characteristic Curie (T_C) or Neel (T_N) temperatures, depending on whether the material is FM/FiM or AFM respectively. At and above these critical temperatures, thermal agitation will destroy these spontaneous magnetic orderings.

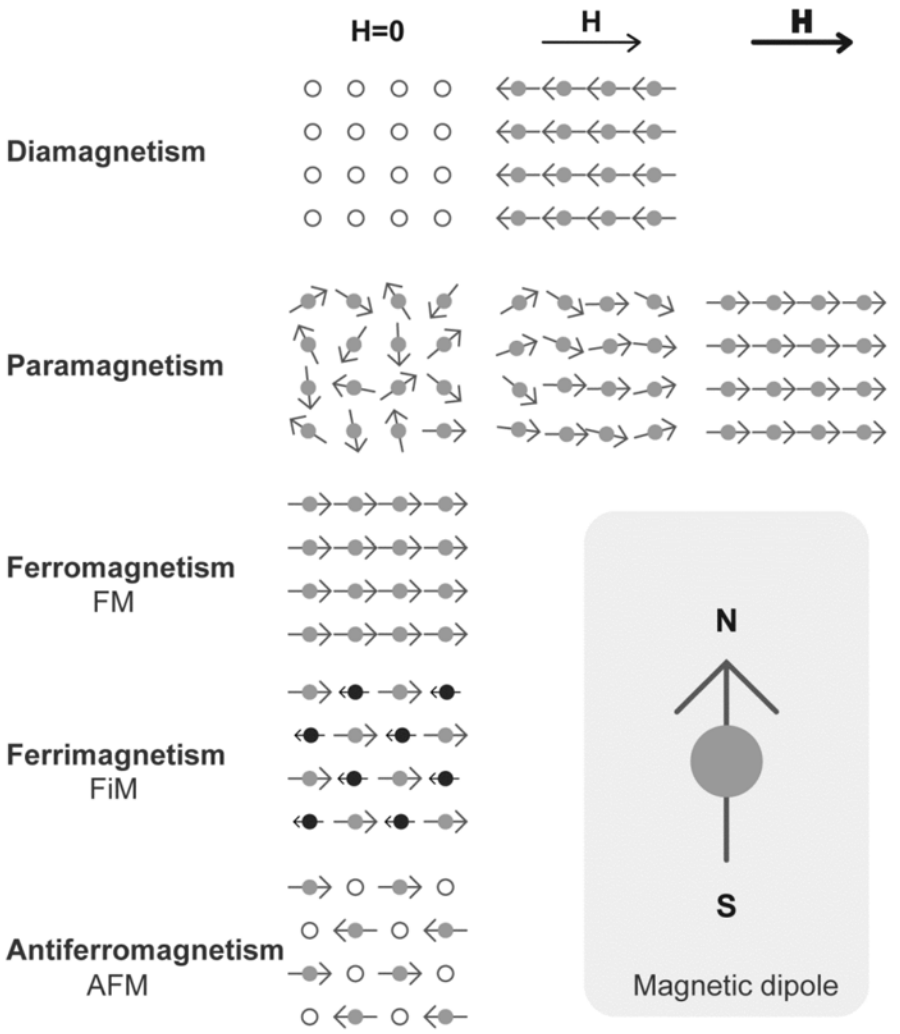

Figure 10 –The different types of magnetic order observed in matter depending on the arrangement of the electronic magnetic dipoles and the external magnetic field, *H*, having null (H=0), lower (H) or higher (**H**) values.

1.3.2.1.1 Magnetic domains and the magnetization hysteresis cycle

By looking at Figure 10, it would seem that ferro and ferrimagnetic materials should have large total magnetic moments, even in the absence of an external magnetic field.

However, this is not the case due to the presence of domain structures in these materials. Magnetic domains are small regions, each spontaneously magnetized to saturation and possessing different net magnetic orientations. This configuration into multi-magnetic domains is produced by the tendency of the material to minimize its total internal energy, of which the two principal contributions, from a magnetic orientation point of view, are the magnetostatic energy and the exchange energy [102].

The magnetostatic energy is a long-range magnetic potential energy created when a magnetic material is present in a magnetic field [100, 102]. In strongly magnetic bodies, such as in a ferromagnetic materials, this magnetic field results from their own two magnetic poles. For a single domain configuration, this field is intense and thus, the resulting magnetostatic energy is large. Partition into several domains can thus decrease the system overall magnetic potential energy.

However, this division is eventually brought to an end by the counteracting, short-range exchange energy [100, 102]. The exchange energy tends to be improved when the magnetic spins or dipole moments of neighboring domains are parallel to each other. Hence, the optimization of exchange coupling energy induces a progressive transition from one domain magnetic orientation to that of the other. This transition zone is commonly known as a Bloch's magnetic wall, or magnetic domain wall, an interface of definite thickness where magnetic moments progressively rotate their orientation from one domain to another (see Figure 11) and in which the majority of exchange energy is concentrated [103, 104]. Eventually, the balance between

both energetic considerations makes for a well-defined amount of magnetic domains and walls within a given material.

In bulk materials and in the absence of an applied magnetic field, the demagnetized state is energetically favored. In such a state, the directions of magnetization of the individual domains are randomly distributed among various possible directions. These directions are determined by the magnetocrystalline anisotropy energy, K, which varies with respect to the crystallographic axis [102] and reflects the symmetry of the neighbors of each atom [100]. Minimum magnetocrystalline anisotropy energies are obtained in directions of easy magnetization.

As a specimen is subjected to increasing external magnetic fields, the domains magnetization remains along directions of easy magnetization at first. However, by means of magnetic wall rotation, domains magnetized close to the field direction grow and those with anti-parallel magnetic orientation tend to shrink and eventually disappear [100]. If sufficiently high magnetic fields are applied, the whole magnetic body is transformed into a mono-domain crystal with its magnetic moment more or less aligned with the applied field, hence displaying maximal magnetization or saturation magnetization, M_s[102].

However, if the external magnetic field is decreased, the magnetization does not follow the initial magnetization curve. Usually, a nonzero or remanent magnetization, M_r, survives as the applied magnetic field goes down to zero. Furthermore, if the field is applied in the opposite direction, the magnetization becomes zero at a magnetic field value H_C called the coercive field or force. As the negative field further increases, magnetization reaches the saturation value again. Such a behavior in magnetization as a function of the applied external magnetic field produces a hysteresis [105]. Figure 12 shows the typical appearance of an M(H) hysteresis cycle.

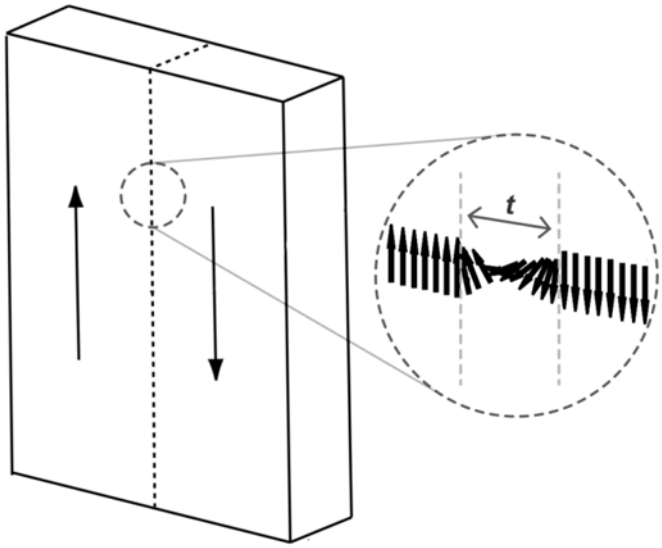

Figure 11 – Representation of a Bloch magnetic wall of thickness *t*. Adapted from [106].

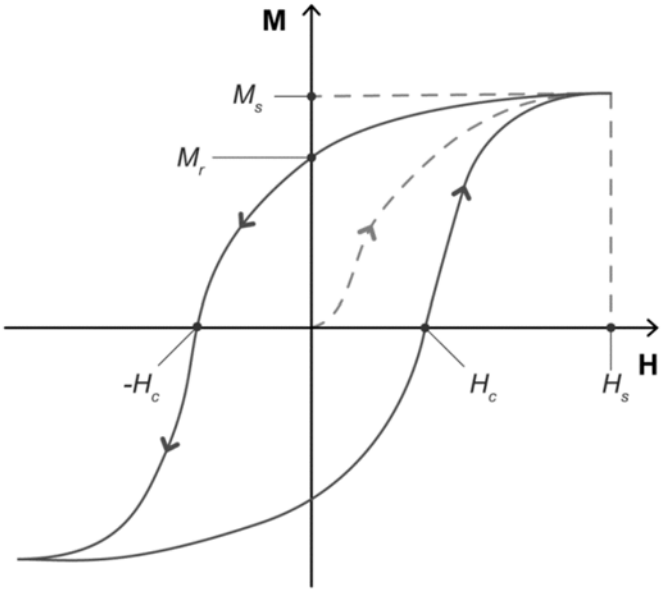

Figure 12 - Typical aspect of an M(H) curve or magnetic hysteresis loop. Adapted from [103].

1.3.2.1.2 Particle size and magnetic behavior

As the particle size is reduced, a series of changes in the particle magnetic structure takes place. Consequently, its magnetic properties in an external magnetic field are altered and deviations from "bulk" behavior are observed. These particularities are unique to the nanostructured state.

The first important singularity is the so-called single to multi-domain transition. As discussed in the previous section, the single-domain particle has all of its individual atomic magnetic moments aligned. Hence its only energetic component is the magnetostatic energy. The multidomain particle exhibits less magnetostatic energy but has one or several Bloch's walls, depending on its size. Thus, it contains re-orienting magnetic moments that increase the exchange energy component.

As the size of magnetic particles decreases, from the bulk towards the nanoscale, the aforementioned competition between the exchange and magnetostatic energies comes out of balance. Indeed, an increasing proportion of the smaller particles magnetic content is located amidst Bloch walls. When the radius of such particles reaches a comparable size to the wall's average thickness, it is energetically more favorable for this particle to arrange as a single magnetic domain particle (see Figure 13).

Such transition occurs in the order of a few nanometers to a few tens of nanometers, depending on the type of material. Several models have been proposed to estimate the critical diameter (D_C) at which the single to multidomain (denoted SD and MD respectively) transition occurs. However, these estimations are often subject to debate and several D_C values have been proposed for the same type of materials. In any case, one of the most recurring expressions allowing estimating D_C in a spherical particle is given by [102, 103]:

$$D_C = 18\frac{\sqrt{AK}}{\mu_o {M_s}^2} \qquad \textbf{Equation 1.8}$$

In which A, the exchange stiffness constant, depends on the type of material and is related to its critical magnetic ordering temperature, K is the

magnetic anisotropy, M_S the saturation magnetization and μ_o the permeability of free space. Figure 14 presents the D_C for different materials while Table 1 summarizes the M_s, K, and D_C values estimated using Equation 1.8 for the four materials that make up the core of this research project, namely iron (Fe), cobalt (Co), nickel (Ni) and magnetite (Fe_3O_4).

In the SD state, the response of nanoparticles to external magnetic fields reflects different spin dynamics as compared to their bulk counterparts. Indeed, in the case of nanoparticles, they are mainly spin rotations rather than magnetic domain wall movements. This difference will be further discussed in section 1.3.2.2, where the magnetic energy loss mechanisms are reviewed.

The second important difference between magnetic nanoparticles and their bulk counterparts is the higher coercive energies found in the former than in the latter. This is mainly due to the fact that energies required to reverse the spin orientation are usually larger than those needed to induce domain-wall movements [102]. Figure 15 shows the dependence of coercivity as a function of particle size for Fe, Co and iron oxide particles. Coming from the microscale, an increase of coercivity is observed as the particle size shrinks, reaching a maximum as the particles transit from the MD to the SD regime (see Figure 16). Indeed, when getting closer to the MD-SD transition size, fewer Bloch walls exist and demagnetization is more energy-consuming since the only way to reverse a single-domain magnetization is through homogenous rotation. Higher applied magnetic fields are thus required to overcome the system anisotropy energy and perform such a rotation that moves the domain away from its easy magnetization axis [102].

Table 1 – Saturation magnetization (M_s), magnetic anisotropy (K) and critical diameter size (D_c) for iron, cobalt, nickel [108] and magnetite [109]

Material	M_s(emu/cm^3)	K(erg/cm^3)	D_C(nm)
Iron (BCC)	1707	4.8×10^5	10
Cobalt (HCP)	1440	4.5×10^6	13
Nickel (FCC)	485	-5.7×10^4	26
Magnetite	460	1.35×10^5	28

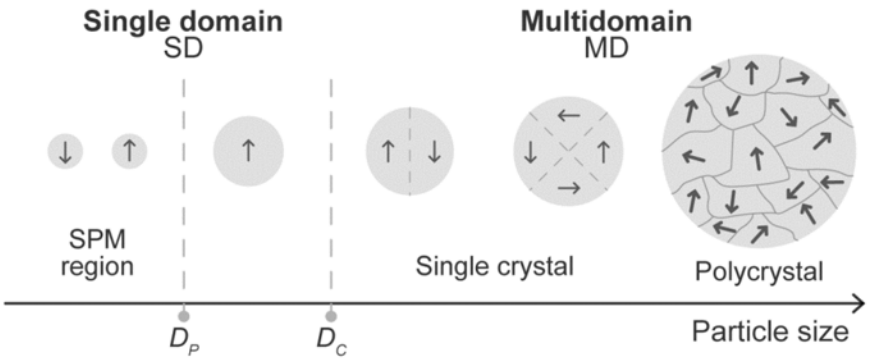

Figure 13 – Changes in magnetic domain arrangements as particle size is increased. D_p and D_c are the critical particle diameters that define the shift from the superparamagnetic (SPM) to the ferr(o/i)magnetic regimes and the single-to-multidomain (SD-MD) transition, respectively For simplicity, the drawn magnetic dipole represents that of the whole particle (in SPM and SD states) or domain (in MD state). Likewise, the domain structure of the polycrystalline specimen has been represented as if each crystallite contained only one single domain, which is usually not the case. Adapted from [100].

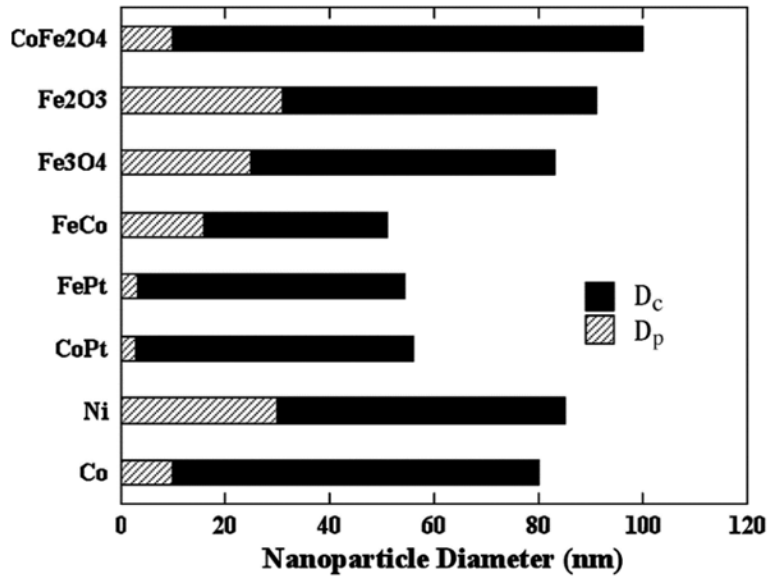

Figure 14 - Critical sizes for the observation of superparamagnetism, D_p, and single-domain, D_c, behavior in a variety of common ferromagnetic nanoparticles. Adapted from [107].

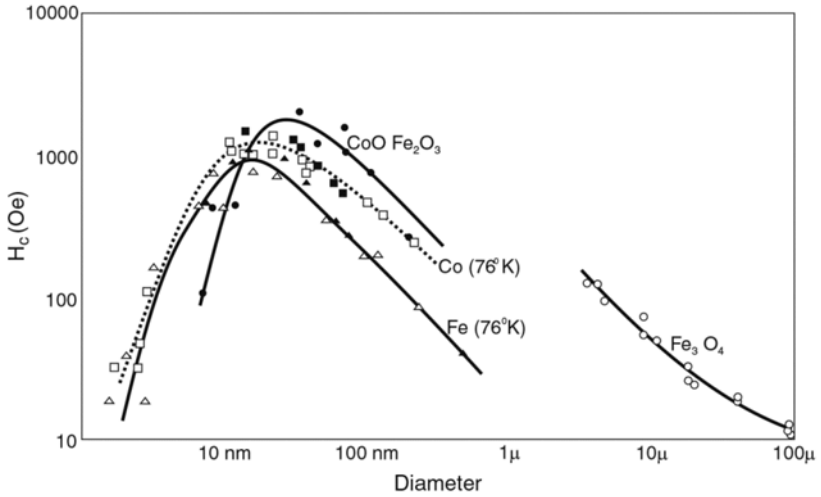

Figure 15 - Experimental relation between coercivity and diameter for particle deriving their coercive force principally from crystal anisotropy energy. Taken from [102].

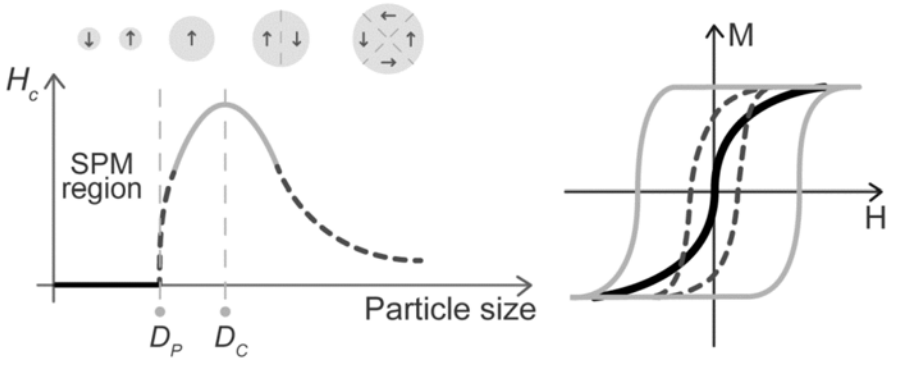

Figure 16 – Changes in coercive field, H_C as a function of particle size (left) and the corresponding superparamagnetic (SPM, black line), single-domain (light gray line), and multidomain (dashed dark gray line) magnetic regimes (right). D_p and D_c are the critical particle diameters that define the shift from the SPM to the ferr(o/i)magnetic regimes and the single-to-multidomain transition, respectively. Adapted from [110].

Nonetheless, below the critical D_G, the coercivity decreases rapidly to zero. This is due to the fact that, as the particle size decreases, the amount of exchange-coupled spins resisting spontaneous magnetic reorientation is decreased and the overall anisotropy energy drops. A critical volume is thus reached, below which thermal agitation overcomes the coercivity of the particle and switches its magnetic configuration intermittently.

Thermal energy and nanoparticle volume are intimately bound and, alongside magnetic anisotropy, define the speed of magnetic spin flipping or relaxation. In the absence of an external magnetic field, for the spontaneous magnetization to reverse, an energy barrier depending on the energetic factors mentioned above must be overcome. The probability of crossing that barrier is greater as the temperature is higher and the nanoparticle volume lower [110]. The time in which this process takes places is called the Néel relaxation (τ_N) and is described by the following expression,

$$\tau_N = \tau_o e^{\left(\frac{KV}{k_B T}\right)} \qquad \textbf{Equation 1.9}$$

Where τ_o is a time constant which usually has the value of 10^{-9}s [100], K is the anisotropy constant, V the particle's volume, k_B is the Boltzmann constant and T the system temperature. In practical conditions of measurement, the interval of time in which the relaxation process is registered, or measurement time (τ_m), will determine the actual magnetic behavior of the nanoparticles under observation.

According to equation 1.9, when the particle diameter shrinks down to a value DP, ambient temperature (~300K) may induce thermal fluctuations that cause a fast and random flipping of the magnetic moment (see Figure 13). If $\tau_m >> \tau_N$, the relaxation is so fast that the nanoparticles appear to lose their stable magnetic order [111]. Furthermore, if an external magnetic field is applied under these conditions, the magnetization of single-domain nanoparticles follows, almost instantly, the field variations so that no hysteresis cycle can be observed (see Figure 16). Likewise, the H_c values are null or close-to-zero. In fact, the system, from a magnetic point of view, behaves like paramagnetic atoms. This particular behavior is known as superparamagnetism in order to differentiate it from bulk matter paramagnetism.

At the limit $\tau_m = \tau_N$, the volume and temperature at which the spin relaxation is hindered or blocked can be found with equation 1.9. However, precise values for the blocking volume, V_T, and temperature, T_B, will depend on the measurement time of the experimental technique used to study the magnetic properties of the sample. For instance, the same nanoparticles can be in the superparamagnetic state in static magnetization experiments ($\tau_m \sim 1$ s) and in the blocked state in Mössbauer spectroscopy measurements ($\tau_m \sim 10^{-8}$ s) [102].

1.3.2.1.3 Surface effects

A particle surface is prone to present defects such as disruptions in the crystalline structure (*e.g.* vacancies or substitutions, changes in the atomic coordination, dangling bonds, lattice disorder, *etc.*), surface strain or even a different chemical composition as compared to its core [112]. These defects have an impact on the particle's magnetocrystalline anisotropy, K. As mentioned in section 1.3.2.1.1, K reflects the symmetry of the neighbors of each atom. Thus, the large perturbation of crystal symmetry at the surface leads to different magnetocrystalline anisotropy values at a nanoparticle's surface and core [113, 114].

As particle size decreases and the surface-to-volume ratio increases, a larger proportion of the atoms is found on the surface of the particle as compared to its core. For example, 0.15% of the atoms of the particle are on its surface when it possesses a $1\mu m$ diameter. If its size decreases to 6 nm in diameter, the proportion of surface atoms grows up to 20% [112]. Consequently, as a particle gets smaller, the contribution of its surface anisotropy becomes more and more pronounced [100].

The surface anisotropy contribution may lead to a complex distribution of directions of the individual spins near the surface [115], provoking changes in magnetic behavior. These changes are commonly known as surface effects, which dominate volume effects at smaller nanoparticle sizes. According to Issa *et al.* [112] these can include (a) the existence of randomly oriented uncompensated surface spins; (b) the existence of canted spins; (c) the existence of a spin-glass-like behavior of the surface spins; or (d) the existence of a magnetically dead layer (MDL) at the surface.

One magnetic property that is particularly sensitive to surface effects is the saturation magnetization, M_s. Indeed, the total magnetization of a nanoparticle is considered to be composed of two components, one due to surface spins and the other due to its core [112]. Consequently, as the NP becomes smaller, surface effects impact the nanoparticle's magnetization, commonly leading to a decrease in its magnitude (see Figure 17). Several of the above-mentioned surface effects have been held responsible for the observed drop in magnetization as NP size is reduced. Most frequently, it has been attributed to increased spin disorder at the surface of the nanoparticles (see Figure 18) [100, 110-113]. Nonetheless, the presence of a surface magnetically dead layer (MDL) due to highly frustrated magnetic coupling has also been evoked often to cause reduced magnetization [116].

However, M_s can also decrease due to surface oxidation. Metal oxides (M_xO_y) formed from the ferromagnetic (FM) Fe, Co and Ni metals are usually antiferromagnetic (AFM) or ferrimagnetic (FiM). Their magnetization values are thus respectively null or lower than that of their FM counterparts. Thus, if a Fe, Co or Ni NP is exposed to air, different types of AFM or FiM M_xO_y can be formed to different extents on its surface. A metallic FM core surrounded by an AFM or FiM M_xO_y shell is thus formed. The overall M_s of such a nanoparticle, which adds up the magnetization contributions of the core and the shell, will thus be lower.

One particular type of interaction, called exchange bias or exchange coupling, can also take place at the interface between a FM core and an AFM shell. Exchange bias (EB) coupling consists in the pinning of interfacial spins in the FM core to the ones of the AFM shell, resulting in extra magnetic anisotropy energy [117] leading to magnetization stability [100]. As mentioned in section 1.3.2.1.2, additional anisotropy energy can induce changes in the observed coercive field (H_c). In the case of EB coupling in such a FM@AFM core-shell structure, it is characterized by coercivity enhancement and hysteresis loop shift along the field axis [100].

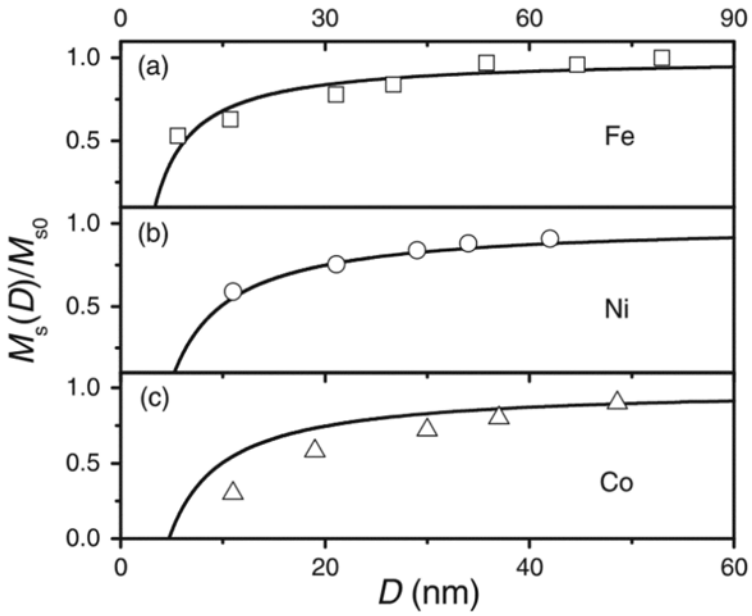

Figure 17 - $M_s(D)/M_{s0}$ as a function of D for (a) Fe, (b) Ni and (c) Co ferromagnetic nanoparticles. The solid lines are plotted in terms of a model described in [118] whereas the circles, triangles and squares denote the experimental results. Taken from [118].

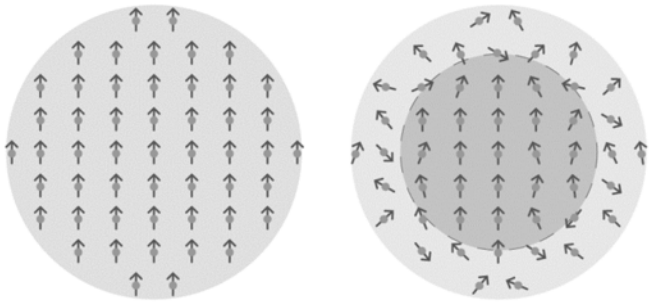

Figure 18 – Schematic representation of an ideal NP in which magnetic spins are perfectly aligned throughout the NP volume (left). In reality, NPs possess a core in which magnetic moments are more orderly disposed and a surface where magnetic spins are disordered (right). Adapted from [100].

1.3.2.2 Magnetic energy loss mechanisms in nanoparticles

As previously mentioned, different loss mechanisms intervene to dissipate the magnetic energy of an EMW when it encounters a magneto-responsive material. In general terms, higher magnetic permeability materials, like metals, show larger rates of magnetic losses given their ability to channel the external magnetic field by providing low resistance paths. Thus, metallic materials can be used to fabricate thinner composites with similar EMI shielding efficiency [120].

In the case of electrically conductive ferromagnetic metals and their alloys, the rate and width of EMW absorption can be increased by the induction of electrical currents, known as Eddy currents [107]. These currents appear mostly in the microwave super high frequency (SHF) band (3 to 30 GHz, see Figure 1) and dissipate energy into the sample through electrical resistance. Losses due to Eddy currents are known to increase as the nanoparticle size increases [107]. Furthermore, as nanoparticles transit from the SD to the MD state, the loss rate is increased roughly four times. These currents can also produce a magnetic field which is opposite in orientation to the external field [119]. In consequence, the total magnetic field is reduced when moving from the nanoparticle surface towards its core. The depth, *s,* at which the magnetic field is reduced by a factor of $1/e$ is called the skin-depth [107]. Beyond *s*-depth, a non-uniform magnetization of the particle might occur, broadening even further the absorption width [119]. The skin depth in the ferromagnetic metals at microwave frequencies is of the order of 1 μm to 100 nm [122]. Therefore, it can be considered that only those nanoparticles whose diameters are below ~100 nm will be homogeneously magnetized.

Magnetic energy can also be spent on the movement of magnetic domain walls and pinning and, to a lesser extent, on the rotation of the materials atomic spins and on domain nucleation [107, 119]. However, domain wall motion, also known as hysteresis loss, is hindered as the incoming EMW's

pulsation is increased over the domain wall resonance frequency. At this point, only magnetization rotation persists, up to the highest frequencies. Such is the specific case of microwave frequencies and ferro and ferrimagnetic materials, which present a particular phenomenon related to magnetization rotation known as the ferromagnetic resonance (FMR) [107].

1.3.2.2.1 The ferromagnetic resonance (FMR) phenomenon

FMR has already been exploited to design EMI shielding materials [120]. Indeed, an intense absorption process takes place at the FMR frequency, the value of which is partially determined by the composition of the FMR-active material. Typically, these materials are magnetically soft metals such as Fe, Co and Ni, their alloys, ferrites and titanates [107].

This physical phenomenon, which was characterized by Kittel in 1946 [122], is analogous to electron paramagnetic resonance (EPR) and, to some extent, to nuclear magnetic resonance (NMR). In a ferromagnetic material, the unpaired electrons possessing a magnetic moment start to precess in an applied magnetic field. Indeed, the latter exerts a torque on the electron magnetic moment. This precession is called the Larmor precession and its frequency, f, for a spherical particle, is given by the product of the gyromagnetic ratio, γ, and the external magnetic field, H_z.

$$f = \frac{\gamma}{2\pi} H_z \qquad \textbf{Equation 1.10}$$

The gyromagnetic ratio can be defined as:

$$\gamma = g\frac{e\mu_o}{2m} \qquad \textbf{Equation 1.11}$$

where μ_o is the permeability constant, e is the charge of the electron, m its mass and g is the Landé factor which depends on the spin-orbit moment coupling.

The resonance phenomenon arises when the energy levels of a quantized system of electronic moments are Zeeman split by a uniform

magnetic field and the system absorbs energy from an electromagnetic wave at sharply defined frequencies corresponding to the transitions between such levels.

In the case of zero static field (H_z=0), the effective anisotropy field (H_a) is responsible for the observed FMR absorption peaks and the above equation thus becomes:

$$f_o = \gamma H_a \qquad \textbf{Equation 1.11}$$

In which H_a is given by:

$$H_a = H_{ac} + H_{as} \qquad \textbf{Equation 1.12}$$

The anisotropy field depends on two factors: the magnetocrystalline anisotropy present in the material, represented by H_{ac} [123], and the shape anisotropy induced by shape effects of the nanoparticles and the dipolar coupling effect between them, represented by $H_{as.}$ This last factor is proportional to the saturation magnetization, M_s, of the material [124].

If both, a non-zero static field and the anisotropy field are to be considered, the Kittel FMR expression becomes:

$$f = \gamma \mu_o (H_z + H_a) \qquad \textbf{Equation 1.13}$$

Thus, as shown in the above-given expression, the FMR frequency shows a linear dependence on the external applied magnetic field, a correlation that has been acknowledged for a wide range of F(i)M materials [123-129].

1.3.2.2.2 Magnetic permeability values around the ferromagnetic resonance frequencies

As mentioned before, due to their magnetic permeability, materials are able to channel an external magnetic field, *H*, which induces a magnetic flux, *B*, within the material itself. At higher frequencies, a measurable time delay occurs between the applied magnetic field and the induced

magnetic flux due to the non-instantaneous re-orientation of magnetic dipoles inside the medium as described above, resulting in a phase shift, θ.

To take into account this delay, the magnetic permeability is expressed in its complex form, possessing two terms: one real, μ', and one imaginary, μ'', given by:

$$\mu = \mu' - i\mu'' \qquad \textbf{Equation 1.14}$$

The real term is related to the material ability to store magnetic energy and its imaginary counterpart accounts for magnetic losses. Therefore, convention assigns positive values to the former while the latter is negative.

As explained in the previous section, the FMR phenomenon induces considerable magnetic energy losses due to absorption. Consequently, Yager and Bozorth [130] demonstrated that, in F(i)M materials, at the resonance frequency, the real part of their magnetic permeability, μ', falls down to zero and then becomes negative while the imaginary term, μ'', drops towards more negative values, and then recovers to zero, as shown in Figure 19.

These modifications in the values of μ' and μ'' change the overall μ value of the material around the FMR frequency, f. A relationship between μ and f is given by the following expression:

$$\mu_r = 1 + \frac{4\pi M_s \gamma f}{(f + i/\tau)^2 - f_{EMW}} \qquad \textbf{Equation 1.15}$$

Where τ is the relaxation time, f_{EMW} is the frequency of the incoming electromagnetic wave, and M_s and γ are the saturation magnetization and the gyromagnetic ratio, respectively.

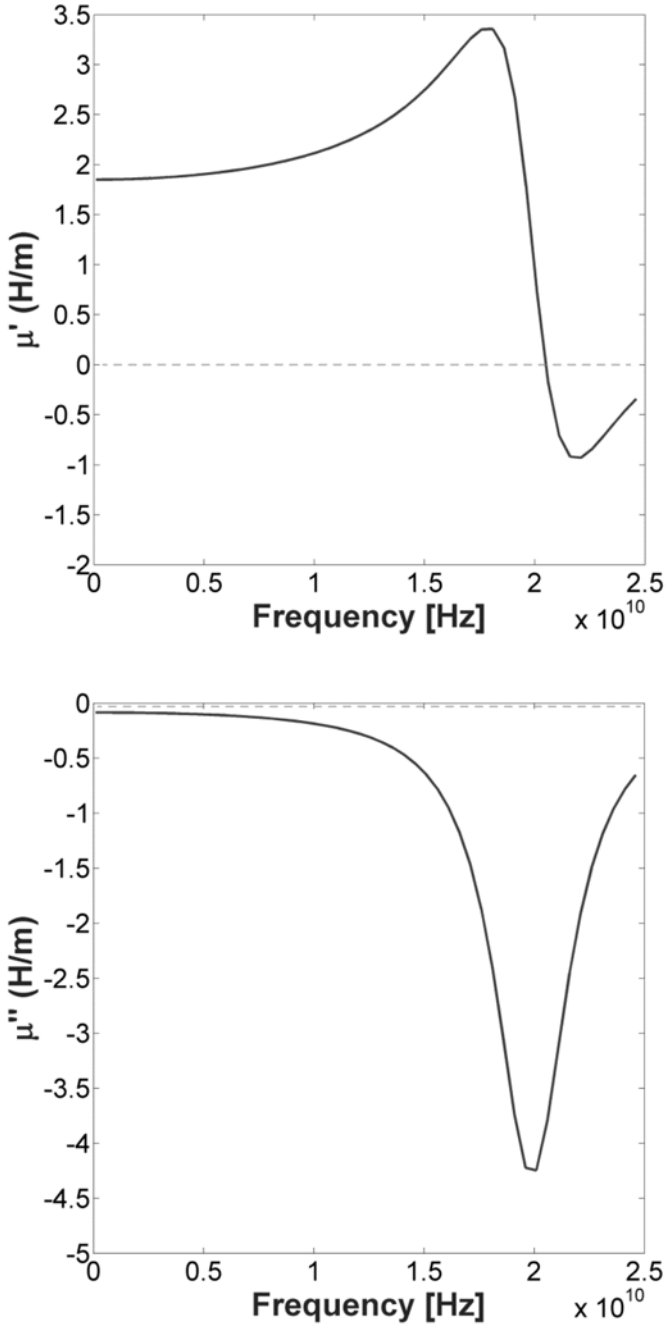

Figure 19 –Simulation of the changes in the μ' and μ'' values around the FMR (20 GHz) for bulk nickel-iron (NiFe) alloy. Made by I. Huynen using Matlab®.

1.4 From the synthesis of novel MNPs@NcS nanocomposites to efficient metamaterial MAMs: thesis scope and objectives

The ultimate goal of this research project is to obtain a new class of metamaterial microwave absorbing materials (MAMs) based on the chemical assembly of magnetic nanoparticles (MNPs) and nanocarbon supports (NcS). These MAMs target absorption frequency bands (*e.g.* between 400 MHz and 40 GHz) correspond to low-power microwave EMWs, currently used in numerous telecommunication systems and therefore related either to EMI issues or EHS risks.

The MNPs will be used to fine-tune the system magnetic permeability, μ. As explained in section 1.3.2.2.1, ferro and ferrimagnetic nanoparticles can be used to modify the values of μ by inducing a ferromagnetic resonance (FMR) phenomenon which will produce a negative μ value around the resonant frequency. Furthermore, it should be possible to control such resonant frequencies and the intensity of their response by changing some of the MNPs' physicochemical characteristics such as their chemical identity, size or loading rate.

In contrast, the NcSs will serve a dual purpose. On the one hand, their conductive nature will be exploited as the main control mechanism defining the system values of relative electrical permittivity, ε_r. Indeed, as it was shown in section 1.3.1, by choosing one type of NcS over another or by chemically functionalizing their surface (*e.g.* through oxidation), different values of conductivity and, consequently, of ε_r, can be obtained. On the other hand, they will support the MNPs, thereby reducing their agglomeration and controlling their size and spatial distribution.

Numerous MNPs@NcS nanocomposites have been synthetized by solvothermal [131-135], hydrothermal [136-138], sol-gel [139-141], electrodeposition [142-144] or thermal decomposition techniques [145-149], to cite just a few. These materials have been proposed for a very wide number of applications such as energy storage devices [136,150, 151], catalysts

[132,141,144,152], the remediation of environmental pollutants [140,153, 154], the design of controlled drug carriers [131, 155] or (bio)sensors [133,156, 157].

Their properties as potential MAMs have also been acknowledged [138, 142, 158, 159-161]. However, there lacks a systematic exploration on how the physicochemical characteristics of both, the MaNPs and NcS, can be tailored through chemical assembly so as to independently control the end-materials magnetic permeability (μ) and electrical permittivity (ε) values, a requisite if the metamaterial design paradigm is to be applied. Also, up to this day, there is no available information on the potential synergistic effects, derived from the combination of these two building blocks, which could also have an impact on the nanocomposites' ε and μ values.

Moreover, this research project will go beyond the state-of-the-art by systematically producing a large number of MNPs and NcS combinations as to offer a library of potential μ and ε values in the microwave range. Afterwards, it will determine how these ε-μ values influence the obtained MNP@NcS nanocomposites electromagnetic response to microwaves.

However, in order to achieve these two last objectives, a new characterization technique will have to be developed. Indeed, traditional electromagnetic characterization techniques for nanopowders [162-164] rely on a Jaumann configuration where frequency-selective absorbing performance is primarily controlled by the thickness of the sample. Thus, a technique allowing to exclusively extract the electromagnetic properties of the as-synthetized nanopowders is needed.

Finally, two novel EMI shielding functionalities will also be developed using the synthetized MNPs@NcS nanocomposites. The first one, based on the Nano4Waves project's original idea, will be produced by dispersing MNPs@MWCNTs powders in a host polycarbonate matrix (PC). The choice of this particular NcS and polymer is based on previous results obtained in our research group. Indeed, the methodologies required to obtain homogenously dispersed MWCNTs@polycarbonate thin MAM films by means of extrusion and hot-pressing have already been optimized [4, 57-59, 67]. Likewise, preliminary investigations on the dispersion in polycarbonate of MNPs and pristine NcS, used as separate components, have also been

performed [165]. Results obtained showed that while the NcS was homogenously dispersed in the polymeric matrix, the MNPs tended to form aggregates heterogeneously distributed throughout the film. The use of MNPs@MWCNTs nanocomposites should allow overcoming such a differential dispersion behavior. In any case, bearing these prior results in mind, the microwave absorption efficiency of the novel MNPs@MWCNTs_PC films will be compared to that of similar composite films formerly produced in our research group or described in the scientific literature [166-168]. In this sense, it will be possible to clearly define the competitive advantage of decorating the MWCNTs with MNPs.

The second MAM prototype is based on the formulation of nanocomposite inks that will be used to inkjet-print these materials as frequency-selective surfaces (FSS) onto a flexible polymeric sheet. Their efficiency as wideband microwave absorbers will be evaluated. To the best of our knowledge, this is a completely novel approach to MAMs design and thus constitutes an exciting new area of research.

1.5 General methodology

In order to accomplish the aforementioned objectives, the present research project was subdivided into three main experimental phases (see Figure 20).

In the first phase, environmentally friendly solvents-based and easily scalable solvothermal, sol-gel and thermal decomposition techniques were employed to deposit seven types of ferro and ferrimagnetic nanoparticles (MNPs) onto up to four different nanocarbon supports (NcS).

More specifically, multi-walled carbon nanotubes (MWCNTs), graphene nanoplatelets (GNPs), graphene oxide (GO) or reduced graphene oxide (rGO) were decorated with iron, cobalt, nickel, their binary (FeCo, FeNi) and ternary (FeCoNi) alloys or magnetite (Fe_3O_4) nanoparticles. In all cases, a tight control on the deposited NPs chemical composition, size and loading rate on the nanocarbon surfaces was sought. Therefore, for each synthetic technique, several key experimental parameters were identified and fine-tuned, to ensure obtaining the desired material characteristics.

The second phase, executed alongside the nanocomposite synthesis, consisted in the electromagnetic (EM) and physicochemical characterization of the obtained nanocomposite powders. For the EM characterization, we developed a novel coplanar transmission line-based network analyzer (VNA) methodology, including the design and construction of two different test cells as well as the development of measurement data extraction and treatment procedures.

A wide number of physicochemical analytical techniques, described in Appendix II, were also applied to thoroughly understand the impact of the different synthetic parameters on the nanocomposite powder characteristics. For instance, powder X-Ray Diffraction (XRPD) was used to verify the formation and purity of the desired crystalline MNPs phases. Electron microscopy techniques such as scanning electron microscopy (SEM) or transmission electron microscopy (TEM) were routinely used to assess the size, shape and distribution of the synthetized MNPs deposited onto the NcS surfaces. Inductively coupled plasma atomic emission spectroscopy (ICP-AES), X-ray photoelectron spectroscopy (XPS) and Time of flight Secondary ion mass spectrometry (ToF-SIMs) were used to elucidate the elemental and molecular composition of the different MNPs, NcS and the nanocomposites formed thereof. Finally, Superconducting Quantum Interference Device (SQUID) magnetometry was employed to survey the magnetic ordering of the synthetized nanocomposites and to assess their magnetic properties.

The third phase implied the design and fabrication of two novel microwave absorbing materials (MAMs) for different EMI shielding applications. On the one hand, a first series of nanocomposites, consisting of MWCNTs decorated with Fe, Co or Ni nanoparticles, were dispersed into polycarbonate to form thin films. On the other hand, inks were formulated with the materials used in this research project and a series of planar frequency-selective-surfaces (FSS) were inkjet-printed onto a polycarbonate sheet. In this case, the prototype's efficiency as a lightweight, thin and flexible ultra-wideband MAM was evaluated.

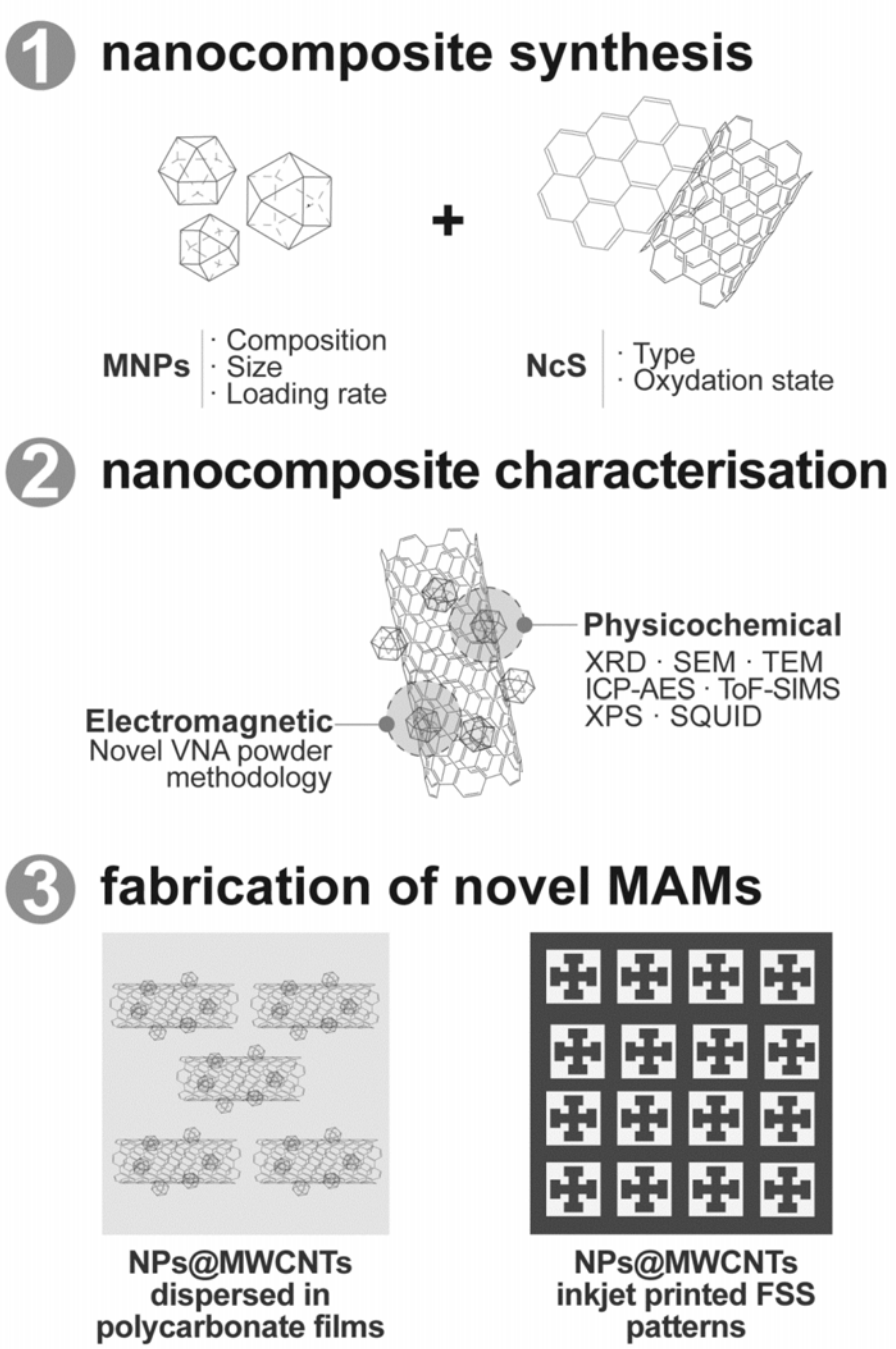

Figure 20 – Schematic representation of the three main phases that constitute the current research project.

1.6 Manuscript outline

Mimicking this research project's general methodology, the present manuscript is also structured into three different parts. Each one conveys the results obtained during the execution of the three main experimental phases described above.

The first section of this manuscript constitutes the core of this research work. It is devoted to the novel synthetic methods developed to create the different microwave-responsive MNPs@NcS nanocomposites. Each one of the four different chapters found in this section addresses the decoration of nanocarbon supports with a particular type of MNP (*e.g.* magnetite, nickel, cobalt, iron and Fe/Co/Ni alloy NPs). The main focus of these chapters is to highlight how different experimental conditions can be varied to control some of these nanocomposites most relevant physicochemical characteristics, such as the MNPs composition, size and loading rate on the NcS.

Results presented in the second section contribute to the fundamental understanding of a metamaterial MAM design paradigm. Its first chapter presents the theoretical principles and experimental undertakings required to develop a novel vector network analyzer (VNA) methodology for the EM characterization of nanocomposite powders. These EM characterization tools were then extensively used to obtain the results shown in the second chapter. They illustrate how to control a MNPs@NcS nanocomposite magnetic permeability and electric permittivity by defining its physicochemical characteristics through chemical assembly. They also prove the high microwave absorption efficiency of these novel materials.

The third and last section deals with the third experimental phase of this research project. Its two chapters are devoted to the design,

fabrication and characterization of the MAMs described at the end of Section 1.5. Thin wide-band absorber films produced by dispersing different MNPs@MWCNTs nanocomposites in a polycarbonate matrix are presented first. Afterwards, the ultra-wide band absorption of frequency selective surfaces, inkjet-printed with MWCNTs-based nanocomposites, is demonstrated.

Finally, a series of conclusive remarks on this research project achievements and yet-to-be solved challenges will be presented, leading the way to a final section concerning several recommendations for future explorations on this subject.

1.7 Bibliography

1. G.L. Stüber Principles of mobile communication, 4th edition. Springer International Publishing AG: Cham, Switzerland. 2017.
2. W. C. Brown, *IEEE T Microw Theory,* 1984, **32**(9), 1230-1242.
3. A. Benslimane, H. Tobiet, QoS classification for mobile networks: international roaming case study. In 5th IEEE International Conference on High Speed Networks and Multimedia Communication, Jeju Island, South Korea, 2002.
4. J-M. Thomassin, C. Jérôme, T. Pardoen, C. Bailly, I. Huynen and C. Detrembleur, *Mater. Sci. Eng. R.*, 2013, **74**, 211-232.
5. C-Y Wang, X-X, Wang and M-S Cao, *J. Mater. Eng.,* 2016, **44**(10), 109-118.
6. M. Joshi, T. Bansala and S. Mukhopadhyay, *Proceedings of the 18th World Textile Conference,* June 20-22, 2018, Istanbul, Turkey, 012012.
7. N. Violette, Electromagnetic compatibility handbook; Springer Netherlands: Amsterdam, 1987.
8. G.J. Rubin, J. Das Munshi, S. Wessely, *Psychosomatic Medicine*, **2005**, *67*, 224–232.
9. D. Belpomme, L. Hardellac, I. Belyaevade, E. Burgio and D. O.Carpenter, *Environ. Pollut.,* 2018, **242**, 643-658.
10. Scientific Committee on Emerging and Newly Identified Health Risks, European Commission, Opinion on potential health effects of exposure to electromagnetic fields (EMF), 2015. Available online at: https://ec.europa.eu/health/sites/health/files/scientific_committees/emerging/docs/scenihr_o_041.pdf
11. M.J. Gruber, E. Palmquist and S. Nordin, *Scand. J. Psychol.,* 2018, **59**(4), 422-427.
12. A.B. Sharma and O.S. Lamba, *Advances in Wireless and Mobile Communications*, 2017, **10**(3), 423-435.
13. A.B. Miller, M.E. Sears, L.L. Morgan, D.L. Davis, L. Hardell, M. Oremus and C.L. Soskolne, *Public Health*, 2019, **7**, Article Number: 223.
14. European Commission. Directive 2014/30/EU on Electromagnetic Conformity (EMC), 2014. Available online at: http://eur-lex.europa.eu/legal-content/EN/TXT/PDF/?uri=CELEX:32014L0030&from=EN.
15. International Electrotechnical Comission (IEC). International norm on Electromagnetic compatibility (CEM)- Part 4-1: Testing and measurement

techniques. Available online at: https://webstore.iec.ch/p-preview/info_iec61000-4-1%7Bed3.0%7Db.pdf
16. Patents US7057472B2 "Bypass filter, multi-band antenna switch circuit, and layered module composite part and communication device using them" and US6975834B1 "Multi-band wireless communication device and method".
17. N. Haider, D. Caratelli, A.G. Yarovoy, *Int. J. Antenn. Propag.* 2013, **2013**, 869170-14.
18. Report of the independent advisory group on non-ionizing radiation, Health Protection Agency of the United Kingdom, Health effects from radiofrequency electromagnetic fields (EMF), 2012. Available online at: https://www.ices-emfsafety.org/wp-content/uploads/2014/.../AGNIR_report_2012.pdf
19. H. Leland Hemming. Architectural Electromagnetic Shielding Handbook: A Design and Specification Guide. IEEE Press: Piscataway, NJ, USA, 2000.
20. N. Dong, C. Lingqi, Y. Xiaowei, M. Xiaokang, S. Xinnan, C. Laifei, Z. Litong, *Ceram. Int.*, 2016, **42**, p9448-9454.
21. H. Zhao, H. Lei, L. Yinxiang, *Mater. Des.*, 2016, **95**, 97-106.
22. P. Karimi, M. Ostoja-Starzewski and I. Jasiuk, *J. Appl. Phys.*, 2016, **120**, 145103.
23. H. Abbasi, M. Antunes and J.I. Velasco, *Prog. Mater. Sci.*, 2019, **103**, 319-373.
24. D.D.L. Chung, *Carbon*, 2001, **39**, 279-285.
25. X. C. Tong. Advanced materials and design for electromagnetic interference shielding. CRC Press: Boca Raton, United States of America. 2008.
26. N. Engheta and R.W. Ziolkowski, Metamaterials: physics and engineering explorations; John Wiley & Sons & IEEE Press: USA, 2006.
27. H. Chen, *J. Mater. Chem.*, 2011, **21**, 6452-6463.
28. F. Bilotti and L. Sevgi, *Int. J. RF Microw. C.E.*, 2012, **22** (4), 422-438.
29. Y. Luo, F. Qin, F. Scarpa, M. Ipatov, A. Zhukov and H-X Peng, "Tuneable metacomposites based on functional fillers" in Novel Functional Magnetic Materials. Ed. A. Zhukov. Springer International Publishing: Cham, Switzerland. 2016 pp. 311-357.
30. V.G. Veselago, *Soviet Physics Uspekhi*, 1968, **10**(4), 509-514.
31. C.M. Soukoulis, J. Zhou, T. Koschny, M. Kafesaki, and E.N. Economou, E. N. *Journal of Physics: Condensed Matter*, 2008, **20**, 304217.
32. D.R. Smith, W. Padilla, D. Vier, S. Nemat-Nasser and S. Schultz, *Phys. Rev. Lett.*, 2000, **84**(18), 4184-4187.
33. A.S. Gangnaik, Y.M. Georgiev and J.D. Holmes, *Chem.Mater.*, 2017, **29**(5), 1898-1917.
34. A. Baron, A. Aradian, V. Ponsinet, P. Barois, *Opt. Laser Technol.*, 2016, **82**, 94-100.
35. D. A. Pawlak, S. Turczynski, M. Gajc, K. Kolodziejak, R. Diduszko, K. Rozniatowski, J. Smalc and I. Vendik, *Adv. Funct. Mater.*, 2010, **20**, 1116-1124.
36. R. N. S. Suryadharma and C. Rockstuhl, *Materials*, 2018, **11**, 213.
37. I. Levchenko, K. Bazaka, M. Keidar, S. Xu, and J. Fang, *Adv. Mater.*, 2018, **30**, 1702226.
38. P. Podsiadlo, G. V. Krylova, A. Demortière, E. V. Shevchenko, *J. Nanopart. Res.*,2011, **13**, 15-32.
39. M. Mayer, M.J. Schnepf, T.A.F. König and A. Fery, *Adv. Opt. Mat.*, 2019, **7**, 1800564-17.
40. S. Gomez-Graña, A. Le Beulze, M. Treguer-Delapierre, S. Mornet, E. Duguet, E. Grana, E. Cloutet, G. Hadziioannou, J. Leng, J.-B. Salmon, V. G. Kravets, A. N. Grigorenko, N. A. Peyyety, V. Ponsinet, P. Richetti, A. Baron, D. Torrent and P. Barois, *Mater. Horiz.*, 2016, **3**, 596-601.

41. C. Li, S. Lee, Z. Qian, C. Woods, S-J Park and Z. Fakhraai, *J. Phys. Chem. C*, 2018, **122**(12), 6808-6817.
42. K. Kim, J-H Huh, D. Yu and S. Lee, *Macromol. Res.*, 2018, **26**(12), 1103-1107.
43. S. N. Sheikholeslami, H. Alaeian, A. L. Koh, and J. A. Dionne, *Nano Lett.*, 2013, **13** (9), 4137–4141.
44. N. S. King, Y. Li, C. Ayala-Orozco, T. Brannan, P. Nordlander and N. J. Halas, *ACS Nano*, 2011, **5**(9), 7254-7262.
45. J. Toudert, X. Wang, C. Tallet, P. Barois, A. Aradian and V. Ponsinet, *ACS Photonics*, 2015, **2**(10) 1443-1450.
46. M. Karg, I. Pastoriza-Santos, J. Pérez-Juste, T. Hellweg, L. M. Liz-Marzán, *Small*, 2007, **3**, 1222-1229.
47. J.-W. Jeon, P. A. Ledin, J. A. Geldmeier, J. F. Ponder, M. A. Mahmoud, M. El-Sayed, J. R. Reynolds, V. V. Tsukruk, *Chem. Mater.* 2016, **28**, 2868-2881.
48. W. Lewandowski, M. Wójcik, and E. Górecka, *Chem. Phys. Chem.*, 2014, **15**, 1283 – 1295
49. I. C. Khoo, A. Díaz, J. Liou, M. V. Stinger, J. Huang and Y. Ma., *IEEE J Sel. Top. Quant.*, 2010, **16**(2), 410-417.
50. I.B. Vendik, O.G. Vendik and M.S. Gashinova, *Tech. Phys. Lett.*, 2006, **26**, 429-433.
51. S.K. Dhawan, K. Singh, A.K. Bakhshi and A. Ohlan, *Synth. Met.*, 2009, 159(21–22), 2259-62.
52. L.D. Hai, V.D. Qui, N.H. Tung, T.V. Huynh, N.D. Dung, N.T. Binh, L.D. Tuyen and V. Dinh Lam, *Opts. Express*, 2018, **26**(25), 33253-33262.
53. H. M. Mesfin, A.C. Baudoin, S. Hermans, A. Delcorte, I. Huynen, C. Bailly, *Appl. Phys. Lett.*, 2014, **105**, 103105.
54. K. Rubrice, X. Castel, M. Himdi and P. Parneix, *Materials*, 2016, **9**, 825.
55. V. K. Singh, A.Shukla, M. K. Patra, L. Saini, R. K. Jani, S. R. Vadera and N. Kumar, *Carbon*, 2012, **50**, 2202-2208.
56. J. Wang, Y. Sun, W. Chen, T. Wang, R. Xu and J. Wanga, *J. Appl. Phys.*, 2015, **117**, 1.4917486.
57. Y. Danlée, I. Huynen and C. Bailly, *Appl. Phys. Lett.*, 2012, **100**, 213105.
58. H. M. Mesfin, S. Hermans, I. Huynen, A. Delcorte, C. Bailly, *Mater. Today Proc.*, 2016, 3(2), 491-496.
59. Y. Danlée, I. Huynen and C. Bailly, *Comp. Sci. Tech.*, 2014, **100**, 182-188.
60. Y. Yonglai, C. G. Mool and L.D. Kenneth, *Nanotechnol.*, 2007, **18**(34), 345701.
61. O.A. Al-Hartomy, A. Al-Ghamdi, F. Al-Salamy, N. Dishovsky, R. Shtarkova, V. Iliev and F. El-Tantawy, *Adv. Compos. Mater.*, 2013, **22**(5), 361-376.
62. T. Narayanan, V. Sunny, M. Shaijumon, P. Ajayan and M. Anantharaman, Electrochem. Solid St., 2009, **12**(4), K21-K24
63. F. Qin and H-X. Peng, *Prog. Mater. Sci.*, 2013, **58**, 183-259.
64. A.P. Singh, P. Garg, F. Alam, K. Singh, R.B. Mathur, R.P. Tandon, A. Chandra and S.K. Dhawan, *Carbon*, 2012, **50**, 3868–3875.
65. G. Bo, M. M. F. Yuen and Y. Terry, Materials, 2016, **9**(12), 1009.
66. Y. Mamunya, L. Matzui, L. Vovchenko, O. Maruzhenko, V. Oliynyk, S. Pusz, B. Kumanek and U. Szeluga, Comp. Sci. Tech., 2019, **170**, 51-59.
67. Y. Danlée, R. Jaiswar, F. Mederos-Henry, H. Mesfin, C. Bailly, A. Delcorte, S. Hermans and I. Huynen, *Proceedings of the 15th IEEE International Conference on Nanotechnology,* July 27-30, 2015, Rome, Italy, 188-191.
68. B. Li and W-H Zhong, "Hybrid polymer nanocomposite systems" in Polymer nanocomposites for dielectrics. Pan Stanford: New York, United States of America. 2017, pp. 171-192.

69. J.E. Atwater and R.R. Wheeler, *Carbon*, 2003, **41**, 1801–1807.
70. A.A. Barba, G. Lamberti, M. d'Amore and D. Acierno, *Pol. Bull.*, 2006, **57**, 587-593.
71. H. W. Kroto, J. R. Heath, S. C. O'Brien, R. F. Curl, and R. E. Smalley, *Nature*, 1985, **318**, 162-163.
72. S. Iijima, *Nature*, 1991, **354**(6348), 56–58.
73. R.H. Baughman, A.A. Zakhidov and W.A. de Heer, *Science*, 2002, **297**(5582), 787-792.
74. A.K. Geim and K.S. Novoselov, *Nat. Mater.*, 2007, **6** (3), 183-191.
75. Press release from the Royal Swedish Academy of Sciences published on the 5/10/2010. Available online at: https://www.nobelprize.org/prizes/physics/2010/press-release/
76. V. Singh, D. Joung, L. Zhai, S. Das, S. Khondaker and S. Seal, *Progress in materials science*, 2011, **56**, 1178-1271.
77. L. Shahriary and A. A. Athawale, *Int. J. Renew. Energy Environ. Eng.*, 2014, **2**(1), 58–63.
78. Q. Le, T. Wang, Y. Zhang and L. Zhang. "Introduction to chemically derived graphene" in Chemically Derived Graphene: functionalization, properties and applications. Ed. J. Zhang. RSC Publishing: London, United Kingdom. 2018, pp. 1-29.
79. D.R. Dreyer, S. Park, C.W. Bielawski and R.S. Ruoff, 2010, *Chem. Soc. Rev.*, 2010, **39**, 228-240.
80. F. Schwierz, *Nat. Nanotechnol.*, 2010, 5, 487-496.
81. C. N. R. Rao, K. Biswas, K. S. Subrahmanyam and A. Govindaraj. *J. Mater. Chem.*, 2009, **19**, 2457-2469.
82. B. Marinho, M. Ghislandi, E. Tkalya, C.E. Koning and G. de With, *Pow. Tech.*, 2012, **221**, 351-358.
83. F. Banhart, J. Kotakoski and A. V. Krasheninnikov, *ACS Nano*, 2010, **5**(1) 26-41.
84. J-A Yan and M. Y. Chou, *Phys. Rev. B*, 2010, **82**, 12540-10.
85. C. Punckt, F. Muckel, S. Wolff, I. A. Aksay, C. A. Chavarin, G. Bacher and W. Mertin, *Appl. Phys. Lett.*, 2013, **102**, 023114-5.
86. P. S. Teo, H. N. Lim, N. M. Huang, C. H. Chia, and I. Harrison, *Ceram. Int.*, 2012, **38** (8), 6411–6416.
87. G. Eda, G. Fanchini and M. Chhowalla, *Nat. Nanotechnol.*, 2008, **3**, 270-274.
88. Y. Wang, Y. Chen, S. D. Lacey, L. Xu, H. Xie, T. Li, V. A. Danner and L. Hu, *Mater. Today*, 2018, **21**(2), 186-192.
89. S. Bellucci, A. Maffuci, S. Maksimenko, F. Micciulla, M. D. Migliore, A. Paddubskaya, D. Pinchera and F. Schettino, *Materials*, 2018, **11**, 2519.
90. K.S. Krishnan and N. Ganguli, *Nature*, 1939, **144**, 667.
91. B. Román-Manso, E. Domingues, F. M. Figuereido, M. Belmonte and P. Miranzo, *J. Eur. Ceram. Soc.*, 2015, **35**, 2723-2731.
92. A. Celzard, J-F Marêché, G. Furdin and S. Puricelli, *J. Phys. D. Appl. Phys.*, 2000, **33**, 3094-3101.
93. L. Pietronero, S. Strässler, H.R. Zeller and M.J. Rice, *Phys. Rev. B.*, 1980, **22**(2), 904-910.
94. M. S. Sarto, A. G. D'Aloia, A. Tamburrano and G. De Bellis, *IEEE T. Electromagn. C.*, 2012, **54**(1), 17-27.
95. H. Wu and L. T. Drzal, *Carbon*, 2012, **50**, 1135-1145.
96. M. Monthioux, P. Serp, E. Flahaut, M. Razafinimanana, C. Laurent, A. Peigney,W. Bacsa, J-M Broto. "Introduction to carbon nanotubes" in Handbook of

Nanotechnology. Ed. B. Bhushan. Springer International Publishing: Cham, Switzerland. 2010, pp. 47-118.
97. N. Hamada, S.I. Sawada and A. Oshiyama, *Phys. Rev. Lett.,* 1992, 68, 1579–1781.
98. J-P Cheng and X-B Zhang, *Proceedings of the 1st IEEE International Conference on Nano/Micro Engineered and Molecular Systems,* January 18 - 21, 2006, Zhuhai, China. 493-496.
99. M. Monthiux. "Introduction to carbon nanotubes" in Carbon Meta-Nanotubes: Synthesis, properties and applications. Ed. M. Monthiux. John Wiley & Sons: New York, USA. 2012, pp. 7-39.
100. Y.A. Kosharov. "Magnetism of nanoparticles: effects of size, shape and interactions" in Magnetic nanoparticles. Ed. S.P. Gubin: Wiley-VCH Verlag GmbH & Co.: Weinheim, Germany. 2009, pp. 197-254.
101. D. Givord and T. Takabatake "Magnetic order" in Reference module in materials science and materials engineering. 2017. Available online at: https://www.sciencedirect.com/science/article/pii/B9780128035818011O9
102. G.C. Papaefthymiou, *Nano Today,* 2009, 4, 438-447.
103. B.D. Culity and C.D. Graham, Introduction to magnetic materials, IEEE Press: Piscataway, NJ, USA, 2009. p.531.
104. V.V. Mody, A. Singh and B. Wesley, *Eur. J. Nanomed.,* 2013, **5**(1), 11-21.
105. N.A. Frey, S. Peng, K. Cheng and S. Sun, *Chem. Soc. Rev.,* 2009, **38**, 2532-2542.
106. J.M.D. Coey, Magnetism and magnetic materials, Cambridge University Press: Cambridge, United Kingdom, 2009, p. 633.
107. K.M. Krishnan, *IEEE T. Magn.,* 2010, **46**(7), 2523-2558.
108. J.V.I. Timonen, R.H.A. Ras, O. Ikkala, M. Oksanen, E. Seppälä, K. Chalapat, J. Li and G. S. Paraoanu. "Magnetic nanocomposites at microwave frequencies" in Trends in nanophysics: theory, experiment and, technology. Eds. A. Aldea and V. Bârsan. Springer Science: London, United Kingdom. 2010, pp. 257-285.
109. V. B. Barbeta, R. F. Jardim, P. K. Kiyohara, F. B. Effenberger and L.M. Rossi, *J. Appl. Phys.,* 2010, **107**, 073913.
110. C. Caizer "Nanoparticle size effect on some magnetic properties" in Handbook of nanoparticles. Ed. M. Aliofkhazraei. Springer International Publishing: Cham, Switzerland. 2016, pp. 475-519.
111. V. Skumryev, S. Stoyanov, Y. Zhang, G. Hadjipanayis, D. Givord and J. Nogués, *Nature*, 2003, **423**, 850-853.
112. B. Issa, I. M. Obaidat, B. A. Albiss and Y. Haik., *Int. J. Mol. Sci.*, 2013, **14**, 21266-21305.
113. R.H. Kodama, *J. Magn. Magn. Mater.*, 1999, **200**, 359-372.
114. D. Lin, A.C. Nunes, C.F. Majkrzak, A.E. Berkowitz, *J. Magn. Magn. Mater.,* 1995, **145**(3), 343-348.
115. A.P. Guimarães, Principles of nanomagnetism, Springer-Verlag: Berlin, Germany, 2009.
116. O. Iglesias and A. Labarta, *Phys. Rev. B,* 2001, **63**, 184416.
117. X. Liu, B.P. Pichon, C. Ulhaq, C. Lefèvre, J.-M. Grenèche, D. Bégin, and S. Bégin-Colin, *Chem. Mater.*, 2015, **27**, 4073−4081.
118. H.M. Lu, W.T. Zheng and Q. Jiang, *Appl. Phys.*, 2007, 40, 320-325.
119. C.B. Craus., *Magnetic properties of nanocrystalline materials for high frequency applications*, PhD thesis, University of Groningen, The Netherlands, 2003.
120. L. B. Kong, L. Liu, Z. Yang, S. Li and T. Zhang. "Magnetic materials for electromagnetic wave absorption" in Magnetic nanomaterials: fundamentals, synthesis and applications. Eds. Y. Hou and D.J. Sellmyer. Wiley-VCH Verlag GmbH & Co.: Weinheim, Germany. 2017, pp. 473-514.

121. Conductor Bulk Resistivity & Skin Depths, RF Café. Available online at: http://www.rfcafe.com/references/electrical/cond-high-freq.htm.
122. C. Kittel, *Phys. Rev.*, 1948, **73** (2), 155-161.
123. G. Goglio, S. Pignard, A. Radulescu, L. Piraux, I. Huynen, D. Vanhoenacker and A. Vander Vorst, *Appl. Phys. Lett.*, 1999, 75(12), pp. 1769-1771.
124. A. Encinas-Oropesa, M. Demand, L. Piraux, I. Huynen and U. Ebels, *Phys. Rev. B*, 2001, 63, pp. 104415.1-6.
125. A. Kharmouche, Proceedings of the 7th International Conference on Nanomaterials: Applications and Properties (NAP), September 10-15, 2017, Odessa, Ukraine, 02MFPM11-2.
126. K. Chalapat, J. V. I. Timonen, M. Huuppola, L. Koponen, C. Johans, R. H. A. Ras, O. Ikkala, M. A. Oksanen, E. Seppäläa and G. S. Paraoanu, Nanotechnol. 2014, 25(48), pp. 485707-14.
127. R. Karim, K.D. McKinstry, J.R. Truedson, and C.E. Patton , *IEEE Trans. Magn.*, 1992, 28(5), pp. 3225-3227.
128. Y. Chen, X. Wang, H. Chen, Y. Gao and N.X. Sun, *IEEE Trans. Magn.*, 2018, 54(11), pp. 6100504-4.
129. F. Mederos-Henry, S. Hermans, I. Huynen, *Microw. Opt. Technol. Lett.*, 2017, **59**(9), 2330-2335.
130. W. Yager and R. Bozorth, *Phys. Rev.*, 1947, **72**(1), 80-81. Z. Ji, X. Shen, Y. Song and G. Zhu, *Mat. Sci. Eng. B*, 2011, **176**, 711-715.
131. X. Shen, J. Wu, S. Bai and H. Zhou, J. Alloy Compd., 2010, 506, 136-140.
132. J. Deng, X. Wen, Q. Wang, Mater. Res. Bull., 2012, 47, 3369-3376.
133. G. Başkayaa, Y. Yıldıza, A. Savka, T. O. Okyaya, S. Erişa, H. Serta and F. Şen, Biosens. Bioelectron., 2017, 91, 728-733.
134. G. Liu, W. Jiang, D. Sun, Y. Wang, F. Li, Appl. Surf. Sci., 2014, 314, 523-529.
135. C. Yu, Y. Sun, X. Fan, Z. Zhao, and J. Qiu, Part. Part. Syst. Charact., 2013, 30(7), 637–644.
136. Q. Wang, L. Jiao, H. Du, Y. Wang and H. Yuan, *J. Pow. Sour.*, 2014, **245**, 101-106.
137. H. Wu, G. Gao, X. Zhou, Y. Zhang, and S. Guo, *Cryst. Eng. Comm.*, 2012, **14**(2), 499-504.
138. X. Zhao, Z. Zhang, L. Wang, K. Xi, Q. Cao, D. Wang, Y. Yang and Y. Du, *Sci. Rep.*, 2013, **3**, 3421.
139. M. Hajizadeh-Oghaz, R. S. Razavi, M. Barekat, M. Naderi, S. Malekzadeh, and M. Rezazadeh, *J. Sol-Gel Sci. Techn.*, 2016, **78**(3), 682–691.
140. N.L.V. Carreño, M.T. Escote, A. Valentini, L. McCafferty, V. Stolojan, M. Beliatis, C.A. Mills, R. Rhodes, C.T.G. Smith, and S.R.P. Silva, *Nanoscale*, 2015, **7**(41), 17.
141. B. Chen, F. Li and G. Yuan, *Catal. Lett.*, **147**, 2877-2885.
142. B-J. Kim, K-M. Bae, Y. S. Lee, K-H. Ana and S-J. Park, *Surf. Coat. Tech.*, 2014, **242**, 125-131.
143. J. Fang, W. Zha, M. Kang, S. Lu, L. Cui and S. Li, *J. Mater. Sci.*, 2013, **48,** 8060–8067
144. G-P Jin, Y-F Ding, P-P Zheng, *J. Power Sources*, 2007, **166**, 80-86.
145. Y. Li, J. Chu, J. Qi and X. Li, *Appl. Surf. Sci.*, 2011, **257**, 6059-6062.
146. L. McCafferty, V. Stolojan, S. G. King, W. Zhang, S. Haq, and S. R. P. Silva, *Carbon*, 2015, **84** (C), 47–55
147. R. Snovski, J. Grinblat, and S. Margel, *J. Magn. Magn. Mater.*, 2012, **324**(1), 90–94.
148. E. Hu, X-Y Yu, F. Chen, Y. Wu, Y. Hu and X.W. Lou, *Adv. Energy Mater.*, 2017, 8(9), 1702476
149. S. Sarkar, N. Giri, A. Mondal and R. Ray, *AIP Conf. Proc.*, 2018, **1953**, 050016.

150. H-S. Kim, H. Lee, K-S. Han, J-H. Kim, M-S. Song, M-S. Park, J-Y. Lee and J-K. Kang, *J. Phys. Chem. B*, 2005, **109**, 8983-8986.
151. X. Huang, X. Zhou, K. Qian; D. Zhao, Z. Liu and C. Yu, *J. Alloy Compd.*, 2012, **514**, 76-80.
152. L. Wang, T. Du, J. Cheng, X.Xie, B. Yang and M. Li, *J. Power Sources*, 2015, **280**, 550-554.
153. F. He, J. Fan, D. Ma, L. Zhang, C. Leung, H. L. Chan, *Carbon*, 2010, **48**, 3139-3144.
154. Y. Yao, S. Miao, S. Liu, L.P. Ma, H. Sun and S. Wang, *Chem. Eng. J.*, 2012, **184**, 326-332.
155. X.Y. Yang, Z.Y. Zhang, Y.F. Ma, Y. Huang, Y.S. Wang and Y.S. Chen. *J. Mater. Chem.*, 2009, **18**, 2710.
156. W. Zhang, X. Zhang, L. Zhang and G. Chen, *Sensor Actuat. B-Chem.*, 2014, **192**, 459-466.
157. H. Teymourian, A. Salimi and S. Kherzrian, *Biosens Bioelectron*, 2013, **49**, 1-8.
158. J. Fang, W. Zha, M. Kang, S. Lu, L. Cui and S. Li, *Mater. Sci.*, 2013, **48**, 8060–8067.
159. J. Xiang, J. Li, X. Zhang, Q. Ye, J. Xu and X. Shen, *J. Mater. Chem. A.*, 2014, **2**, 16905-16914.
160. B. Quan, X. Liang, G. Ji, J. Ma, P. Ouyang, H. Gong, G. Xu and Y. Du, *ACS Appl. Mater. Inter.*, 2017, **9**(11), 9964-9974.
161. B. Quan, X. Liang, G. Ji, Y. Zhang, G. Xu and Y. Du, *ACS Appl. Mater. Inter.*, 2017, **9**(44), 38814-38823.
162. Y. Zhan, F. Meng, Y. Lei, R. Zhao, J. Zhong and X. Liu. *Mater Lett.*, 2011, **65**, 1737-1740.
163. P. Liu, Y. Huang and X. Zhang, *J. Alloy Compd.*, 2014, **617**, 511-517.
164. G. Li, L. Wang, W. Li and Y. Xu. *RSC Adv.*, **2015**, 5, 8248-8257.
165. D. Kettels, 2015. The combined use of graphene nanoplatelets and magnetite nanoparticles in polymer host matrices to design novel multilayer EMI shielding structures in the microwave range (MSc dissertation). Université Catholique de Louvain, Louvain-la-Neuve, Belgium.
166. S. Pande, A. Chaudhary, D. Patel, B.P. Singh and R.B. Mathur, *RSC Adv.*, 2014, **4**, 13839-13849.
167. N. Bagotia, V. Choudhary and D.K. Sharma, *Compos. Part B –Eng.*, 2017, **124**, 101-110.
168. S. Barrau, P. Demont, A. Peigney, C. Laurent and C. Lacabanne, *Macromolecules*, 2003, **36**, 5187-5194.

part

I

controlled chemical assembly of magnetic nanoparticles and nanocarbon supports

chapter 2

Decoration of nanocarbon solids with magnetite nanoparticles

In this chapter, we compare three decoration methods of different nanocarbon solids (NcS) with magnetite nanoparticles (MaNPs), namely covalent linkage, direct co-precipitation and solvothermal synthesis. The influence of each method on the obtained nanocomposites most relevant characteristics has been studied. Also, the impact of the variables controlling the solvothermal decoration of a variety of NcS is investigated in detail, such as the nature of the iron precursor and the NcS (type and oxidation state), the reaction temperature, time and water content.

Related publications

F. Mederos-Henry, B. Pichon, Y. Tchuitio Yagang, A. Delcorte, C. Bailly, I. Huynen and S. Hermans. **Decoration of nanocarbon solids with magnetite nanoparticles: towards microwave metamaterial absorbers.** *J. Mater. Chem. C*, 2016, **3**, 3290.

Collaborators

Yzaora Tchuitio Yagang (IMCN/MOST), Benoit Pichon (UNISTRA/IPCMS, France).

Magnetite (Fe_3O_4), a ferrimagnetic iron(II,III) oxide with a cubic inverse spinel structure, is considered of primordial scientific and technological importance given its unique magnetic and electrical properties, low cost and feasibility of large-scale production. Nanocomposites obtained by decoration of NcS with magnetite nanoparticles (MaNPs) have already been reported in the scientific literature for very diverse applications such as the production of energy storage devices [1-3], the remediation of environmental pollutants [4, 5], the design of controlled drug carriers [6] or biosensors [7], to mention just a few. However, up to this date, there is no evidence that any such nanomaterial has been tested as a microwave metamaterial absorber.

Magnetite's microwave absorbing properties have already been acknowledged and partially investigated [8, 9], restricted however to a Jaumann configuration where frequency-selective absorbing efficiency is primarily controlled by the thickness of the sample, while a ferromagnetic resonance (FMR) mechanism has not been evidenced nor exploited to induce losses in such materials.

Most commonly, these magnetite/carbon nanocomposites have been produced through solvothermal [1, 10-12] or hydrothermal [3, 13] strategies, direct co-precipitation of iron (II) and (III) salts on the NcS [5, 15], the covalent bonding of nanoparticles onto the NcS [4, 15] or thermal decomposition of an iron precursor [17]. As far as we know, no study has yet been published on the comparative advantages and drawbacks that each technique offers. Instead, only a few general challenges faced during the creation of these materials have been mentioned [4, 18], such as reaching a tight control over the MaNPs loading rate, anchoring them strongly to the NcS to avoid leaching or distributing them homogeneously over the NcS surface.

In this study, we compare nanocomposites obtained either by the covalent linkage of MaNPs to graphene oxide (GO), or their deposition onto this NcS by a direct coprecipitation or a solvothermal strategy. Our aim is to obtain for the first time a direct comparison of these three synthetic methods with

the same nanocarbon solid. More particularly, we compare chemical identity, size, loading rate and spatial distribution of the nanoparticles deposited over the NcS in each case. In order to go beyond the state-of-the-art in the field, and to obtain a tight control over the final characteristics of the nanocomposites obtained, we studied the solvothermal method more thoroughly, on different NcS types, to unravel the key parameters that can be fine-tuned in a predictive manner to obtain the desired materials. The magnetic properties of the obtained materials were studied using SQUID.

2.1 Materials and methods

2.1.1 Materials and characterization techniques

Multi-walled carbon nanotubes (MWCNTs, 95%C purity) were obtained from Nanocyl (Belgium). Graphene oxide (GO) and reduced graphene oxide (rGO) were purchased at Nanoinnova Technologies SL (Spain) while graphene nanoplatelets (GNPs) were supplied by TIMCAL (Switzerland). All other reactants were supplied by Sigma Aldrich, Merck, Alfa Aesar or VWR and engaged as received. More details on each reactant are provided in Appendix I while the different physicochemical characterization techniques employed are described in Appendix II.

2.1.2 Synthetic methods

2.1.2.1 Synthesis of oxidized multi-walled carbon nanotubes (ox-MWCNTs)

As reported elsewhere [18], 50 mg of MWCNTs were suspended in 100 mL concentrated HNO_3 (65%) and heated, under reflux (100 ºC), for 2 hours under constant magnetic stirring. The resultant product was recovered by filtration over a PTFE membrane filter (Sartorious Stedim Biotech filter type 118, 0.45 m pore size) and rinsed abundantly with Milli-Q water, until a neutral pH was obtained. Afterwards, it was rinsed once more with 50 mL methanol and dried under vacuum at ambient temperature overnight.

2.1.2.2 *Direct co-precipitation (DCOP) decoration of graphene oxide (GO) as a model nanocarbon solid (NcS) with magnetite nanoparticles (MaNPs)*

The following synthetic procedure was adapted from the methodology reported by Yao *et al.* [5].

In a three-necked round bottom flask, 100 mg of GO were suspended in 28 mL Milli-Q water, sonicated for 60 minutes (VWR Ultrasound cleaner 1200-THD, sonication power: 60 W) and deoxygenated under a continuous argon flux for another 60 minutes. In parallel, the amounts of $FeCl_3 \cdot 6H_2O$ and $FeCl_2 \cdot 4H_2O$ required to achieve a certain Fe/GO (% w/w) loading rate (LR) (e.g. 161 mg and 59 mg of the Fe(III) and Fe(II) salts respectively for a 50% LR) were mixed in a 5 mL glass vial, which then was evacuated thrice using a combination of vacuum/argon cycles. 2 mL of Milli-Q water, previously deoxygenated with an argon current, were then added through a septum producing an aqueous solution of Fe ions with a 0.5 molar ratio of Fe(II)/Fe(III). The latter solution was added dropwise into the graphenic suspension under argon flux and vigorous stirring. The mixture was then stirred for another 24 hours, keeping a controlled argon atmosphere. Afterwards, the solution was heated to 80 °C and drops of ammonium hydroxide (NH_4OH, 28% w/v aqueous solution) were added until the solution's pH was set to 10. Then, 1.1 mL of hydrazine monohydrate ($N_2H_2 \cdot H_2O$) were added and the mixture was refluxed for 5 hours. The obtained product was separated by magnetic decantation, rinsed with Milli-Q water and dried under vacuum, at room temperature, for 12 hours.

2.1.2.3 *Covalent linkage (COV) of MaNPs to graphene oxide (GO) as a model NcS*

In all cases, sonication was performed using a VWR Ultrasound cleaner 1200-THD. Sonication power is specified for each reaction step.

2.1.2.3.1 Synthesis of unsupported MaNPs by direct coprecipitation

Unsupported MaNPs were synthetized following a procedure reported by Gao *et al.* [19] that was modified in order to keep an oxygen-free, argon atmosphere throughout the procedure.

In a Schlenk flask, 50 mL of Milli-Q water were mixed with 10 mL of a 1M HCl solution and deoxygenated for an hour using a continuous argon flux. 5.46 g of iron (III) chloride hexahydrate ($FeCl_3 \cdot 6H_2O$), 2.01 g of iron (II) chloride tetrahydrate ($FeCl_2 \cdot 4H_2O$) and 600 mg of polyethylene glycol 2000 (PEG-2,000) were placed in a second Schlenk flask, which was then purged thrice using a combination of vacuum/argon cycles. By creating vacuum in the second flask, the acidified aqueous solution was transferred from the first flask through a nitrile tube in order to dissolve the powders and produce an oxygen-free aqueous solution of Fe ions with a 0.5 molar ratio of Fe(II)/Fe(III). This solution was then transferred in the same manner to a previously Ar-purged dozer and added dropwise, under argon atmosphere and magnetic stirring, into 100 mL of a 1M sodium hydroxide (NaOH) solution containing 1.00 g of PEG-2,000 that had been previously deoxygenated and heated to 60 ºC. A black precipitate formed immediately and once the addition of the iron-containing solution was completed, the dozer was replaced by a spiral cooler and the mixture was stirred for 2 more hours at 60 ºC while being kept under argon atmosphere. Afterwards, the product was separated by magnetic decantation and washed thrice with deoxygenated, Milli-Q water. The resulting product noted ***M*** was dried overnight under vacuum at room temperature and then stored in a glovebox.

2.1.2.3.2 Synthesis of magnetite@silica core-shell nanoparticles (M@Si)

The magnetite@silica core-shell nanoparticles were synthetized using a method established by Gao *et al.* [19]

A solution containing 38 mL Milli-Q water and 160 mL absolute ethanol was deoxygenated for an hour using a continuous argon flux. 160 mg of

product ***M*** was grinded in the glovebox and then added to the above-mentioned solution. The resulting suspension was sonicated for 2 hours (sonication power: 80 W), after which its pH was set to 12 by using 0.05 mL tetramethylammonium hydroxide (TMAOH), followed by the addition of 4 mL tetraethoxysilane (TEOS). The reaction mixture was magnetically stirred under argon atmosphere for 12 hours at room temperature. The obtained product noted ***M@Si*** was separated by magnetic decantation, rinsed ten times, alternating Milli-Q water and ethanol, and dried under vacuum at room temperature for 12 hours.

2.1.2.3.3 Functionalization of magnetite@silica core-shell nanoparticles (f-M@Si)

The synthesis of (3-Aminopropyl)triethoxysilane (APTES)-functionalized magnetite@silica core-shell nanoparticles was executed using a procedure inspired from the methods reported by Liu *et al.* [20] and Kokate *et al.* [21].

In a Schlenk flask, 80 mg of product M@Si were dried overnight under vacuum, at room temperature. 15 mL of freshly distilled toluene were added and the mixture was sonicated for 60 minutes (sonication power: 60 W). Afterwards, 2 mL of (3-aminopropyl)triethoxysilane (APTES) were added through a septum. The suspension was then refluxed at 80°C for 3 hours. The solid noted ***f-M@Si*** was separated using magnetic decantation, rinsed nine times alternating toluene, methanol and Milli-Q water, and dried under vacuum at room temperature for 12 hours.

2.1.2.3.4 Synthesis of an acyl chloride derivative of graphene oxide (GO-Cl)

The GO-Cl derivative synthesis was executed following a modified version of the method proposed by Vidick [22] for the synthesis of acyl chloride derivatives of oxidized carbon nanotubes.

75 mg of graphene oxide (GO) were placed in a round-bottom flask and sonicated in 40 mL dried toluene (sonication power: 60 W) for an hour.

Afterwards, 5.6 mL thionyl chloride ($SOCl_2$) were added and the reaction mixture was refluxed at 120 °C for 5 hours. The product was filtered, rinsed extensively with toluene and dried overnight under vacuum, at room temperature.

2.1.2.3.5 Covalent linkage of functionalized core-shell nanoparticles and graphene oxide acyl chloride derivative (COV)

The covalent linkage of the functionalized magnetite@silica core-shell NPs and the acyl chloride derivative of GO was executed following a method used by Vidick [22].

Two vials containing each 2 mL of freshly distilled toluene and 25 mg of *f*-M@Si or GO-Cl were sonicated for 60 minutes (sonication power: 40 W). Afterwards, both suspensions were mixed and 13 mL of freshly distilled toluene were added. The mixture was then placed under reflux at 100 °C for 4 hours. The obtained product was magnetically decanted, washed ten times with toluene and dried under vacuum at room temperature for 12 hours.

2.1.2.4 Solvothermal (SOLV) decoration of different NcS with magnetite nanoparticles

In this research project, solvothermolysis was performed by dispersing both the NcS and iron precursor in a glycol, which simultaneously served as solvent and reducing agent. Several synthetic parameters could easily be varied, such as the type of engaged nanocarbon solid and its degree of oxidation, the nature of the iron precursor, the composition of the solvent mixture, the reaction temperature and time as well as the amount of water present in the system.

Our goal was to pinpoint the impact of these parameters on the final nanocomposites characteristics. Accordingly, we tested four solvothermal variations in which several of these parameters were modified. These variations are summarized in Table 1 and briefly described hereafter.

Table 1 - Experimental conditions of the different solvothermal methods considered

Method	NcS	Fe Precursor	Solvent mixture (%v/v)	Temp. (ºC)	Time
SOLV-A	GO, GNPs MWCNTs, ox-MWCNTs	$FeCl_3{\cdot}6H_2O$	50% EG 25% PEG-400 25% water	180	24 h
SOLV- B	GO	$Fe(acac)_3$	80% EG 20% water	260	80min
SOLV- C	GO, rGO, GNPs	$Fe(acac)_3$	EG	180	16 h
SOLV- D	MWCNTs, GNPs	$Fe(acac)_3$	TREG	250	40 min

2.1.2.4.1 SOLV-A method

The SOLV-A synthesis was adapted from the methodology described by Huang *et al.* [23].

100 mg of a NcS were dispersed into a mixture composed of 27 mL ethylene glycol (EG), 13 mL polyethylene glycol 400 (PEG-400) and 13 mL Milli-Q water. The suspension was sonicated for 2 hours. Afterwards, a certain amount of $FeCl_3{\cdot}6H_2O$ was added under magnetic stirring in order to obtain the desired Fe/NcS (% w/w) loading rate (LR) (e.g. 242 mg for a 50% LR). After complete dissolution of the salt, crushed NaOH pellets were added until the solution's pH value was set to 13. The mixture was then transferred into a stainless-steel autoclave vessel, heated up to 180ºC (approx. 50 minutes) and maintained at that temperature for 23 hours.

2.1.2.4.2 SOLV-B method

The synthetic methodology reported by Wan *et al.* [24] was modified to develop the SOLV-B procedure

100 mg of a NcS and the required amount of $Fe(acac)_3$ needed to achieve a particular Fe/NcS LR (e.g. 316 mg for a 50% LR) were added to a mixture composed of 10 mL EG and 2 mL Milli-Q water. The mixture was magnetically stirred until dissolution of the $Fe(acac)_3$ complex. Afterwards, it was sonicated for 2 hours. The suspension was transferred into a stainless

steel autoclave vessel, heated up to 260 ºC (approx. 80 minutes) and maintained at that temperature for 80 minutes.

2.1.2.4.3 SOLV-C method

The SOLV-C method was inspired from the procedures reported by Shena *et al.* [25]

100 mg of a NcS and the required amount of $Fe(acac)_3$ needed to obtain a particular Fe/NcS LR (e.g. 316 mg for a 50% LR) were dispersed into 180 mL EG and sonicated for 30 minutes. Afterwards, 80 μL of hydrazine monohydrate ($N_2H_2{\cdot}H_2O$) were slowly added under magnetic stirring. The suspension was transferred into a stainless-steel autoclave vessel, heated up to 180 ºC (approx. 50 minutes) and maintained at that temperature for 15 hours.

2.1.2.4.4 SOLV-D method

The SOLV-D synthesis was adapted from the methodology proposed by Pennetreau [26]

100 mg of a NcS were suspended in 50 mL triethylene glycol (TREG). The suspension was sonicated for 15 minutes. The amount of $Fe(acac)_3$ needed to achieve a particular Fe/NcS LR (e.g. 316 mg for a 50% LR) was added and the mixture was magnetically stirred for 10 minutes. It was then transferred into a stainless-steel autoclave vessel, heated up to 250ºC (approx. 50 minutes) and maintained at that temperature for 40 minutes.

In all the described SOLV procedures: a) sonication was performed in a VWR ultrasound cleaner USC 1200-THD at 80 W sonication power; b) the Parr Instrument Company (USA) 300 mL-stainless-steel autoclave vessel was fitted with a matching PTFE liner to avoid direct contact between the reaction media and the steel; c)the autoclave's temperature was automatically regulated by a Parr 4836 temperature controller (Parr Instrument Company, USA) having an average heating rate of 4 ºC/min; d) the autoclave's inner atmosphere was not purged nor modified in any manner during the synthesis, while the system pressure was left to build up

during heating without any type of external control; e) when the heating time was completed, the autoclave was immediately immersed in an ice bath and cooled down to ambient temperature; and f) the obtained products were separated by magnetic decantation, filtered over a PVDF filter (Millipore GVWP02500, 0.22 m pore size) and rinsed six times, alternating Milli-Q water and ethanol. Afterwards, they were dried under vacuum, at room temperature for 12 hours.

2.2 Results and discussion

Direct co-precipitation, solvothermal synthesis and covalent linkage were used to produce a series of MaNPs@NcS nanocomposites, where NcS are carbon nanotubes or graphenic powders (see Table 2). The obtained MaNPs@NcS nanocomposites were extensively characterized in order to identify the influence of experimental parameters on the obtained nanocomposites physicochemical characteristics. The results obtained for each synthetic technique are compared below using the MaNPs@GO nanocomposite as a model study. Afterwards, results regarding the in-depth investigation of the variables controlling the solvothermal MaNPs decoration of a variety of NcS will be presented.

Table 2 - Overview of the different synthetic methods used in this study

Synthetic method	Code	NcS used	Fe precursor	References
Covalent linkage	COV	Acyl-functionalized GO	$FeCl_2{\cdot}4H_2O$ $FeCl_3{\cdot}6H_2O$	[5]
Direct co-precipitation	DCOP	GO	$FeCl_2{\cdot}4H_2O$ $FeCl_3{\cdot}6H_2O$	[19-22]
Solvothermolysis	SOLV-A	GO, GNPs MWCNTs, ox-MWCNTs	$FeCl_3{\cdot}6H_2O$	[23]
	SOLV- B	GO	$Fe(acac)_3$	[24]
	SOLV- C	GO, rGO, GNPs	$Fe(acac)_3$	[25]
	SOLV- D	MWCNTs, GNPs	$Fe(acac)_3$	[26]

2.2.1 Comparison of MaNPs@GO nanocomposites obtained by the solvothermal (SOLV-A), direct co-precipitation (DCOP) and covalent linkage (COV) methods

Graphene oxide (GO) was decorated with magnetite nanoparticles (to give MaNPs@GO nanocomposites) using direct co-precipitation, solvothermolysis and covalent bonding techniques. Our findings demonstrate that the most relevant characteristics of the obtained nanocomposites, such as the chemical identity, size, loading rate and spatial distribution of the nanoparticles over the NcS, are strongly determined by the chosen synthetic method.

Similar cuboidal or elongated prismatic morphologies were observed in all the MaNPs deposited onto or covalently attached to GO. However, the measured average particle sizes and particle size distributions were different for each technique. The MaNPs found in the DCOP nanocomposite (Figure 1b) are the smallest and their size distribution is the narrowest. On the contrary, those directly co-precipitated in the absence of any NcS (Figure 1a), used later for the COV product, were larger and possessed wider size distributions, revealing a templating effect of the NcS as previously claimed [8, 18, 27, 28]. The SOLV-A method (Figure 1c) also produced larger particle sizes and wider size distributions than those obtained for the DCOP nanocomposite, possibly due to the higher reaction temperatures and longer reaction times used.

In terms of the deposited nanoparticles' phase composition, the solvothermal strategy systematically produced an iron oxide phase with a spinel structure. Rietveld refinement analyses of XRPD data were performed in order to determine the contribution of magnetite and maghemite. In all cases, the latter product was found to be a subsidiary phase (<2%), possibly present as a magnetite@maghemite core@thin shell structure as observed by Baaziz *et al.* [29]. Thus, for practical

purposes, we herein assume the nanoparticles to be mostly pure magnetite (Figure 2a). By opposition, the direct co-precipitation method led to a lepidocrocite contamination (Figure 2b), whose amount varies from batch to batch (Figure 2b dotted line for a repeated synthesis). This type of impurity has already been observed by other authors [30, 31]. Oxyhydroxides impurities are problematic for our intended applications given that they are non-magnetic and can readily transform into other iron-containing species [32]. If present, no real control over the end-product composition and its resultant electromagnetic properties can be expected.

When considering the known chemistry of iron oxides, hydroxides and oxyhydroxides (see Appendix III), it becomes clear that the direct co-precipitation (DCOP) approach, known as the classical magnetite synthesis, might not be the best choice if a pure Fe_3O_4 phase is desired. Indeed, it is evident that the DCOP experimental conditions can easily lead to the formation of parasitic phases via undesired iron-containing species, due to the simultaneous presence of Fe(II) and Fe(III) ions [30-33]. This is even worse if oxygen has not been well evacuated from the reaction atmosphere [31, 34] or if the Fe(II)/Fe(III) molar ratio is not strictly kept at a value of 0.5 [31].

Each methodology also produced significantly different spatial distribution of the MaNPs over the NcS. In the case of the covalent linkage strategy, we observed that functionalized silica-coated MaNPs were randomly distributed all over the graphenic sheets (Figure 3a, b), as well-individualized particles or nanosized agglomerates (Figure 3c).

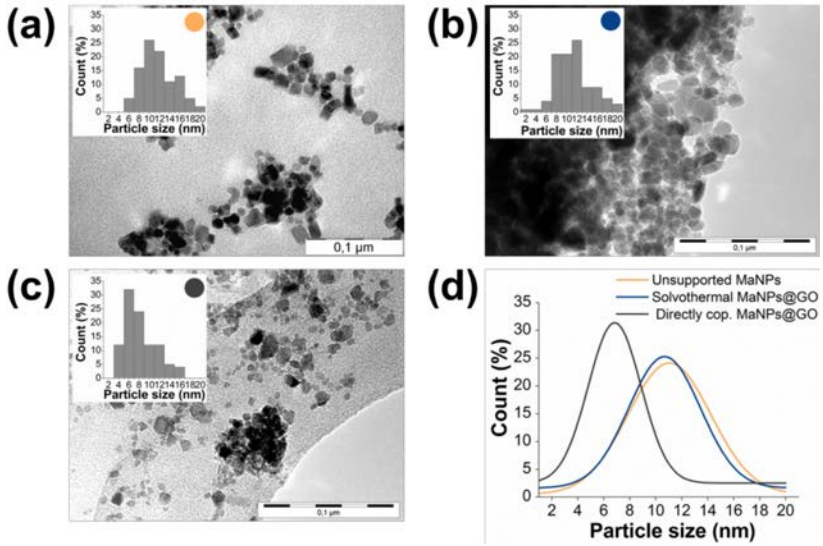

Figure 1 - TEM images and (inset) histograms of particle size distribution of (a) unsupported MaNPs used for the COV method, (b) solvothermally deposited MaNPs@GO and (c) directly co-precipitated MaNPs@GO nanocomposites; (d) Gaussian-function fitting of experimental particle size data.

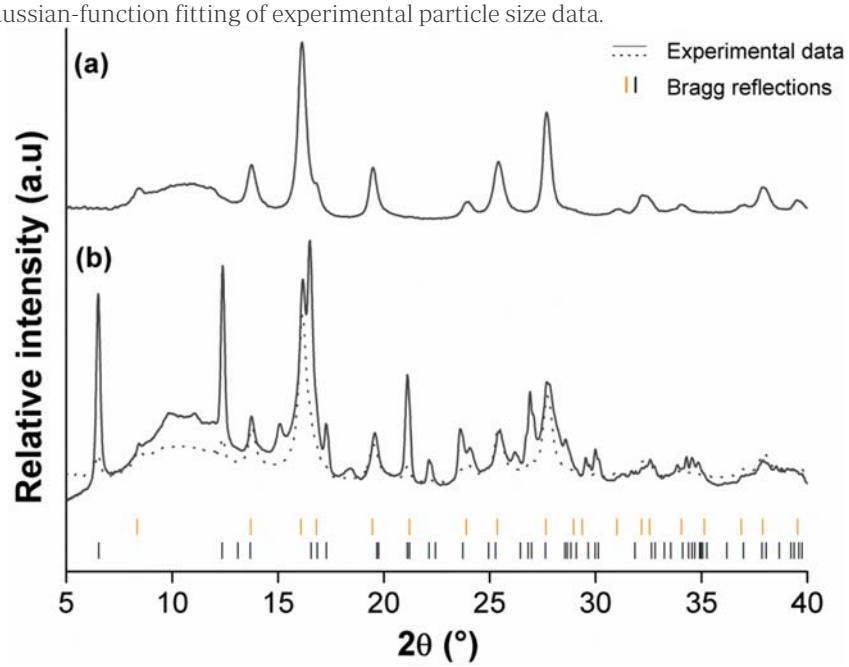

Figure 2 - XRPD diffraction patterns of MaNPs@GO nanocomposites obtained by (a) SOLV-A and (b) DCOP strategies. In the case of the latter, the synthesis was repeated (dotted black line). Orange and black lines indicate Bragg reflections belonging to magnetite and lepidocrocite phases respectively.

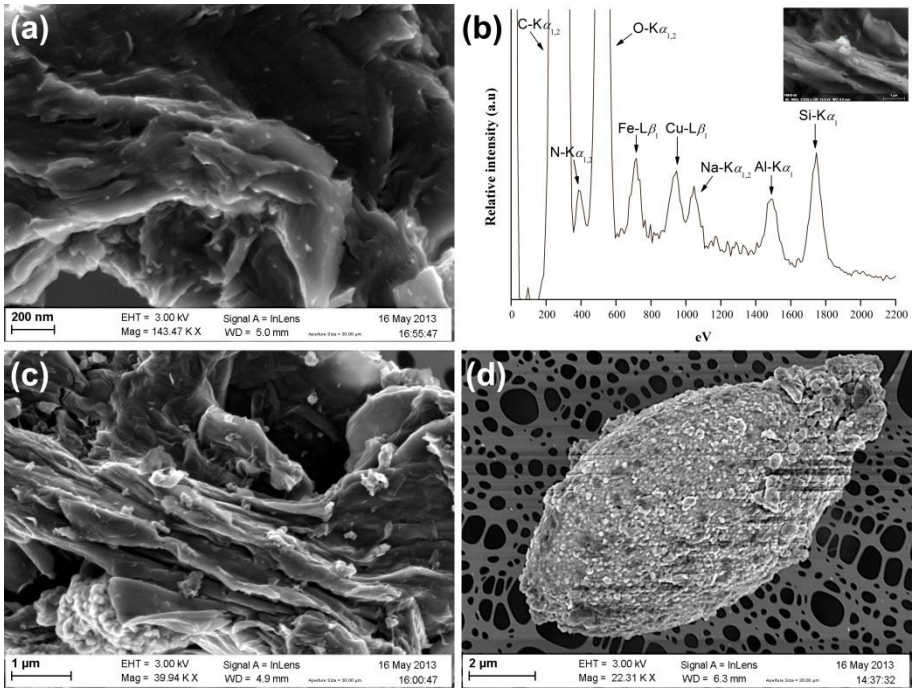

Figure 3 - (a) SEM image of the end product resulting from the multi-step covalent linkage methodology; (b) EDX spectrum obtained from a particle (inset picture): Fe, Si and N signals confirm the presence of functionalized silica-coated MaNPs. Cu and Al signals belong to the sample holder while the presence of Na can be traced back to the synthesis of the unsupported MaNPs; (c) SEM image of individualized and nanosized agglomerates attached to the graphenic surface; (d) SEM image of large micrometric agglomerates.

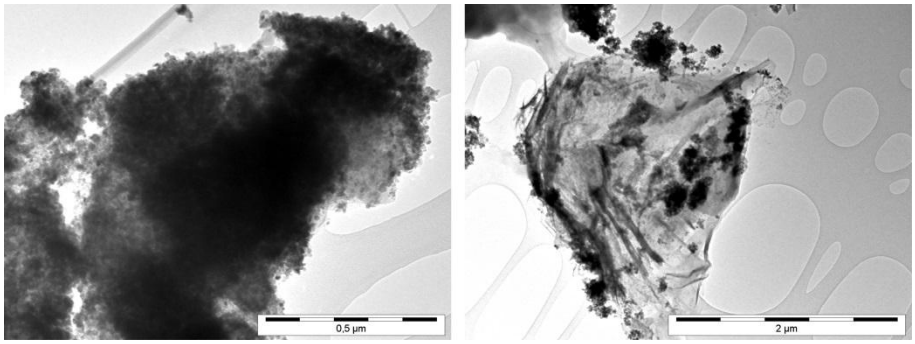

Figure 4 - TEM images of (left) the solvothermal and (right) the direct co-precipitation products.

However, much larger micrometric aggregates coexist independently of the NcS (Figure 3d), composed of magnetite-silica core-shells nanoparticles agglomerated by means of magnetic dipole-dipole interactions. These large, independent, agglomerates can locally modify the resultant material's electromagnetic behavior and are thus undesirable.

The SOLV-A strategy produced a nanocomposite in which the NcS was homogeneously and densely decorated with MaNPs, while in the product obtained by direct co-precipitation, the particles seemed to randomly agglomerate on certain areas of the NcS (Figure 4). The observed difference in the nanoparticles' spatial distributions is possibly related to the interaction between the graphenic surface and the intermediate species formed in each case, as explained below.

Under the experimental conditions used in the DCOP synthesis, the initial pH value is low (pH=2.0). Only a slight fraction of GO's carboxylic acid groups is expected to be ionized [35]. In consequence, a minor percentage of the total positively charged iron ions is in close contact with the graphenic surface, while the rest remains in the reaction media. Once the pH is raised to 10, magnetite particles begin to form, both over the GO's surface and in solution. Given the strong magnetic dipole-dipole interactions existing between MaNPs crystallites [29], the particles formed on the nanocarbon surface attract those precipitating from solution, causing them to agglomerate.

In the case of the solvothermal strategy, the early creation of a strongly basic reaction medium not only causes the formation of diverse $Fe_xO_yH_z$ species [1, 30], but also deprotonates a larger number of GO's acidic groups than under the DCOP conditions [35]. This confers a net negative charge to the NcS surface [35] that attracts the positively-charged iron

species found in the reaction media. Those species are then transformed into MaNPs during the solvothermal reaction, producing the homogeneous distribution observed in Figure 4, left.

Concerning the MaNPs loading rate, the solvothermal procedure comparatively offers a much simpler way of modifying the amount of MaNPs that can be loaded onto the NcS by simply adjusting the amount of Fe(III) precursor engaged in the reaction. However, the direct co-precipitation method allows for slightly higher mass Fe/GO loadings than the solvothermal approach: 37% loading rate for the former versus 33% for the latter (50% intended in both cases), with the same NcS. The amount of covalently linked MaNPs is considerably inferior to the ones obtained with the two other techniques.

2.2.2 Influence of the solvothermal experimental parameters on the nanocomposite characteristics

According to the results presented above, the nanocomposites produced via the solvothermal strategy are more homogeneous, simpler to produce and to modify, hence more appropriate for our targeted applications.

Consequently, we decided to further explore solvothermolysis by pinpointing the impact of different experimental parameters on the final nanocomposites characteristics. These parameters are described in section 2.1.2.4. and the resulting solvothermal variations that were tested are summarized in Table 1. Obtained results are described hereafter in terms of the achieved MaNPs chemical identity, morphology, particle size, loading rates and spatial distribution over the NcSs. Finally, the magnetic properties of a series of MaNPs@GO nanocomposites are described.

2.2.2.1 Deposited nanoparticles' chemical identity, morphology and particle size

Pure magnetite crystallites were identified by XRPD in the products obtained by all four solvothermal methods. No other iron-containing parasitic phases were detected in any case. However, for identical loading rates of 50% Fe/NcS and independently of the NcS used, important differences where observed between the samples produced with the $FeCl_3 \cdot 6H_2O$ salt or the $Fe(acac)_3$ complex (Figure 5). In the case of the former, all characteristic magnetite reflections are present while, in the case of the latter, only the most intense reflections stand out from the background. Furthermore, at low loading rates, e.g. 10% Fe/NcS, signals were still detectable for nanocomposites produced with the iron salt precursor while only signals corresponding to the NcS could be observed in samples synthetized using the iron complex. The striking difference in signal intensity was found to be due to both, the crystallites sizes as well as their abundance.

Indeed, TEM inspection of the obtained nanocomposites revealed that the type of iron precursor produces a significant difference in the size of the deposited MaNPs. Independently of the NcS used, samples produced using the iron salt were composed of prismatic magnetite nanoparticles with average sizes comprised between 8 and 13 nm approximately (Table **3**). Instead, in the samples produced with the iron complex, the deposited MaNPs were difficult to observe given their extremely reduced size: the average particle size did not exceed 2.2 nm. Nonetheless, a similar prismatic morphology was also observed in those rare particles of larger size that were found in these samples.

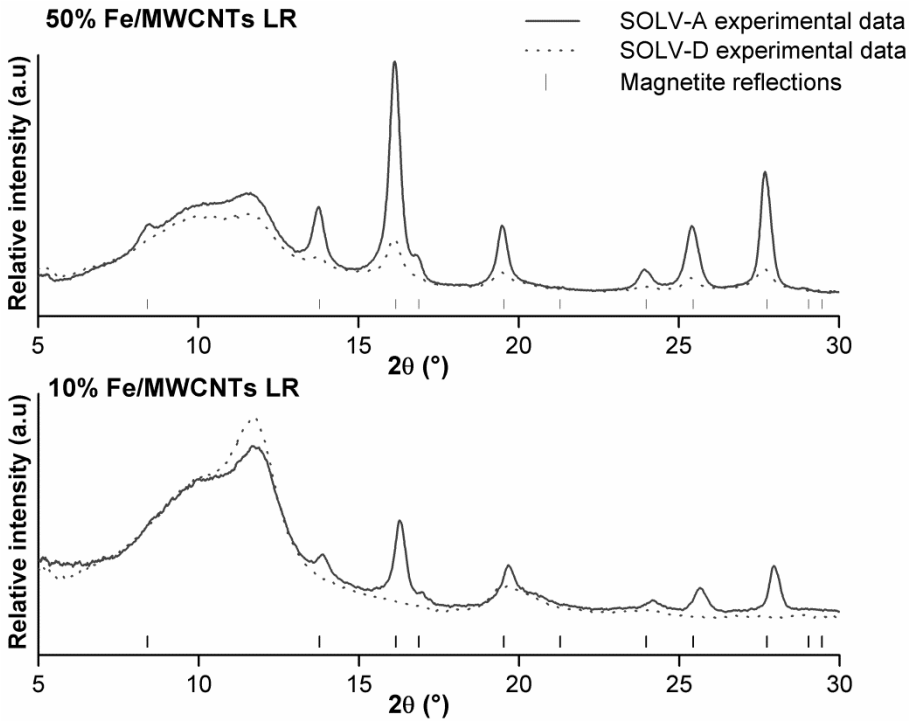

Figure 5 - XRPD diffractograms of MaNPs@MWCNTs produced with methods using an iron salt (SOLV-A) and an iron complex (SOLV-D) precursor at different Fe/NcS loading rates. Gray vertical lines indicate Bragg reflections belonging to magnetite.

In the scientific literature [32], reaction time and temperature are usually regarded as the main critical factors controlling the obtained MaNPs size. However, our findings show that the obtained size differences cannot be attributed to reaction temperature. Indeed, as shown in Table 1, the iron complex is exposed to identical or higher reaction temperatures in methods SOLV-C or SOLV-D, respectively, than the iron salt precursor in method SOLV-A. Nonetheless, as mentioned above, MaNPs found in SOLV-A products are from six to ten times larger (Table 3) than those obtained by the SOLV-C or SOLV-D methods.

Another critical factor that seems to govern the deposited MaNPs particle size is the amount of water included in the reaction mixture, as proven by the results obtained with the SOLV-B method. In this approach, $Fe(acac)_3$ is also used as the iron precursor and its reaction conditions combine those used in methods SOLV-C and SOLV-D except that 20% (v/v) water is included in the reaction medium. As shown in Table 3, for the same NcS and intended LR, the deposited MaNPs size (5.8 ± 2.1 nm) is almost five times the size obtained using the SOLV-C method (1.3 ± 1.8 nm), notwithstanding the much shorter reaction times used in method SOLV-B.

Determining why water has such an important effect on the deposited MaNPs size requires an understanding of the mechanism underlying the polyol solvothermal decomposition of $Fe(acac)_3$ and its transformation to magnetite. Even though some limited explanations regarding this particular reaction system can be found in the work of Deng *et al.* [11], a thorough mechanistic study has yet to be performed. Nonetheless, it is known that water plays an essential role in the hydrolysis reactions leading to the formation of intermediary hydroxide and oxyhydroxides species [32] that could be involved in the formation

of magnetite under the used solvothermal reaction conditions. Thus, its presence in larger quantities than those produced by the thermal decomposition of the glycol moieties [11, 36] would seem to yield larger amounts of magnetite available for crystal nucleation and growth onto the NcS. Whatsoever, the total amount of water in the system should be kept below 60% (v/v %). Indeed, it has been shown [11] that, in similar reaction systems, a hematite phase is formed when water exceeds this concentration limit.

Another factor that has a non-negligible effect on the deposited MaNPs size is the oxidation degree of the NcS. Results shown for SOLV-A and SOLV-C methods in Table 3 indicate that the MaNPs size decreases as the number of oxygenated functions on the NcS surface increases, both in carbon nanotubes and in graphenic solids, independently of the type of iron precursor used. These results tend to prove that, after electrostatically attracting the iron-containing species existing in the reaction mixture, the solid's oxygenated functions serve as nucleation sites to the forming MaNPs. Thus, the higher density of oxygenated functions on the surface of the NcS produces a higher nucleation rate and the resulting particle size decreases, as observed. The formation of Fe-O-C bonds between Fe_3O_4 and a NcS surface through the latter's oxygenated functions has been considered [16, 37] to explain the stabilization of deposited MaNPs toward excessive sintering when similar MaNPs@graphene nanocomposites were subjected to thermal annealing. In this case, our results prove that the NcS' oxygenated functions can also be used to tune the deposited MaNPs sizes.

Table 3 - Influence of the solvothermal method experimental conditions on the average size of MaNPs deposited onto different NcS as measured by TEM.

Method	SOLV-A			SOLV-B
NcS	MWCNTs	ox-MWCNTs	GO	GO
% Fe/NcS LR	50%	50%	10%	10%
Avg. size / nm	13.2 ± 5.9	8.5 ± 3.3	11.0 ± 3.9	5.8 ± 2.1

Method	SOLV-C		SOLV-D	
NcS	GO	GNPs	GNPs	MWCNTs
% Fe/NcS LR	10%	10%	10%	50%
Avg. size / nm	1.3 ± 1.8	2.2 ± 1.0	1.8 ± 1.0	2.0 ± 2.9

Table 4 - Amounts of loaded iron onto different NcS determined by TGA analysis (50% Fe/NcS LR aimed at)

	SOLV-A			
NcS	MWCNTs	ox-MWCNTs	GO	GNPs
% Fe/NcS LR	18	21	37	29

	SOLV-C			SOLV-D	
NcS	GO	rGO	GNPs	GNPs	MWCNTs
% Fe/NcS LR	19	15	13	13	12

2.2.2.2 MaNPs loading rate

The amount of MaNPs that can be loaded solvothermally onto a NcS seems to depend on the nature of both the iron precursor and the NcS itself.

For instance, TGA results showed that independently of the NcS nature, a lower Fe/NcS LR was systematically obtained when the $Fe(acac)_3$ complex was used as an iron precursor in methods SOLV-C or SOLV-D (see Table 4, page 88). Moreover, a similar thermal event spanning between 200 ºC and 400 ºC was observed in all the TGA profiles of the SOLV-C and SOLV-D products. This temperature range matches the one observed during the thermal decomposition of the iron complex itself (see Figure 6), suggesting that, under these reaction conditions, the iron precursor is only partially decomposed. Accordingly, when aiming a 50% Fe/NcS LR, a similar amount (approx. 25%) of partially decomposed complex was found in all SOLV-C nanocomposites, independently of the used NcS, being slightly lower (19%) in the SOLV-D products. These results can be attributed to the lower reaction temperature used in the SOLV-C approach, which leads to a higher rate of remaining undecomposed complex.

As shown in Table 4, when applying the SOLV-A methodology to ox-MWCNTs and MWCNTs, aiming at 50% Fe/NcS LR, it was found that the obtained value was slightly higher for the oxidized sample (21%) than for its non-oxidized counterpart (18%). Using the same synthetic conditions, a more accentuated difference was found when comparing the loading rate obtained for GO (37%) and GNPs (29%). A similar trend was also observed when decorating GO, rGO or GNPs using the SOLV-C approach. In this case, while aiming for a 50% Fe/NcS LR in all products, the obtained LR was the highest for the GO product (19%), followed by rGO (15%) and lowest when using GNPs (13%) (Figure 6), in agreement with the decreasing amount of oxygenated functions found in these graphenic solids as determined by XPS (see Appendix II). These results indicate that the oxygenated functions also have an influence on the MaNPs loading rate and not only on their size. As mentioned before, electrostatic interactions can be established between the oxygenated functions present on the NcS and some of the iron-containing species found in solution. This interaction would be responsible for bringing both components in close contact before and during the formation of MaNPs, generating a higher LR as the concentration of oxygenated functions on the NcS increases. The higher loading rates observed in the SOLV-A products could also be due to the basic pH values used in this methodology. Indeed, as mentioned before, such a basic environment would produce a higher concentration of ionized oxygenated species and thus increase the extent of electrostatic interactions.

The overall effective surface of the different NcS also seems to influence the obtained Fe/NcS LR. Indeed, textural analysis by nitrogen physisorption of GO and GNPs indicate a much higher specific surface area for the former NcS than for the latter (50 m^2/g and 16 m^2/g respectively, similar to the values reported in [38]). This difference can be explained in terms of the degree of graphene sheet stacking present in each NcS sample. Indeed, our XRPD and TEM results confirm that the GNPs are composed of highly stacked graphenic sheets while in GO these are more individualized.

As mentioned before, one of the advantages of the solvothermal approach is that the amount of loaded MaNPs onto the NcS can be easily modified. Using the SOLV-A method, the amount of $FeCl_3{\cdot}6H_2O$ was adjusted to create a series of nanocomposites with Fe/GO LRs varying from 10% to 50%. The TGA analyses of such nanocomposites indicate that an excellent correlation between the expected and obtained LRs was maintained up to loadings of 30% (Figure 7). At higher LR, a saturation plateau seems to be reached.

2.2.2.3 MaNPs spatial distribution over the NcS surface

As described before, when compared to the DCOP and COV linkage methodologies, the solvothermal strategy produced, at high Fe/NcS LR (e.g. 50%), a nanocomposite in which the NcS was homogeneously and densely decorated with MaNPs. Nanocomposites of lower Fe/NcS LRs, ranging from 10% to 40%, were also produced using the SOLV-A methodology. The SEM and TEM inspection of these five products revealed that the spatial distribution over the NcS surface remained homogeneous in all cases (Figure 8). It also showed that the MaNPs stacked less onto each other at lower LRs, forming what seemed like patches of MaNPs monolayers deposited onto the NcS surface (Figure 8c). Nonetheless, it was also observed that some areas of the solid were left uncovered when engaging the lowest LR value (10%).

The MaNPs spatial distribution was also affected by the presence of oxygenated functions on the NcS surface. This effect was highlighted when decorating pristine and oxidized MWCNTs using the SOLV-A method at a 10% LR value (Figure 9). Indeed, smaller MaNPs distributed along the MWCNTs surface when these were previously oxidized, contrasted with only larger particle agglomerates found in the pristine-MWCNTs decorated samples. These results further prove that the NcS' oxygenated functions are serving as nucleation sites during the MaNPs formation and growth.

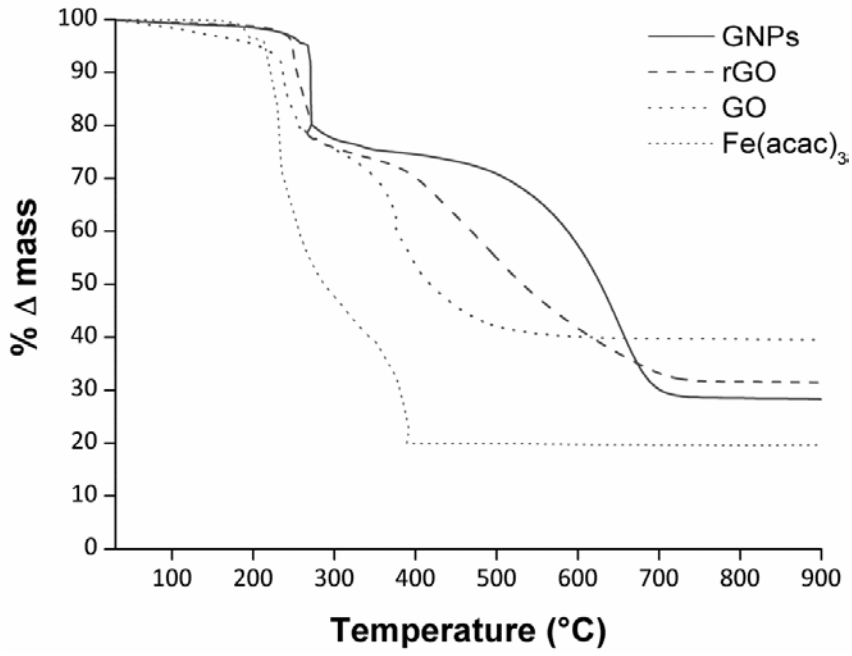

Figure 6 - Thermograms for the thermal decomposition under air of a $Fe(acac)_3$ reference sample and three SOLV-C nanocomposites produced using different NcS and an intended 50% Fe/NcS loading rate.

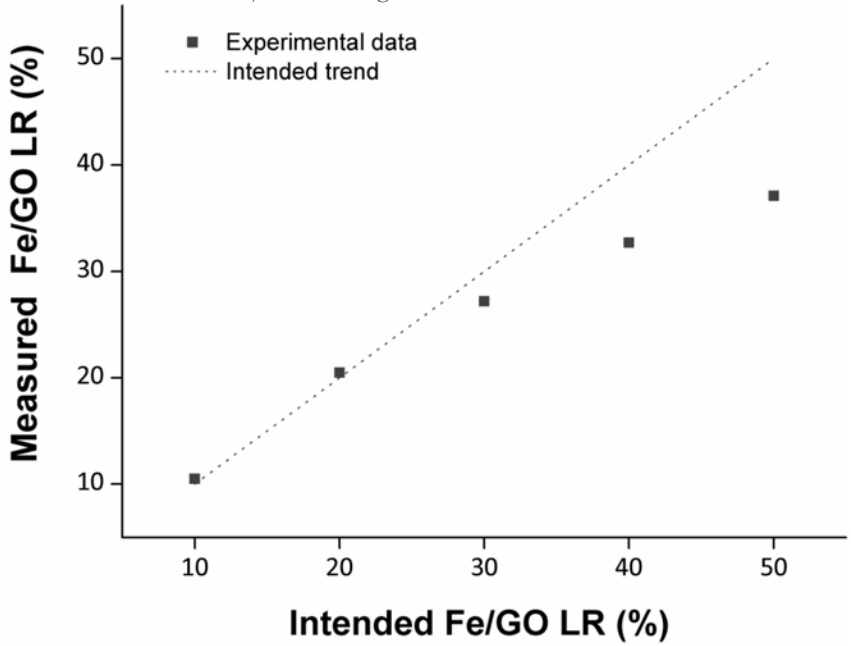

Figure 7 - Intended vs. measured (by TGA analysis) % Fe/GO loading rates (LR).

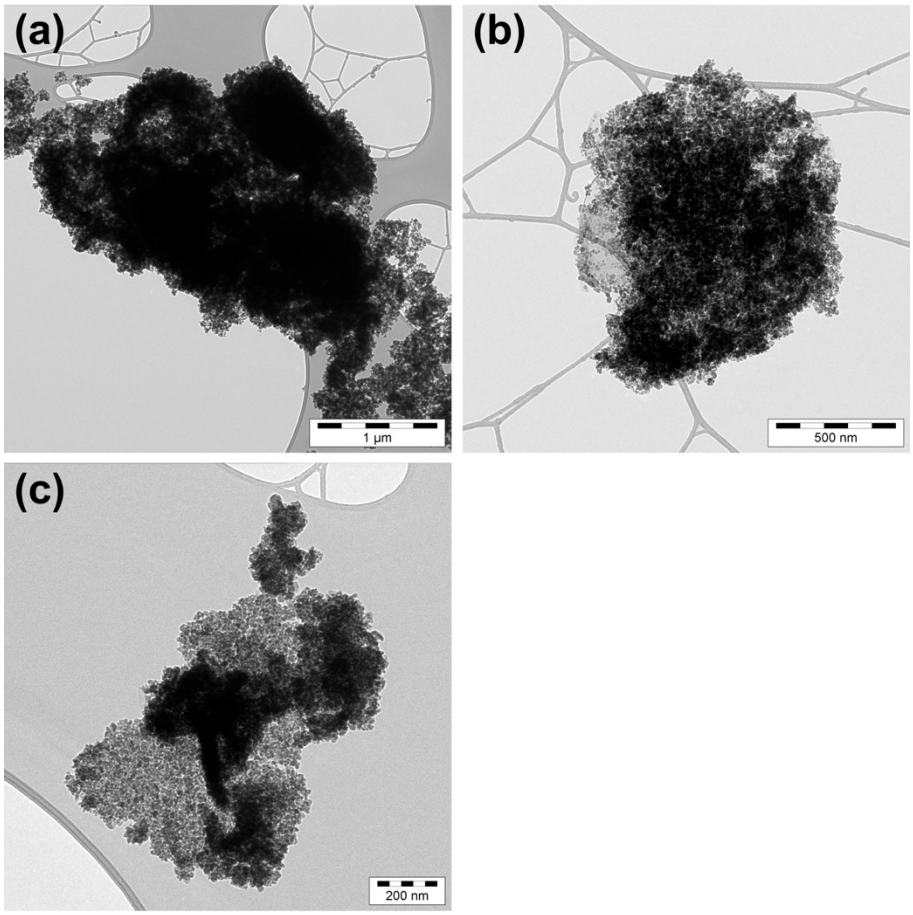

Figure 8 - TEM images of MaNPs@GO nanocomposites produced via the SOLV-A method at (a) 50%, (b) 30% and (c) 10% Fe/NcS LR.

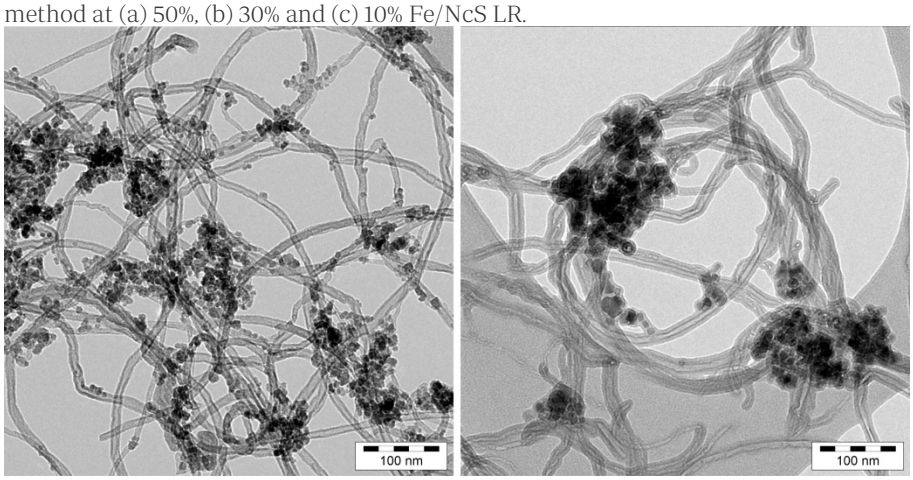

Figure 9 - TEM images of MaNPs deposited onto oxidized (right) or pristine (left) MWCNTs using the SOLV-A method.

2.2.2.4 MaNPs@GO nanocomposites magnetic characterization

The magnetic properties of MaNPs@GO nanocomposites with 10%, 30% and 50% Fe/NcS LR produced by the SOLV-A method have been studied by SQUID magnetometry. Magnetization curves recorded against magnetic field, from one direction to the opposite one, show perfect overlapping at 300 K which corresponds to superparamagnetic behavior for all of them (Figure 10a-c). In contrast, hysteresis loops exhibit coercive fields (H_c) of about 350 Oe at 5 K, which corresponds usually to ferrimagnetic iron oxide nanoparticles [29].

Magnetization saturation values at 300 K also agree with the measured size of the nanoparticles (see Table 5). These values are much lower than bulk values for magnetite (92 emu/g) because of surface effects and the oxidation of Fe(II) at the nanoparticle's surface which generates vacancies and disorder [29]. The lowest Fe/NcS LR sample (10%) shows a lower H_c value that may be explained by larger surface effects or the presence of undetected slightly smaller nanoparticles.

In addition, temperature dependent magnetization (M(T)) curves (Figure 10d) bring deeper information on the collective properties of nanoparticles. Zero field cooled (ZFC) curves exhibit a maximum at a temperature (TMAX) whose value decreases with the density of MaNPs deposited on the NcS' surface (Table 5).

Given the fact that the deposited MaNPs feature similar sizes, this decrease of TMAX could be correlated to weaker dipolar interactions due to larger interparticle distances. The non-saturation of the field cooled (ZF) curve at low temperature for the least loaded sample, in contrast to the two other samples, seems to support this hypothesis since it is correlated to the (quasi) absence of dipolar interactions as observed for iron oxide nanoparticles 2D assemblies [39]. Nonetheless, an in-depth analysis of such interactions still requires to be performed.

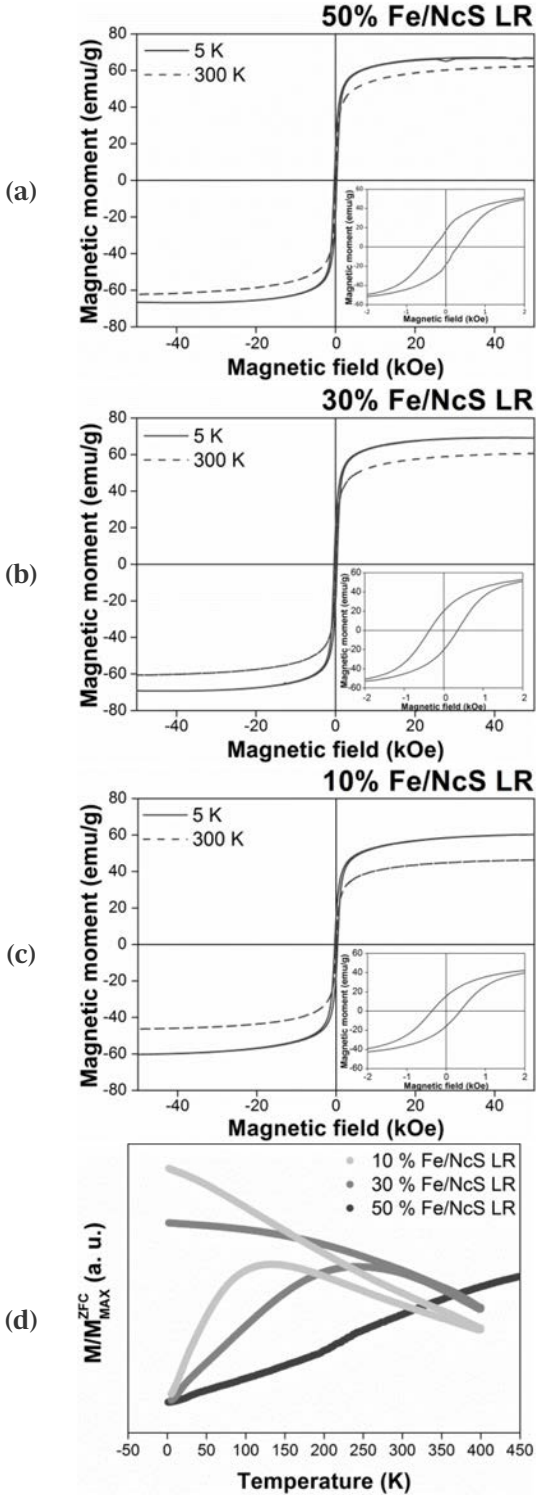

Figure 10 - Magnetization curves recorded against an applied magnetic field for 10% (a), 30% (b) and 50% (c) Fe/GO LR samples produced with the SOLVA method, and d) against temperature. Insets are M(H) curves recorded at 5 K at low fields.

Table 5 - Magnetic properties and average MaNPs sizes of 10%, 30% and 50% Fe/GO samples produced via the SOLV-A method.			
Fe/GO %LR	10%	30%	50%
M_s @ 300 K (emu/g)	46	61	61
H_c (Oe)	360	350	300
T_{MAX}(K)	135	248	290
Average NP size (nm)	11.0 ± 4.0	11.1 ± 4.3	12.3 ± 3.9

2.3 Conclusions

In this chapter, we have demonstrated that each considered synthetic method (direct co-precipitation, solvothermolysis and covalent bonding) produces MaNPs@GO nanocomposites with different physicochemical characteristics. To the best of our knowledge, it is the first time that such a systematic comparison is performed. Considering our intended applications, the direct co-precipitation technique presents two main drawbacks: the difficulty of reproducibly controlling the nanocomposite's final composition, and consequently its electromagnetic properties; and the relatively heterogeneous and highly stacked spatial distribution of the MaNPs over the graphenic surface. As for the covalent linkage method, it requires lengthy and complex experimental manipulations in order to achieve the final product, particularly when compared to the solvothermal method. Furthermore, it produces large, micrometric MaNPs agglomerates, coexisting independently along with the desired nanocomposites and which, under the experimental conditions used, are impossible to isolate. For these reasons, we consider that the solvothermal route has an overall increased performance.

Accordingly, the in-depth study of the polyol solvothermal methodology led us to identify a series of critical factors governing the decoration of different nanocarbon solids that had not been identified before. Regarding the deposited MaNPs chemical identity, morphology and particle size, we have proven that, besides reaction time and temperature, the choice of the iron precursor and the reaction system water content as well as the oxidation degree of the NcS support all play a fundamental role. We have also

demonstrated that the amount of MaNPs that can be loaded onto the NcS also rely upon the nature of the iron precursor and the type of NcS and its oxidation state. Indeed, we have shown that if the NcS is more oxidized, a larger amount of smaller MaNPs can be loaded with a more homogeneous spatial distribution. We believe that this is due to the establishment of electrostatic interactions between the oxygenated functions found on the NcS and the ionic iron species found in solution, especially at the higher pH values used in some of our tested methods.

Finally, we have characterized the magnetic properties of some of the solvothermally produced nanocomposites. Our results are characteristic for ferrimagnetic iron oxide nanoparticles in a superparamagnetic state.

2.4 Bibliography

1. X. Huang, X. Zhou, K. Qian; D. Zhao, Z. Liu and C. Yu, *J. Alloy Compd.*, 2012, **514**, 76-80.
2. B. Li. H. Cao, J. Shao, M. Qu, and J. H. Warner, *J. Matter. Chem.*, 2011, **21**, 5069.
3. Q. Wang, L. Jiao, H. Du, Y. Wang and H. Yuan, *J. Pow. Sour.*, 2014, **245**, 101-106.
4. F. He, J. Fan, D. Ma, L. Zhang, C. Leung, H. L. Chan, *Carbon*, 2010, **48**, 3139-3144.
5. Y. Yao, S. Miao, S. Liu, L.P. Ma, H. Sun and S. Wang, *Chem. Eng. J.*, 2012, **184**, 326-332.
6. X.Y. Yang, Z.Y. Zhang, Y.F. Ma, Y. Huang, Y.S. Wang and Y.S. Chen. *J. Mater. Chem.*, 2009, **18**, 2710.
7. H. Teymourian, A. Salimi and S. Kherzrian, *Biosens. Bioelectron.*, 2013, **49**, 1-8.
8. Y. Zhan, F. Meng, Y. Lei, R. Zhao, J. Zhong, and X. Liu, *Mater. Lett.*, 2011, **65**, 1737-1740.
9. P. Liu, Y. Huang and X. Zhang, *J. Alloy Compd.*, 2014, 596, 25-31; b) P. Liu, Y. Huang and X. Zhang, *Mater Lett.*, 2014, **129**, 25-31
10. X. Shen, J. Wu, S. Bai and H. Zhou, *J. Alloy Compd.*, 2010, **506**, 136-140.
11. J. Deng, X. Wen, Q. Wang, *Mater. Res. Bull.*, 2012, **47**, 3369-3376.
12. J. Wan, W. Cai, J. Feng, X. Meng and E. Liub, *J. Mater. Chem.*, 2007, **17**, 1188.
13. H. Wu, G. Gao, X. Zhou, Y. Zhang, and S. Guo, *Cryst. Eng. Comm.*, 2012, **14**(2), 499-504.
14. P. Liu, W. Zhong, Z. Wu, J. Qiu, *Chem. Eng. J.*, 2013, **219**, 10-18.
15. Y. Zhan, Z. X. Yang, F. Meng, J. Wei, R. Zhao and X. Liu, *J. Colloid Interf. Sci.*, 2011, **363**, 98-104.
16. W. Baaziz, L. Truong-Phuoc, C. Duong-Viet, G. Melinte, I. Janowska, V. Papaefthymiou, O. Ersen, S. Zafeiratos, D. Begin, S. Begin-Colin and C. Pham-Huu, *J. Mater. Chem. A.*, 2014, **2**, 2690.
17. Y. Li, J. Chu, J. Qi and X. Li, *Appl. Surf. Sci.*, 2011, **257**, 6059-6062.
18. S. Hermans, V. Bruyr and M. Devillers, *J. Mater. Chem.*, 2012, **22**, 14479.
19. M. Gao, W. Li, J. Dong, Z. Zhang and B. Yang, *World J. Condens. Matter Phys.*, 2011, **1**, 49-54.
20. Z. Liu, Z. Ma, J. Xing, and H. Liu *J. Magn. Magn. Mater.*, 2004, **270**, 1-6.
21. M. Kokate, K. Garadkar and A. Gole (2013) *J. Mater. Chem. A*, 2013, **1**, 2022-2029.

22. D. Vidick, 2012, *Functionalization of nano-structured carbons for the preparation of supported heterometallic cluster-derived nanoparticles*. PhD Thesis. Université Catholique de Louvain, Louvain-la-Neuve, Belgium.
23. X. Huang, X. Zhou, K. Qian, D. Zhao, Z. Liu, and C. Yu, *J. Alloy. Compd.*, 2012, **514**, 76-80.
24. J.Wan, W. Cai, J. Feng, X. Meng and E. Liu, *J. Mater. Chem.*, 2007, **17**, 1188-1192.
25. X. Shena, J. Wua, S. Baia, and H. Zhoub, *J. Alloy. Compd.*, 2010, **506**, 136–140.
26. F. Pennetreau, 2016, Xanthates as a tool for carbon nanotubes and graphene functionalization. Application in supported catalysis. PhD Thesis. Université Catholique de Louvain, Louvain-la-Neuve, Belgium.
27. J. Guo, R. Wang, W.W. Tjiu, J. Pan, and T. Liu, *J. Hazard. Mater.*, 2012, **225-226**, 63-73.
28. V. Singh, D. Joung, L. Zhai, S. Das, S. Khondaker and S. Seal, *Prog. Mater. Sci.*, 2011, **56**, 1178-1271.
29. W. Baaziz, B.P. Pichon, S. Fleutot, Y. Liu, C. Lefevre, J.M. Greneche, M. Toumi, T. Mhiri and S.Begin-Colin, *J. Phys. Chem. C*, 2014, **118** (7), 3795–3810.
30. I. Martínez-Mera, M.E. Espinosa-Pesqueira, R. Pérez-Hernández and J. Arenas-Alatorre, *Mater. Lett.*, 2007, **61**, 4447-4451.
31. R. Massart, and V. Cabuil, J. Chim. Phys., 1987, **84** (7-8), 967-973.
32. Cornell, R.M. and Schwertmann, U. (2003) The iron oxides. Structure, properties, reactions, occurrences and uses (2nd ed). Wiley-VCH; Darmstadt, Germany. 664 pp.
33. M.E. Mendoza, F. Donado, R. Silva, M.A. Pérez. and J.L. Carrillo, *J. Phys. Chem. Solids*, 2005, **66**, 927-931.
34. S. Qu, H. Yang, D. Ren, S. K, G. Zou, S. Li and M. Li, *J. Colloid Interf. Sci.*, 1999, **215**, 190-192.
35. B. Konkena and S. Vasudevan, *J. Phys. Chem. Lett.*, 2012, **3**, 867-872.
36. S. E. Skrabalak, B. J. Wiley, M. Kim, E. V. Formo and Y. Xia, *Nano Lett.*, 2008, **8**(7), 2077-2081.
37. J. Zhou, H. Song, L. Ma and X. Chen, *RSC Adv.*, 2011, **1**, 782-791.
38. P. Han, H. Wang, Z. Liu, X. Chen, W. Ma, J. Yao, Y. Zhu and G. Cui, *Carbon*, 2011, **49**, 693-700.
39. D. Toulemon, B.P. Pichon, X. Cattoen, M.W.C. Man and S. Begin-Colin, *Chem. Commun.*, 2011, **47** (43), 11954.

chapter 3

Solvothermal decoration of multi‐walled carbon nanotubes with nickel nanoparticles

In this chapter, three novel solvothermal methods allowing to decorate multi‐walled carbon nanotubes (MWCNTs) with metallic nickel nanoparticles (NiNPs) are presented. Several reaction parameters have been varied, such as the type of NiNPs precursor, reaction time and temperature or the concentration of a capping agent, polyvinylpyrrolidone (PVP). The impact of such variations on the nanocomposites NiNPs composition and size distributions have been elucidated. Finally, zzcharacteristics and the nanocomposites magnetic properties is clearly established.

Related publications

F. Mederos-Henry, S. Depaifve, A. Wolf, R. A. Hermann, A. Delcorte, C. Bailly, I. Huynen and S. Hermans. **Nanocomposites with size-controlled Ni nanoparticles supported on MWCNT for efficient frequency-selective microwave absorption**. *CSTE,* 2019, in press.

S. Depaifve, 2015, **Nanoparticules de nickel et d'oxyde de cobalt supportées sur graphène : production de métamatériaux**, UCLouvain, Master Thesis.

A. Wolf, 2016, **Métamatériaux à base de nanoparticules magnétiques supportées sur structure nanocarbonée dans une matrice polymérique,** UCLouvain, Master Thesis.

Collaborators

Sébastien Depaifve (IMCN/MOST) and Arnaud Wolf (IMCN/MOST).

As mentioned in section 1.3.2.2, ferromagnetic transition metals such as iron, cobalt and nickel, possess a high magnetic permeability. This characteristic allows them to channel external magnetic fields by providing low resistance paths that create larger rates of magnetic losses. Thus, Ni NPs grafted onto a NcS could be exploited to produce efficient microwave-absorbing nanocomposites.

A few nanocomposites obtained by decoration of MWCNTs with NiNPs have already been reported in the scientific literature for diverse applications such as the production of energy storage devices [1], catalysts [2], or sensors [3], to mention just a few. Most commonly, these nanocomposites have been produced by thermal [4] or chemical reduction [3], electroless deposition [5] or solvothermal [6] strategies.

In this study, we have developed three novel polyol solvothermal synthetic procedures in which ethylene glycol serves as both solvent and sole reduction agent. Indeed, research conducted by Skrabalak *et al.* [7] has shown that metallic ions, such as Ni^{2+}, can be reduced to their corresponding metal by glycoaldehyde, an intermediate product formed by the thermal oxidation of ethylene glycol (EG) in air.

Furthermore, we tested and adjusted various synthetic parameters in order to produce markedly different NiNPs size distributions. For instance, we studied the effect of varying the type of NiNPs precursor and the speed at which it is added to the reaction medium, the concentration of the capping agent polyvinylpyrrolidone (PVP), alongside reaction time and temperature.

The impact of the different NiNPs size distributions on the microwave absorption properties of these materials will be demonstrated in Chapters 6 and 7. However, the magnetic properties of the obtained nanocomposite powders, studied by SQUID magnetometry, will be presented here.

3.1 Materials and methods

3.1.1 Materials and characterization techniques

NC3100 multi-walled carbon nanotubes (MWCNTs, 95%C purity) were obtained from Nanocyl (Belgium). All other reactants were supplied by Bayer Material Science, Alfa Aesar or VWR and used as received. More details on each reactant are provided in Appendix I while the different physicochemical characterization techniques employed are described in Appendix II.

3.1.2 Solvothermal synthesis of Ni@MWCNTs nanocomposites

Three different solvothermal methods were developed to produce Ni@MWCNTs nanocomposites with different nickel nanoparticle (NiNPs) size distributions. The first was carried out at ambient pressure (noted AP) while the other two were performed in an autoclave (noted AC).

In all cases, reactant proportions were aimed at producing 50% Ni/C mass loading rate (LR) nanocomposites. Sonication stages were always performed in a VWR ultrasound cleaner USC 1200-THD at 80 W sonication power. The obtained products were separated from the reaction medium by magnetic decantation and then recovered by filtration over a PVDF filter (Millipore GVWP02500, 0.22-μm pore size). Afterwards, they were all purified by rinsing six times, alternating Milli-Q water and ethanol. Finally, they were dried under vacuum at room temperature for 12 hours.

3.1.2.1 Ni@MWCNTs nanocomposites produced by ambient pressure (AP) solvothermal synthesis

This synthetic pathway was specifically developed for this research project. In a typical synthesis, 100 mg of MWCNTs were placed in a two-necked round-bottom flask. 76 mL of ethylene glycol (EG) were added and the suspension was sonicated for 120 minutes. Afterwards, 640 mg of polyvinylpyrrolidone (M.W. 10,000, PVP-10,000) were added, under vigorous stirring, to obtain a 8 mg/L capping agent concentration. After complete

dissolution of PVP, the suspension's pH was set to 10.5 by adding an aqueous 1M NaOH solution dropwise in order to promote the deprotonation of ethylene glycol and increase its reductive power [8]. A reflux condenser was mounted on the central neck while the other was capped with a rubber septum. Subsequently, the suspension was heated up to 230 °C in an oil bath.

Separately, 203 mg of nickel (II) chloride hexahydrate ($NiCl_2.6H_2O$) were added to 4 mL EG and vigorously stirred until the salt was completely dissolved. The solution was then transferred into a syringe. By using a syringe pump (kdScientific, USA), it was added dropwise to the former hot suspension at a speed of 4 mL/h, under stirring. Overall, the reaction mixture was heated for 15 hours. Reaction products were then recovered, purified and dried as described above.

3.1.2.2 One-pot autoclave (AC) solvothermal syntheses

Two different autoclave solvothermal procedures were developed, inspired by the work of Tian *et al.* [9]. In one synthesis, a nickel (II) salt was used as NiNPs precursor while a nickel (II) complex was employed in the second. Each procedure is detailed below.

Nevertheless, in both methods, the autoclave's temperature was automatically regulated by a Parr 4836 temperature controller (Parr Instrument Company, USA) having an average heating rate of 4 °C/min. The autoclave's inner atmosphere was never purged nor modified in any manner during the syntheses, while the system pressure was left to build up during heating without any type of external control. Reaction solutions were continuously stirred at 300 rpm while heating. When reaction time was completed, the autoclave was immediately immersed in an ice bath and cooled down to ambient temperature. In all cases, reaction products were recovered, purified and dried as described above.

3.1.2.2.1 Using a nickel salt precursor (AC-S)

MWCNTs (100 mg) were dispersed in 80 mL of ethylene glycol (EG) and sonicated for 120 minutes. 203 mg of $NiCl_2.6H_2O$ were then added to the above suspension under vigorous stirring and sonicated for 10 more minutes. Subsequently, enough PVP-10,000 was added to reach a 5, 8, 12 or 16 mg/L capping agent concentration. The mixture was then sonicated for another 10 minutes.

After sonication was completed, an aqueous 1M NaOH solution was added dropwise, under vigorous stirring, until a pH value of 10.5 was reached. After stirring for 45 minutes, the mixture was transferred into a 300 mL stainless steel autoclave vessel with a Teflon lining and heated to 220 °C for 3 hours.

3.1.2.2.2 Using a nickel complex precursor (AC-C)

100 mg of MWCNTs were dispersed in 80 mL of ethylene glycol (EG) and sonicated for 120 minutes. 219 mg of nickel (II) acetylacetonate ($Ni(acac)_2$) were then added to the above suspension under vigorous stirring. Subsequently, an aqueous 1M NaOH solution was added dropwise, under vigorous stirring, until a pH value of 10.5 was reached.

After stirring for 45 minutes, the mixture was transferred into a 300 mL stainless steel autoclave vessel with a Teflon lining and heated to 190 °C, 210 °C or 230 °C, for 7 or 15 hours.

3.1.3 Ni@MWCNTs nanocomposites thermal annealing

Once dried, the AP and AC-S products synthetized using a 8 mg/L PVP concentration as well as the AC-C nanocomposite were thermally annealed in order to promote particle growth by sintering. The samples were placed in a porcelain combustion boat and heated up to 500°C for 2h, under Ar/H_2 95/5 atmosphere, in a tubular furnace (Carbolite Gero STF16, United Kingdom). The temperature was increased and decreased at a rate of 1.7°C/min. The recovered powder was stored in air with no special precautions.

3.2 Results and discussion

The main goal of this part of the project was to decorate multi-walled carbon nanotubes (MWCNTs) with metallic nickel nanoparticles (NiNPs) possessing different size distributions. Accordingly, three novel synthetic methods were developed and several reaction conditions were tested. For instance, different types of NiNPs precursors, various reaction times, temperatures and pressures as well as four different concentrations of a capping agent, polyvinylpyrrolidone (PVP), were tested.

The impact of the different experimental conditions on the NiNPs nanocomposites size distributions alongside other relevant characteristics (e.g. NiNPs composition, loading rate and spatial distribution over the MWCNTs surface) will be discussed below for each synthetic technique.

3.2.1 Ni@MWCNTs nanocomposites produced by ambient pressure (AP) solvothermal synthesis

For the first synthetic method tested, we chose to work at low Ni precursor concentration. Indeed, Rosicka and Sembera [10] have shown that maintaining a low precursor concentration prevents the deposited NPs from agglomerating and growing uncontrollably. NPs aggregation and consequent growth depends on the collision between reactive species. Therefore, at low concentrations, the probability that the nanoparticle precursor species found in solution interact with those already deposited onto the support is strongly reduced.

As described in section 3.1.1.1, in this synthetic method, Ni^{2+} ions were very slowly added to the reaction medium by using a syringe pump. In that manner, the NPs precursor concentration was kept low, producing the results shown in Figure 1, top. The TEM images show that MWCNTs were densely covered with extremely small (<1 nm) NPs.

Nonetheless, a few large NPs were also found (Figure 1, middle). Polyvinylpyrrolidone (PVP) is typically used to stabilize metallic NPs during

their synthesis, preventing their aggregation and limiting their growth [11]. Accordingly, when employing PVP (M.W. 10,000) at a 8 mg/L concentration, the larger NPs mostly disappeared (Figure 1, bottom).

XRPD investigation of these nanocomposites revealed only one signal that could be attributed to a nickel phase. As shown in Figure 2, the diffraction peak around 2θ = 20º corresponds to the main reflection of the nickel face-centered cubic (Ni-fcc) phase. Its breadth can be attributed to the extremely reduced size of the deposited NiNPs. In addition, its low intensity seems to indicate that the deposited nanoparticles are poorly crystalline. As for the reflection around 2θ = 12º, it has been attributed to the ordered arrangement of the MWCNTs' concentric cylinders of graphitic carbon [12].

The as-deposited NPs were then grown in a subsequent thermal annealing step. Figure 3 shows the Ni@MWCNTs nanocomposites obtained after thermal annealing at 500 °C. The deposited NiNPs grew to an average size of 13.6 ± 4.4 nm and showed a narrow size distribution. Furthermore, contrasting with the diffractogram obtained before thermal annealing, the characteristic Ni-fcc reflections were clearly detected by XRPD (see Figure 2).

However, additional diffraction peaks of weaker intensity were observed around 19º, 21.5º and 27.8º 2θ angles. Recently, these reflections have been attributed to a nickel carbide phase [13]. Nickel carbide phases have been produced by exposing nickel powders to a CO gas flux at temperatures as low as 250 ºC [14]. Therefore, this minority phase was possibly formed as PVP chains surrounding the NiNPs decomposed, especially given the reductive thermal annealing conditions used. Indeed, Su *et al.*[13] have shown that such metallic carbide phases can form when a NiNP surrounded by a carbon-rich layer is exposed to high temperatures, as an intermediate product of the pyrolysis process.

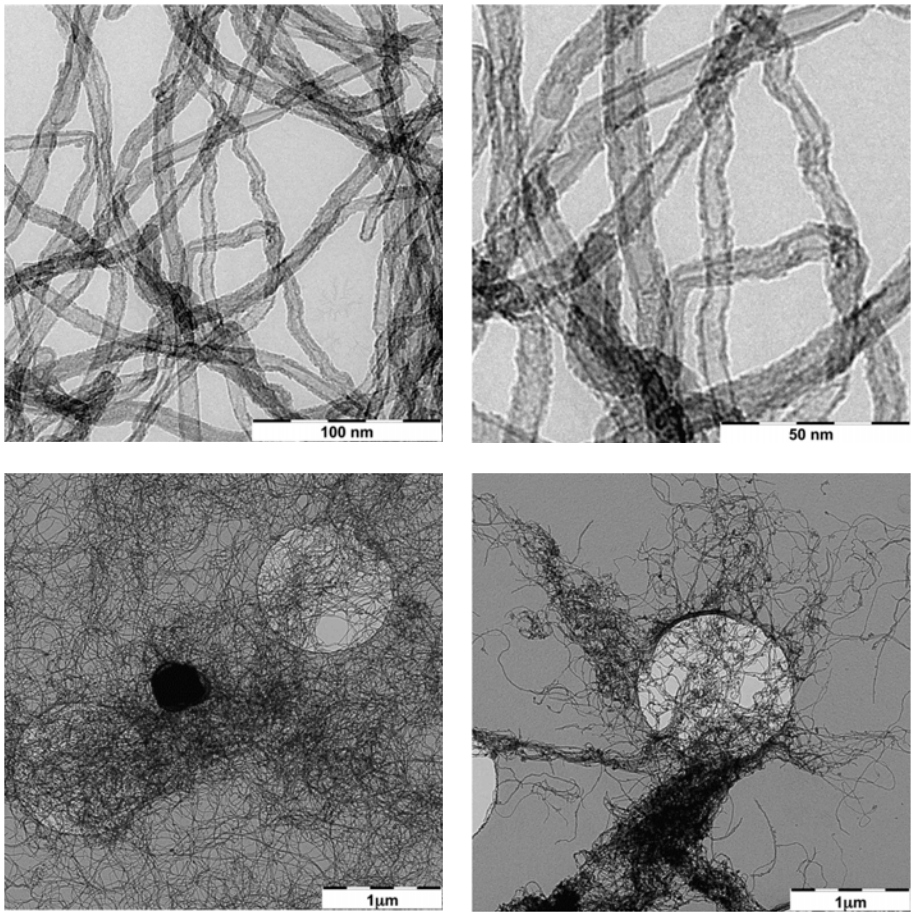

Figure 1 – TEM images showing ultrasmall NPs covering the MWCNTs surface after the AP synthesis (top row). A few large NPs were observed when no PVP was used (bottom row, left), but mostly disappeared at a 8 mg/L PVP concentration (bottom row, right).

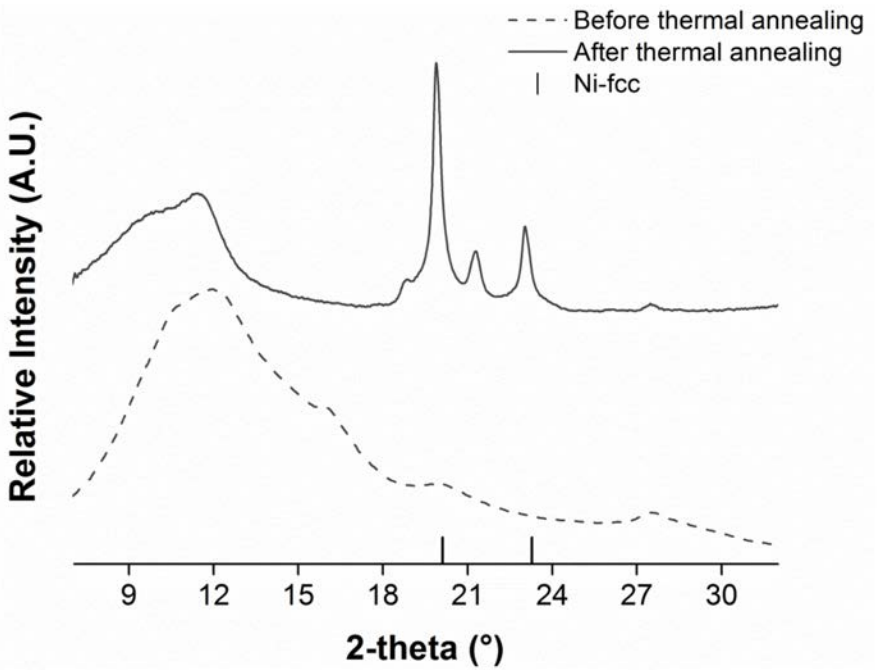

Figure 2 - XRPD diffractograms of the AP products synthetized using a 8 mg/L PVP concentration, before and after thermal annealing.

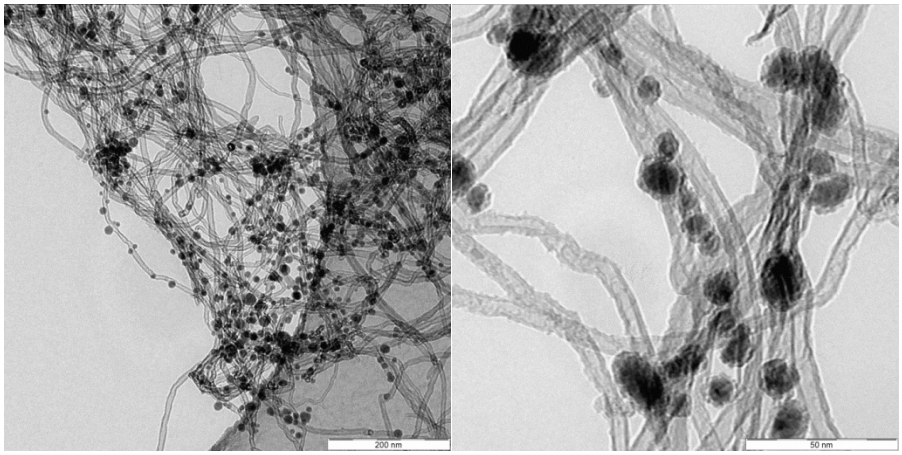

Figure 3 - TEM images of the AP Ni@MWCNTs nanocomposite synthetized using a 8 mg/L PVP concentration, after thermal annealing (left). A lighter shell was found around the NiNPs (right).

McCafferty *et al.* [15] have also shown that, when cooling down, carbides can partly decompose and exude carbon to the nanoparticle surface. An amorphous or graphitic carbon layer is thus formed around the NP. Interestingly, TEM observations of the nanocomposites after thermal annealing show the presence of a lighter shell layer surrounding the NiNPs (see Figure 3, right). Su *et al.* [13] have recently produced nickel nanocatalysts using similar thermal annealing procedures as the one used in this synthesis. Their results also show the formation of a light-colored, graphitic shell surrounding the NiNPs.

As shown in Figure 4, XPS analysis of the AP nanocomposite after thermal annealing confirms the presence of metallic nickel (Ni^0). However, oxidized nickel species such as oxides, hydroxides or oxyhydroxides, quantified globally by the Niox and Niox_sat components, were detected in almost equal amounts. Their relatively high concentration might be explained by the fact that XPS is a surface analysis technique with a sampling depth of approximatively ~3.9 nm for nickel oxide or metallic nickel [16]. Thus, if the oxide is to be found on the surface of the NP, as a passivation layer, the relative amount of the Niox+Niox_sat components will be enhanced comparatively to that of Ni^0. In addition, the fact that no oxidized nickel was detected by XRPD suggests it is either poorly crystalline or amorphous.

3.2.2 Ni@MWCNTs nanocomposites produced by one-pot autoclave (AC) solvothermal syntheses

Two one-pot polyol autoclave solvothermal methodologies were tested. In the first synthesis, code-named AC-S, Ni@MWCNTs nanocomposites were produced with a nickel (II) chloride salt precursor and varying amounts of PVP-10,000 as capping agent. In the second one, hereafter identified as AC-C, only a nickel (II) acetylacetonate ($Ni(acac)_2$) complex was employed with no capping agent.

These experimental variants sought to control the deposited NiNPs size by modifying the availability of Ni^{2+} ions in the reaction media. Indeed, the nickel salt is expected to be completely dissociated when dissolved in ethylene glycol (EG), the chosen diol solvent [17]. Consequently, Ni^{2+} ions are readily available for reduction and NiNPs formation. However, changing the capping agent concentration should modulate the NiNP growth speed [11]. By opposition, when $Ni(acac)_2$ is used, Ni^{2+} ions are gradually released as the complex thermally decomposes. In this sense, the use of a Ni complex could mimic the effect of slowly adding a Ni precursor, as demonstrated in section 3.1.

Results obtained with both synthetic procedures are presented below.

3.2.2.1 AC-S Ni@MWCNTs nanocomposites

As in the AP synthesis, nickel (II) chloride was also used as NPs precursor and ethylene glycol (EG) as solvent and reducing agent in the AC-S method. However, the full quantities of the different reactants were engaged before starting the autoclave synthesis. Given $NiCl_2$ is completely dissociated when dissolved in EG [16], as stated above, the Ni^{2+} concentration in the AC-S reaction medium was higher than the one achieved in the AP synthesis. Under these conditions, the more abundant Ni^{2+} species were readily available for reduction, seeding onto the MWCNTs and growing into larger NPs as shown in Figure 5.

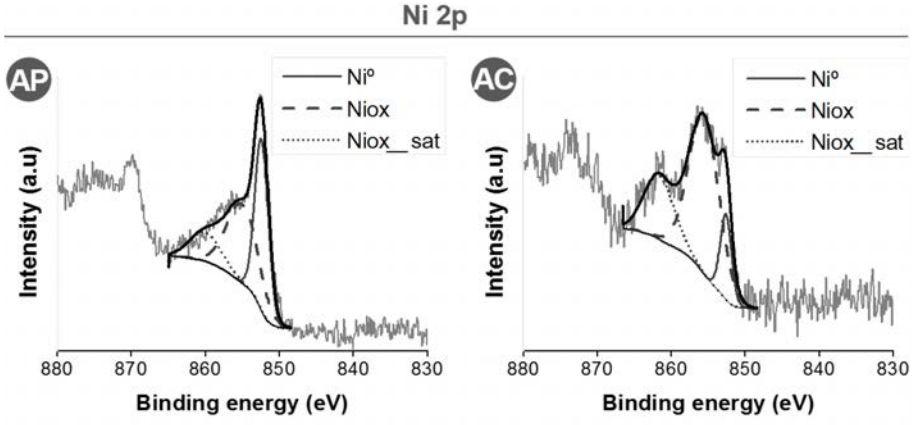

Relative concentration (%)		
Sample	Ni°	Niox + Niox_sat
AP	41	59
AC	13	87

Figure 4 - XPS spectra of the Ni 2p peak for the AP and AC-S Ni@MWCNTs nanocomposites after thermal annealing. Both products were synthetized using a 8 mg/L PVP concentration. The Ni 2p3/2 peak has been fitted with three components corresponding to metallic (Ni°) and oxidized (Niox + Niox-sat) nickel.

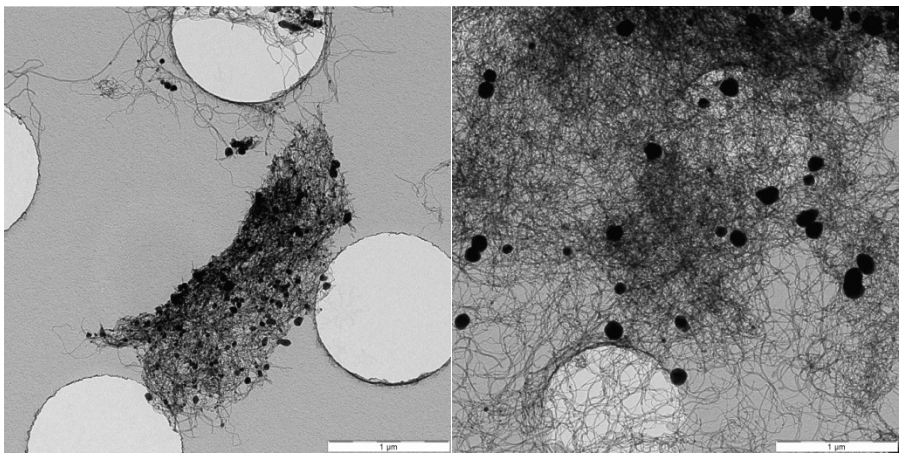

Figure 5 - TEM images showing the AC-S Ni@MWCNTs nanocomposite before (left) and after (right) thermal annealing

Also, it has been shown that employing PVP as a capping agent and varying its concentration can influence a metallic NP growth speed [10]. Consequently, various concentrations of PVP-10,000 were tested. Our results show that there is a clear correlation between the size of the deposited NPs and the engaged concentration of PVP-10,000. As shown in Figure 6, the NPs get smaller as the capping agent concentration is increased. Also, the narrowest NPs size distributions were obtained at 12 mg/L and 16 mg/L PVP-10,000 concentrations. However, the capping agent concentration had no significant effect on the amount of NPs loaded onto the MWCNTs (see Table 1).

As for the AP nanocomposites, the thermal annealing of the AC-S products had a strong impact on the size of the deposited NPs. For instance, when using a 8 mg/L PVP-10,000 concentration, the thermally treated AC-S NPs almost doubled their average size (130 ± 47 nm) as can be observed in Figure 5, right.

XRPD results show that the deposited AC-S NPs consist of a pure face-centered cubic (Ni-fcc) crystalline phase, independently of the capping agent concentration used (see Figure 7). The Ni-fcc phase was preserved after the thermal annealing process and no trace of other nickel-containing species were found with this preparation technique.

Nonetheless, XPS analyses indicate that oxidized nickel is present in larger amounts than its metallic counterpart (see Figure 4). As for the thermally annealed AP nanocomposites, these results suggest that the oxide layer is to be found on the surface of the deposited nanoparticles. Furthermore, considering the size of the deposited AC-S NiNPs, the emitted photoelectrons will originate mostly from their outermost layer. If this layer is partly oxidized, the XPS spectra will show an artificially high amount of such a species. Also, the fact that no trace of oxidized nickel was found by XRPD suggests that this shell is either poorly crystalline or amorphous as observed above using the AP synthetic method.

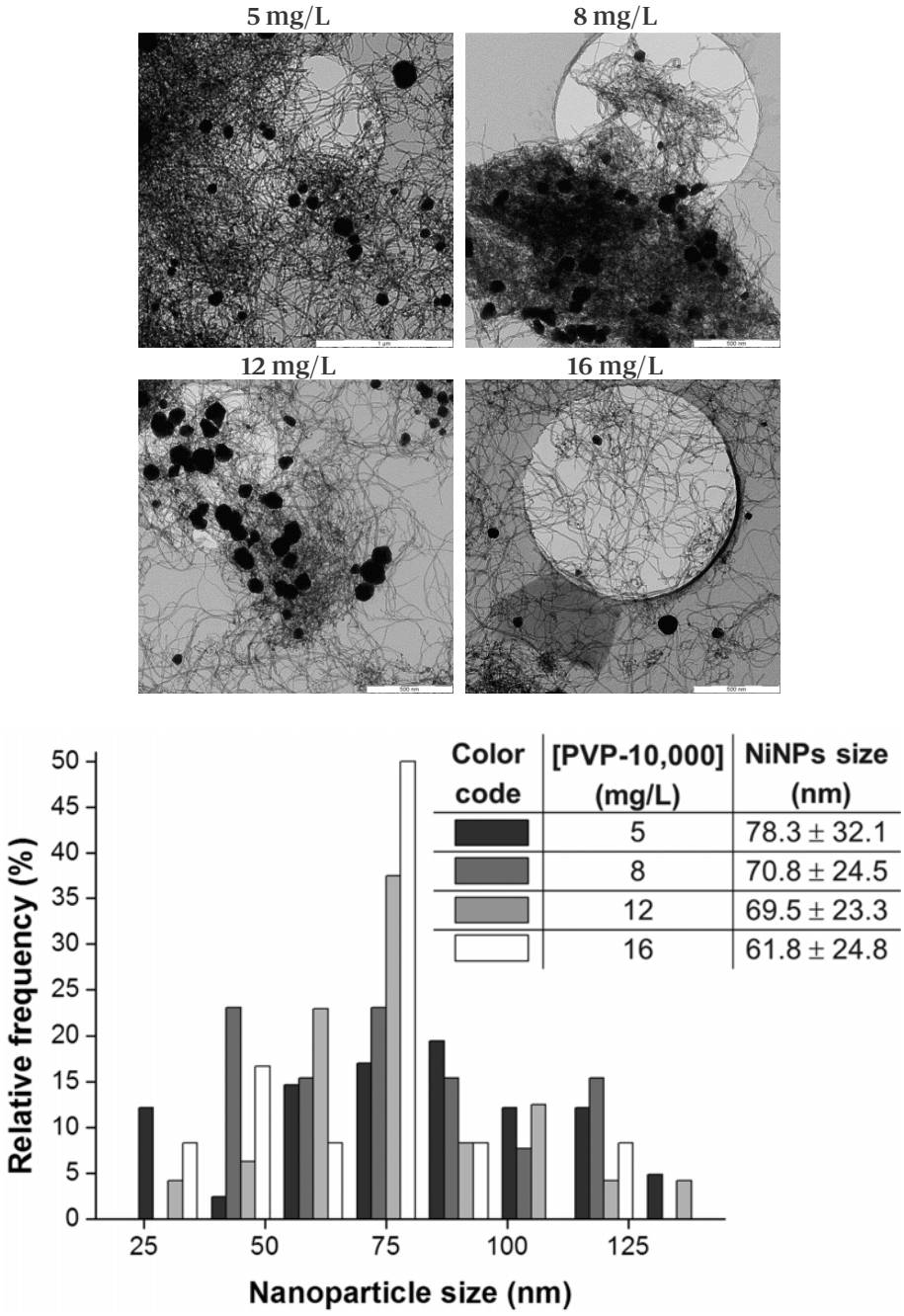

Figure 6 - TEM images (top) and NiNPs size distribution histograms (bottom) for the AC-S nanocomposites synthetized at different PVP-10,000 concentrations.

Table 1 - Ni/C % LR determined by TGA for the different synthetized nanocomposites.

Synthetic method	[PVP-10,000] (mg/L)	Ni/C % LR (%)
AP	8	21
AC-S	5	27
	8	28
	12	30
	16	28
AC-C-7h	-	25
AC-C-15h	-	24

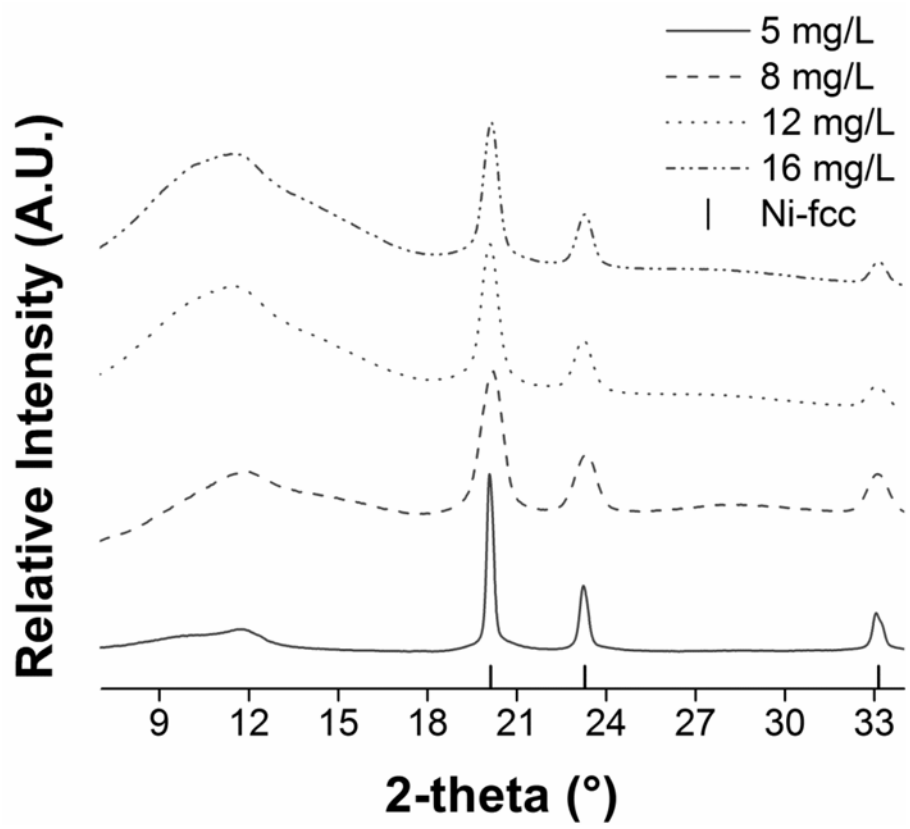

Figure 7 - XRPD diffractograms of the AC-S nanocomposites synthetized with different PVP-10,000 concentrations.

3.2.2.2 AC-C Ni@MWCNTs nanocomposites

Thermal decomposition of $Ni(acac)_2$ has been extensively studied by Von Hoene *et al.* [18]. Their results show that the decomposition process onsets between 200 °C and 250°C. Consequently, a temperature of 230 °C was initially chosen for the AC-C synthesis. As in the AC-S nanocomposites, XRPD results indicate that the deposited NiNPs are mainly constituted of a Ni-fcc phase. Nonetheless, low-intensity hexagonal close-packed (Ni-hcp) reflections were also clearly identified (see Figure 7).

Murdikoudisa *et al.* [19] demonstrated that Ni-hcp is a metastable phase that can be formed at higher reaction temperatures. However, when compared to Ni-fcc, Ni-hcp NPs possess much lower saturation magnetization (M_s) and coercivity (H_c) values [19]. It is so weakly ferromagnetic that some authors like Kotoulas *et al.* [20] consider this Ni phase lying at the threshold of antiferromagnetism. This weak ferromagnetic character makes the hcp phase unsuitable for our intended applications. Therefore, different reaction temperatures were tested to eliminate this minority phase in the AC-C products. As shown in Figure 8, the Ni-hcp reflections were weaker but persistent at 210°C. They finally disappeared when performing the synthesis at 190°C.

In the case of AC-C products, bimodal NiNPs size distributions were found. As it can be observed in Figure 9, ultrasmall NiNPs (< 1 nm) covering the entire MWCNT surface were formed alongside much larger (> 300 nm) nanoparticles. Initial AC-C reaction time was the same as in the AP synthesis (15 h). When halved to 7 reaction hours, only the smallest NiNPs were formed (see Figure 10, left). These results are similar to those obtained for the AP nanocomposite, the

main difference being that no capping agent was used in the AC-C synthesis. Thus, in order to promote the NPs growth, the 7h AC-C product was thermally annealed too, in the same manner as the AP nanocomposite.

Interestingly, the annealing treatment produced NiNPs with a similar average size (16.7 ± 6.4 nm) than those found in the AP product (13.6 ± 4.4 nm). However, the annealed AC-C product possessed a markedly heterogeneous size distribution (see Figure 10, right). This difference could be attributed to partially decomposed $Ni(acac)_2$ complex remaining on the surface of the MWCNTs before annealing. Indeed, the TGA thermograms for the AC-C products show a thermal decomposition process whose temperature range matches that of the pure complex precursor (see Figure 11). TGA results also show that larger amounts of partially decomposed complex are found when the reaction is stopped after only 7h. When heated to 500 °C, $Ni(acac)_2$ is finally completely decomposed. Localized variations in nickel concentration are obtained initially, depending on the amount of leftover $Ni(acac)_2$ complex. Annealed NiNPs grow accordingly, creating the heterogeneous size distributions observed.

As shown in Table 1, TGA results also show that the amount of loaded NiNPs is slightly inferior in the AC-C nanocomposites than in their AC-S counterparts. Nonetheless, the Ni/C %LR is superior in both types of AC nanocomposites than in the AP product. Finally, they highlight that reducing the AC-C reaction time from 15 to 7 hours does not seem to influence the loaded amount of NiNPs.

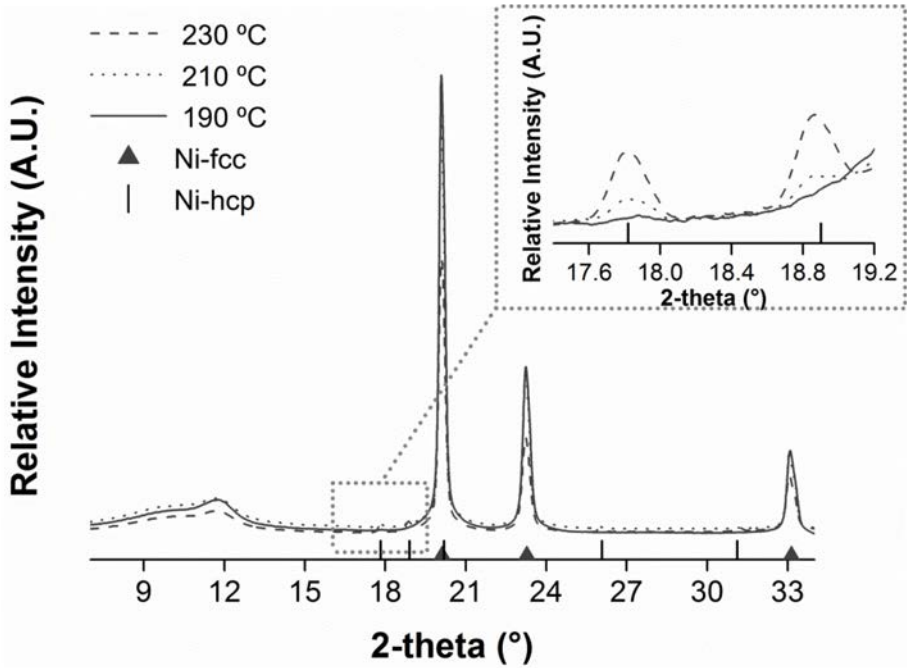

Figure 8 - XRPD diffractogram of the AC-C products at different reaction temperatures.

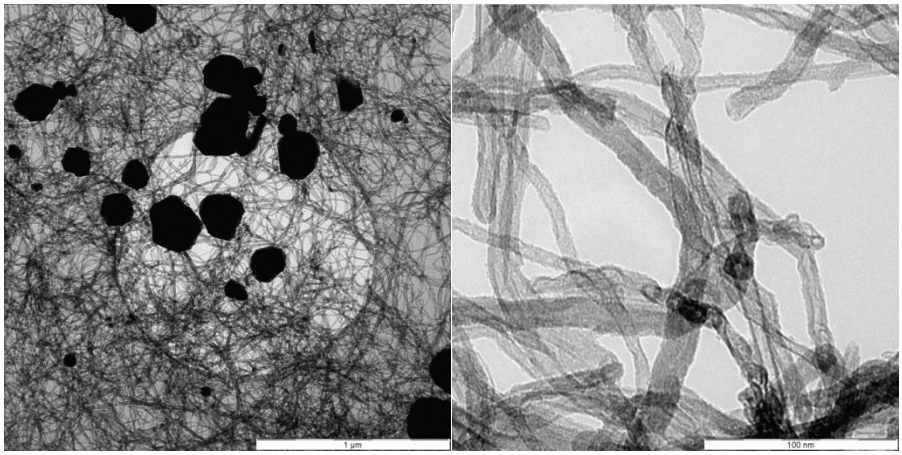

Figure 9 - TEM images of the AC-C product obtained after 15h of autoclave reaction at 190 ºC. Large NiNPs (left) are found alongside ultrasmall NPs (right) which cover the entire MWCNTs surface.

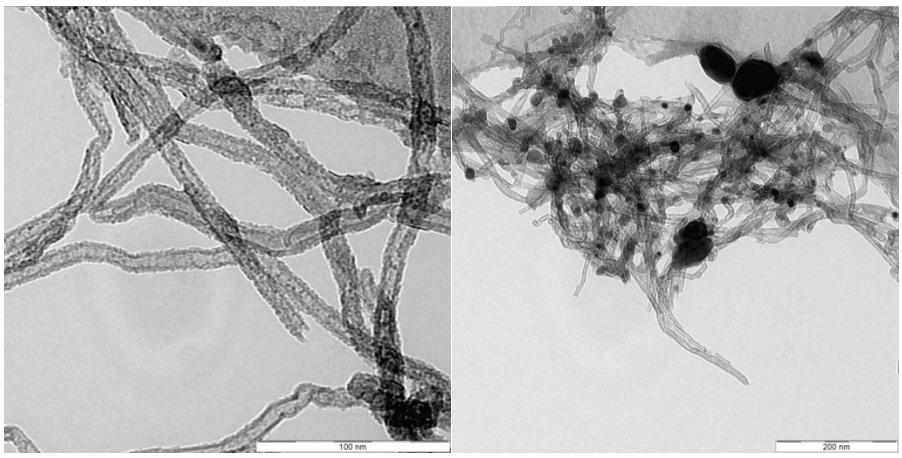

Figure 10 - TEM images of the AC-C product obtained after 7h of autoclave reaction at 190 ºC before (left) and after (right) thermal annealing.

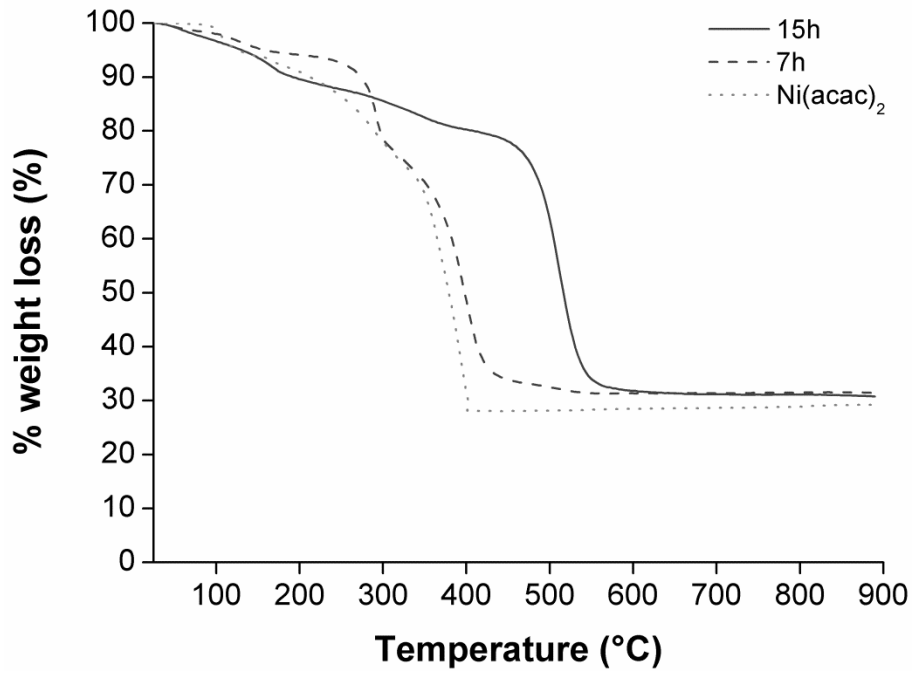

Figure 11 - Thermograms for the thermal decomposition under air of $Ni(acac)_2$ and AC-C nanocomposites synthetized at 190 ºC during 7 h and 15 h.

3.2.3 Ni@MWCNTs nanocomposites magnetic characterization

As shown in sections 3.2.1 and 3.2.2, the AP and AC-C nanocomposites presented similar average sizes after thermal annealing. Nevertheless, the AC-C NiNPs showed a wider size distribution possibly due to the presence of unreacted Ni precursor at first. Therefore, it was decided not to proceed with the magnetic characterization of this particular nanocomposite and to discard it from further experimental work.

The magnetic properties of the thermally annealed Ni@MWCNTs AC-S and AP nanocomposite powders synthetized with a 8 mg/L PVP concentration were studied by SQUID magnetometry. Their magnetization curves recorded against magnetic field are shown in Figure 12. As can be observed, their magnetic properties are strikingly different. While the AP NiNPs are superparamagnetic, those found in the AC-S product show a ferromagnetic behavior. Accordingly, significant differences were found in their mass saturation magnetization (M_S), intrinsic coercivity (H_C) and the remanent magnetization (M_r) values. While the AC-S nanocomposite attained an M_S value similar to that of bulk Ni (~55 emu/g), the AP nanocomposite reached only 40 emu/g. Also, the AC-S product possesses H_C and M_r values of ~100 Oe and ~5 emu/g, respectively, while in the AP nanocomposite they are practically zero as expected for superparamagnetic NPs.

These remarkable differences are certainly due to the difference in NiNPs size found in each nanocomposite. As discussed in section 1.3.2.1.2, NiNPs with a diameter smaller than ~25 nm, such as those found in the AP product (~13 nm), are expected to be superparamagnetic. Superparamagnetic NPs have low M_S and H_C values at room temperature because of either surface effects

(*e.g.* higher surface spin disorder, as described in section 1.3.2.1.3) or thermal excitation, which is sufficient to produce rapid magnetic spin reversals [22, 23].

On the contrary, NiNPs having a diameter above ~80 nm are expected to be ferromagnetic and multi-domain (*e.g.* composed of several magnetic domains). This would be the case of the AC-S nanocomposite, whose NiNPs have an average diameter of ~130 nm. Accordingly, these NiNPs possess a strong magnetic ordering at room temperature alongside a lower surface-to-volume ratio (*e.g.* lower impact of surface spin disorder), both factors producing the higher M_s value recorded. However, their multi-domain nature is also the most probable cause for the nanocomposite's relatively low H_c (see section 1.3.2.1.2).

Finally, it is interesting to notice that the hysteresis curve of the AC-S powder denotes the presence of an exchange bias (EB), resulting from the pinning of interfacial spins in the AFM nickel oxide shell to the ones of the FM metallic nickel core. EB coupling results in extra magnetic anisotropy energy, which contributes to the H_c and produces a shift in the hysteresis curve[24].

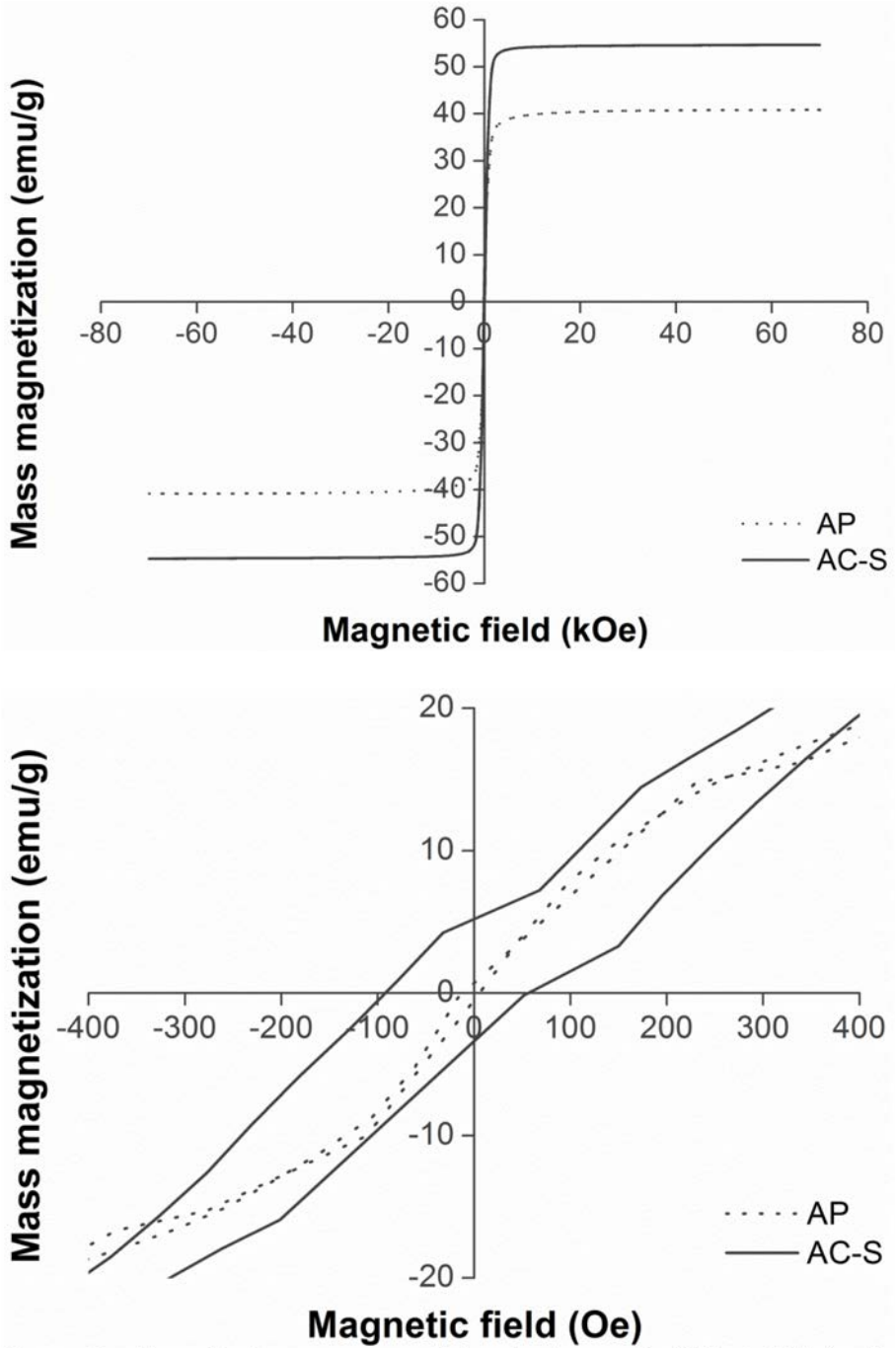

Figure 12 - Magnetization curves recorded against magnetic field at 295K for the thermally annealed AP and AC-S Ni@MWCNTs nanocomposites synthetized using a 8 mg/L PVP concentration (top). A detail of the curves (bottom) highlights the difference in H_c and M_r values for these materials.

3.3 Conclusions

We developed three novel solvothermal methods employing ethylene glycol as both solvent and sole reduction agent to decorate multi-walled carbon nanotubes (MWCNTs) with metallic nickel nanoparticles (NiNPs). Two of them were performed in an autoclave (AC-S and AC-C) and one was performed at ambient pressure (AP). Also, different Ni precursors were tested: a $NiCl_2.6H_2O$ salt (AC-S and AP) and a $Ni(acac)_2$ complex (AC-C). All three syntheses were followed by thermal annealing, producing nanocomposites with markedly different size distributions.

Obtaining distinct size distributions was achieved by creating different Ni^{2+} concentrations in the reaction media. In those methods were the concentration was kept low, either by slowly adding the nickel salt precursor (AP) or by slowly decomposing the $Ni(acac)_2$ complex (AC-C), ultrasmall NiNPs (< 1 nm) were obtained. On the contrary, much larger NiNPs deposited onto the MWCNTs when adding the full amount of nickel salt precursor at the beginning of the reaction (AC-S).

In both syntheses with the nickel salt (AC-S and AP), particle agglomerates were observed. These were avoided by using polyvinylpyrrolidone (PVP, M.W.10,000) as capping agent at 8 mg/L concentration. It was also observed that further increasing the concentration of this same capping agent to 12 or 16 mg/L slightly reduced the deposited NiNPs size.

In the case of the AC-C synthetic technique, we observed that lower reaction temperatures had to be used in order to obtain only the desired Ni-hcp crystalline phase. However, in such conditions, larger amounts of undecomposed Ni complex remained in the reaction products. Therefore, wider NiNPs size distributions were obtained after thermally annealing the AC-C nanocomposite (16.7 ± 6.4 nm) in comparison to their AP counterparts (13.6 ± 4.4 nm).

Consequently, only the AP and AC-S nanocomposites' magnetic properties were characterized using SQUID magnetometry. According to their different

size distributions, the AP NiNPs were found to be superparamagnetic while their AC-S counterparts were weakly ferromagnetic. The impact of these differences on the microwave absorption properties of MAM films produced with these nanocomposites will be further explored in Chapter 8.

3.4 Bibliography

1. H-S. Kim, H. Lee, K-S. Han, J-H. Kim, M-S. Song, M-S. Park, J-Y. Lee and J-K. Kang, *J. Phys. Chem. B*, 2005, **109**, 8983-8986.
2. L. Wang, T. Du, J. Cheng, X. Xie, B. Yang and M. Li, *J. Power Sources*, 2015, **280**, 550-554.
3. W. Zhang, X. Zhang, L. Zhang and G. Chen, *Sensor Actuat. B-Chem.*, 2014, **192**, 459-466.
4. C-T. Hsieh, Y-W. Chou and W-Y. Chen, *J. Solid State Electrochem.*, 2008, **12**, 663-669
5. B-J. Kim, K-M. Bae, Y. S. Lee, K-H. Ana and S-J. Park, *Surf. Coat. Tech.*, 2014, **242**, 125-131.
6. G. Baskayaa, Y. Yıldıza, A. Savka, T. O. Okyaya, S. Erisa, H. Serta and F. Sen, *Biosens. Bioelectron.*, 2017, **91**, 728-733.
7. S.E. Skrabalak, B.J. Wiley, M. Kim, E.V. Formo and Y. Xia, *Nano Lett.*, 2008, **8**, 2077-2081.
8. T. Matsumoto, K. Takahashi, K. Kitagishi, K. Shinoda, J.L. Cuya Huaman J.Y. Piquemal and B. Jeyadevan, *New J. Chem.*, 2015, **39**, 5008-5018.
9. Y. Tian, Y. Liu, F. Pang, F. Wang and X. Zhang, *Colloid Surface A*, 2015, **464**(0), 96-103.
10. D. Rosická and J. Sembera, *Nanoscale Res. Lett.*, 2011, **6**(1). 527-536.
11. K.M, Koczkur, S. Mourdikoudis, L. Polavarapu and S.E. Skrabalak, *Dalton Trans.*, 2015, **44**, 17883-17905.
12. Y. Zhang, S. Xiao, Q. Wang, S. Liu, Z. Qiao, Z. Chi, J. Xu and J. Economy, *J. Mater. Chem.*, 2011, **21**, 14563-14568.
13. Y. Su, C. Chen, X. Zhu, Y. Zhang, W. Gong, H. Zhang, H. Zhao, and G. Wang, *Dalton Trans.*, 2017, **46**, 6358-6365.
14. J. Kleefeld and L.L. Levenson, *Thin Solid Films*, 1979, **64**, 389-393.
15. L. McCafferty, V. Stolojan, S. G. King, W. Zhang, S. Haq, and S. R. P. Silva, *Carbon.*, 2015, **84**, 47–55.
16. S. Tanuma, C.J. Powell and D.R. Penn, *Surf. Interface Anal.*, 2011, **43**, 689-713.
17. H.M. Trimble, *Ind. Eng. Chem.*, 1931, **23**(2), 165–167.
18. J. Von Hoene, R.G. Charles and W.M. Hickam, *J. Phys. Chem.*, 1958, **62**(9), 1098–1101
19. S. Mourdikoudisa, K. Simeonidisa, A. Vilalta-Clementea, F. Tunab, I. Tsiaoussisa, M. Angelakerisa, C. Dendrinou-Samarac and O. Kalogirou, *J. Magn. Magn. Mater.*, 2009, **321**(18), 2723-2728.
20. A. Kotoulas, M. Gjoka, K. Simeonidis, I. Tsiaoussis, M. Angelakeris, O. Kalogirou and C. Dendrinou-Samarac, *J. Nanopart. Res.*, 2011, **13**(5), 1897-1908.
21. K.M. Krishnan, *IEEE T. Magn.*, 2010, **46**(7), 2523-2558.
22. H.M. Lu, W.T. Zheng and Q. Jiang, *Appl. Phys.*, 2007, 40, 320-325.
23. G.C. Papaefthymiou, *Nano Today*, 2009, 4, 438-447.
24. X. Liu, B.P. Pichon, C. Ulhaq, C. Lefèvre, J.-M. Grenèche, D. Bégin, and S. Bégin-Colin. *Chem. Mater.*, 2015, **27**, 4073–4081.

chapter 4

Sol‐gel decoration of graphene oxide with zero‐valent iron and iron/cobalt /nickel carbon‐protected alloy nanoparticles

In this chapter we present a new type of nanomaterials based on reduced graphene oxide (GO) decorated with zero‐valent Fe@γ‐Fe_2O_3 and Fe/Co/Ni carbon‐protected alloy nanoparticles (NPs). These were created using the Pechini sol‐gel method. Synthetic parameters were varied in order to determine their influence on the deposited NPs size and spatial distribution. Extensive physicochemical characterization of the synthetic products was performed to determine the exact chemical nature of the different deposited NPs and their influence on the nanocomposites magnetic properties.

Related publications

F. Mederos-Henry, J. Mahin, B. P. Pichon, M. M. Dîrtu, Y. Garcia, A. Delcorte, C. Bailly, I. Huynen and S. Hermans. **Novel microwave absorbers based on zero-valent Fe@γ–Fe_2O_3 and Fe/Co/Ni carbon-protected alloy nanoparticles supported on reduced graphene oxide.** *Nanomaterials*, 2019, 1196.

J. Mahin, 2016, **Synthesis of iron-based nanoparticles supported on nanocarbons for the production of metamaterials**, UCLouvain, Master Thesis.

Collaborators

Julien Mahin (IMCN/MOST), Benoit P. Pichon (UNISTRA/IPCMS, France), Marinela M. Dîrtu (IMCN/MOST) and Yann Garcia (IMCN/MOST).

As mentioned in the introduction to the previous chapter, ferromagnetic nanoparticles of Fe, Co or Ni induce magnetic losses that can be exploited to produce novel EMI shielding materials. MNPs of Fe, Co and Ni and their alloys have been deposited onto different nanocarbon materials such as graphene [1] or graphene oxide [2], carbon nanotubes [3] or carbon nanofibers [4]. Such MNPs@NcS nanocomposites have been produced using a wide range of synthetic techniques. Wet chemical solvothermal [5], hydrothermal [1] or inert atmosphere thermal [1] reduction processes, carbonization [4], direct [2] or electroless [3] plating are just a few of them.

In this chapter, we propose a novel preparative approach to obtain zero-valent iron (ZVI) and binary or ternary Fe/Co/Ni alloy NPs supported on graphene oxide (GO), based on the Pechini method.

The Pechini method is a type of sol-gel synthesis technique starting from a polymerizable metal complex precursor. It was first described in the Pechini patent [6] within the context of alkaline earth titanates and niobates film deposition for the production of capacitors. The advantages of the Pechini method include its relative simplicity, use of widely available reagents and creation of homogeneous products. Therefore, it is nowadays commonly used for the synthesis of many materials including laser gain materials [7], superconductors [8], perovskites [9], catalysts [10] and nanoparticles [11].

In the Pechini process, metal salts (usually nitrates) are dissolved alongside citric acid to form a metal citrate complex. In a second step, ethylene glycol is added and the solution is heated to induce a polyesterification reaction. This results in the formation of a complex-polyester gel with metallic atoms evenly distributed among the polymer matrix (see Figure 1). The obtained gel is then calcined at high temperature causing the pyrolysis of the polymer. Calcination usually produces nanoparticles with a homogeneous particle size [12].

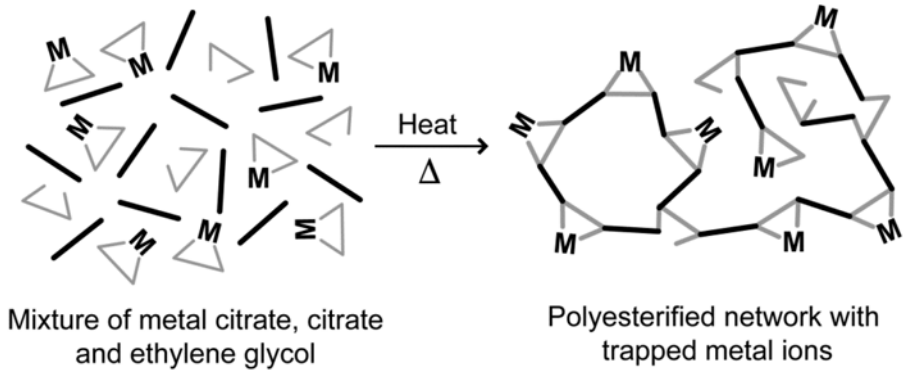

Figure 1 - Schematic representation of the Pechini method. Adapted from Danks *et al.* [12].

The Pechini process is generally used to obtain oxides. However it has been claimed that if the calcination step is carried out under inert or reducing atmosphere, metal@graphitic carbon core-shell nanoparticles (NPs) can be synthesized [13]. Such a shell would favor the long-term stability of ZVI or iron-containing alloy NPs, required by our intended applications. Indeed, it could function as a barrier for oxygen diffusion into the metallic or alloy core, effectively preventing the NPs from oxidation [14]. It is known that the ZVI NPs can be readily oxidized and form non-magnetic iron oxides such as wustite (FeO) or hematite (α-Fe_2O_3) [15]. In such cases, the FMR-related EM absorption properties would be irremediably lost.

Yhr Pechini preparation of carbon-protected ZVI NPs@GO has already been reported in the scientific literature [13]. In this chapter, we show for the first time that this synthetic method can also be used to synthetize binary and ternary Fe/Co/Ni alloy NPs supported on graphene. This is particularly valuable for the ternary FeCoNi@GO nanocomposite for which only one synthetic report is available in the scientific literature [16]. However, the proposed methodology offers a poor control over the composition of the obtained product, resulting in a mixture of several binary and ternary alloy phases.

4.1 Materials and methods

4.1.1 Materials and characterization techniques

Graphene oxide (GO) was purchased from Nanoinnova Technologies SL (Spain). All other reactants were supplied by Across, Alfa Aesar, Merck, Sigma Aldrich or VWR and engaged as received. More details on each reactant are provided in Appendix I while the different physicochemical characterization techniques employed are described in Appendix II.

4.1.2 Synthesis of ferromagnetic iron-based nanoparticles supported on graphene oxide

The synthesis of ZVI@GO nanocomposites was inspired by a Pechini-type method described in the scientific literature [13]. A typical synthesis is described below for a ZVI@GO product with a 50 % Fe/C mass loading rate.

50 mg of graphene oxide (GO), 180.8 mg of iron (III) nitrate nonahydrate ($Fe(NO_3)_3 \cdot 9H_2O$), 516 mg of citric acid (CA) and a magnetic stir bar were introduced in a small round-bottom flask. 3.3 mL of ethanol were added, the flask was closed with a septum and the mixture was stirred until complete dissolution of the reactants. The suspension was then sonicated at 80 W for 1 hour (VWR ultrasound cleaner USC 1200-THD) in order to disperse GO. 112 µL of ethylene glycol (EG) were added and the suspension was heated with a reflux condenser in an oil bath at 90 °C for 3 hours. The suspension was then poured in a porcelain combustion boat and placed in a drying oven under vacuum at 30 °C for 2 hours. The obtained gel-covered ceramic plate was introduced in a tubular furnace (Carbolite Gero STF16, United Kingdom) and heated to 750 °C for 2h under Ar/H_2 95/5 atmosphere. The temperature was increased and decreased at a rate of 1.7 °C/min. The recovered powder was stored in air with no particular precautions.

The citric acid:ethylene glycol (CA:EG) and citric acid:metal (CA:M) ratios used in the example above were of 1:1.5 and 6:1, respectively. We decided to also test three other CA:EG (1:1, 1:1.5 ,1:11) and two CA:M (3:1, 6:1) reactant ratios in order to determine the optimal proportions required to deposit NPs with homogeneous size and spatial distributions onto GO.

Once the optimal synthetic conditions were determined, the same methodology described above for ZVI NPs was used to deposit FeCo, FeNi, and FeCoNi alloy NPs onto GO. In all cases, the CA:EG ratio and CA:M ratios were of 1:1.5 and 6:1 respectively. Adapted quantities of $Fe(NO_3)_3{\cdot}9H_2O$, $Co(NO_3)_2{\cdot}6H_2O$ and $Ni(NO_3)_2{\cdot}6H_2O$ salts were used as precursors to obtain the desired equimolar binary or tertiary alloy compositions.

4.2 Results and discussion

A tight control on the deposited NPs chemical composition, size and spatial distribution on the nanocarbon surface is essential for our intended applications. Indeed, as discussed in section 1.3.2, the ferromagnetic resonance (FMR) phenomenon depends on the system's magnetic properties, such as its saturation magnetization (M_s). These characteristics are themselves dependent on compositional and morphological factors.

Consequently, we first determined the optimal Pechini reactant proportions required to deposit ZVI NPs with homogeneous size and spatial distributions onto graphene oxide (GO). Their chemical composition was then thoroughly studied. In a subsequent step, using the optimal conditions determined for the ZVI@GO synthesis, three different Fe, Co and/or Ni alloys were produced and fully characterized. Finally, the nanocomposites magnetic properties were determined.

4.2.1 Optimization of the citric acid to ethylene glycol (CA:EG) and to metal precursor (CA:M) ratios

In the Pechini synthesis, the viscosity of the gelled precursor has a direct influence on the homogeneity of the end products [17]. Therefore, numerous investigations have attempted to identify the critical factors that influence the gel viscosity [17-19]. These results highlight the crucial role played by the citric acid to ethylene glycol molar ratio (CA:EG) and the citric acid to metal molar ratio (CA:M). Furthermore, they show that the gel viscosities are optimized when using molar CA:EG and CA:M ratios ranging from 1:1.5 to 1.5:1 and 1:1 to 6:1, respectively [19].

In this study, three different CA:EG (1:1, 1:1.5, 1:11) and two CA:M (3:1, 6:1) ratios were tested for the ZVI@GO synthesis. TEM characterization of the obtained nanocomposites confirms that these ratios strongly influence the deposited ZVI NPs size and spatial distribution.

As shown in Table 1, the smallest ZVI NPs possessing the narrowest size distributions are obtained at lower CA:EG ratios using the 6:1 CA:M ratio. Also, lower CA:EG and CA:M ratios favor the deposition of ZVI NPs onto a GO surface in a more homogeneous and dense manner (see Figure 2).

Based on these results, we infer that the different CA:EG and CA:M ratios are influencing the ZVI NPs size and spatial distribution by changing the length of the polyester chains that make up the gels as well as the spacing between them (see Figure 3, top). Indeed, when using excess quantities of EG (1:11 CA:EG ratio), the resulting chains are presumably shorter than when using equimolar EG and CA quantities. Furthermore, unreacted EG moieties dilute the system, spacing the polymerized chains apart. The shorter and more diluted chains distribute heterogeneously over the surface of GO. When calcined in the tubular oven, they induce the formation of ZVI NPs in

localized areas. Possibly because of thermal sintering effects, the heterogeneously deposited NPs also possess a wider size distribution.

On the other hand, the reason why the ZVI NPs size and density are increased at lower CA:M ratios is illustrated in Figure 3, bottom. As the amount of CA moieties is decreased, the coordinated metallic ions are closer to each other in the polymer gel chains. When calcined, the ZVI NPs are thus deposited closer to each other and, eventually, sinter to form larger particles.

The Fe/C mass loading rate (%LR) of ZVI NPs deposited onto GO was determined by TGA. When aiming at 50% ZVI NPs LR, the obtained loading rate varied from a minimum of 38% to a maximum of 48%. The obtained results show that the %LR decreases as the amounts of EG and CA increase (see Table 2). This trend can be explained by considering the highly reductive atmosphere used in the tubular oven [e.g. H_2/Ar (5/95 %v/v) gas stream at 750 ºC]. Under these conditions, residual carbon coming from EG or CA is expected to graphitize and deposit onto GO [13]. Therefore, when using larger proportions of the different carbon-containing reactants, such as in the CA:EG 1:11 or the CA:M 6:1 ratios, larger amounts of graphitic carbon might be found in the end products. This additional carbon might artificially decrease the Fe/C % LR.

Also, the iron precursor amount was varied and the EG and CA quantities were adjusted to easily vary the wt. %LR. Nanocomposites with approximately 20%, 30%, 40% and 60% ZVI NPs wt. %LRs were thus obtained straightforwardly (see Figure 4).

Table 1 - ZVI NPs size distributions obtained using different CA:M and CA:EG ratios

CA:EG ratio	CA:M ratio	
	3:1	6:1
1:1	16.8 ± 6.5 nm	14.8 ± 4.7 nm
1:1.5	17.9 ± 8.1 nm	14.3 ± 7.2 nm
1:11	8.3 ± 9.6 nm	19.7 ± 10.4 nm

Table 2 - Fe/C mass loading rate (%LR) obtained using different CA:M and CA:EG ratios as obtained by TGA. A 50% LR was aimed at, in all cases

CA:EG ratio	CA:M ratio	
	3:1	6:1
1:1	48	48
1:1.5	44	41
1:11	43	38

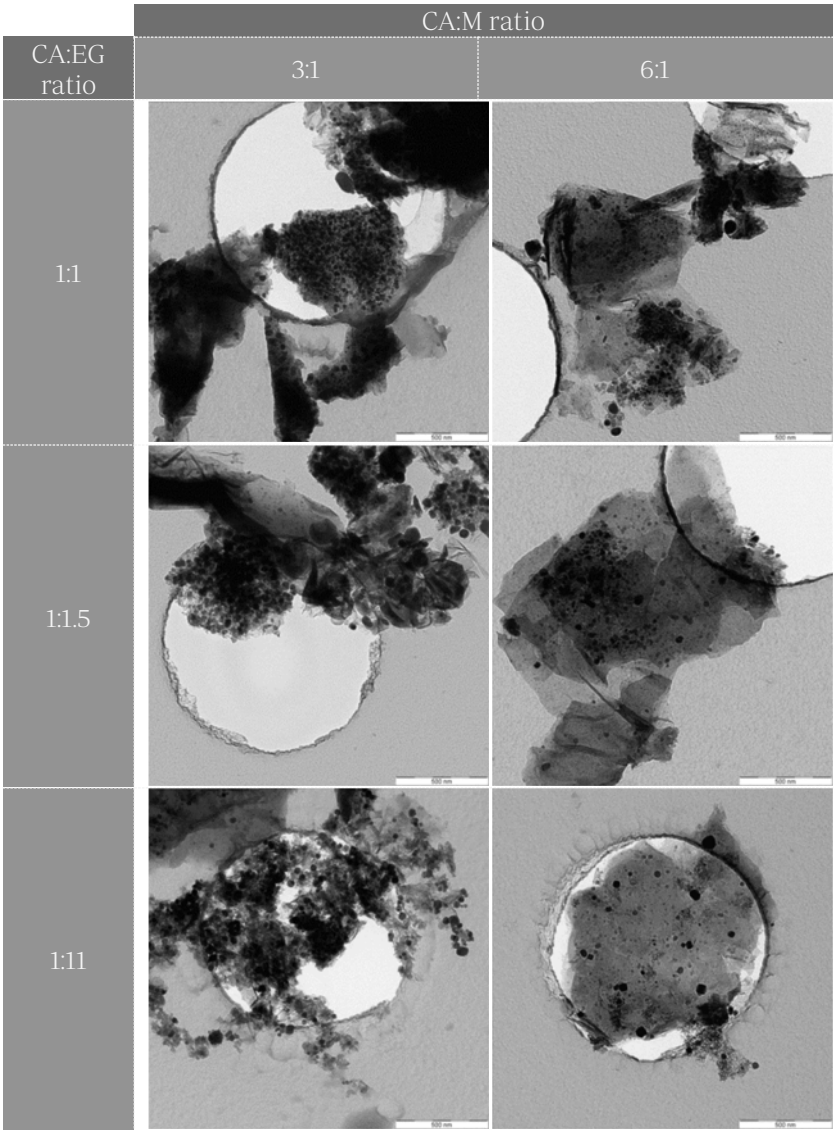

Figure 2 - Representative TEM images of ZVI@GO nanocomposites synthesized using different combinations of CA:EG and CA:M ratios.

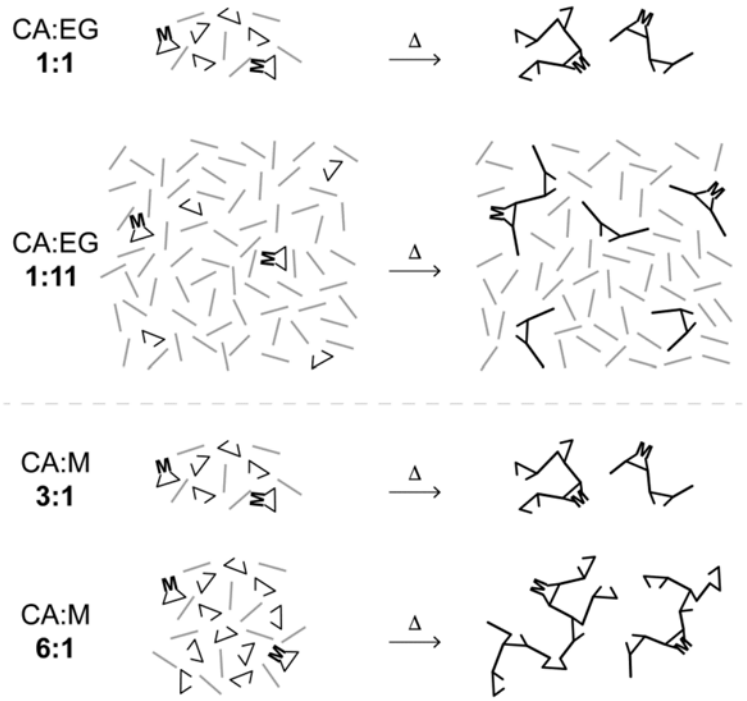

Figure 3 - Schematic representation of the influence of the citric acid (CA) to ethylene glycol (EG) or metal (M) molar ratios (top and bottom figures, respectively).

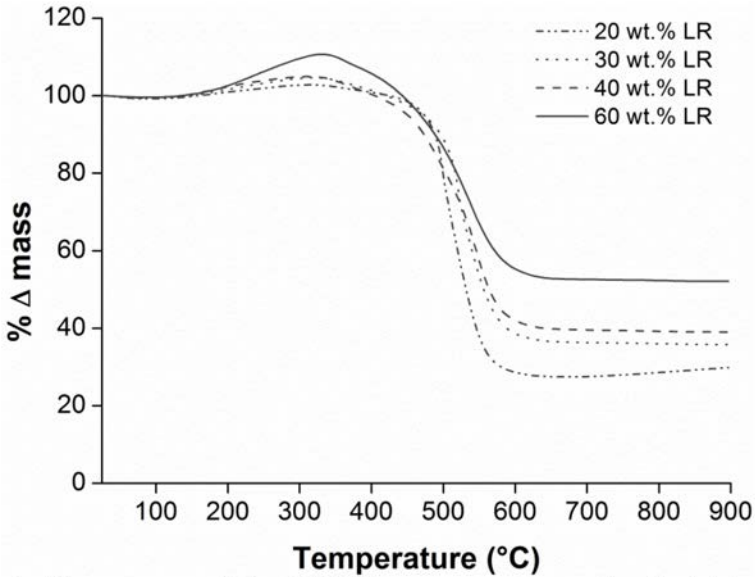

Figure 4 - Thermograms of the ZVI@GO nanocomposites under air obtained with 20%, 30%, 40% and 60% ZVI NPs wt. %LRs.

4.2.2 Characterization of the chemical composition of the ZVI nanoparticles deposited onto GO

The ZVI nanocomposites were characterized by XRPD. As shown in Figure 5, the recorded spectra show a broad reflection around 12° 2θ which can be attributed to poorly ordered, short range interactions between (0 0 2) planes of reduced graphene oxide (rGO) [20, 21]. These graphitic reflections can be explained by the fact that GO is partially reduced to rGO under the H_2/Ar (5/95 %v/v) atmosphere used in the present synthetic procedure. Once reduced, rGO graphitic sheets interact via π–π stacking interactions similarly to graphite planes [22]. Moreover, graphitic deposits formed from CA or EG during the heating step might also contribute to this signal.

As for the NPs, they seem to be composed of a mixture of cubic iron phases. Indeed, characteristic body-centered cubic (bcc) and face-centered cubic (fcc) reflections were detected (see Figure 5). Bcc reflections are the most intense, and therefore this crystalline phase is assumed to be the most abundant. Fcc reflections are even less intense at the lower CA:EG ratios (1:1 and 1:1.5), independently of the CA:M ratio (not shown). A reflection around 16° 2θ suggests that maghemite (γ-Fe_2O_3) is also present in lesser amounts. Nonetheless, its broadness might indicate that the iron oxide is poorly crystalline.

Mössbauer investigation of a ZVI@GO nanocomposite synthesized using 1:1.5 CA:EG and 6:1 CA:M ratios also revealed three different iron species and allowed to quantify them. Indeed, as shown in Figure 6a and Table **3**, two well-defined sextet patterns and a weak broad singlet were identified. The splitting of the first sextet (δ = 0.11(1) mm.s^{-1}) presents an internal field (B_{hf}) value of ~34.1 T, which is consistent with iron in bcc arrangements [23]. The second sextet (δ = 0.43(1) mm.s^{-1}) presents

a B_{hf}~39 T value which is characteristic of maghemite [24], while the singlet, with an isomer shift (δ) of 0.05 $mm.s^{-1}$, is typical of superparamagnetic fcc-Fe nanoparticles [25]. Based on the quantification of assigned site-populations, the as-synthesized ZVI NPs seem to be mainly composed of bcc-Fe (86%) and maghemite (10%), with the fcc-Fe phase accounting for the rest (4%). No evidence of other iron oxides was found in our data [26, 27].

Compared to our Mössbauer results, XPS analyses show a larger proportion of iron oxide. As can be observed in Figure 7, the oxidized iron component (Fe-ox) is more abundant than its metallic iron (Fe^0) counterpart. These results might indicate that the oxide, in this case maghemite, is found on the surface of the deposited nanoparticles. Indeed, XPS is a surface-sensitive technique with a sampling depth of ~4.5 and 5 nm for iron and maghemite, respectively [28]. Therefore, the emitted photoelectrons will originate mostly from the outermost layer of the sampled NPs. If this layer is mainly composed of maghemite, the XPS spectra will show an artificially higher fraction of the Fe-ox component, as was observed in the previous chapter for Ni.

Confirmation of such a core-shell structure was obtained by TEM and HRTEM. Figure 8 shows representative TEM and HRTEM images in which the ZVI NPs are visualized with a darker core clearly differentiated from a surrounding lighter shell layer. The outer shell has an irregular thickness with an average value of 3.1 ± 0.7 nm. Also, in some cases, a very light circle between the core and the shell was observed. This might be a local decohesion upon cooling due to the Fe^0 core and the γ-Fe_2O_3 shell having different thermal expansion coefficients [29].

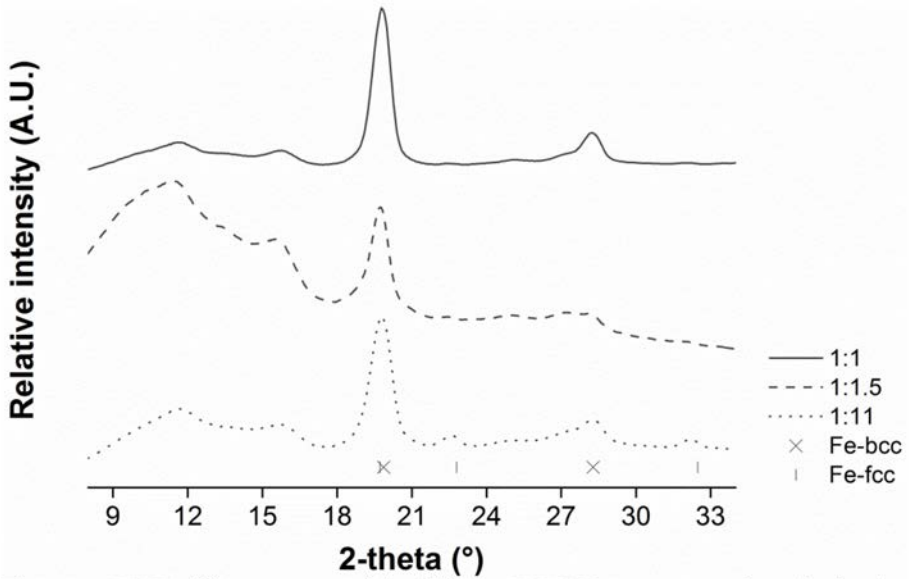

Figure 5 - XRPD diffractograms of the different ZVI@GO nanocomposites obtained at 1:1, 1:1.5, 1:11 CA:EG and a 6:1 CA:M ratios.

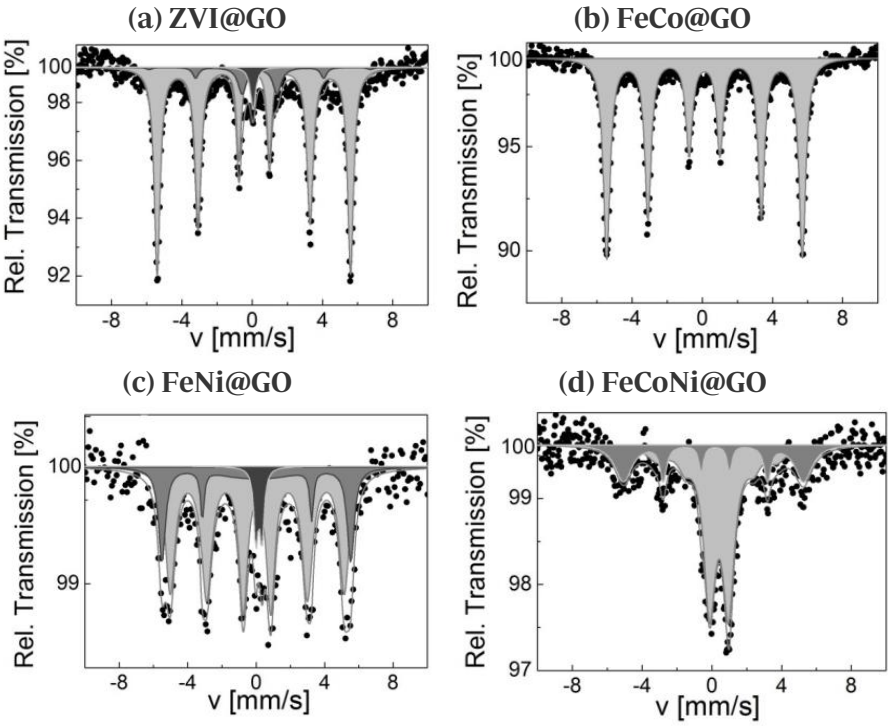

Figure 6 - ^{57}Fe Mössbauer spectra at 77K of ZVI and Fe/Co/Ni alloy nanoparticles deposited on graphene oxide (GO): (a) ZVI@GO; (b) FeCo@GO; (c) FeNi@GO; and (d) FeCoNi@GO.

Table 3 - ^{57}Fe Mössbauer parameters for ZVI and Fe/Co/Ni alloy nanoparticles deposited on graphene oxide (GO)

	T (K)	δ (mm/s)	ε, ΔE_Q (mm/s)	$B_{\eta\phi}$ (T)	Γ /2 (mm/s)	Relative Area (%)	Sites
ZVI	77	0.05(1)	-	-	0.18*	4	γ–Fe (fcc)
		0.11(1)	0	34.1	0.21(1)	86	α–Fe (bcc)
		0.43(1)	0	39.0	0.28*	10	γ–Fe_2O_3
FeCo	77	0.12(1)	0	34.6	0.22(1)	100	FeCo alloy
FeNi	77	0.16(1)	0.35(1)	-	0.15*	6	Superparamag. phase
		0.027(1) 0.06(2)	-0.018(1) 0.01(1)	34.1 31.5	2.0(1) 0.29(1)	24 70	FeNi (fcc) alloy
FeCoNi	77	0.35(1)	-0.07(1)	21.2	0.40(1)	30	Fe carbide
		0.15(1)	-0.05(1)	32.0	0.17(1)	70	FeCoNi (fcc) alloy

(1) δ: isomer shift (with respect to α-Fe at r.t.); ε, ΔE_Q: quadrupole splitting; $\Gamma/2$: half width at half maximum;

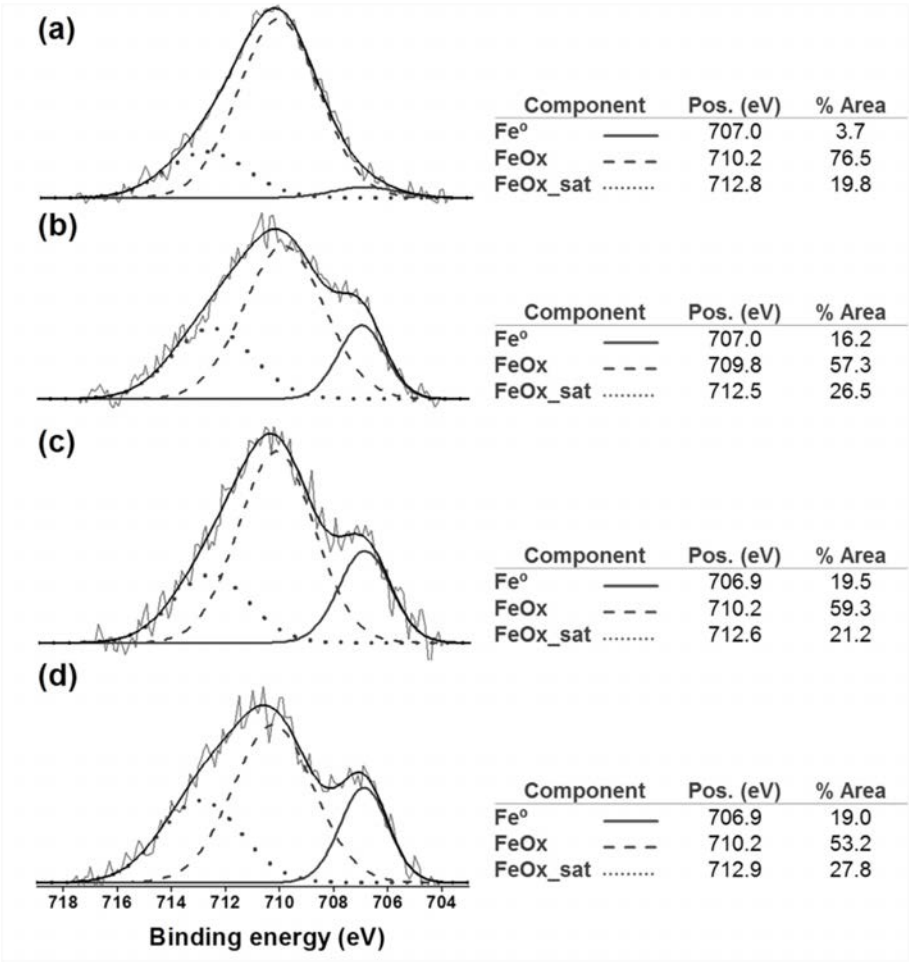

Figure 7 - XPS Fe2p$_{3/2}$ peak region showing metallic (Fe^0) and oxidized (Feox+Feox sat) components in (a) ZVI, (b) FeCo, (c) FeNi and (d) FeCoNi alloy NPs deposited on GO.

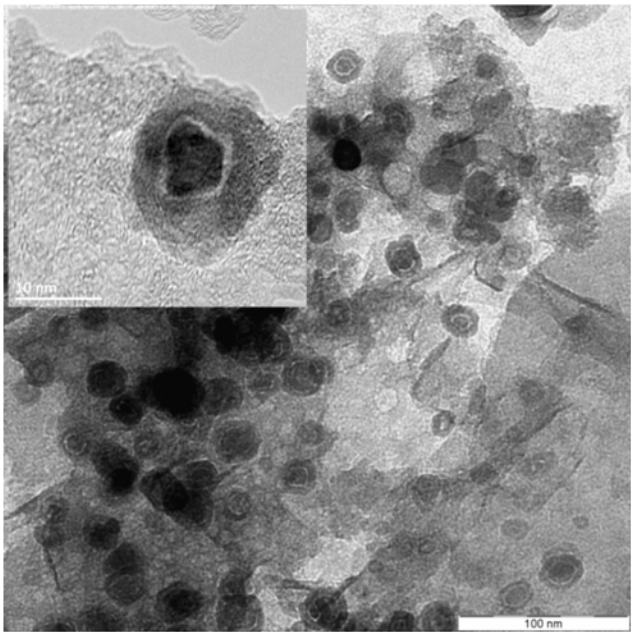

Figure 8 – TEM and HRTEM (inset, upper left corner) images of a ZVI@GO nanocomposite prepared with 1:1.5 CA:M and 3:1 CA:EG ratios.

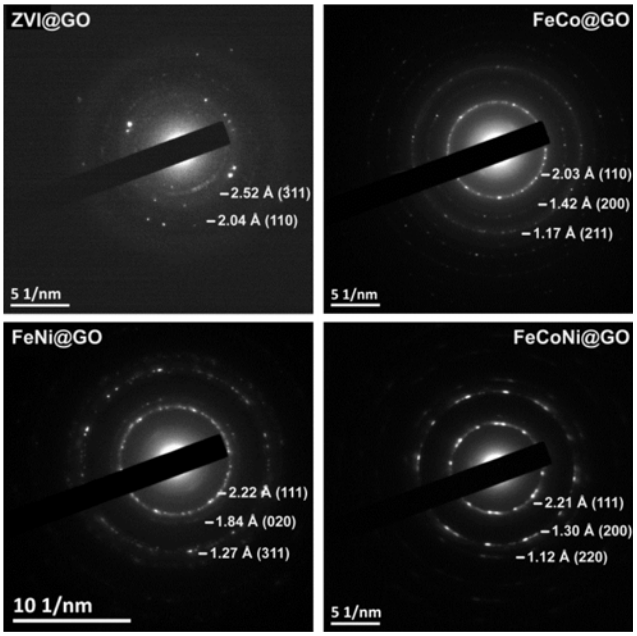

Figure 9 - Electron diffractogramms collected during HRTEM observation of the different nanocomposites. Calculated lattice spacing (in Angstroms, Å) and their corresponding (h k l) indices are included for each product.

In agreement with our XRPD, XPS and Mössbauer results, lattice parameters calculated from HRTEM micrographs and electron diffraction patterns showed that the nanoparticles' core is composed of metallic iron while maghemite is found in the shell [34] (see Figure 9). The presence of an iron oxide layer on the surface of ZVI NPs obtained by a similar synthetic methodology has already been described [13]. However, to the best of our knowledge, this is the first time that the metal oxide phase is fully characterized and identified as maghemite.

4.2.3 Synthesis and characterization of Fe/Co/Ni alloy NPs deposited onto GO

Based on the results obtained with the ZVI@GO synthesis, 1:1.5 CA:EG and 6:1 CA:M ratios were chosen to perform the syntheses of Fe-containing alloy nanocomposites. Three types of equimolar binary (FeCo and FeNi) and tertiary (FeCoNi) alloy NPs were deposited onto GO using the same Pechini methodology.

TEM observations were used to characterize the size distribution of alloy NPs deposited over the graphenic sheets. In contrast with what was observed for the ZVI NPs, all the alloy NPs size distributions are bimodal (see Figure 10). Also, in all these nanocomposites, the smaller NPs are more abundant than the larger ones. However, their particular average values vary slightly from one alloy to the other. For instance, in the FeNi and FeCo nanocomposites, the size of the smallest NPs is centered on 11 nm while in the FeCoNi alloy its average value is 8 nm. As for the larger NPs, central values around 25 nm were observed for both the FeCo and FeCoNi nanocomposites, being slightly higher (28 nm) for the FeNi products.

As in the ZVI nanocomposites, distinct core-shell structures were observed in all alloy samples (see Figure 11). The observed shells also

have an irregular thickness but they are significantly thinner (2.3 ± 0.5 nm) than those observed in the ZVI NPs samples. Furthermore, they possess a clearly layered structure with an average ~3.30Å layer interspacing value that is characteristic for graphite [31]. As mentioned before, obtaining a graphitic shell is important to ensure the long-term stability of the deposited NPs. Indeed, such a carbon shell is expected to limit oxygen diffusion into the metallic core, effectively preventing the NPs oxidation [14]. Also, TOF-SIMs analysis of the alloy nanocomposites (see Figure 12) showed the presence of small amounts of binary metal oxides resulting from alloy oxidation, possibly at the surface of the NPs core.

The NPs cores were thoroughly studied by different characterization techniques. First of all, ICP and point SEM-EDX analyses were performed to determine their composition (see Table 4). Both measurements confirmed that the global composition of the samples approaches the desired 1:1 or 1:1:1 elemental ratio for the binary and tertiary alloys, respectively.

The three alloy nanocomposites were also characterized by XRPD to determine their constitutive crystalline phases. FeNi and FeCoNi NPs were found to be exclusively composed of fcc crystals. However, FeCo nanoparticles are composed of primitive (simple) cubic crystallites (see Figure 13). The obtained results are coherent with previous reports on these alloys' crystallographic structures [32, 33]. Also, as shown in Figure 9, lattice parameters calculated from HRTEM micrographs and electron diffraction patterns confirmed that the desired alloy phases were obtained in all cases [34].

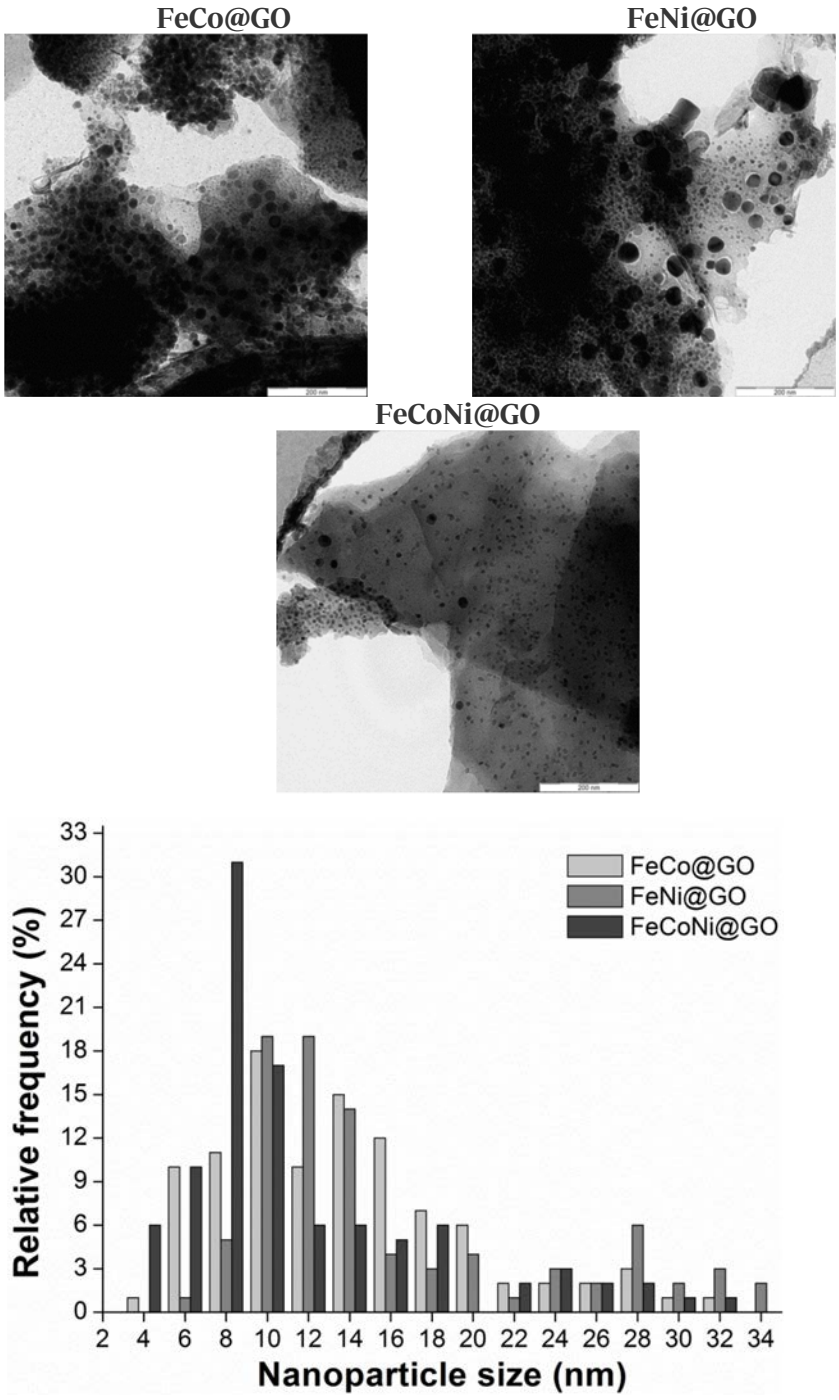

Figure 10 - Typical TEM images (top) and NPs size distribution histograms (bottom) for the alloy nanocomposites.

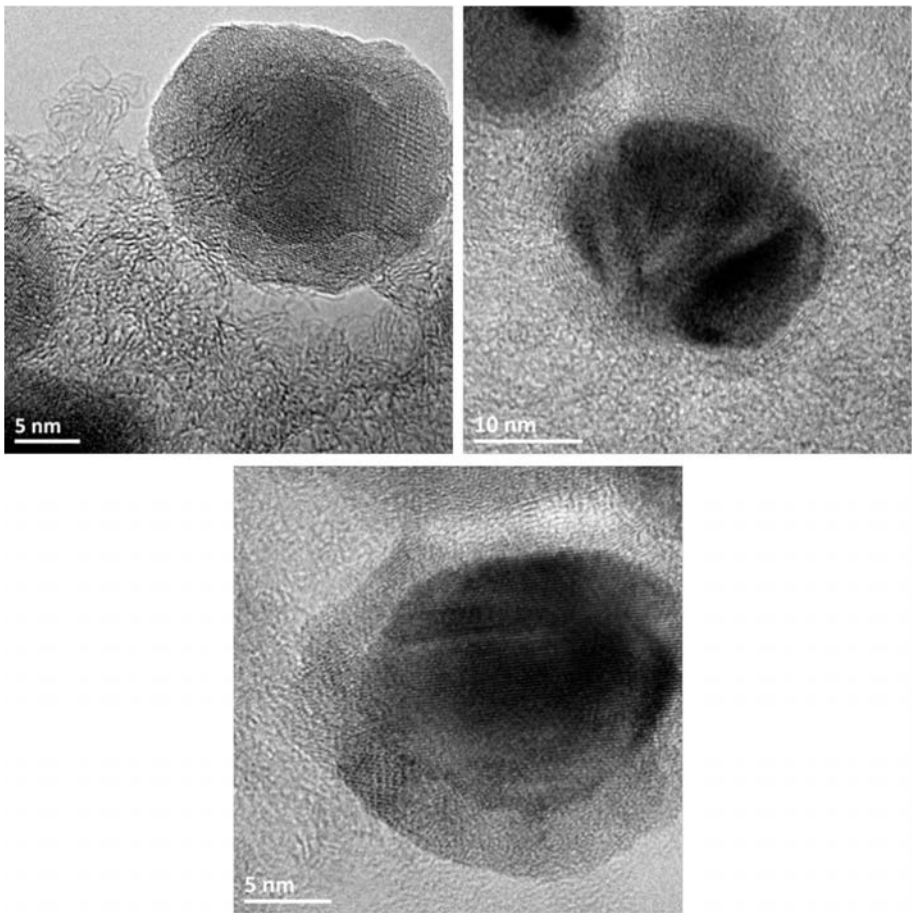

Figure 11 – HRTEM images illustrating core-shell structures found in FeCo@GO (top, left), FeNi@GO (top, right) and FeCoNi@GO (bottom) nanocomposites.

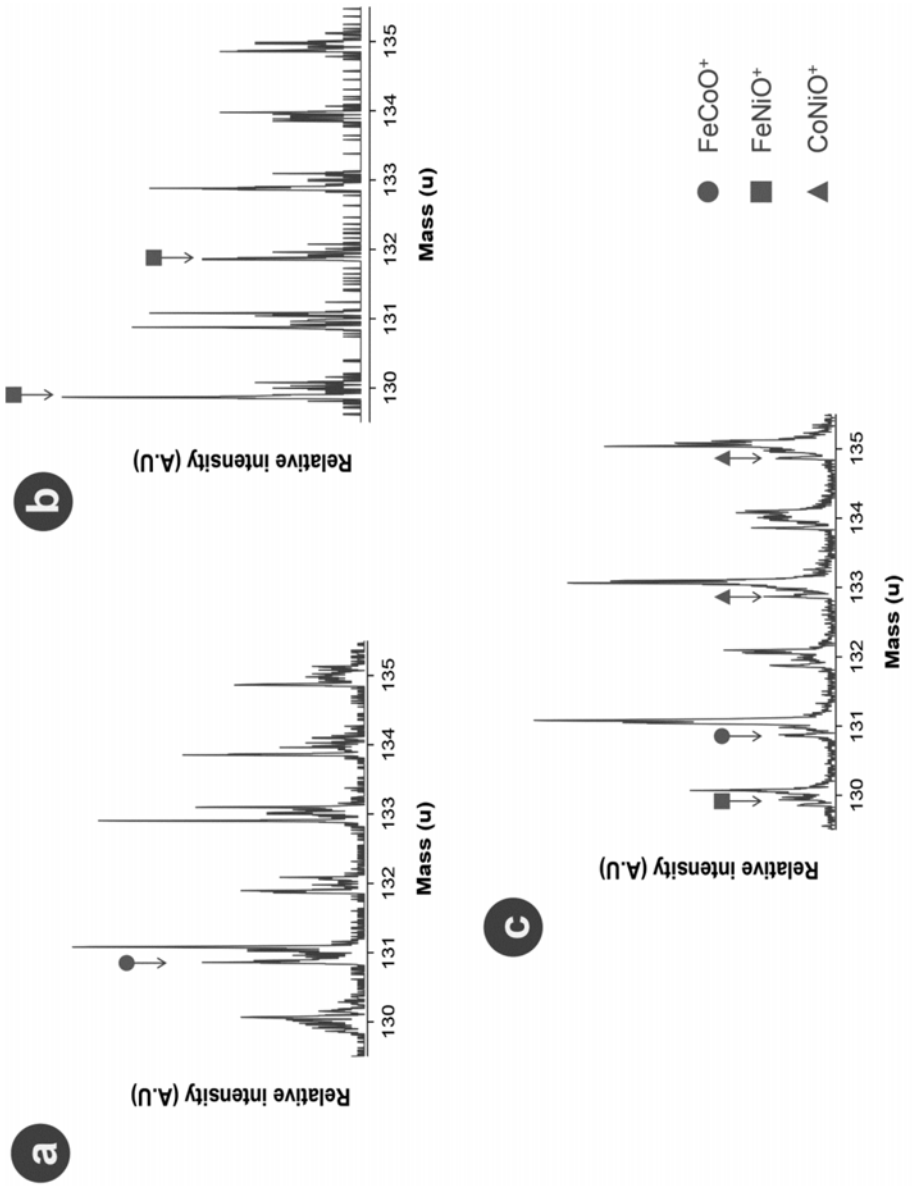

Figure 12 - ToF-SIMs spectra of the (a) FeCo@GO (b) FeNi@GO and (c) FeCoNi@GO nanocomposites showing the presence of binary metal oxides moieties.

Table 4 - Elemental mass composition (wt.%) for the different alloy nanocomposites determined by EDX and ICP.

	EDX			ICP		
Alloy NPs	% Fe	% Co	% Ni	% Fe	% Co	% Ni
FeCo	47± 4	53 ± 6	-	49	51	-
FeNi	48 ± 3	-	52 ± 3	52	-	48
FeCoNi	30 ± 8	36 ± 5	34 ± 6	32	34	34

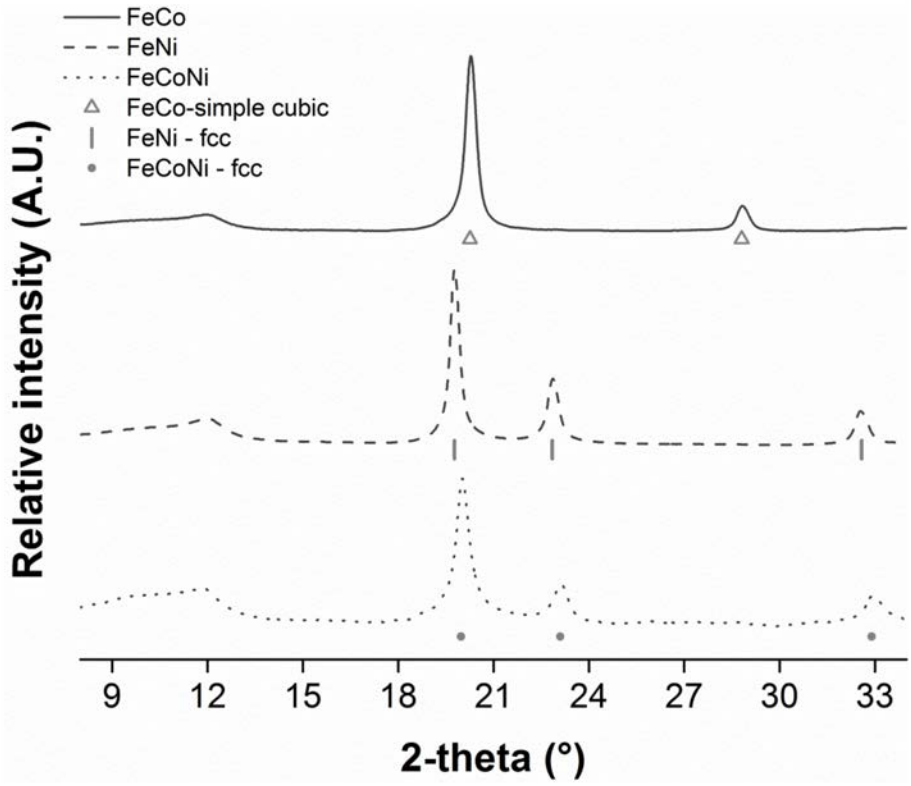

Figure 13 - XRPD diffractograms of the different alloy nanocomposites obtained at 1:1.5 CA:EG and 6:1 CA:M ratios.

A deeper understanding of the different Fe alloy-nanocomposites structure and composition was gained by Mössbauer spectroscopy (see Figure 6b-d and Table 3). For instance, in the FeCo@GO nanocomposite, a sextet (100% sites population) characterized by an isomer shift (δ) of 0.12(1) mm/s and an internal field (B_{hf}) of ~34.6T was identified at 77K. Similar B_{hf} and δ values have already been described for a FeCo alloy [35]. Furthermore, the B_{hf} value indicates that the alloyed atoms are distributed in a relatively ordered manner. Indeed, it has been found that B_{hf} values larger than ~34.8T [36] denote increasing degrees of substitutional disorder in FeCo alloys, a completely disordered state being characterized by a B_{hf} ~ 36T value [37].

In the FeNi@GO product, a first magnetic sextuplet (approximately 70% sites population) at δ = 0.06(2)mm/s and a distribution of hyperfine fields with B_{hf}~31.5T was observed. These values are typical for disordered FeNi alloys in the composition range 35-50% of Ni possessing a fcc arrangement [38, 39]. A second sexted (24 % population), with δ= 0.027(1) mm/s B_{hf}~34.1T was also identified. Such δ and B_{hf} values are clearly indicative of an ordered FeNi alloy with a lower percentage of Ni. Finally, a third signal (6%), with a δ = -0.07(1) mm/s value, can be attributed to the presence of superparamagnetic FeNi NPs in the nanocomposite [38, 40-42].

For the FeCoNi@GO nanocomposite, a sextuplet (70% of sites population) with a B_{hf} ~32T value was identified. This value seems to indicate a homogeneous distribution of Fe, Co and Ni atoms in the fcc matrix. A second sextuplet (30% of sites population) is found at δ= 0.35(1) mm/s with a B_{hf}~21.2 T. These values might indicate the presence of a fcc carbide phase, Fe_3C or Fe_4C [25, 43], which has already been identified at room temperature for similar materials [44].

In accordance with ToF-SIMs results, XPS analyses of these nanocomposites clearly show the presence of iron oxides (see Figure 7 and in Appendix IV.3, Figures 4 and 5). However, the fact that such chemical species were not detected

by XRPD nor Mössbauer indicate that they are poorly crystalline and present in very limited quantities (less than 2%). As mentioned in section 4.2, these results suggest that oxidized iron might be found on the surface of the alloy NPs. Nonetheless, when compared to their ZVI counterpart, the amount of oxidized iron is proportionally much lower in all alloy NPs compared to Fe° (see Figure 7). This result shows that alloy NPs are more resistant towards oxidation than ZVI NPs. This effect is documented in the scientific literature [45] and is explained by the higher reduction potential of cobalt ($E°\ Co/Co^{2+}$ = -0.28 V) and nickel ($E°\ Ni/Ni^{2+}$ = -0.25 V) as compared to iron ($E°\ Fe/Fe^{2+}$ = -0.45 V) [46].

4.2.4 Characterization of the nanocomposites magnetic properties

Finally, the magnetic properties of the ZVI and Fe/Co/Ni alloy nanocomposites were studied by SQUID magnetometry. Magnetization curves recorded against magnetic field from one direction to the opposite one do not overlap at 300 K, which corresponds to a weak ferromagnetic behavior for all of them (see Figure 14, top).

Given the sizes of our nanoparticles that are mostly below the superparamagnetic limit (SPM) critical size (see Table 5), such a ferromagnetic behavior was unexpected. However, the presence of ferrimagnetic (FiM) γ-Fe_2O_3 or antiferromagnetic (AFM) Fe/Co/Ni oxides at the surface of the ZVI or alloy nanoparticles, respectively, might explain the presence of a coercive field at room temperature. Indeed, both types of oxides can increase the effective magnetic anisotropy energy of the deposited NPs. In the case of the γ-Fe_2O_3 shell layer, such an increase might be due to the presence of noncollinear or canting spin arrangements possessing a larger anisotropy than the core [46]. Consequently, an interfacial core-shell coupling which increases the magnetic anisotropy energy of the whole NP can be expected. As for the surface AFM metal oxides, they are characterized by magnetic anisotropies much smaller than the ones of ferromagnetic (FM) metals. Thus, we expect some exchange bias (EB) coupling at

the interface between the metal core and the oxidized shell. EB coupling consists in the pinning of interfacial spins in the FM core to the ones of the AFM shell [48], also resulting in extra magnetic anisotropy energy.

Table 5 shows the saturation magnetization (M_S) obtained for the ZVI and alloy nanocomposites. The M_S value for the ZVI@GO nanocomposite falls between those found for similarly sized ZVI or maghemite NPs [46-50]. In this sense, it reflects the core-shell composition of the deposited ZVI NPs and the relative abundance of each phase, as discussed above. In the case of the different alloy nanocomposites, the M_s decreases in the order FeCo>FeCoNi>FeNi. The obtained trend matches the one observed for bulk metallic Fe (218 emu/g)>Co (161 emu/g)>>Ni (54 emu/g) M_S values [51].

The fact that the obtained saturation magnetization values are lower than those for the bulk ferromagnetic metals can be explained by the reduced sizes of the deposited NPs. Indeed, it is considered that NPs possess a disordered magnetic spin layer at their surfaces [52]. As the NPs size decreases, the disordered layer to NPs radius ratio becomes significant. Such surface spin disorder reduces the M_S value for smaller nanoparticles [53]. Nonetheless, the observed trend clearly shows that as the amount of Fe and/or Co increases in the alloy NP composition, its M_S becomes larger.

As also shown in Table 5, the FeCo alloy shows larger intrinsic coercivity (H_c) and remanent magnetization (M_r) values than the FeNi or FeCoNi alloys. This can be attributed to the higher content of Co in the corresponding FeCo binary alloy. Indeed, Co has the largest intrinsic coercivity and remanent magnetization [54]. Therefore, higher Co contents in a particular alloy increase its H_c and M_r values, as observed for the FeCo@GO nanocomposite.

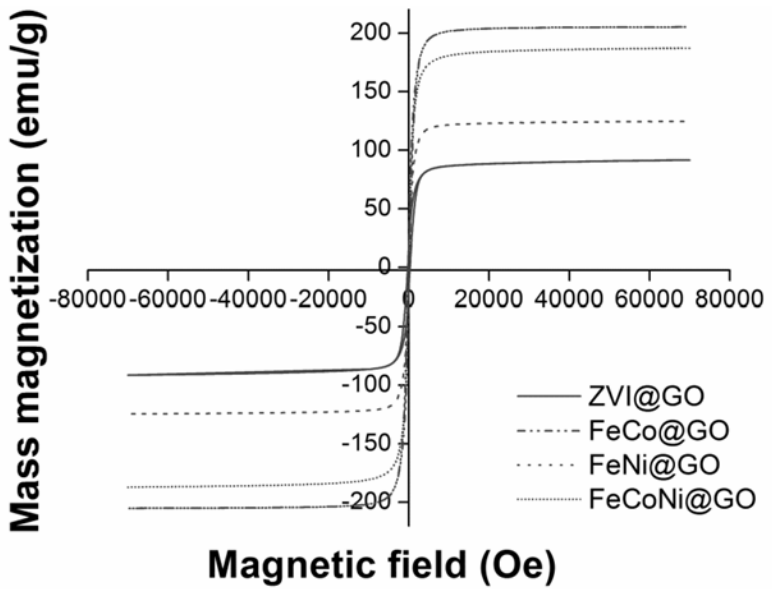

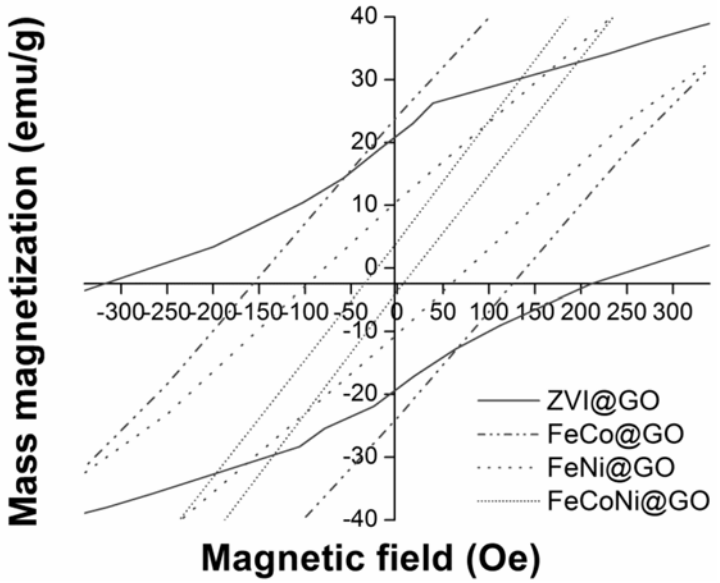

Figure 14 - ZVI and Fe/Co/Ni alloy nanocomposites M_s (top), H_c and M_r values (bottom) obtained from full magnetization curves recorded against an applied magnetic field at 300K. A loading rate of 50 wt.% metal/GO was aimed at in all cases.

Table 5 – Magnetic properties at 300 K of the ZVI and Fe/Co/Ni alloy nanocomposites. A loading rate of 50 wt. % was aimed at, in all cases.

Nanocomposite	SPL[(1)] (nm) [55, 56]	% NPs < SPL[(2)]	M_S (emu/g)	M_r (emu/g)	H_c (Oe)
ZVI@GO	~17	83%	91	20	265
FeCo@GO	~22	90%	205	24	141
FeNi@GO	~30	84%	124	11	78
FeCoNi@GO	-	-	187	4	21

(1) Superparamagnetic limit
(2) Percentage of NPs whose size is below the superparamagnetic limit

4.3 Conclusions

Using the Pechini sol-gel method, graphene oxide was decorated with ZVI@maghemite or Fe/Co/Ni alloys@carbon core@shell nanoparticles.

ZVI and FeCo, FeNi, or FeCoNi alloys were clearly identified in the different synthesized samples. In this study, only equimolar binary and ternary Fe/Co/Ni ratios were obtained. Elemental composition results prove that our method allows for a tight control of the deposited alloy NPs elemental composition. Core-shell structures were observed in the four different nanocomposites. Nonetheless, their composition varied. Indeed, in the case of metallic iron, the shell was found to be composed of maghemite (γ-Fe_2O_3) while graphitic carbon was found surrounding the different alloy NPs. This result ensures that the deposited alloy NPs will be protected against air-driven oxidation processes.

Certain synthetic parameters, such as the molar citric acid to ethylene glycol ratio (CA:EG) and the molar citric acid to metal ratio (CA:M), were systematically studied in order to determine their influence on the deposited NPs spatial distribution and size. It was found that the deposited NPs distribute more homogeneously over the nanocarbon surface when ethylene glycol and citric acid are used in similar quantities (1:1 and 1:1.5 ratios). These lower CA:EG ratios also create smaller NPs with narrower size distributions. Nonetheless, under the same synthetic conditions, ZVI NPs presented a monomodal size distribution while bimodal distributions were observed in the three different types of alloy NPs.

The magnetic properties of the different nanocomposites were also studied. All nanocomposites were found to be ferromagnetic at room temperature. Other properties such as saturation magnetization (M_s), the intrinsic coercivity (H_c) and the remanent magnetization (M_r) varied according to the chemical nature of the deposited NPs.

4.4 Bibliography

1. X. Zhao, Z. Zhang, L. Wang, K. Xi, Q. Cao, D. Wang, Y. Yang and Y. Du, *Sci. Rep.*, 2013, **3**, 3421.
2. J. Fang, W. Zha, M. Kang, S. Lu, L. Cui and S. Li, *Mater. Sci.*, 2013, **48**, 8060–8067.
3. B-J Kim, K-M Bae, Y.S. Sil Lee, K-H Ana and S-J Park, *Surf. Coat. Tech.*, 2014, **42**, 125-131.
4. J. Xiang, J. Li, X. Zhang, Q. Ye, J. Xu and X. Shen, *J. Mater. Chem. A*, 2014, 2, 16905-16914.
5. G. Liu, W. Jiang, D. Sun, Y. Wang, F. Li, *Appl. Surf. Sci.*, 2014, **314**, 523-529.
6. Pechini, Maggio P. Sprague Electric Co, assignee. Patent US3330697 A. 11 July 1967.
7. M. Galceran, M. C. Pujol, M. Aguiló, and F. Díaz, *J. Sol-Gel Sci. Techn.*, 2007, **42**(1), 79–88.
8. Yu, K., Shi, Z.-X., Qian, S.-M. Gongneng Cailiao, *J. Funct. Mater.*, 2005, **35**(SUPPL.), 898-902+906,
9. M. E. Amano, I. Betancourt, M. J. Arellano-Jimenez, J. L. Sánchez-Llamazares, and C. F. Sánchez-Valdés, J. *Sol-Gel Sci. Techn.*, 2015, **78**(1), 1–7
10. Y. Lu, L. Chen, Y. Li, Y. Huang, H. Cheng, and H. J. Seo, *J. Nanopart. Res.*, 2015, **17**(10), 405.
11. M. Hajizadeh-Oghaz, R. S. Razavi, M. Barekat, M. Naderi, S. Malekzadeh, and M. Rezazadeh, *J. Sol-Gel Sci. Techn.*, 2016, **78**(3), 682–691.
12. E. Danks, S. R. Hall, and Z. Schnepp, Mater. Horiz., 2016, **3**, 91–112.
13. N.L.V. Carreño, M.T. Escote, A. Valentini, L. McCafferty, V. Stolojan, M. Beliatis, C.A. Mills, R. Rhodes, C.T.G. Smith, and S.R.P. Silva, *Nanoscale*, 2015, **7**(41), 17.
14. E. Ye, B. Liu and W. Y. Fan, *Chem. Mater.*, 2007, **19**(15), 3845–3849.
15. Cornell, R.M. and Schwertmann, U. The iron oxides. Structure, properties, reactions, occurrences and uses (2nd ed). Wiley-VCH; Darmstadt, Germany, 2003. p. 365-367.
16. C. Wang, F-Y Kang, J-L Gu, *J. Inorg. Mater*, 2010, **25**(4), 408-410.
17. V. Petrykin and M. Kakihana. "Chemistry and applications of polymeric gel precursors" in Handbook of Sol-Gel Science and Technology: Processing, Characterization and Applications. Ed. Sumio Sakka. Kluwer Academic Publishers: London, United Kingdom. 2005. 77-104.
18. A. Mashreghi and F. Davoudi, *Mater. Sci. Semicond. Process.*, 2015, **30**, 618–624.
19. X. Li, V. Agarwal, M. Liu, and W. S. Rees, *J. Mater. Res.*, 2000, **15**(11), 2393–2399.
20. M. Z. Kassaee, E. Motamedi, and M. Majdi, *Chem. Eng. J.*, 2011, **172**(1), 540–549.
21. F. Tuz Johra, J-W. Lee, W-G Jung, *J. Ind. Eng. Chem.*, 2014, **20**(5), 2883–2887.
22. L. Stobinski, B. Lesiak, A. Malolepszy, M. Mazurkiewicz, B. Mierzwa, J. Zemek, P. Jiricek, and I. Bieloshapka, *J. Electron Spectrosc.*, 2014, **195**, 145–154.
23. R. Ray, S. Das, M. Patra and M. Thakur, *Nanoscience Methods*, 2012, **1**, 1-8.

24. I. N. Zakharova, M. A. Shipilin, V. P. Alekseev and A. M. Shipilin, *Tech. Phys. Lett.*, 2012, **38**(1), 55-58.
25. B. Wei, M. Shima, R. Pati, S. K. Nayak, D. J. Singh, R. Ma, Y. Li, Y. Bando, S. Nasu and P. M. Ajayan, *Small*, 2006, **2**, 804-809.
26. J. M. Vargas, L. M. Socolovsky, G. F. Goya, M. Knobel and D. Zanchet, *IEEE Trans. Magn.*, 2003, **39**, 2681-2683.
27. N. N. Greenwood and T. C. Gibb, in Mössbauer Spectroscopy, Springer Netherlands: Dordrecht, the Netherlands, 1971. pp. 239-303.
28. A.P. Grosvenor, B.A. Kobe and M.S. McIntyre, *Surf. Sci.*, 2004, **565**, 151-162.
29. H. Wise and J. Oudar, Material Concepts in Surface Reactivity and Catalysis, Dover Publications INC: New York, USA, 1990. p.199-238.
30. Fe reference Powder Diffraction File (PDF) 00-006-0696 (2017) ; γ-Fe_2O_3 reference PDF 00-039-1346 (2017).
31. A.T. Balaban and D.J. Klein, *Carbon*, 1997, **35**(2), 247-251.
32. ASM Handbook Volume 3: Alloy Phase Diagrams. Eds. H. Okamoto, M. E. Schlesinger, E. M. Mueller. ASM International: Ohio, United States of America, 1992.
33. E.P. Wohlfarth, Ferromagnetic materials: a handbook on the properties of magnetically ordered substances, Vol.2. North Holland Pub. Co.: Amsterdam, The Netherlands, 1999.
34. FeCo reference Powder Diffraction File (PDF) 00-049-1568 (2017) ; FeNi reference PDF 04-009-3507 (2017); FeCoNi reference PDF 04-016-6385 (2017).
35. B. de Mayo, D. W. Forester, and S. Spooner, J. Appl. Phys., 1970, 41, 1319.
36. A. Narayanasamy, T. Nagarajan, P. Muthukumarasamy and T.N. Radhakrishnan, *J. Phys. F: Met. Phys.*, 1979, **9**, 2261.
37. D. Kodama, K. Shinoda, K. Sato, Y. Konno, R.J. Joseyphus, K. Motomiya, H. Takahashi, T. Matsumoto, Y. Sato, K. Tohji, B. Jeyadevan, *Adv. Mater.*, 2006, **18**, 3154.
38. A. Djekoun, B. Bouzabata, A. Otmani and J. M. Greneche, *Catal. Today*, 2004, **89**, 319-323.
39. A. Guittoum, A. Layadi, A. Bourzami, H. Tafat, N. Souami, S. Boutarfaia and D. Lacour, *J. Magn. Magn. Mater.*, 2008, **320**, 1385-1392.
40. H. N. Ok and M. S. Han, *J. Appl. Phys.*, 1973, **44**, 1932-1933.
41. A. Guittoum, A. Layadi, A. Bourzami, H. Tafat, N. Souami, S. Boutarfaia and D. Lacour, *J. Magn. Magn. Mater.*, 2008, **320**, 1385-1392.
42. C. M. dos Santos, A. F. Nogueira Martins, B. C. Costa, T. Soares Ribeiro, T. Pinheiro Braga, J. M. Soares, J. M. Sasaki, *J. Nanomater.*, 2016, **2016,** 1637091.
43. T. Shinjo, F. Itoh, H. Takaki, Y. Nakamura and N. Shikazono, *J. Phys. Soc. Jpn.*, 1964, **19**, 1252-1252.
44. M. Shinga, Y. Maeda, and Y. Nakamura, *J. Phys. Soc. Jpn.*, 1974, **37**, 363-370.
45. A. P. Douvalis, R. Zboril, A. B. Bourlinos, J. Tucek, S. Spyridi, and T. Bakas, *J. Nanopart. Res.*, 2012, **14**(9), 1130.
46. P. Vanýsek, "Electrochemical Series" in Handbook of Chemistry and Physics: 93rd Edition. Ed. William M. Haynes. Chemical Rubber Company Press: Boca Raton, United States of America, 2012. 5–80.
47. W. Baaziz, B.P. Pichon, S. Fleutot, Y. Liu, C. Lefevre, J-M. Greneche, M. Toumi, T. Mhiri and S. Begin-Colin, *J. Phys. Chem. C*, 2014, **118**(7), 3795–3810.
48. X. Liu, B. P. Pichon, C. Ulhaq, C. Lefèvre, J.-M. Grenèche, D. Bégin, and S. Bégin-Colin, *Chem. Mater.*, 2015, **27**, 4073–4081.
49. H. Kura, M. Takahashi and T. Ogawa, *J. Phys. Chem. C*, 2010, **114**(13), 5835-5838.
50. C.J. Serna and M.P. Morales "Maghemite (γ-Fe_2O_3): a versatile colloidal material" in Surface and Colloid Science, Ed. E. Matijevic and M. Borkovec, Springer US: New York, USA, 2004. p. 27-81.

51. B.D. Culity and C.D. Graham, Introduction to magnetic materials, IEEE Press: Piscataway, NJ, USA, 2009. p.531.
52. R.H. Kodama, *J. Magn. Magn. Mater.*, 1999, **200**, 359-372.
53. A.G. Kolhatkar, A.C. Jamison, D. Litvinov, R.C. Willson and T. R. Lee, Int. *J. Mol. Sci.*, 2013, **14**, 15977-16009.
54. K.E. Marusak, A.C. Johnston-Peck, W-C. Wu, B.D. Anderson and J.B. Tracy, *Chem. Mater.*, 2017, **29**, 2739-2747.
55. F. Mazaleyrat, M. Ammar, M. LoBue, J.-P. Bonnet, P. Audebert, G.-Y.Wang, Y. Champion, M. Hÿtch, E. Snoeck, *J. Alloy Compd.*, 2009, **483**, 473-478.
56. A.P. Guimarães, Principles of nanomagnetism, Springer-Verlag: Berlin, Germany, 2009.

chapter 5

Decoration of multi‐walled carbon nanotubes with zero‐valent iron and cobalt nanoparticles

In this chapter, we present two new types of nanocomposites based on MWCNTs decorated with zero‐valent iron (ZVI) or cobalt nanoparticles. The former type of nanocomposite was obtained by a thermal decomposition reaction of the cyclopentadienyliron dicarbonyl dimer complex. The latter was produced by following the solvothermal ambient‐pressure methodology presented previously for the Ni@MWCNTs nanocomposites.

Related publications

J. Mahin, 2016, **Synthesis of iron-based nanoparticles supported on nanocarbons for the production of metamaterials**, UCLouvain, Master Thesis.

A. Wolf, 2016, **Métamatériaux à base de nanoparticules magnétiques supportées sur structure nanocarbonée dans une matrice polymérique**, UCLouvain, Master Thesis.

Collaborators

Julien Mahin (IMCN/MOST) and Arnaud Wolf (IMCN/MOST).

In the previous chapters, we have shown how different synthetic techniques can be used to decorate various nanocarbon supports, such as MWCNTs, with diverse ferromagnetic or ferrimagnetic NPs. However, when compared to other magnetic NPs (MNPs), ferromagnetic metallic Fe, Co or Ni NPs have higher saturation magnetization (M_s) and thus higher magnetic permeability (μ) values. Therefore, their respective MNP@MWCNTs nanocomposites should allow fabricating more efficient MAMs [1], one of this research project's main objectives. Nevertheless, bare metallic MNPs, and more particularly zero-valent iron (ZVI) NPs, are sensitive to aerial oxidation. Therefore, an inert carbon shell is often added to protect the air-sensitive NPs [2].

In Chapter 3, we presented the results obtained for the decoration of MWCNTs with metallic NiNPs. These nanocomposites were obtained by using either an ambient pressure or an autoclave solvothermal method (see sections 3.2.1 and 3.2.2 respectively) which produced very different NiNPs size distributions. Interestingly, the former synthetic approach produced NiNPs covered by what seemed to be a protective carbonaceous layer. We thus decided to test the ambient pressure solvothermal approach with a cobalt precursor in order to obtain analogous Co@MWCNTs nanocomposites.

Likewise, in Chapter 4, we showed what could be achieved by using a sol-gel Pechini type technique for the decoration of graphene oxide (GO) with ZVI and Fe/Co/Ni alloy NPs. Even though we clearly proved that the alloy NPs were surrounded by a graphitic shell, we were not able to observe such a protective layer in the case of the ZVI NPs. Therefore, in this chapter, we shall discuss the results obtained by switching our synthetic approach towards a thermal complex decomposition reaction inspired by the work of McCafferty *et al.* [3].

Indeed, these researchers claim to have obtained carbon-protected ZVI@MWCNTs by mixing the MWCNTs and a cyclopentadienyliron

dicarbonyl dimer complex [$Fe_2Cp_2(CO)_4$], followed by heating in a tubular furnace at high temperatures under inert atmosphere. A few other similar procedures exist [4-6] but none that allows to deposit protected ZVI@C core-shell NPs on MWCNTs in a single step.

5.1 Materials and methods

5.1.1 Materials and characterization techniques

NC3100 multi-walled carbon nanotubes (MWCNTs, 95%C purity) were obtained from Nanocyl (Belgium). All other reactants were supplied by Bayer Material Science, Alfa Aesar or VWR and used as received. More details on each reactant are provided in Appendix I, while the different physicochemical characterization techniques employed are described in Appendix II.

5.1.2 Synthesis of MNPs@MWCNTs nanocomposites

The two synthetic techniques employed to produce the ZVI@MWCNTs and Co@MWCNTs nanocomposites will be briefly presented below.

5.1.2.1 ZVI@MWCNTs nanocomposites produced by ambient pressure (AP) complex decomposition

In a typical procedure, a solution of 1 g of cyclopentadienyl iron dicarbonyl dimer complex [$Fe_2Cp_2(CO)_4$] in 20 mL tetrahydrofuran (THF) was prepared. Meanwhile, 100 mg of MWCNTs were placed in a ceramic combustion boat. The engaged quantities of complex and MWCNTs aimed at producing a final Fe/C % loading rate (% LR) of 315%.

The complex solution and the MWCNTs were then mixed using a dry impregnation technique. Such a methodology consists in adding the liquid to the solid, drop by drop, until the former was no longer absorbed by the latter. Throughout this operation, the MWCNTs were continuously tossed with a metallic spatula. Once the solvent

evaporated and the paste dried out, addition of the liquid was resumed until the entire solution volume was added.

Afterwards, the combustion boat was placed in a tubular oven and heated to 900°C under Ar/H_2 (95%/5%) atmosphere for 4 hours. The temperature was increased and decreased at a rate of 100°C/hour.

The powder was extracted from the oven and placed in a glass vial. Sufficient concentrated hydrochloric acid (HCl, 37% w/w) was then added so as to completely cover the powder. The mixture was capped and left to stand for 24 hours. Afterwards, the powder was separated from the acidic supernatant by magnetic decantation and washed 5 times with 30 mL of ethanol. Finally, it was dried in a vacuum drying oven at room temperature overnight and stored in air with no special precautions.

5.1.2.2 Co@MWCNTs nanocomposites produced by ambient pressure solvothermal synthesis

A similar methodology to that described in section 3.1.2.1 for the AP Ni@MWCNTs nanocomposites synthesis was followed to solvothermally decorate MWCNTs with Co NPs. Indicated reactant proportions aim at obtaining a Co/C mass loading rate (LR) of 50%.

MWCNTs (100 mg) were placed in a two-necked round-bottom flask. 76 mL of ethylene glycol (EG) were added and the suspension was sonicated for 120 minutes. Afterwards, 640 mg of polyvinylpyrrolidone (M.W. 10 000, PVP-10 000) were added, under vigorous stirring, to obtain a 8 mg/L capping agent concentration. After complete dissolution of PVP, the suspension pH was set at 7 by adding an aqueous 1M NaOH solution dropwise. A reflux condenser was mounted on the central neck while the other was capped with a rubber septum. Subsequently, the suspension was heated up to 230 °C in an oil bath.

Separately, 211 mg of cobalt (II) acetate tetrahydrate ($Co(CH_3COO)_2.4H_2O$) were added to 4 mL EG and vigorously stirred until the salt was completely dissolved. The solution was then transferred into a syringe. By using a syringe pump (kdScientific, USA), it was added dropwise to the former hot suspension at a speed of 4 mL/h, under stirring. Overall, the reaction mixture was heated for 15 hours.

Reaction products were then separated from the reaction medium by magnetic decantation and then recovered by filtration over a PVDF filter (Millipore GVWP02500, 0.22 μm pore size). Afterwards, they were purified by rinsing six times, alternating Milli-Q water and ethanol. Finally, they were dried under vacuum at room temperature, for 12 hours.

The as-obtained powders were then thermally annealed in order to promote particle growth by sintering. The samples were placed in a porcelain combustion boat and heated up to 500°C for 2h, under Ar/H_2 95/5 atmosphere, in a tubular furnace (Carbolite Gero STF16, United Kingdom). The temperature was increased and decreased at a rate of 100°C/hour. The recovered powder was stored in air with no special precautions.

5.2 Results and discussion

Results obtained for the new ZVI@MWCNTs and Co@MWCNTs nanocomposites syntheses will be briefly discussed below. As with the other nanocomposites presented in Chapters 2 through 4, special emphasis will be given to the impact of different experimental conditions on the MNPs composition, size and spatial distribution over the MWCNTs surface.

5.2.1 Characterization of the ZVI@MWCNTs nanocomposites produced by thermal decomposition

In order to produce ZVI@MWCNTs nanocomposites, the nanocarbon support was impregnated with a solution containing a large amount of iron cyclopentadienyl dicarbonyl dimer complex [$Fe_2Cp_2(CO)_4$]. Following impregnation, the mixture was heated to 900°C under an Ar/H_2 (95/5%) atmosphere, during which carbon-capped Fe° nanoparticles should form.

The size and spatial distribution of the deposited NPs were investigated by TEM microscopy. As shown in Figure 1, left, the NPs possess a wide size distribution, ranging from about twenty to several hundredths of nanometers. This might be due to the high Fe-precursor concentrations and/or temperatures used during the thermal decomposition reaction [3].

Higher magnification inspection of the nanocomposite powders revealed the presence of a lighter shell layer surrounding the NPs (see Figure 1, right). In the work of McCafferty *et al.* [3], such shell layers have been characterized as being composed of carbon, partly amorphous, partly graphitic.

The formation mechanism of such a carbon shell surrounding metallic NPs has been reviewed by Moisala *et al.* [7]. According to these authors, the complex ligands decompose and form carbon monoxide (CO). Given the high temperature used in the synthesis, CO disproportionation is prohibited so that the only thermodynamic and kinetic likely process is the dissolution of carbon into the forming Fe NPs. This dissolution process yields a carbon-saturated Fe NP. The slow cooling of such NPs, as used in this synthetic methodology, favors the segregation of carbon towards the NP surface. Layers of carbon are thus produced around the NPs.

The obtained powder was also characterized by XRPD. As shown in Figure 2, the recorded spectrum shows three distinctive sets of reflections. The first one is broad, centered around 12° 2θ and is most possibly due to either the ordered arrangement of the MWCNTs' concentric cylinders of graphitic carbon [8] or the presence of the graphitic shell around the Fe NPs. The second set is composed of two intense reflections at ~20° and 45° 2θ values which can be attributed to iron's body-centered cubic (bcc) phase. Finally, a series of less intense reflections at 2θ ~17° and 22° indicate that a cementite (Fe_3C) phase is also present. Considering the relative intensity of the bcc-Fe and cementite reflections, it seems that the former phase is more abundant than the latter.

The presence of the Fe_3C phase in the ZVI@MWCNTs nanocomposite can be explained by the carbon dissolution process into the Fe NPs, as explained above. Indeed, during this dissolution, various Fe-C alloys can form. However, under the employed reaction conditions, cementite is formed prevalently given it is the thermodynamically most favorable iron carbide [9]. However, the coexistence of Fe, C and Fe_3C as found in the deposited ZVI@carbon core-shell NPs is unexpected. Indeed, at room temperature, the thermodynamic equilibrium favors exclusively the formation of bcc-Fe and C phases [9]. Even though numerous authors have made similar findings when synthetizing carbon-coated FeNPs at high temperatures [2, 10-12], the persistence of this metastable phase at room temperature in the nanoscale has not yet been explained.

Interestingly, as opposed to the results published by McCafferty *et al.* [3], no crystalline iron oxide phase was detected by XRPD. This notable difference might be due to the highly reductive reaction atmosphere (Ar/H_2, 95/5%) used in our synthetic methodology as compared to theirs (*e.g.* 100% N_2).

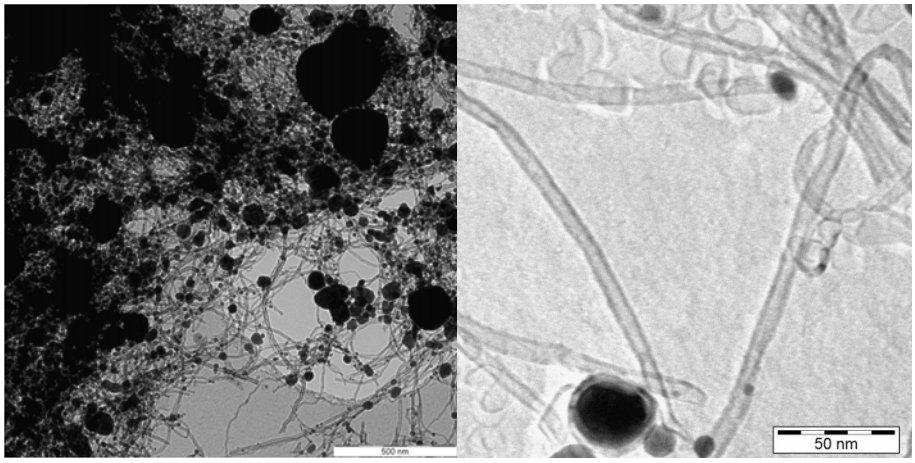

Figure 1 - TEM images showing the typical aspect of the obtained ZVI@MWCNTs nanocomposites and the wide distribution of the deposited Fe NPs sizes (left). Higher magnification inspection of the products (right) revealed the presence of a lighter shell layer surrounding the NPs.

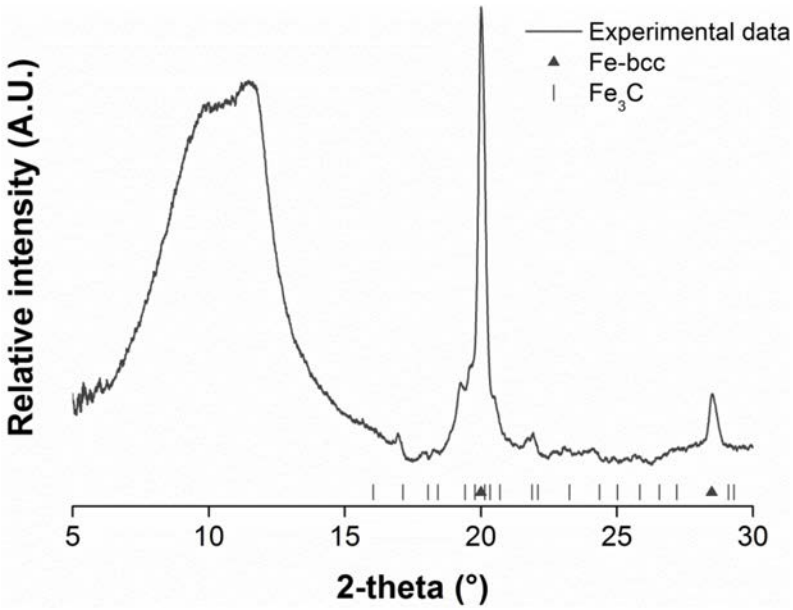

Figure 2 – XRPD diffractogram of the ZVI@MWCNTs nanocomposite after the thermal decomposition reaction.

5.2.1.1 ZVI@MWCNTs resistance to hydrochloric acid etching

In order to test the protection efficiency of the carbon shell layers, we decided to expose the as-obtained ZVI@MWCNTs nanocomposite powders to concentrated hydrochloric acid for 24 hours. The resultant solution acquired a yellowish tinge and bubbling could be observed, reactions that can be attributed to the oxidation and dissolution of iron. Nonetheless, the whole powder retained a response to an external magnetic field.

Altogether, these observations seemed to indicate that a partial dissolution of the deposited ZVI NPs took place. TGA confirmed such partial dissolution by revealing a tenfold drop, in the % Fe/C loading rate (%LR), from 328% to 29%, after the acidic wash. XRPD investigation of the recovered powders also showed a decrease in the intensity of the bcc-Fe reflections (see Figure 3). On the contrary, the reflections assigned to the cementite phase became more evident, as a result of the carbide's resistance to HCl dissolution. Therefore, the acidic treatment enriched the ZVI@MWCNTs nanocomposites in their cementite content.

TEM characterization of the nanocomposite powder after the acidic treatment confirmed likewise the partial dissolution of the ZVI NPs. Moreover, it surprisingly revealed that such dissolution was somewhat size-selective. Indeed, the larger particles disappeared while the smaller ones remained, distributed homogeneously over the MWCNTs surface (see Figure 4). It was also found that the remaining NPs size distribution narrowed down to 14.9 ± 4.9 nm. Alongside the smaller NPs, large lightly-colored structures were observed, attached to the MWCNTs (see Figure 5). As shown in Figure 6, SEM investigation of

these objects seem to indicate that they are the empty carbon shells of the largest nanoparticles in which the ZVI core was dissolved by HCl.

Our hypothesis explaining such a dramatic difference after acid washing is that the carbon protection layer is complete and uniform only around the smaller nanoparticles. The shell of the larger ones is probably incomplete and/or presents defects or holes, allowing the acid to penetrate towards the metallic core. Hence these are found empty after acid etching. Imperfect coatings have already been observed by researchers producing carbon shells around metallic MNPs [3, 10]. As explained by Moisala *et al.* [7], this is most probably due to a poor diffusion of carbon towards the nanoparticle surface. As the deposited ZVI NPs get larger, diffusion is hindered and the formed carbon shell is most probably incomplete and/or imperfect.

When the acid etching treatment was repeated onto different ZVI@MWCNTs batches, we observed that the obtained NPs size distributions were similar. We thus implemented systematically the HCl bath as a way of post-synthetically controlling the deposited NPs size distribution, and quality of carbon coating, for further use of these materials in MAM applications (see Chapter 8).

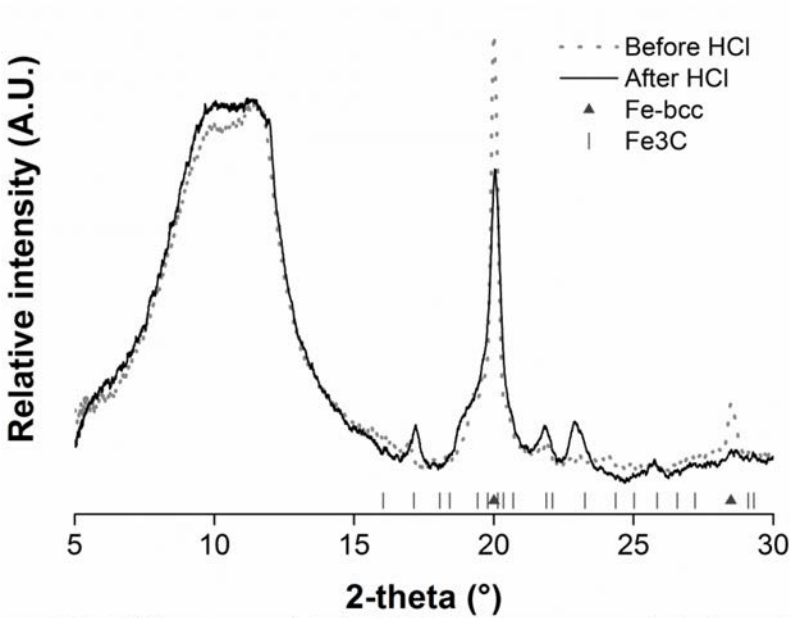

Figure 3 - XRPD diffractogram of the ZVI@MWCNTs nanocomposite before and after HCl etching.

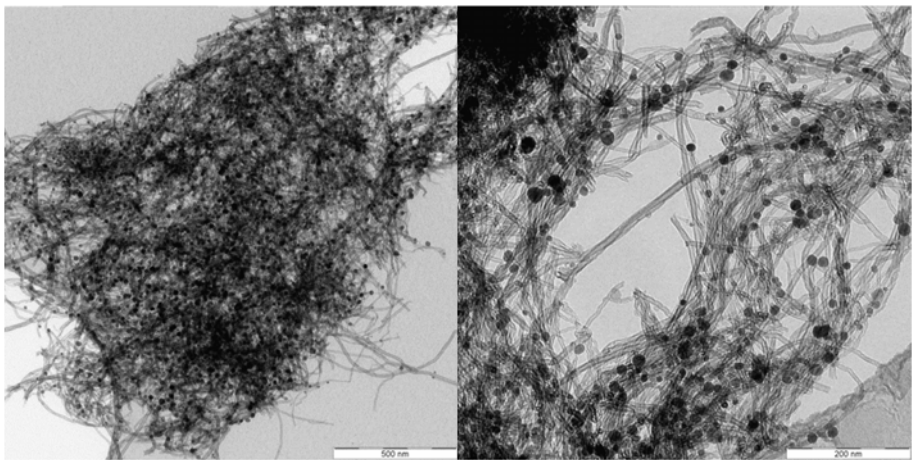

Figure 4 - TEM images showing the typical aspect of the ZVI@MWCNTs nanocomposite after HCl treatment (left). A higher magnification inspection revealed the narrower size distribution of the undissolved ZVI NPs (right).

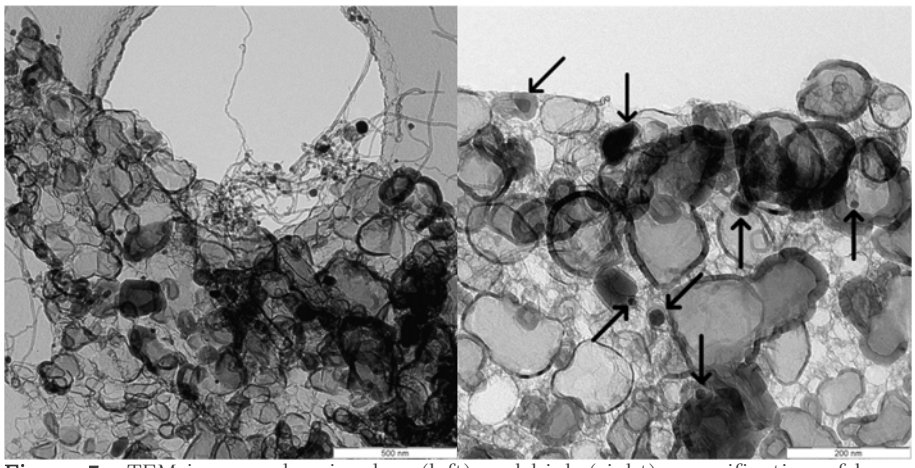

Figure 5 - TEM images showing low (left) and high (right) magnification of large, lightly-colored structures (empty carbon vesicles) attached to the MWCNTs found alongside the undissolved ZVI NPs after HCl etching (indicated by black arrows).

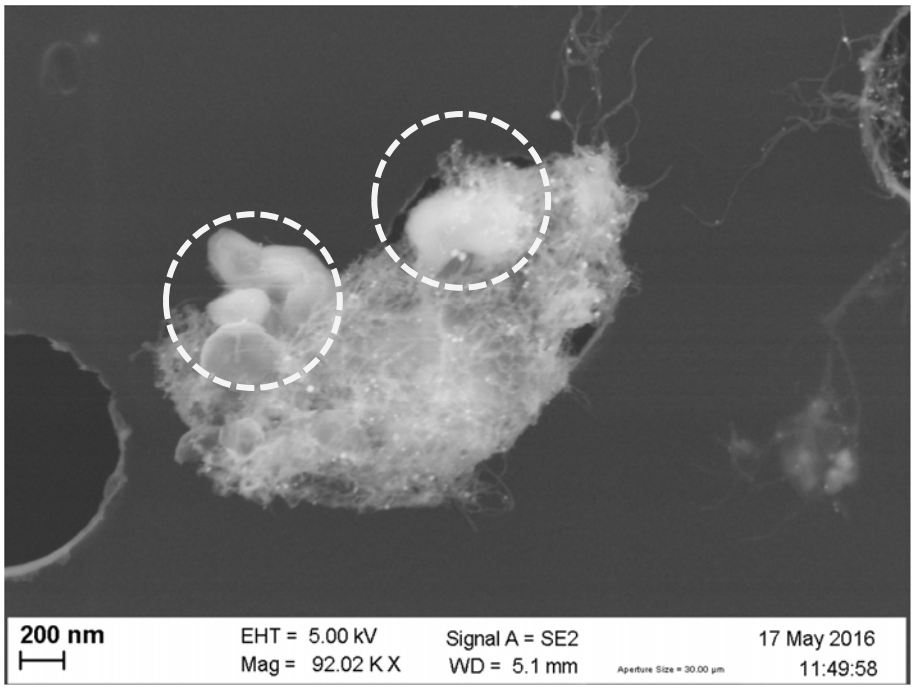

Figure 6 - SEM image of a ZVI@MWCNTs nanocomposite after HCl treatment. The white dashed circles indicate what seem to be the empty carbon shells that once covered the largest ZVI NPs dissolved by HCl.

5.2.2 Characterization of the Co@MWCNTs nanocomposites produced by ambient pressure (AP) solvothermal synthesis

The solvothermal strategy employed to decorate MWCNTs with CoNPs was in many ways similar to that described in section 3.1.2.1 for the AP Ni@MWCNTs nanocomposite. However, some changes had to be implemented in order to obtain the desired product.

The first one was the pH at which the solvothermal reaction was performed. In this case, a neutral reaction medium (pH=7) was employed, instead of the basic conditions used for the Ni@MWCNTs synthesis (pH=10). As shown in Appendix IV.2, the neutral pH value was chosen to favor the formation of the metallic cobalt phase according to the Pourbaix diagram for the Co system [13].

The second change concerns the choice of the cobalt salt precursor. Initially, a chloride precursor ($CoCl_2 \cdot 6H_2O$) was employed, as for the Ni@MWCNTs products. However, the obtained nanocomposite was unreactive to an external magnetic field. It was thus decided to use cobalt acetate tetrahydrate ($Co(CH_3COO)_2 \cdot 4H_2O$). Indeed, when considering the reduction mechanism of metallic salt precursors by ethylene glycol studied by Joseyphus *et al.* [14] and finally elucidated by Matsumoto *et al.* [15], it is clear that the cobalt acetate salt should be favored over its chloride counterpart. These authors have shown that the active species in this reduction reaction is the monoanion state of ethylene glycol (EG^-) followed by the formation of cobalt ethylene glycoxide. Given the neutral pH conditions employed in this reaction, EG^- can only be formed in the presence of the basic acetate ion. Furthermore, once formed, it must coordinate the cobalt (II) cation in order for cobalt ethylene glycoxide to be formed and the reduction to proceed. Moreover, it has been shown that the chloride anion

coordinates with the Co cation forming comparatively more stable chemical bonds than with the acetate ligand [14, 16]. Thus, it is easier for the cobalt derived from the acetate salt to form a complex with EG^- than when the chloride salt is employed.

When performing the synthesis using $Co(CH_3COO)_2{\cdot}4H_2O$, the nanocomposite powder did react to an external magnetic field. In addition, XRPD characterization of the synthetic product after thermal annealing confirmed that metallic cobalt had been produced during the reaction. The diffractogram presented in Figure 7 shows that the obtained product is mostly composed of face-centered cubic (fcc) crystallites. This crystalline phase is considered metastable at ambient temperature given bulk metallic cobalt prefers to adopt a hexagonal close packed (hcp) crystal structure at temperatures below 415°C. Nonetheless, similar results have been observed by Kitakami *et al.* [17], who also demonstrated that a size-related phase transition from Co-hcp to Co-fcc occurs as the particle size is reduced below 300 Å. As also shown in Figure 7, a faint reflection located around 2θ = 19° indicates the presence of crystalline CoO in the Co@MWCNTs nanocomposite after thermal annealing.

XPS analysis confirmed that the deposited CoNPs contain both metallic and oxidized cobalt (CoOx+CoOx_sat) species (see Figure 8). Similarly to what was discussed in section 3.2.1 for the Ni_{AP} nanocomposite, the oxidized cobalt species are found on the surface in higher concentrations than their metallic counterpart. However, the relative amount of Co^0 is much lower than that of Ni^0 in the AP Ni@MWCNTs nanocomposite, even though both synthetic techniques are very similar.

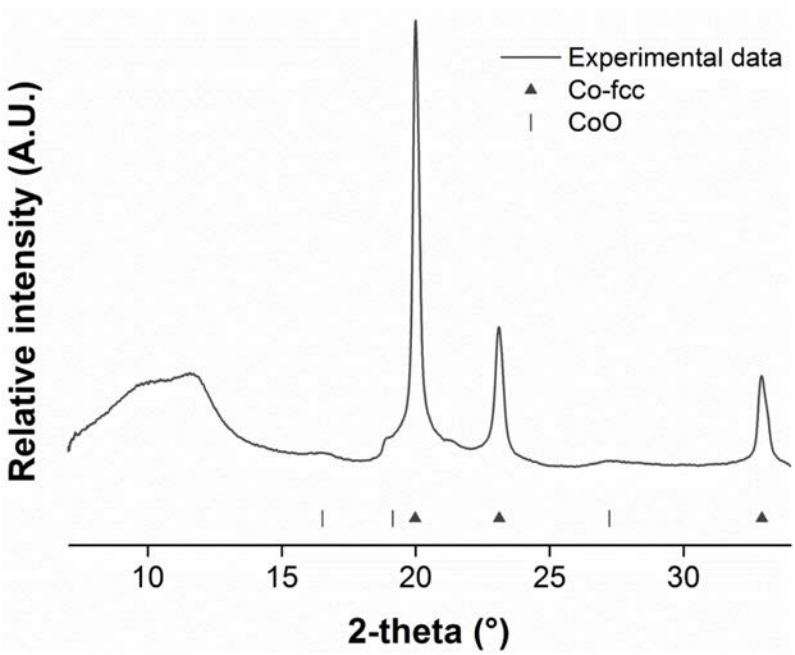

Figure 7 - XRPD diffractogram of the Co@MWCNTs nanocomposite after thermal annealing.

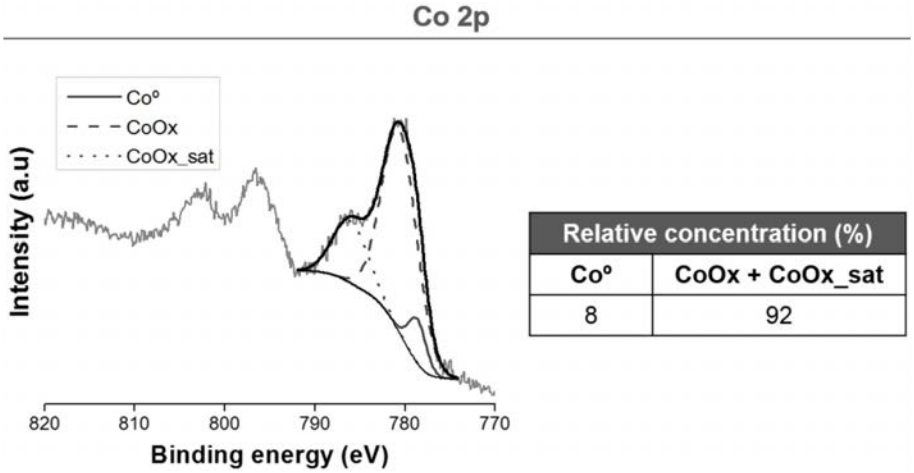

Relative concentration (%)	
Co°	CoOx + CoOx_sat
8	92

Figure 8 - XPS spectrum of the Co 2p peak for the Co@MWCNTs nanocomposite after thermal annealing. The Co 2p3/2 peak has been fitted with three components corresponding to metallic (Co^0) and oxidized (CoOx + CoOx-sat) cobalt.

This might be partly due to cobalt slightly lower reduction potential than that of nickel (E° Co/Co^{2+} = -0.28 V and E° Ni/Ni^{2+} = -0.25 V, according to ref. 18) which makes it more sensitive to oxidation. Furthermore, XPS is a surface analysis technique with a sampling depth of approximatively ~3.7 nm for cobalt oxide or metallic cobalt [18]. Therefore, as stated before, if the cobalt oxide phase is more abundant and found on the surface of the CoNP, as a passivation layer, the relative amount of the CoOx+CoOx_sat components will be enhanced comparatively to that of Co^0.

As with the Ni_{AP} nanocomposite, TEM inspection of the Co@MWCNTs product before thermal annealing showed that the nanotubes were densely covered with extremely small (~1.5 nm) NPs (see Figure 9, top). After thermal annealing at 500°C, the CoNPs grew up to an average size of 24.1 ± 10.0 nm. Thus, compared to the NiNPs in the Ni_{AP} nanocomposite, the deposited CoNPs were larger and possessed a larger size distribution (see Figure 9, middle).

A close inspection of the deposited CoNPs also showed the presence of a thin, lighter shell layer surrounding some of the NPs (see Figure 9, bottom). Arora *et al.* [20] and Chen *et al.* [21] have observed the formation of similar core@shell structures when exposing CoNPs to a thermal treatment. They claim that the shell, mainly composed of carbon, originates from the thermally-induced carbonization of the capping agent employed in the reaction. In this case, it would thus have been formed by the thermal decomposition of PVP-10,000, as discussed for the Ni@MWCNTs nanocomposites (see sections 3.2.1 and 3.2.2.2).

Finally, TGA analysis of the nanocomposite showed that a 39% Co/C loading rate (%LR) was achieved with this synthetic procedure.

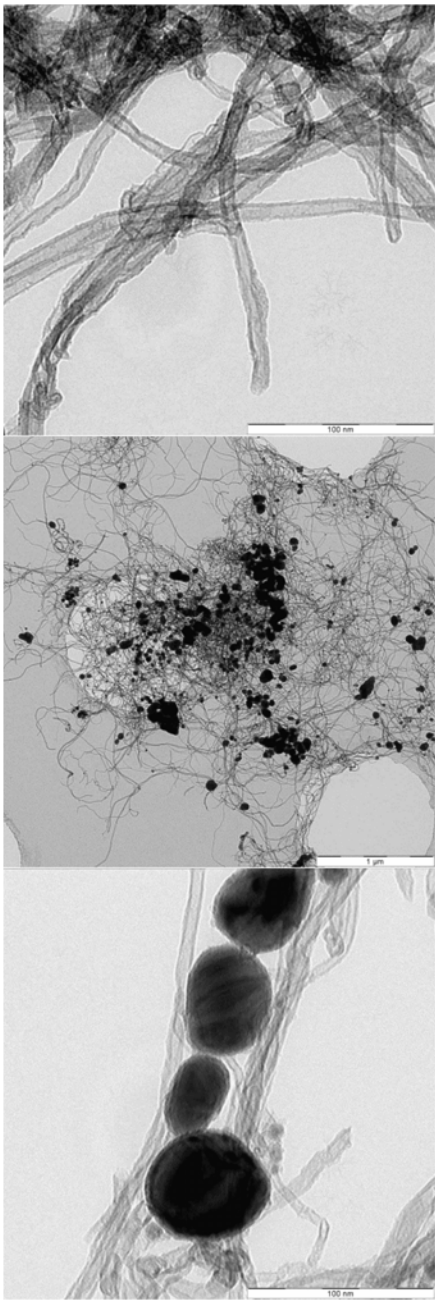

Figure 9 - TEM images showing ultrasmall CoNPs covering the MWCNTs surface after the synthesis (top). Growth of the deposited NPs is achieved by thermal annealing (middle). A thin, lighter shell layer is observed around the nanoparticles (bottom).

5.3 Conclusions

In this chapter, we have shown two synthetic methods allowing to decorate MWCNTs with metallic zero-valent iron (ZVI) or cobalt nanoparticles.

The ZVI@MWCNTs nanocomposite was obtained by thermally decomposing an iron cyclopentadienyl dicarbonyl dimer complex under Ar/H2 (95/5%) atmosphere. XRPD characterization of the nanocomposites allowed to confirm the presence of metallic bcc-iron, alongside a less abundant cementite (Fe3C) phase. TEM investigation of the obtained nanocomposites allowed identifying a lightly-colored shell, possibly composed of carbon, around the ZVI NPs. This shell should offer the ZVI NPs an enhanced protection against aerial oxidation. Nevertheless, the deposited NPs were found to possess a wide size distribution, ranging from about twenty to several hundredths of nanometers. The ZVI NPs size distribution was unexpectedly narrowed down to 14.9 ± 4.9 nm by post-synthetically treating the nanocomposite powders with concentrated hydrochloric acid. This treatment etched the largest ZVI NPs, decreasing by a tenfold factor the Fe/C % loading rate (LR).

A solvothermal strategy, similar to the one used for the NiAP Ni@MWCNTs nanocomposite, was employed to produce a Co@MWCNTs nanocomposite. A neutral pH value, based on the Pourbaix diagram for cobalt, and a suitable cobalt precursor (cobalt acetate tetrahydrate) were chosen to favor the formation of the metallic cobalt phase. XRPD investigation of the obtained nanocomposite confirmed the presence of fcc-Co crystallites, as the main constitutive phase. The solvothermal treatment deposited ~1.5 nm sized CoNPs, which were grown, by thermal annealing at 500°C, up to an average size of 24.1 ± 10.0 nm. As for the ZVI@MWCNTs, TEM inspection of the Co@MWCNTs nanocomposite allowed to detect a light shell surrounding the deposited NPs. This shell, possibly made of carbon, should also protect the CoNPs from aerial oxidation.

Using the synthetic methodologies described in this chapter and in Chapter 3, we are now able to produce MWCNTs decorated with NPs of the three

ferromagnetic transition metals (Fe, Co and Ni). The impact of these different NPs on the microwave absorption properties of MAM films, produced with these nanocomposites, will be further explored in Chapter 8.

5.4 Bibliography

1. L. B. Kong, L. Liu, Z. Yang, S. Li and T. Zhang. "Magnetic materials for electromagnetic wave absorption" in Magnetic nanomaterials: fundamentals, synthesis and applications. Eds. Y. Hou and D.J. Sellmyer. Wiley-VCH Verlag GmbH & Co.: Weinheim, Germany. 2017, pp. 473-514.
2. J. Zhu, S. Pallavkar, M. Chen, N. Yerra, Z. Luo, H.A. Colorado, H. Lin, N. Haldolaarachchige, A. Khasanov, T.C. Ho, D.P. Young, S. Wei and Z. Guo, *Chem. Commun.,* 2013, **49**(3)., 258-260.*
3. L. McCafferty, V. Stolojan, S. G. King, W. Zhang, S. Haq, and S. R. P. Silva, *Carbon*, 2015, **84** (C), 47–55.
4. C. Yu, Y. Sun, X. Fan, Z. Zhao, and J. Qiu, *Part. Part. Syst. Charact.*, 2013, **30**(7), 637–644.
5. R. Snovski, J. Grinblat, and S. Margel, *J. Magn. Magn. Mater.*, 2012, **324**(1), 90–94.
6. E. Hu, X-Y Yu, F. Chen, Y. Wu, Y. Hu and X.W. Lou, *Adv. Energy Mater.*, 2017, **8**(9), 1702476
7. A. Moisala, A.G. Nasibulin and E.I. Kauppinen, *J. Phys.: Condens. Matter*, 2003; **15**(42),:S3011-S3035.
8. Y. Zhang, S. Xiao, Q. Wang, S. Liu, Z. Qiao, Z. Chi, J. Xu and J. Economy, *J. Mater. Chem.*, 2011, **21**, 14563-14568.
9. H. Näfe, *Acta Mater.*, 2009, **57**(14), 4074–4080.
10. V.A. Tsurin, A.Ye. Yermakov, M.A. Uimin, A.A. Mysik, N.N. Shchegoleva, V.S. Gaviko, and V.V. Maikov, *Fiz. Tverd. Tela+*, 2014, **56**(2), 287–300.
11. B. David, N. Pizúrová, O. Schneeweiss, P. Bezdika, I. Morjan, and R. Alexandrescu, *J. Alloys Compd.*, 2004, **378**(1-2), 112-116.
12. Q. Yan, C. Wan, J. Liu, J. Gao, F. Yu, J. Zhang and Z. Cai, *Green Chem.,* 2013, **15**(6), 1631-1640.
13. N. Takeno, Atlas of Eh-pH diagrams: intercomparison of thermodynamic databases. National Institute of Advanced Industrial Science and Technology, Geological Survey of Japan open file report No. 419. Tokyo, Japan, 2005. 287 pp.
14. R.J. Joseyphus, T. Matsumoto, H. Takahashi, D. Kodama, K. Tohji and B. Jeyadevan, *J. Solid State Chem.*, 2007, **180**, 3008-3018.
15. T. Matsumoto, K. Takahashi, K. Kitagishi, K. Shinoda, J.L. Cuya Huaman J.Y. Piquemal and B. Jeyadevan, *New J. Chem.*, 2015, **39**, 5008-5018.
16. L. Poul, S. Ammar, N. Jouini and F. Fievet, *J. Sol-Gel Sci. Technol.*, 2003, **26**, 261-265.
17. O. Kitakami, H. Sato, Y. Shimada, F. Sato and M. Tanaka, *Phys. Rev. B.,* 1997, **56**(21), 13849-13854.
18. P. Vanýsek, "Electrochemical Series" in Handbook of Chemistry and Physics: 93rd Edition. Ed. William M. Haynes. Chemical Rubber Company Press: Boca Raton, United States of America, 2012. 5–80.
19. S. Tanuma, C.J. Powell and D.R. Penn, *Surf. Interface Anal.*, 2011, **43**, 689-713.
20. N. Arora and B. R. Jagirdar, *J. Mater. Chem.*, 2012, **22**, 20671-20679.
21. Y. Chen, K.Y. Liew and J. Li, *Appl. Surf. Sci.,* 2009, **255**, 4039-4044.

part I

summary conclusions

As shown throughout Part I, different solvothermal, sol-gel and thermal decomposition techniques were explored to deposit seven types of ferro and ferrimagnetic nanoparticles onto four different nanocarbon supports. Thanks to these synthetic endeavors, MWCNTs, GNPs, GO or rGO were decorated with iron, cobalt, nickel, their binary (FeCo, FeNi) and ternary (FeCoNi) alloys or magnetite (Fe_3O_4) nanoparticles.

For all three synthetic methods, a lengthy, in-depth study of their governing experimental parameters allowed us identifying how to gain a precise control over the deposited NPs chemical composition, size and loading rates. Obtaining nanoparticles consisting only of the desired chemical phase, with different narrow size distributions and at high NP loading rates were the criteria through which these methods were continuously evaluated. This constant evaluation was performed by the complementary use of nine different characterization techniques. Results thus obtained also allowed linking these physicochemical characteristics to the magnetic properties exhibited by the nanocomposites.

In the case of the solvothermal method, the decoration of different nanocarbon supports with magnetite (MaNPs) or metallic nickel (NiNPs) nanoparticles were used as the main case studies. The impact of the NPs precursor and the speed at which it was added to the system, the reaction temperature, time and pressure, the pH of the system, the degree of oxidation of the NcS, the amount of water in the system, the type and concentration of capping agent and a post-synthetic thermal annealing treatment were all carefully evaluated. By systematically varying these parameters, it was possible to better understand their impact on the physicochemical criteria mentioned above.

This methodology proved to be both, versatile and precise. Indeed, it allowed us to decorate most of the NcS with varying loading rates of phase-pure NiNPs or MaNPs, obtaining reproducible results. Furthermore, it proved to be a reliable technique for the scaled-up, batch production of larger quantities of some of these nanocomposites needed for the MAM prototypes presented in Part III. Finally, in the specific case of NiNPs, we were able to

obtain very different but narrow NP size distributions. The lessons learned during these in-depth studies were transposed with relatively good results to the decoration of MWCNTs with cobalt nanoparticles.

For the Pechini sol-gel method, the deposition of zero-valent iron nanoparticles (ZVI) onto graphene oxide was chosen as the model system. Synthetic parameters such as the molar citric acid to ethylene glycol ratio (CA:EG) and the molar citric acid to metal ratio (CA:M), were systematically varied and evaluated in the same manner as described above. Once the best synthetic conditions were determined (e.g. 1:1.5 CA:EG and 6:1 CA:M ratios, H2/Ar (5/95 %v/v) gas stream at 750 ºC, etc.) they were used to successfully produce three different equimolar binary (FeCo and FeNi) and tertiary (FeCoNi) iron alloy nanoparticles, all deposited onto GO. Interestingly, this method simultaneously produced a graphitic shell surrounding the metallic cores, ensuring the protection of the deposited NPs against air-driven oxidation processes. As compared to other methodologies used to obtain similar materials, the Pechini synthesis is relatively simple to execute. Also, the ease with which the composition of the deposited NPs can be varied to produce binary or tertiary Fe-Co-Ni alloys, with very reproducible results, is remarkable. This is particularly relevant for the ternary FeCoNi nanocomposite, for which only one synthetic report has been published in the scientific literature. However, this methodology offers a poor control over the composition of the obtained product, resulting in a mixture of several binary and ternary alloy phases. We have thus achieved a significative advancement in the controlled production of this type of materials.

The third synthetic methodology used in this research project, involving the thermal decomposition of an iron-complex, was developed to specifically deposit graphite-protected ZVI NPs onto MWCNTs. However, compared to the above-described solvothermal and Pechini methods, this methodology was not investigated in so much depth. Parameters such as the Fe/C loading rates, reaction time or temperature were only rapidly screened. Results obtained with the synthetic parameters described in this manuscript were considered the most reproducible and satisfactory. Nevertheless, the fact that

the control of the deposited ZVI NPs size distribution depends on a post-synthetic acid etching treatment is not optimal. Furthermore, the fact that empty graphitic shells are left attached to the MWCNTs surface, after acid etching, is unsettling. Indeed, we cannot assure that they are completely uninfluential on the conductivity of the nanocomposite, and thus on its overall EM properties.

part

II

unraveling the interactions between microwaves & the MNPs@NcS nanocomposite powders

chapter 6

A novel electromagnetic (EM) characterization method for nanocomposite powders

In this chapter, we present a novel Vector Network Analyzer (VNA) based transmission line (TL) broadband characterization method. It has been developed specifically for this research project in order to retrieve the electromagnetic (EM) properties of lossy nanocomposite powders in the microwave range. Two types of TLs prototypes have been designed and tested, namely a coplanar waveguide (CPW) and a microstrip (MS) setup.

Related publications

F. Mederos-Henry, S. Hermans and I. Huynen. **Coplanar Waveguide Method for Microwave and Ferromagnetic Resonance Characterization of Nanocarbon Powders decorated with Magnetic Nanoparticles.** *Microw. Opt. Technol. Lett.*, 2017, 59(9), 2330–2335.

F. Mederos-Henry, S. Hermans and I. Huynen, **Microwave Characterization of Metal-Decorated Carbon Nanopowders Using a Single Transmission Line**. *J. Nanomater.*, 2019, Article ID 3280461.

Support scientists and technicians

Souley Djandjandi, Rajkumar Jaiswar, Pascal Simon, David Spote, Ester Tooten, Loïc van Oldeneel tot Oldenzeel, Victor Xhurdebise, all members of ICTEAM/ELEN and Winfab & Welcome technological platforms.

Microwave characterization of materials is of prime interest for a number of applications. The knowledge of their electromagnetic (EM) constitutive parameters (e.g. complex permittivity, ε_r, and associated electrical conductivity, σ, or the magnetic permeability, μ_r) is mandatory to design a number of microwave devices such as electromagnetic absorbers, attenuators and resistors.

Over the past years, various characterization methods were proposed using different test cell topologies such as waveguide, coaxial or planar. At microwaves and millimeter waves, the permittivity is derived from the variation of the reflection coefficient [1] measured at the input of a shorted waveguide [2] or a resonant cavity [3] loaded with a solid sample. For liquids or powders, transmission lines (TL) combining transmission and reflection measurements are preferred: they use waveguides or TEM (Transverse Electric Magnetic) transmission lines, coaxial [4] or not [5, 6].

In this research project two TL topologies, namely a coplanar-waveguide (CPW) and a microstrip, were designed and tested. Both test cells allow to directly characterize the as-synthetized nanocomposite powders, without any type of sample preparation. This is a major improvement over current powder EM characterization methodologies [*e.g.* 7-9], in which materials under study must be mixed with a binder such as paraffin in order to facilitate their manipulation. Most commonly, the mixture is transformed into a thin slab of controlled thickness that can then be measured. Nonetheless, as shown in Figure 1, the intensity and frequency of certain microwave phenomena, such as absorption or reflection, are strongly dependent on sample thickness [9]. Under these conditions, the powder's microwave behavior is masked by the sample's thickness-derived effects, as it is impossible to differentiate one from another. By contrast, with our test cells, we can undoubtedly establish that the obtained responses derivate exclusively from the nanocomposites powders under study.

The second main development introduced by our EM characterization methodology relates to the extraction of the magnetic permeability and electric permittivity of the materials under study. Traditional TL methods suffer from strong uncertainties when the test cell's length is a multiple of half-wavelengths since transmission and reflection measurements [10] or reflection measurements only [11] are used to extract the EM parameters.

To overcome these problems and achieve a broadband characterization, we exploited a property of the Line-Return-Line (LRL) self-calibration method [12] that provides as by-product the propagation constant from which the permittivity ε_r is extracted [13]. Our formulation does not include reflection measurements and hence does not suffer from half-wave uncertainties. However, the propagation constant cannot discriminate between permittivity ε_r and permeability μ_r since it involves only their product. ε_r can be extracted for non-magnetic materials only. Hence, we propose to use a single TL, successively measured twice: once empty and once filled with our nanopowders. This combination enables to retrieve the sample's ε_r and μ_r parameters simultaneously, requiring the fabrication of a single TL. The retrieval of ε_r and μ_r is possible by exploiting two different features. Firstly, the permittivity is extracted by combining the empty line measurement with the measurement of the filled line under a high-DC magnetic field. This ensures that the permeability of the material is equal to unity during the measurement. Secondly, the permeability is extracted from the combination of the measurement of the filled line under zero-DC magnetic field and the prior measurement of the empty line.

The EM characterization measurements were performed with a Vector Network Analyzer (VNA) instrument as described by Huynen *et al.* [14]. Even though this technique has been widely used for the analysis of electrical circuits operating at high frequencies, it is definitely not a common characterization tool used by chemists. Thus, a brief explanation of the principles governing this instrument will be given below before introducing the extraction methodology and the test cell fabrication methods.

6.1 Vector Network Analyzer (VNA) instrumentation and experimental setup

VNAs are able to measure the four scattering or S-parameters (S_{11}, S_{22}, S_{12} and S_{21}) that account for either the reflection or transmission of a microwave signal by a sample-filled test cell, also called Device under test (DUT). To do so, a microwave of power P_s with a frequency sweeping over a determined range, is delivered to the DUT by means of two ports conventionally named "port 1" and "port 2".

The VNA microwave source switches to deliver the microwave either at port 1 or at port 2, thus allowing to characterize the reflection and transmission of signals through the DUT in two directions, from port 1 to port 2 and vice versa. Thus, the S_{21} and S_{12} parameters denote the fraction of the wave's power that is transmitted through the DUT, either from port 1 to port 2 or, in the other direction, from port 2 to port 1. On the other hand, the S_{11} and S_{22} parameters indicate the wave's power reflected by the DUT at port 1 or port 2 respectively.

Throughout the research project, EM characterization was performed using two VNA instruments. The first one, an Anritsu 37369A 40 GHz (Anritsu, Japan), was used for routine analysis of the obtained materials. Higher resolution measurements were achieved using an Agilent N5245A PNA-X 70 GHz instrument (Agilent Technologies, U.S.A.) in which the intermediate frequency (IF) filter bandwidth could be adjusted.

For the ferromagnetic resonance (FMR) experiments, DUTs were characterized under DC magnetic field applied perpendicularly to the sample using a NTM 10400M-260 electromagnet supplying magnetic field values ranging from 0 to 9 kOersteds (kOe). Figure 2 shows the experimental setup. The DUT was placed in the gap of the electromagnet, and connected to one end of a set of long coaxial cables using a pair of Anritsu 36801K right angle launchers. The other coaxial cables ends were connected to the ports of the VNA, placed away from the electromagnet's intense DC magnetic field.

Prior to any measurement set, a 12-terms standard calibration was performed on the VNA to remove spurious effects provoked by the connection system. Data acquisition was achieved using Labview. Matlab® codes expressly written for this project allowed standardizing data treatment and calculations needed for the EM characterization of the materials under study. More specifically, three data extraction and treatment procedures were developed: one to characterize the ferromagnetic resonance (FMR) phenomenon in these materials, a second one to extract their ε_r and μ_r parameters and the last one to calculate their microwave absorption ratio and shielding effectiveness.

These procedures will be described in the following sections after shortly reviewing the fabrication of the two transmission line (TL) topologies specifically designed for this project.

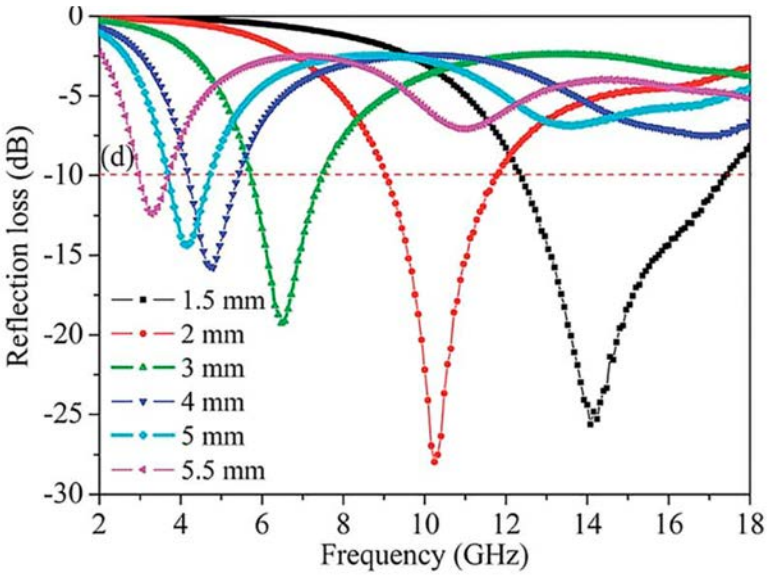

Figure 1 – Reflection loss (RL) curve of a $Fe_{0.64}Ni_{0.36}$@porous activated carbon ball nanocomposite. Frequency-dependent reflection behavior is controlled by the paraffin-slab thickness in which the nanopowder was dispersed. Taken from [9].

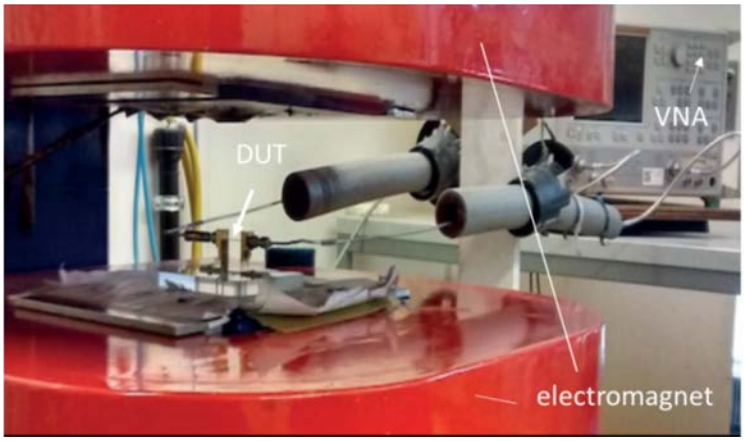

Figure 2 - Experimental configuration for VNA measurements under DC magnetic field.

6.2 Transmission line (TL) test cells fabrication

Both TL test cells, the coplanar waveguide and the microstrip, were laser-etched on different Teflon Rogers™ (Ro) substrates using an Oxford J-1064/355 pulsed laser system. Details about each fabrication procedure are given below.

6.2.1 Coplanar waveguide (CPW) topology

The CPW TL consisted of a Ro4350B substrate stripped of its bottom copper layer. Two parallel lines, each having a volume of 22.8 mm^3, were laser-etched lengthwise on the top copper substrate, exposing the substrate. For this etching procedure, the 355 nm laser was chosen, operated at 0.5 W, a speed of 200 mm/s and a frequency of 200 kHz, pulsing every 10 ps for 11 cycles. Leaving the lines edges untouched, their central section were fully etched through the thickness of the substrate by using the 1064 nm laser at 1.6 W during four cycles, while the speed, frequency and pulse length were kept constant. More details about the dimensions of the obtained device as well as a representation of the interaction between the electric and magnetic fields of the incoming microwave and the sample can be found in Figure 3.

6.2.2 Microstrip (MS) topology

As shown in Figure 4, the microstrip design required a two Rogers-substrate configuration. Two cavities, each having a volume of 38.4 mm^3, were laser-etched through the top Ro3010 substrate using the same procedure as described above for the 1064 nm laser operation. The inter-cavity central section of the substrate was conserved in order to structurally strengthen the TL, facilitating its manipulation. The substrate was then almost completely stripped of its top and bottom copper layers except for the central microstrip. The stripping was performed in order to prevent short circuits between the central

microstrip and ground in case of highly conductive nanopowders. The bottom layer was machined out of a Ro4003 substrate for which only the bottom copper layer was conserved. Afterwards, two connectors were soldered onto the microstrip using tin welding.

As for the CPW TL, Figure 4 also shows how the electric and magnetic fields of the incoming microwave interact with the sample in the MS cavities. As shown there, the electric field tends to penetrate more into the sample-holding cavities as compared to the CPW TLs. This property, typical of a MS design, coupled to the larger volume of the etched cavities which accommodates as much as ~68% more nanopowder than its CPW counterpart, should be advantageous in terms of sensibility.

6.2.3 TL filling methodology

In both cases, the same method was employed to fill the TL. The nanopowders were mixed with ethanol in order to form a slurry that could be introduced into the TLs rectangular cavities. A Teflon spatula was then used to compact the samples. The procedure was repeated thrice in order to compactly fill the cavities. Afterwards, the as-filled TLs were dried overnight under vacuum, at ambient temperature, to eliminate the solvent. Finally, nanopowder leftovers were removed with a thin cotton swab impregnated with ethanol in order to clean the TL surface.

A piece of cellotape was put on bottom and top of the CPW substrate before and after filling the cavities with the nanopowder respectively, and on top of microstrip substrate after filling, to ensure that the low-density powder was kept enclosed in the cells. Tests were performed to verify that the cellotape had no effect on the TL line EM characteristics. In order to reuse the TL, the devices were simply carefully cleaned using ethanol before moving from one powder sample to another.

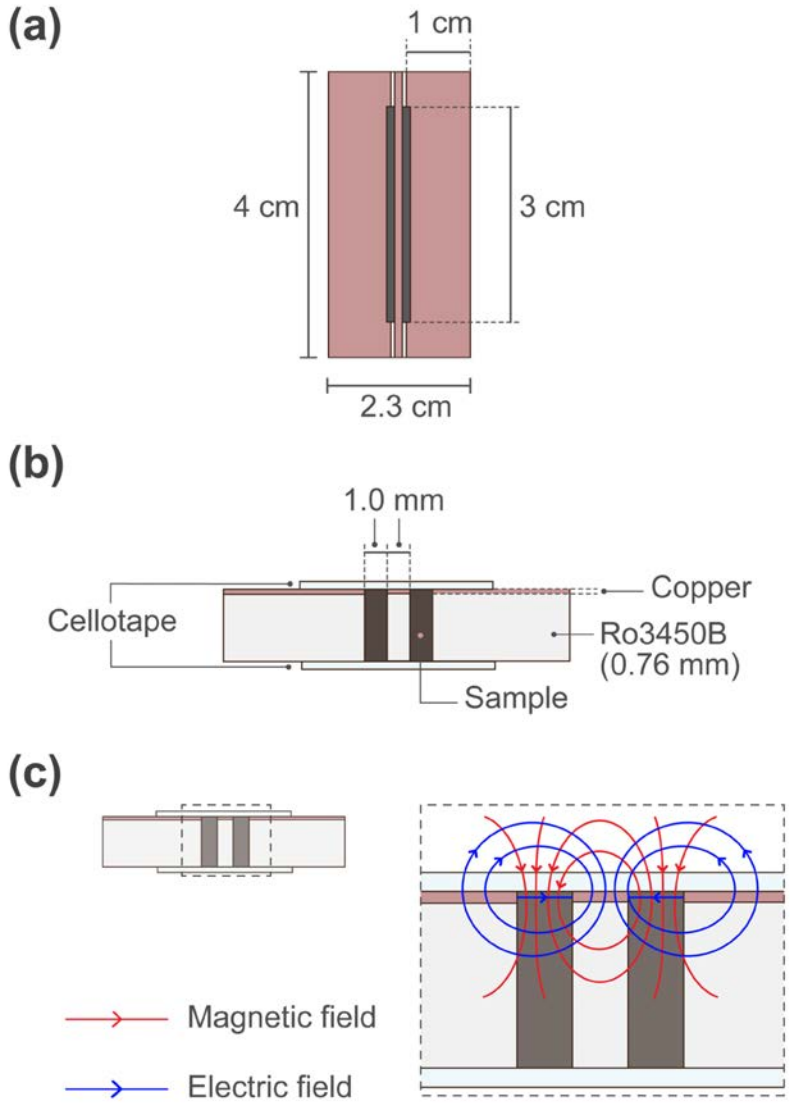

Figure 3 – (a) Top and (b) side views of the coplanar waveguide (CPW) transmission line (not to scale), showing its components and dimensions. The Teflon substrate is represented in light grey whereas the top copper layer is colored in dark pink, cellotape in light blue, and nanopowder in black. (c) Representation of the electrical and magnetic fields of the incoming microwave interacting with the sample.

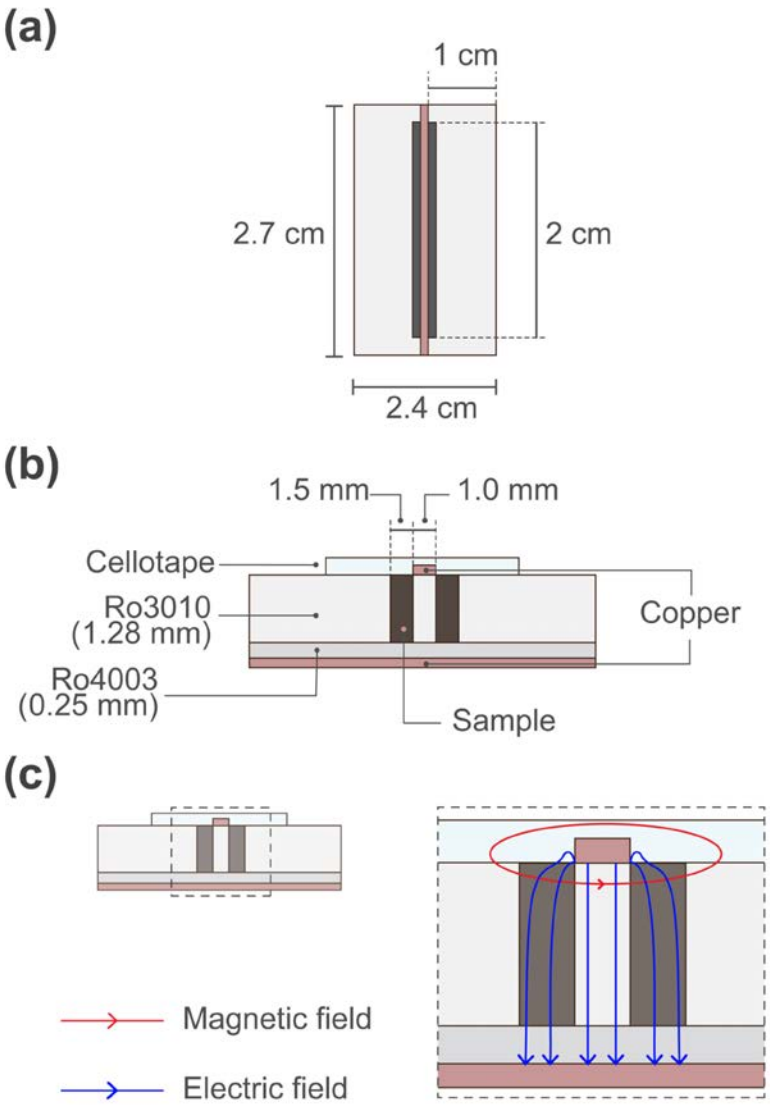

Figure 4 - (**a**) Top and (**b**) side views of the microstrip (MS) transmission line (not to scale), showing its components and dimensions. The Teflon substrate is represented in light grey whereas the top copper layer is colored in dark pink, cellotape in light blue, and nanopowder in black. (**c**) Representation of the electrical and magnetic fields of the incoming microwave interacting with the sample.

6.3 EM data extraction procedures

6.3.1 Characterization of the electrical permittivity (ε_r) and the magnetic permeability (μ_r)

Figure 5 shows a schematic view of the measurement configuration, adapted from [13]. Port A stands for the connection between the VNA microwave source and the TL input while port B relates the TL output and the VNA detector. These ports include attenuators, directional couplers, cables and connectors existing between the VNA's source/detector and the TL's input/output, respectively.

The obtained S-parameters are used to calculate the propagation constant, which takes into account the whole cross-section of the TL used, including the surrounding air. Consequently, the extraction method for the relative permeability (μ_r) and permittivity (ε_r) of the nanopowders from the obtained propagation constant follows three steps:

a) The effective ε_e and μ_e parameters, denoted by subscript "*e*", are obtained from the measured S-parameters.

b) The ε_s and μ_s, named substrate parameters, are retrieved from their ε_e and μ_e counterparts. These parameters encompass the TL substrate as well as the nanopowder itself.

c) Finally, the nanopowders' ε_r and μ_r parameters are obtained by multiplying the substrate parameter by a volumetric factor, *V*.

Thus, to first obtain ε_e and μ_e, let us start with the expression representing the transmission of a microwave signal from source to detector for a filled TL:

$$S_{21filled} = S_{21A} e^{-\gamma_{filled} L} S_{21B} \qquad \textbf{Equation 6.1}$$

If the TL is kept empty, Equation 6.1 becomes

$$S_{21empty} = S_{21A} e^{-\gamma_{empty} L} S_{21B} \qquad \textbf{Equation 6.2}$$

In both cases, the propagation constant, γ_m, is given by

$$\gamma_m = i2\pi f\sqrt{\varepsilon_{e,m}\mu_{e,m}}/c_o \qquad \textbf{Equation 6.3}$$

with m being either filled or empty, L is the length of the line, c_o is the light velocity in air and f is the frequency of the signal.

From these equations and using the ratio $S_{21filled}/S_{21empty}$, we can derive

$$\frac{\gamma_{filled}-\gamma_{empty}}{2\pi fL/c_o} = -ln\frac{S_{21filled}}{S_{21empty}}/(2\pi fL/c_o) = i\left(\sqrt{\varepsilon_{e,filled}\mu_{e,filled}}-\sqrt{\varepsilon_{e,empty}\mu_{e,empty}}\right) \qquad \textbf{Equation 6.4}$$

Given the empty line is filled with air: $\varepsilon_{e,empty} = \mu_{e,empty} = 1$. Thus, we use another measurement performed on the filled line in order to extract ε_e. A high magnetic field (9 kOe) is applied during the frequency measurement of the filled line in order to move any magnetic effect above the frequency range under scope, resulting into $\mu_{e\,filled} = 1$, yielding

$$\frac{\gamma_{filled}-\gamma_{empty}}{2\pi fL/c_o} = -ln\frac{S_{21filled}}{S_{21empty}}/(2\pi fL/c_o) = i\sqrt{\varepsilon_{e,filled}} - 1 \qquad \textbf{Equation 6.5}$$

From these last two equations, the permittivity and the permeability of the whole TL cross-section are extracted. The permittivity, ε_e, is obtained from (6.5), using the measurement under high magnetic field ensuring that $\mu_e = 1$ so that only ε_e is involved and can be retrieved. Then the permeability μ_e is obtained by introducing the permittivity in (6.4).

For the microstrip topology shown in Figure 4 the substrate's permittivity, ε_s, is retrieved from the effective one ε_e using the following expression derived from [15]:

$$\varepsilon_s = 2\times\frac{\varepsilon_e - 1 + F}{1+F} \qquad \textbf{Equation 6.6}$$

Where F is given by:

$$F = \frac{1}{\sqrt{1+12T/W_s}} + 0.04\{1-(W_s/T)^2\} \qquad \textbf{Equation 6.7}$$

Where T is the total thickness of the substrate and W_s the width of the microstrip. Given the microstrip dimensions shown in Figure 4, F=0.231.

The substrate permeability, μ_s, is retrieved from the chart shown in Figure 6. The chart is derived from expressions found in [16]. The μ_e values found for the studied nanopowders are low, close to 1.02. Thus, using Figure 6, the corrected substrate permeability μ_s value would thus be equal to 1.011 x 1.02 = 1.0312. This slight difference represents less than a 2% correction.

For the CPW line topology shown in Figure 3, obtaining relative ε_r and μ_r values from the effective ones is much simpler since the following assumptions hold [17]:

$$\varepsilon_s = 2(\varepsilon_e - 1) \qquad \textbf{Equation 6.7}$$

and

$$\mu_s = 2(\mu_e - 1) \qquad \textbf{Equation 6.8}$$

Finally, we are able to retrieve the contribution of the sole nanopowder by using a simple volumetric factor taking into account the volume occupied by the nanopowder in the cavities as compared to the total volume present around the central strip conductor. If the width of each cavity is noted as W, and the width of the central strip is noted as W_s, then the parameters of the sole nanopowder are obtained from ε_s and μ_s by using the multiplicative factor V:

$$V = \frac{2W + W_s}{2W} \qquad \textbf{Equation 6.9}$$

Factor V compensates the volumetric dilution of the powder in the substrate. Thus:

$$\varepsilon_r = V\varepsilon_s \qquad \textbf{Equation 6.10}$$

and

$$\mu_r = V\mu_s \qquad \textbf{Equation 6.11}$$

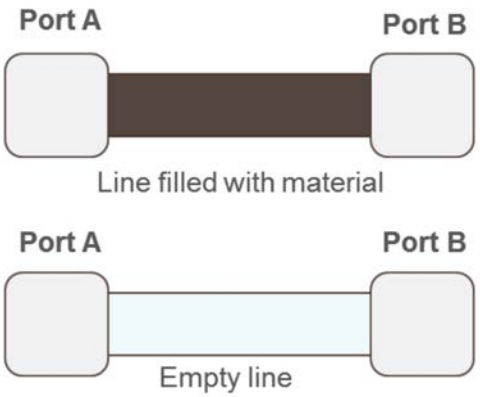

Figure 5 - Schematic representation of the measurement configuration.

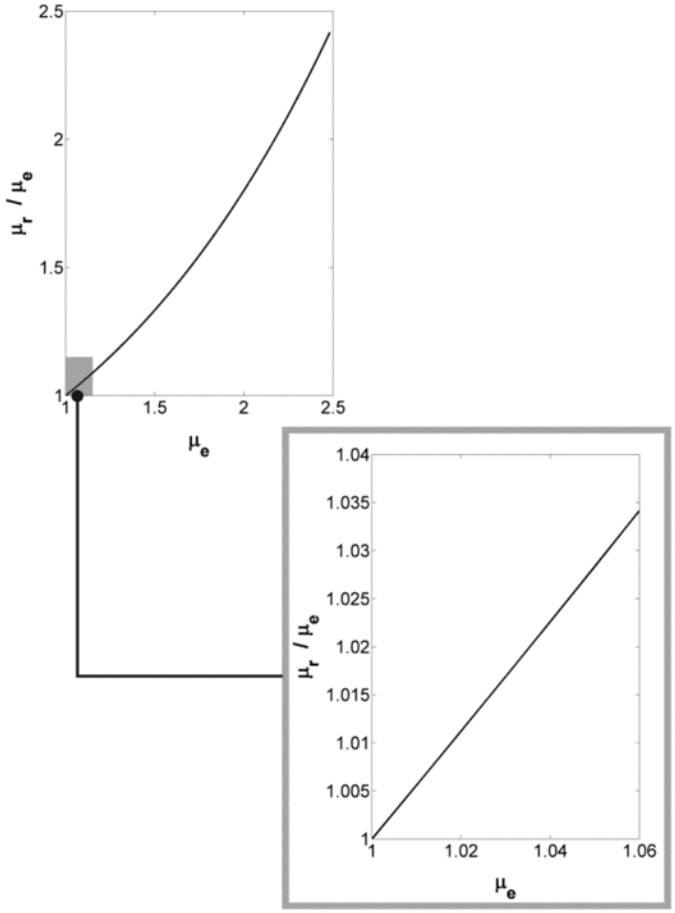

Figure 6 - Ratio of relative by effective permeability μ_r/μ_e for the microstrip topology of Figure 4 calculated from equation in [16].

6.3.1.1 *Phenomenological model for complex permittivity*

The extracted relative permittivity, ε_r, was fitted using a model previously developed for conductive inclusions dispersed in an insulating matrix [16], as illustrated in Figure 7. In the present research, conductive inclusions are the nanocomposite particles (NcPs), while the insulating matrix is air, the whole forming the powder under study. According to the model in [16], the random distribution of NcPs is approximated by a network of grains, separated by air. Each grain is assumed to be conductive, having an equivalent resistor, and strongly coupled to his neighbors by a capacitor. The resulting model is a 2-layered transmission line. Its equivalent permittivity has the following expression:

$$\frac{1}{\varepsilon_{eff}} \triangleq \frac{1}{\left(\varepsilon_r + \frac{\sigma_{NcP}}{i\omega\varepsilon_o}\right)} = \frac{H_1}{\frac{H_1}{\varepsilon_{NcPs} + \frac{\sigma_{NcP}}{i\omega\varepsilon_o}} + H_2} \Big/ (H_1 + H_2)$$

Equation 6.12

where ε_{NcPs} is the dielectric constant of the NcPs and σ_{NcPs} their conductivity, ε_o is the permittivity of vacuum. These variables are the different inputs for the phenomenological model.

H_1 and H_2 are the NcPs and air layers thicknesses, respectively. They are related by a filling factor, f, defined as the ratio $f = H_2/(H_1 + H_2)$, which models the proximity between the NcPs inducing capacitive coupling responsible for the variation in frequency of the dielectric constant and conductivity of the nanocomposite agglomerate (see Figure 7) . When the phenomenological model is used to fit the measurements, values of f give an insight on the compacity of the nanopowder, hence on the reproducibility of the filling method of the cavities. It also allows to eliminate the air fraction's contribution to the powder's electrical permittivity, exclusively representing that of the nanocomposite.

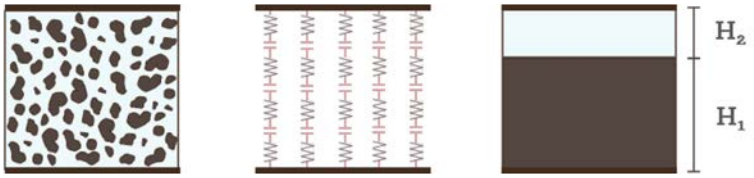

Figure 7 - Schematic representation of phenomenological model. Left: topology of a nanocomposite powder; center: equivalent circuit; and right: two-layered equivalent transmission line, where *H1* and *H2* are the NcPs and air layers thicknesses, respectively.

6.3.2 Characterization of the ferromagnetic resonance (FMR) phenomenon

As discussed in Section 1.3.2.2, the MNPs are expected to induce a ferromagnetic resonance (FMR) absorption in the microwave frequency range. In order to characterize it, a standardized Matlab® background subtraction technique was developed. This technique is based on the normalization of two measurements performed on each sample: the first one at a given value of DC magnetic field in order to determine the FMR frequency at this value, and the second one for a DC field value of 9 kOe. This high magnetic field value ensures that the FMR phenomenon occurs in a frequency range well above 40 GHz, so that this particular measurement represents losses due to cables, connectors and mismatch of the microstrip line to the 50 Ω reference impedance of the VNA measuring instrument.

Subtraction of the two curves provides a normalized response free of spurious losses from which an accurate value of the FMR frequency is retrieved, as the minimum of the normalized transmission. The procedure is illustrated in Figure 8: for a raw value of 15.92 GHz

extracted from the curve at 0 kOe, the corrected value provided by the normalized curved is equal to 15.88 GHz.

After background subtraction, the Matlab® routine calculates the first and second derivative of the absorption curve at each magnetic field in order to detect the relative and absolute minima. For each absorption curve, the absolute minimum represents the material's FMR frequency at that given magnetic field. The use of such a standardized data treatment Matlab® routine ensures a homogeneous treatment of all experimental data.

The position (or value) of the FMR frequency is independent from the microwave measurement system. Any error on FMR should be due to an uncertainty of the DC bias field, hence on the stability of the current source in the electromagnet, which is carefully controlled in our experimental setup.

For instance, Figure 9 presents the FMR frequency at 2 kOe of a nanopowder sample measured 5 times at different intervals, over a period of 6 months. For each measurement, the FMR frequency was found at the absorption minima using our automatized Matlab® routine, as described above. Results presented in Table 1 demonstrate that the as-found FMR frequency shows minimal variance, demonstrating the robustness of our experimental setup and data-extraction procedures.

Considering these results, we can affirm that a frequency shift or difference as small as ~0.1 GHz is significant and can be considered as the signature of a material/wave interaction and not an artifact of the measurement configuration.

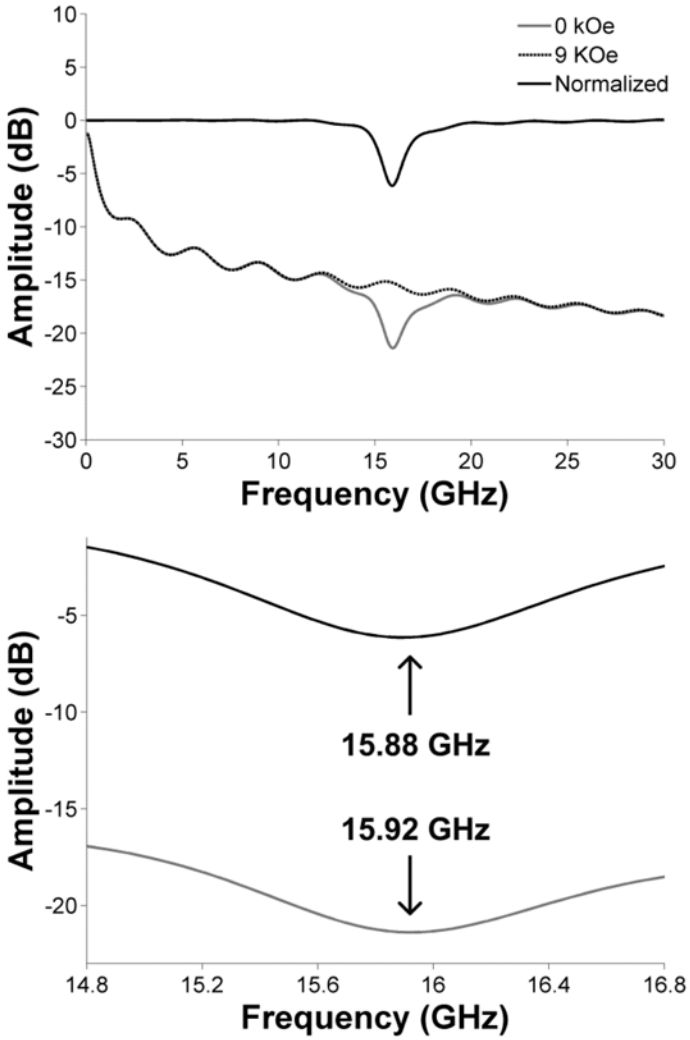

Figure 8 - Effect of the normalization procedure on the S_{21} transmission curves (above) and the retrieval of the FMR frequency (below) for a MaNPs@GO (50% Fe/NcS LR) sample.

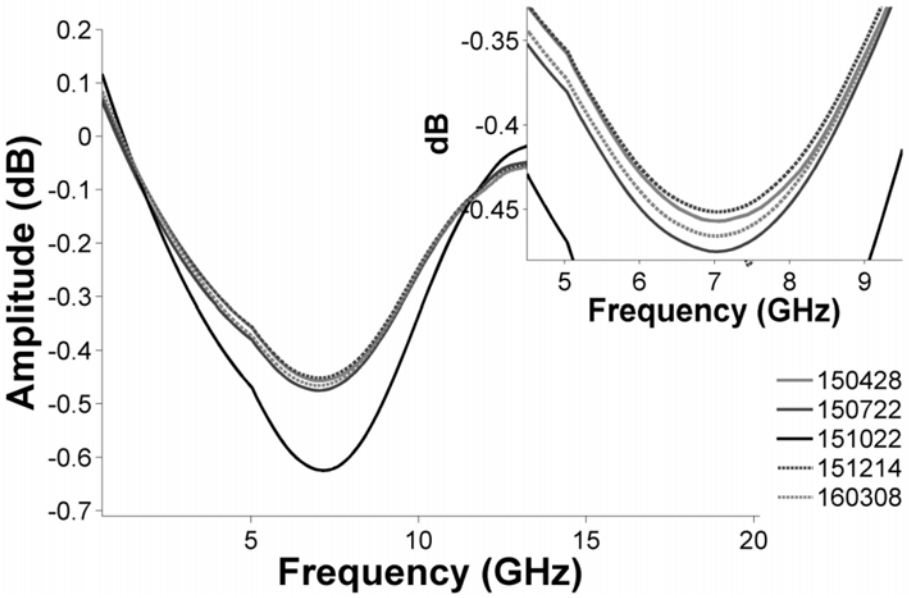

Figure 9 - S_{21} transmission curves showing a MaNPs@GO (50% Fe/NcS LR) nanopowder's FMR frequency at 2 kOe measured at different dates. Inset: closer look on four measurements bearing high resemblance.

Table 1 – FMR frequency at 2 kOe determined from the S_{21} transmission curves of the measurements performed at different dates

Date (YYMMDD)	FMR f (GHz)
150428	7.03
150722	7.03
151022	7.13
151214	7.03
160308	7.03
Average	7.05
Standard Deviation	0.04

6.3.3 Characterization of the shielding effectiveness and absorption ratio

As mentioned in section 1.1.1, the overall purpose of EM shielding is to prevent the propagation of an incident EMW from one medium to another by means of single or multiple reflections and/or absorption of the incoming EMW.

Therefore, the absorption or shielding effectiveness of a given material, SE_T, can be expressed as a sum of the EMW losses due to absorption, single and multiple reflections, denoted SE_A, SE_R and SE_{MR} respectively:

$$SE_T = SE_A + SE_R + SE_{MR} \qquad \textbf{Equation 6.13}$$

And it is empirically expressed as the logarithmic evaluation of the transmission, T, expressed in decibels (dB):

$$SE_T = -10logT \qquad \textbf{Equation 6.14}$$

The scattering or S-parameters, S_{11} and S_{21} defined in section 6.1 can be related to the incoming (P_{in}), reflected (P_{ref}) and transmitted (P_{out}) microwave power and thus to the reflection, R, and transmission, T, coefficients presented in section 1.1.1, by the following two equations:

$$|S_{11}|^2 = \frac{P_{ref}}{P_{in}} = R \qquad \textbf{Equation 6.15}$$

$$|S_{21}|^2 = \frac{P_{out}}{P_{in}} = T \qquad \textbf{Equation 6.16}$$

So that the absorption ratio is then found by:

$$A = \frac{P_{abs}}{P_{in}} = \frac{P_{in} - P_{ref} - P_{out}}{P_{in}} = 1 - R - T = 1 - |S_{11}|^2 - |S_{21}|^2 \qquad \textbf{Equation 6.17}$$

While the empirical shielding effectiveness is given by:

$$\mathrm{SE}_T = 10 \log \left| \frac{1}{|S_{21}|^2} \right| \qquad \textbf{Equation 6.18}$$

6.4 Conclusions

In this chapter, we have presented a novel VNA-based EM characterization technique specifically developed for fluffy nanocomposite powders such as the ones synthetized in this research project.

This novel tool is based on two measures of a single transmission line (TL), the first in which the TL is kept empty and the second one filled with the nanopowders. Using both measurements and a three-step procedure executed by a series of Matlab routines, it is possible to extract the complex permittivity, ε, and magnetic permeability, μ, of these materials in the microwave range.

Also, two different designs of TL test cells, a coplanar waveguide (CPW) and a microstrip (MS), were designed, machined and tested. These test-cells can easily be cleaned and re-filled with different nanopowders so that only one of them is needed to measure a large number of samples. The nanocomposite samples can be used directly after synthesis, without any type of sample preparation or additive. Thus, our method ensures that the obtained responses derivate exclusively from the nanocomposites powders under study.

Based on the measurement of S-parameters, our method also allows for the extraction of the material's dielectric constant and conductivity, which is successfully validated by implementing a phenomenological model. This model includes, as input parameters, the dielectric constant and conductivity of nanoparticles and a filling factor modelling the distance between particles. In consequence, it also enables to assess the quality of the filling of the transmission lines' cavities with the nanopowders.

As it will be further shown in Chapter 7, our methodology also allows to accurately retrieve the FMR behavior of our ferr(o/i)magnetic nanopowders. Although the proposed extraction method is used here for nanopowders, it can also be applied to other materials such as ferrites, liquids, or ferrofluids, provided they can easily be inserted in the cavities.

6.5 Bibliography

1. M. Sucher and J. Fox, Handboook of Microwave measurements, vol.2, Polytechnic Press of the Polytechnic Institute of Brooklyn: Brooklyn, USA, 1963. Chapter 9.
2. G. Kent, 1991, *Microwave J.*, **34**, 72-82.
3. M. Olyphant Jr, "Practical dielectric measurement of CLAD microwave substrates", Cu-Tips Note 8.
4. J. Huang, K. Wu, P. Morin and C. Alkyel, 1996, *IEEE T. Microw. Theory*, **44(5)**, 770-777.
5. K.H. Baek, J.I. Sung and W. Park, 1996, *IEEE Microw. Guided W.*, **5**(1), 3-5.
6. J.L. Medina, A. Serrano and F.J.Mendieta, 1993, *Microwave J.*, **36**(3), 82-93.
7. Y. Zhan, F. Meng, Y. Lei, R. Zhao, J. Zhong and X. Liu. *Mater Lett.,* 2011, **65**, 1737-1740.
8. P. Liu, Y. Huang and X. Zhang, *J. Alloy Compd.*, 2014, **617**, 511-517.
9. G. Li, L. Wang, W. Li and Y. Xu. *RSC Adv.*, **2015**, 5, 8248-8257.
10. E. Ni, 1992, *IEEE T. Instrum. Meas.*, **41**(4), 495-499.
11. H.B. Sequeira, 1991, *Microwave J.*, **34**(3), 73-85.
12. H.J. Eul and B. Schiek, 1991, *IEEE T. Microw. Theory*, **39**(4), 724-731.
13. I. Huynen, C. Steukers and F. Duhamel, 2001, *IEEE T. Instrum. Meas.*, **50**(5), 1343-1348.
14. I. Huynen, 2013, Measurement of microwave electromagnetic properties of magnetic nanowires using a Vector Network Analyzer. Unpublished manuscript.
15. D. Pacckiaraj, K.J. Vinoy and A. Kalghatgi, *Int. J. RF Microw. C. E.*, 2012, **22** (1), 124-130.
16. K. Yeo and M. Lancaster, High Frequency PostGraduate student colloquium, 17 September 1999, Leeds, United Kingdom. 105-110.
17. J. Laskar, A-V. Pham, S. Chakraborty and M. M. Tantzeris. "On-Wafer Measurement at the W-Band" in Advanced Integrated Communication Microsystems. Eds. A-V. Pham, J. Laskar and M. M. Tantzeris. Wiley, IEEE Press, 2009, p. 430.
18. A. Saib, L. Bednarz, R. Daussin, C. Bailly, X. Lou, J.-M. Thomassin, C. Pagnoulle, C. Detrembleur, R. Jerome, and I. Huynen, 2006, *IEEE T. Microw. Theory*, (EuMC2005 Special Issue), **54**(6, part II), June 2006, 2745-275442

chapter 7

Magnetic nanoparticles and nanocarbon supports as control mechanisms of a material's magnetic permeability and electric permittivity in the microwave range

In this chapter, we present the results obtained during the EM characterization of the different MNPs@NcS nanocomposites synthetized throughout this research project. These results illustrate the link between the nanocompositesí physicochemical characteristics and their ε and μ values in the microwave range. They thus contribute to the understanding of the core theoretical principles underlying the *Nano4Waves* metamaterial design paradigm.

Collaborators

Sébastien Depaifve (IMCN/MOST), Julien Mahin (IMCN/MOST) Arnaud Wolf (IMCN/MOST), Yzaora Tchuitio Yagang (IMCN/MOST).

As stated in section 1.4, the main objective of this research project is to obtain a new class of microwave absorbing materials (MAMs) based on the chemical assembly of different types of magnetic nanoparticles (MNPs) and nanocarbon supports (NcS).

As shown throughout Part I, Chapters 2 to 5, different synthetic techniques were developed to produce such MNPs@NcS nanomaterials. Particular effort was placed in finding which synthetic parameters governed certain targeted physicochemical characteristics, and in obtaining well-controlled materials. For the MNPs, special attention was given on how to control their chemical composition, their size and their loading rate. Likewise, we varied the type and oxidation state of the NcSs in order to determine their impact on the MNPs@NcS characteristics.

The developed synthetic methodologies allowed obtaining seven types of ferro and ferrimagnetic nanoparticles with various sizes and loading rates in a controlled manner. Furthermore, we achieved to graft these MNPs onto as many as five different nanocarbon supports of different topologies and with various degrees of oxidation. Thus, a wide diversity of MNPs@NcS nanocomposites with particular combinations of the targeted physicochemical characteristics can now be produced (see Table 1).

As discussed in sections 1.3.1 and 1.3.2, the magnetic nanoparticles' composition, size or loading rate are expected to control the products' magnetic permeability, μ, while the nanocarbon supports' type or oxidation degree should greatly determine their electrical permittivity, ε. Such is the core theoretical principle of the Nano4Waves metamaterial design paradigm, which should lead to diverse, function-targeted, highly effective MAMs.

Table 1 – General overview of the nanocomposites synthetized in this research project

NP Type	Code	NcS	Average size*	Loading rate ranges*	Reference
Magnetite	MaNPs	GO	1, 2, 6, 9, 11, 12 & 13 nm	12% to 37%	Chapter 2
		rGO			
		GNPs			
		MWCNTs			
		ox-MWCNTs			
Zero-valent iron	ZVI NPs	GO	8, 14, 15, 17, 18 & 20 nm	38% to 48%	Chapters 4 & 5
		MWCNTs	15 nm	29 %	
Cobalt	CoNPs	MWCNTs	24 nm	39%	Chapter 3
Nickel	NiNPs	MWCNTs	13 & 130 nm	22% to 31%	Chapter 5
Fe/Co/Ni alloys	FeNi NPs	GO	Similar bimodal size distributions centered on 8-11 nm and 25-28 nm	26%	Chapter 4
	FeCo NPs			27%	
	FeCoNi NPs			23%	

***** Average MNP size and loading rate vary according to the employed synthetic conditions. Indicative values and ranges are given.

However, in order to fully explore the potential of this approach to a MAM's design, a novel EM characterization technique specially adapted to nanocomposite powders was required. Consequently, a VNA-based characterization tool, its related test cells and data extraction methodologies were developed specifically for this research project, as reported in Chapter 6.

By applying this characterization technique to a series of chosen MNPs@NcS products, it was possible to unveil the link between the nanocomposites' physicochemical characteristics and their ε and μ values in the microwave range. Further unexpected synergistic effects between MNPs and NcS, particularly influencing the materials' ε values, were also found. All these novel relationships as well as the microwave absorption and shielding efficiencies of these materials will be illustrated in the following three sections.

7.1 The role of magnetic nanoparticles in the control of magnetic permeability

By decorating various NcS with different types of MNPs of carefully controlled composition, size and loading rate, we ought to find how these MNPs characteristics modify the intensity and/or frequency of the ferromagnetic resonance (FMR) and thus, the value of the relative magnetic permeability, μ_r.

As discussed in section 1.3.2.2.1, the relationship between the FMR phenomenon and the permeability of ferri/ferromagnetic materials is modelled by the following expression:

$$\mu_r = 1 + \frac{4\pi M_s \gamma f}{(f + i/\tau)^2 - f_{EMW}} \qquad \textbf{Equation 7.1}$$

As also mentioned in section 1.3.2.2, the FMR phenomenon is the main magnetic energy loss mechanism in the microwave range for F(i)M materials. Indeed, in the FMR phenomenon, an incoming microwave is absorbed if its frequency matches the energy difference between two quantized states of Larmor precession or magnetic moment rotation.

An appropriate FMR expression fitting the type of materials synthetized during this research project would be:

$$f = \gamma \mu_o (H_z + H_a) \qquad \textbf{Equation 7.2}$$

This equation shows that in the absence of an external applied magnetic field, H_z, the model predicts a natural or zero-field FMR absorption frequency, f_o, due to the anisotropy field, H_a. However, as H_z is applied and its value increased, f should shift towards higher frequencies.

Figure 1 presents the typical result obtained when monitoring the S_{21} transmission parameter of a given MNPs@NcS nanocomposite as a static H_z is applied. As predicted by the FMR theory, one first absorption process is observed in the absence of an applied magnetic field (H_z =0 kOe) due to H_a. Its frequency, f_o, is determined by identifying the absorption minima in the H_z =0 absorption curve. Likewise, as H_z increases, a series of absorption processes are recorded at increasing f values.

Interestingly, the absorption peaks are broad, each absorption process spanning over a few gigahertz. This feature can be due to the polycrystalline and disordered spatial distribution of the MNPs@NcS in the nanocomposite powder. Indeed, Kittel [1] predicted that the value of the applied magnetic field, H_z, required for resonance at a fixed frequency depends on the direction of the crystal axes relative to the shape axes of the specimen. Thus, in a polycrystalline specimen, the resonance is broader than in a single crystal of the same material, since the distribution in direction of the crystal axes causes a distribution in field strengths for resonance. In those nanocomposites possessing metallic MNPs, it could also be due to the formation of Eddy currents stemming from the changing magnetic fields inside the nanoparticles [2].

A second characteristic feature of these F(i)M materials in the microwave range is presented in Figure 2. The shown spectra were obtained by subtracting the S_{12} parameter values from their S_{21} counterparts, thus highlighting any difference in the transmission of the incoming microwave between the two VNA ports. The non-zero signal resulting from the S_{21}-S_{12} parameter subtraction denotes a non-reciprocal transmission of the microwave. This behavior is expected when a coplanar waveguide, such as the one used for the characterization of the nanocomposite powders, lies onto a ferri or ferromagnetic substrate (*e.g.* the nanopowder) [3].

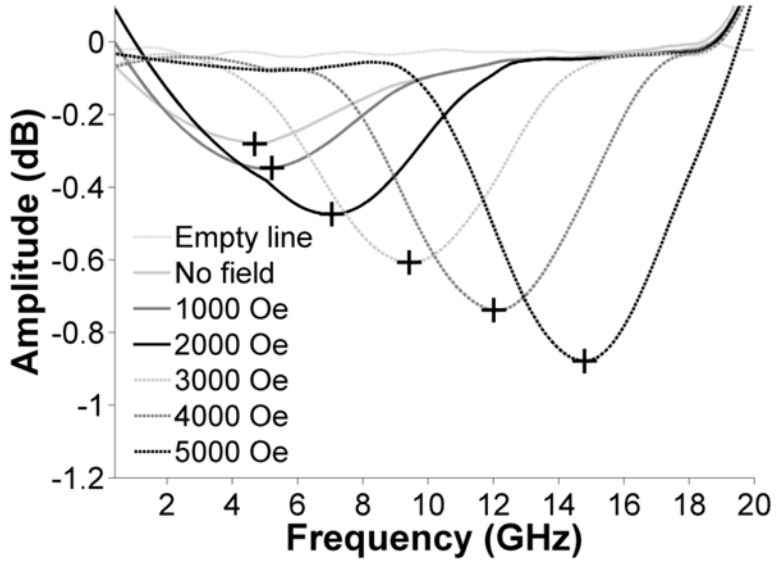

Figure 1 – Typical FMR behavior observed in S_{21} power transmission for a MNPs@NcS nanocomposite. Experimental data belongs to a 50% Fe/NcS LR MaNPs@GO nanocomposite produced with the SOLV-A method. Black crosses indicate absorption frequency minima. Measurement performed with the CPW transmission line.

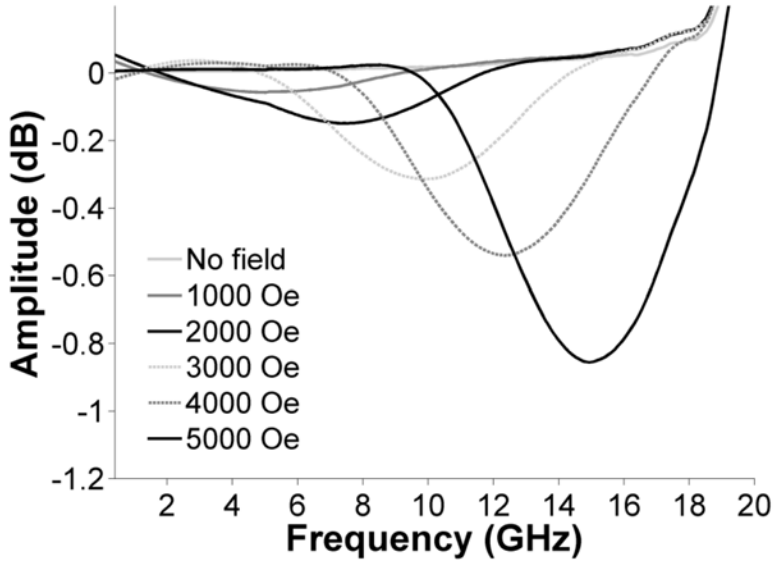

Figure 2 - Difference between S_{21} and S_{12} parameters denoting non-reciprocal power transmission in a 50% Fe/NcS LR MaNPs@GO nanocomposite produced with the SOLV-A method.

The intensity of the FMR phenomenon was found to depend on the deposited MNPs purity as well as on their loading rate onto the NcS. For instance, Figure 3, left, shows FMR absorption data for the SOLV and DCOP MaNPs@GO nanocomposites synthetized as described in Chapter 2. It clearly stands out that, for similar Fe/NcS LRs, the FMR absorption is more intense in the SOLV product given it contains only pure MaNPs while varying amounts of magnetite and lepidocrocite NPs are present in the DCOP powders (see section 2.2.1). Likewise, Figure 3, right, shows the FMR absorption intensity of SOLV-A MaNPs@GO nanocomposites with 10%, 30% and 50% intended Fe/NcS LRs. It is clear that the absorption intensity sharply increases as a larger quantity of MaNPs is present.

As for the FMR absorption frequency, *f*, it was found to be dependent on the chemical identity and size of the deposited MNPs.

In order to illustrate the influence of the chemical composition of the deposited MNPs on the FMR absorption frequency, five different iron-based nanocomposites (Magnetite, ZVI, FeCo, FeNi and FeCoNi NPs) possessing GO as the NcS were chosen. Figure 4 shows the different nanocomposites' natural FMR frequency plotted as a function of their recorded saturation magnetization, M_S (see sections 2.2.2.4 and 4.2.4). The natural FMR *f* was obtained by extrapolation at zero applied magnetic field of the linear regression performed on the resonant frequency, *f*, versus applied magnetic field curve (see Figure 5). For these nanocomposites, the obtained results clearly evidence that their natural FMR frequency increases alongside their M_S. Given that the different deposited NPs possess similar average sizes, their different chemical composition is most probably responsible for the observed changes in M_S and thus in *f*.

Indeed, f is directly dependent on the M_s of the MNPs@NcS nanocomposite, as shown in section 1.3.2.2.

Interestingly, the ZVI@GO nanocomposite does not follow this trend, its natural FMR frequency being higher than expected for the recorded M_s. In fact, such a natural FMR frequency value would rather correspond to the M_s of similarly-sized ZVI NPs (*e.g.* ~175 emu/g as extrapolated from the values reported by Kura *et al.* [5]). This observation suggests that the γ-Fe_2O_3 shell is not contributing to the FMR absorption process, which is solely due to the α-Fe core.

The FMR absorption at zero applied magnetic field of a α-Fe@γ-Fe_2O_3 core@shell nanoparticle was calculated by a numerical simulation using a chain matrix formalism described elsewhere [3, 6]. The simulation aimed at determining the relative contribution of the core and the shell to the natural FMR frequency of the ZVI@GO nanocomposites. The obtained results, shown in Figure 6, agree with those observed experimentally. They also show that the natural FMR frequency is mainly due to the ZVI core since the thin maghemite shell's contribution is extremely weak. Indeed, given maghemite's M_s value is three times inferior to that of α-Fe, the imaginary component of relative magnetic permeability, responsible for the FMR absorption, is thrice as low too.

As for the impact of the deposited MNPs size on the FMR absorption frequency, please refer to Chapter 8, section 8.2.2.

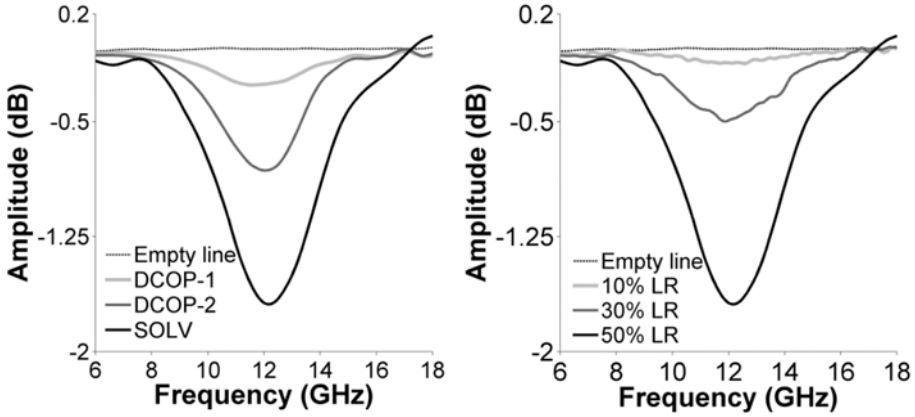

Figure 3 - FMR intensity response at 4 kOe influenced by (a) purity of deposited NP and (b) NPs loading rate onto NcS, in this case MaNPs deposited onto GO supports.

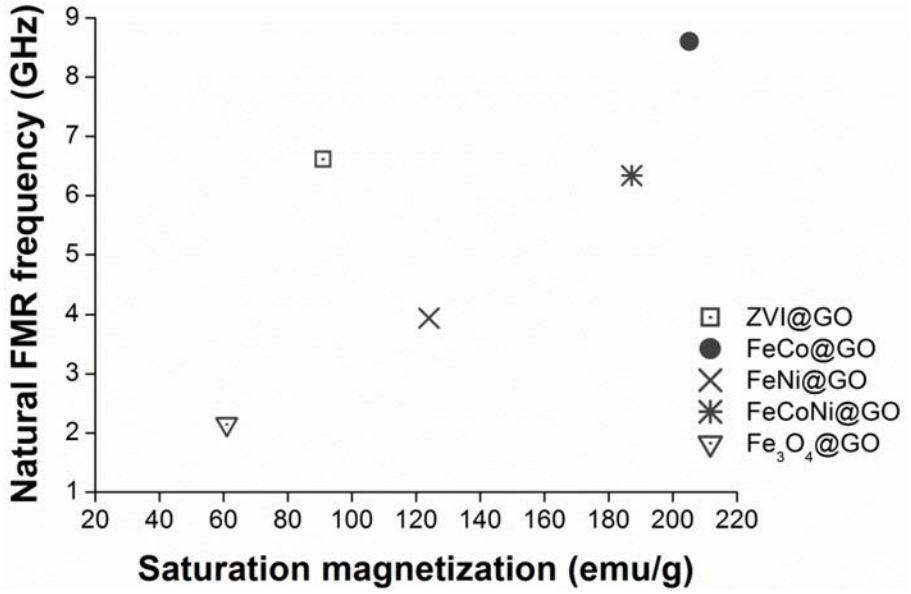

	MNP@GO nanocomposites				
	Fe_3O_4	FeNi	FeCoNi	ZVI	FeCo
Natural FMR *f* (GHz)	2.1	3.9	6.3	6.6	8.6
M_s (emu/g)	61	124	187	92	205

Figure 4 - Dispersion relation between the recorded natural FMR frequencies, *f*, and the saturation magnetization values, M_s, for the different Fe-containing MNP@GO nanocomposites.

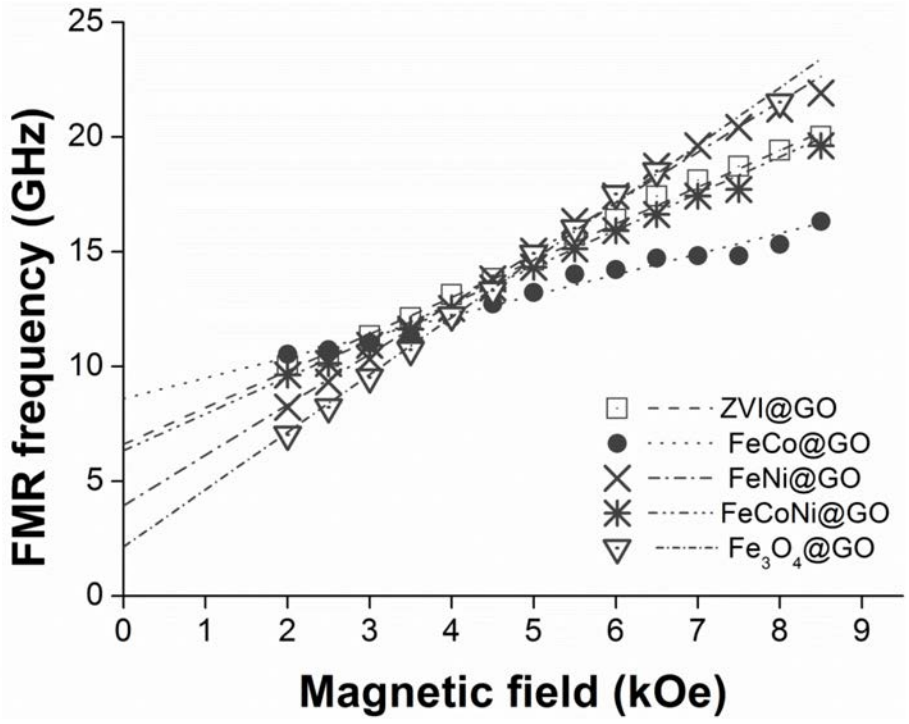

Figure 5 - Dispersion relation between the applied magnetic field and the FMR absorption frequency for five Fe-containing MNP@GO nanocomposites. Symbols represent the experimental data. The dotted lines are the linear regressions of such data.

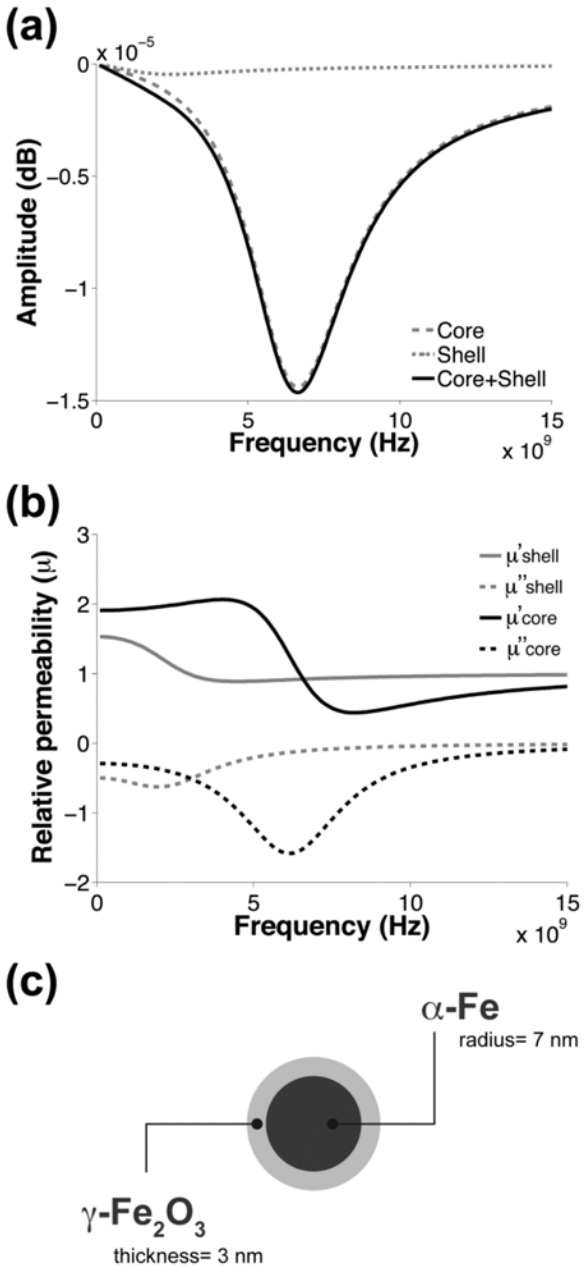

Figure 6 - Results for the chain matrix formalism simulation of (a) zero-field FMR absorption (S_{21} parameter) of a α–Fe@γ-Fe_2O_3 core@shell NP; and (b) the real (μ') and imaginary (μ'') components of the core and shell's relative permeability, μ_r. The dimensions of the simulated NP are shown in (c) and are based on TEM observations of the ZVI@GO nanocomposite produced using 6:1 CA:M and 1:1.5 CA:EG ratios (see section 4.2.1).

Finally, by using the methodology described in section 6.3, the MNPs@NcS relative complex permeability, μ_r, could be extracted and its real, μ', and imaginary, μ'', parts plotted. Figure 7 and Figure 8, respectively, show the behavior of these parameters for a ZVI@GO nanocomposite at different H_Z and for five Fe-containing MNPs@GO nanocomposites at H_Z=1 kOe.

As expected, μ'' is negative for these nanocomposites and it drops around the FMR absorption. Therefore, some of the factors governing the FMR phenomena described above impact the behavior of the μ'' value too. For instance, Figure 7 illustrates how, as the FMR f increases due to the increasing H_Z, the drop in the value of μ'' is displaced toward higher frequencies too. Also, the drop in the μ'' value occurs at different frequencies if the deposited MNPs' composition is changed, as shown in Figure 8. This result is particularly important given it demonstrates μ'' can be controlled by using different types of MNPs.

By opposition, the value of μ' remains relatively constant for all samples, decreasing only slightly over the measured microwave range and never reaching negative values as expected to happen around the FMR frequency [4]. This result suggests that the magnetic losses induced by the as-synthetized nanopowders are inferior to those observed in bulk F(i)M materials. This can be due to two main reasons. Firstly because the nanocomposites possess lower M_s values, given well-known surface effects happening at the nanoscale (see section 1.2.3.1.4) or surface oxidation (as illustrated for the different metallic MNPs in Chapters 3 through 5). Secondly, because the overall magnetic content per unit of mass is lower in these nanocomposites than in bulk F(i)M materials. Indeed, the loaded MNPs make up for only a slight fraction of the total weight of the nanocomposite (see Table 1), the NcS and air accounting for most of the powder's volume.

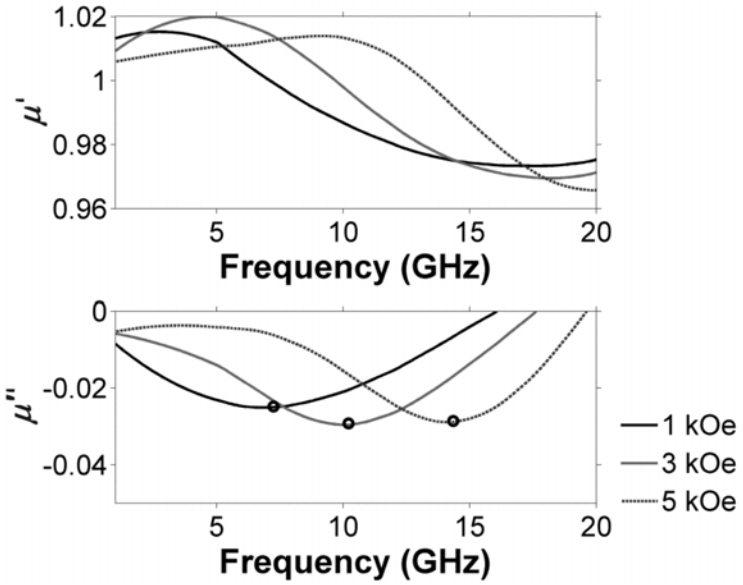

Figure 7 – Complex permeability terms extracted for a ZVI@GO nanopowder with 50% Fe/C LR. Circles indicate location of minima corresponding to FMR frequency.

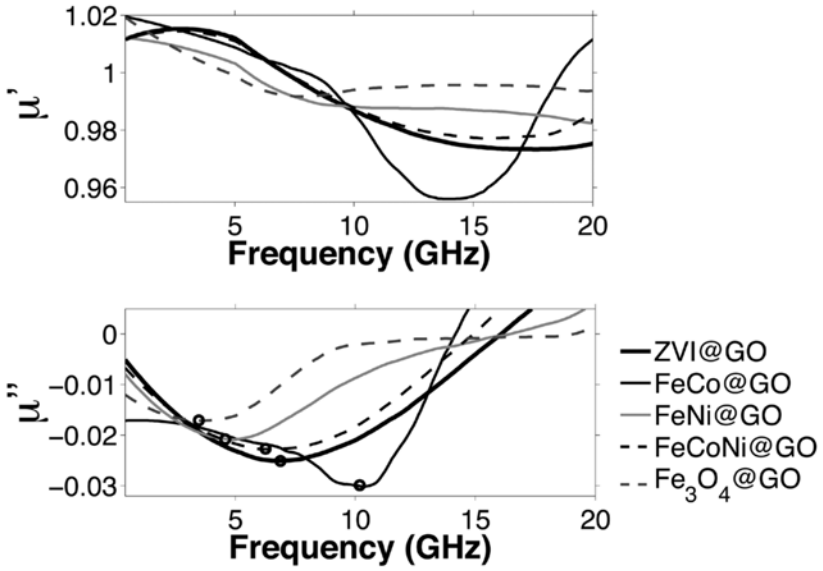

Figure 8 - Complex permeability terms extracted for five Fe-containing MNP@GO nanocomposites with 50% Fe/C LR. Circles indicate location of minima corresponding to FMR frequency at 1 kOe applied magnetic field.

7.2 The role of nanocarbon supports in the control of electrical permittivity

Five different NcS were employed all over this research project: graphene oxide (GO), reduced graphene oxide (rGO), graphene nanoplatelets (GNPs), multi-walled carbon nanotubes (MWCNTs) and oxidized multi-walled carbon nanotubes (ox-MWCNTs).

As mentioned in section 1.3.2, in the Nano4Waves project these NcS serve a dual purpose. On the one hand, as shown in Chapter 2, they are meant to support the MNPs, can reduce their agglomeration and contribute to control their size. On the other hand, by choosing NcS with different shapes (*e.g.* graphenic sheets *vs.* nanotubes) or by chemically modifying their surface (*e.g.* through oxidation), we expect to obtain different conductivity, σ, and electrical permittivity, ε_r, values.

Figure 9 and Figure 10 show the ε_r and σ obtained for four different NcS (GNPs, rGO, GO and ox-MWCNTs) measured using the microstrip (MS) transmission line (see section 6.2.2). It is important to note that, in all cases, the measured values of σ are well below those reported for some of the NcS in the scientific literature [7-9]. However, it is well known that measurements of electrical conductivity in powders depend on the sample preparation methods [9], since both the air and the interface between the particles offer extra resistance to charge transport.

The application of pressure should increase the measured conductivity by enlarging the contact area between the particles. Nonetheless, authors like Marinho *et al.* [9] have shown that even at the theoretical maximum degree of compaction, single particle conductivity is generally not reached, since the contact defects cannot be completely eliminated.

In the EM characterization methodology described in Chapter 6, we considered these issues and devised repeated pressure applications to compact as much as possible the measured powders. Also, in the phenomenological model underlying the fitting of the measured data, we introduced a filling factor, f, which informs us on the degree of compacity of the analyzed nanopowders (see section 6.3.1) and thus on the reproducibility of the filling method of the cavities. The fact that the estimated filling factor is similar for all samples ($f \approx 0.35$, *e.g.* ~35% air in the TL cavities) ensures that comparisons can be directly drawn between each other.

Thus, let us compare the results for the three graphenic NcS whose degree of oxidation, as measured by XPS (see Appendix IV.I), increases in the order GNPs<rGO<<GO. As described in Section 1.3.1, it is known that by varying the NcS' oxidation degree, one can modify the number of defects in the carbon network and thus impact its charge carrier transport and conductivity [7]. Indeed, the oxidation of graphene or GNPs implies the partial destruction of the aromatic sp^2 network. Therefore, GO's conductivity, as compared to that of its non-oxidized precursors, is lowered to such an extent that it is considered as an insulator [7, 8]. As for rGO, its electrical properties vary according to the degree of reduction which can partially restore the lost sp^2 network, and should theoretically be found in between those of GO and graphene. Our results perfectly illustrate these principles, showing that the conductivity reached at high frequency for rGO is lower than that for GNPs, while GO is nearly an insulator over the whole frequency range.

Figure 10 also shows the ε_r and σ results obtained for ox-MWCNTs. According to XPS, this NcS' oxidation degree is low and similar to that of pristine GNPs. Nonetheless, the conductivity of the ox-MWCNTs is inferior to that of GNPs, as expected. Indeed, due to shape effects, carbon nanotubes tend to be less conductive than their graphenic counterparts [9].

Interestingly, the electrical properties of these materials also seem to be dependent on the amount and composition of MNPs loaded onto a particular NcS. For instance, Figure 11 shows how the relative permittivity (ε_r) and conductivity (σ) values for the 50% intended Fe/NcS LR MaNPs@GO nanocomposite are significantly lower than that of its 10% Fe/NcS LR counterpart. This is probably due to the poor electrical conductivity of the magnetite phase, which hinders electron transport over the nanocomposite surface. However, if the deposited MNPs are metallic and thus conducting (for example Ni, see Figure 12), there is a significant increase in both ε_r and σ throughout the studied frequency range.

To the best of our knowledge, it is the first time that such synergistic effects, illustrating the intimate interactions between MNPs and their NcS, are demonstrated.

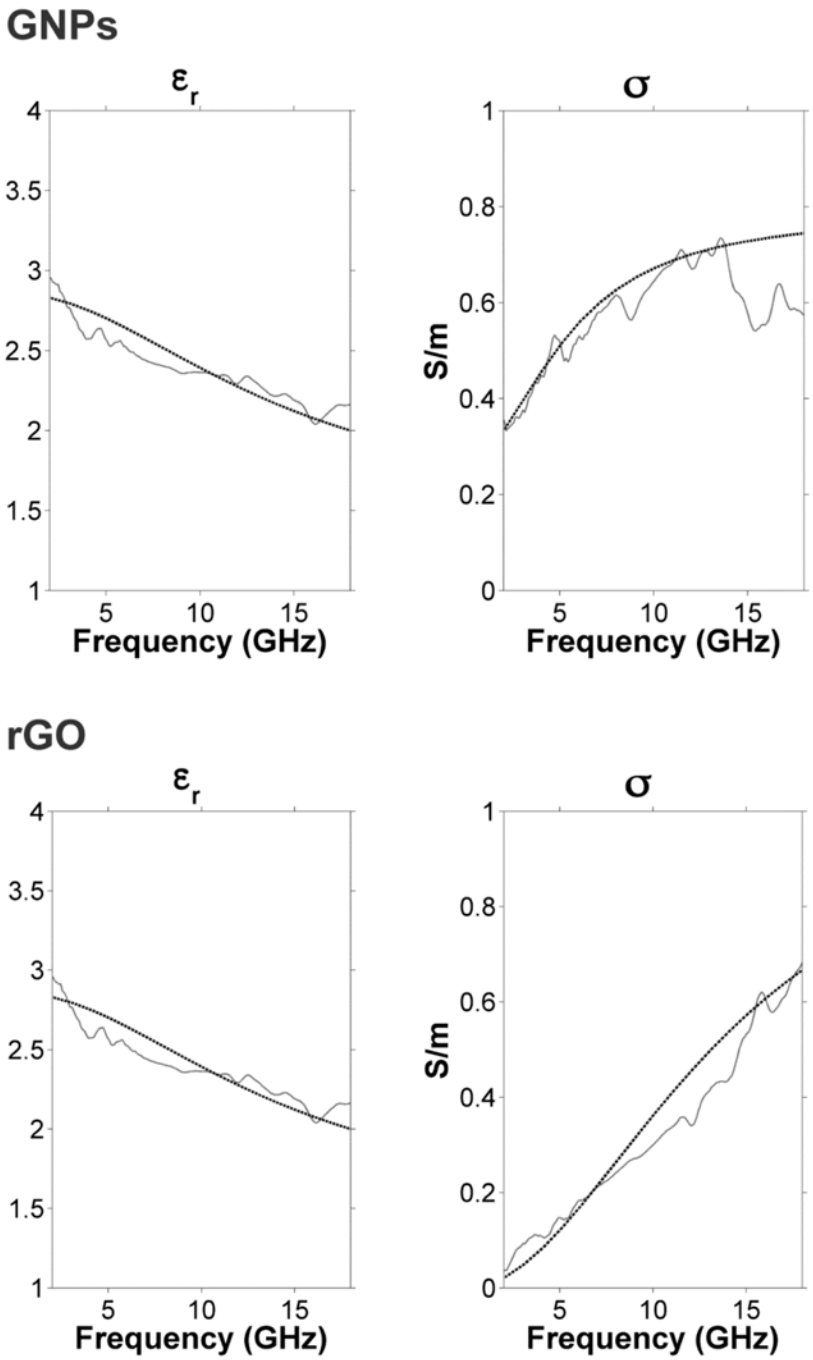

Figure 9 - Relative permittivity (left) and conductivity (right) extracted for pristine GNPs (top) and rGO (bottom). Solid line shows extraction from measurement, dashed line shows the phenomenological prediction as described in section 6.3.1.

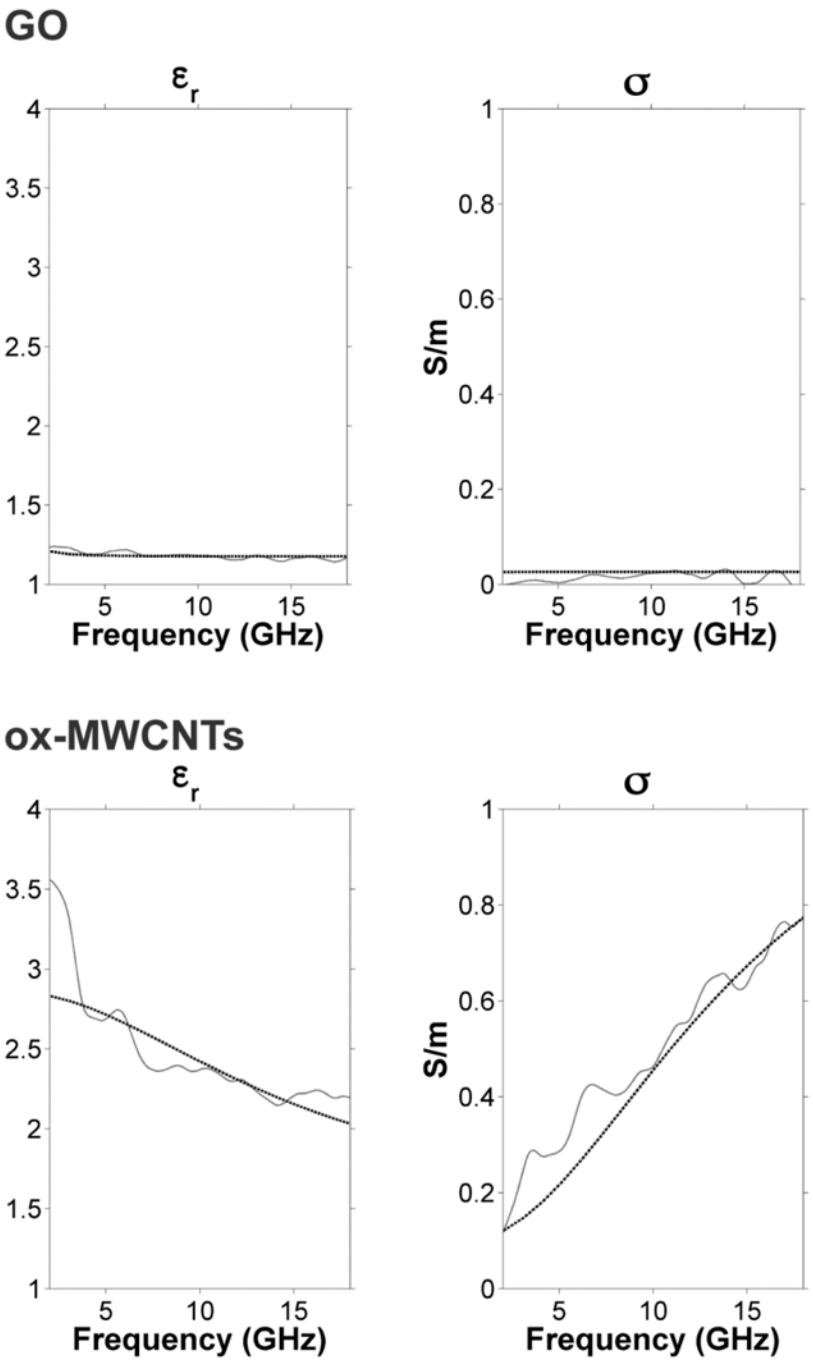

Figure 10 - Relative permittivity (left) and conductivity (right) extracted for pristine GO (top) and ox-MWCNTs (bottom). Solid line shows extraction from measurement, dashed line shows the phenomenological prediction as described in section 6.3.1.

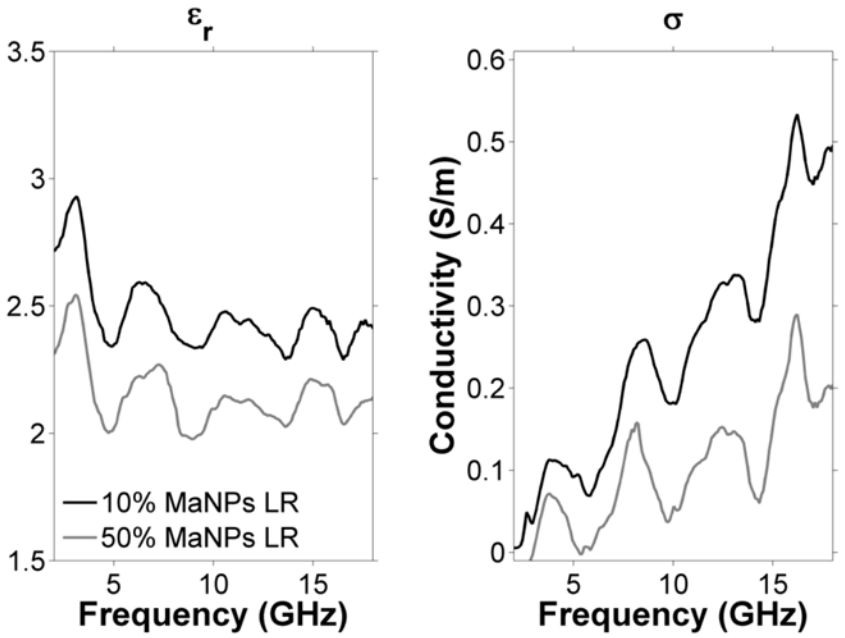

Figure 11 - Relative permittivity (left) and conductivity (right) extracted for the 10% and 50% intended Fe/NcS LR MaNPs@GO nanocomposites produced with the SOLV-A method.

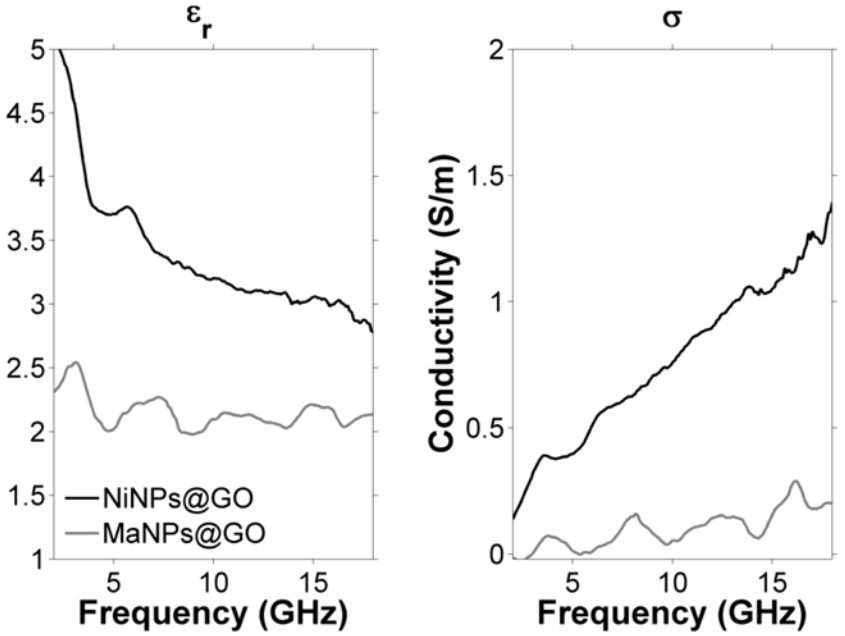

Figure 12 - Relative permittivity (left) and conductivity (right) extracted for NiNPs@GO and MaNPs@GO nanocomposites with a 50% MNPs loading rate.

7.3 Microwave absorption and shielding efficiency of the MNPs@NcS nanocomposites

Understanding how to independently control the values of μ and ε by manipulating some of the nanocomposites' physicochemical characteristics during their chemical assembly was demanded by the Nano4Waves metamaterial design paradigm. The previous sections show some examples of how both electromagnetic parameters can be manipulated by modifying the stated physicochemical parameters of both, the MNPs and the NcS. Nonetheless, the efficiency of the different nanocomposites as novel MAM materials has yet to be demonstrated.

As a reminder, in section 1.3, it was shown that the microwave absorption ratio, *A*, could be evaluated in terms of the reflectance, *R* and the transmission, *T*, of the incoming microwave by the following expression

$$A = \frac{P_{abs}}{P_{in}} = \frac{P_{in} - P_{ref} - P_{out}}{P_{in}} = 1 - R - T = 1 - |S_{11}|^2 - |S_{21}|^2 \qquad \textbf{Equation 7.3}$$

Furthermore, according to Thomassin *et al.* [10], the empirical shielding effectiveness (SE_T) of our novel nanocomposites can be found by

$$\mathrm{SE}_T = 10 \log\left(\frac{1}{|S_{21}|^2}\right) \qquad \textbf{Equation 7.4}$$

As indicated by Equations 7.3 and 7.4 , *R, T* and SE_T can be extracted from the S_{11} and S_{21} parameters measured during the VNA-based EM characterization of our materials.

Figure 13 and Figure 14, respectively, show the microwave (0.4 to 20 GHz) absorption ratio and shielding effectiveness of the iron-based nanocomposites synthetized by the Pechini method (see Chapter 4). On the one hand, it can be observed that the microwave absorption efficiency of these new materials ranges from 60% to 100%, while their shielding effectiveness varies between 20 and 70 dB, depending on the nature of the metallic particles grafted onto GO.

On the other hand, it is interesting to note that the order for either *A* or *SE* is FeCo > FeCoNi > ZVI > FeNi. As a reminder, these MNPs were grafted onto the same NcS at a similar intended LR (50%). Thus, this trend derives exclusively from the deposited nanoparticles and demonstrates that both, *A* and *SE*, depend on these nanocomposites' effective magnetic content as expressed by their saturation magnetization (M_S) values. As shown in Equation 7.1, higher M_S produces higher magnetic permeability (μ) values. Higher μ materials efficiently channel the external magnetic field by providing low resistance paths (see section 1.3.2). The magnetic energy of the incoming microwave can then be more effectively dissipated by means of magnetic loss mechanisms such as the FMR.

Considering these results and those presented throughout Chapters 2 to 4, it is possible to identify three distinct physicochemical parameters that have to be optimized in order to increase the nanocomposite's M_S, μ, and ultimately, their microwave absorption efficiency. By adjusting the synthetic parameters, one should thus aim at a) loading a high rate of MNPs onto the NcS; b) using MNPs possessing high intrinsic M_S (*e.g.* Fe, Co, Ni metals and their alloys, for instance); and/or c) depositing larger NPs that nonetheless remain beneath the multidomain threshold.

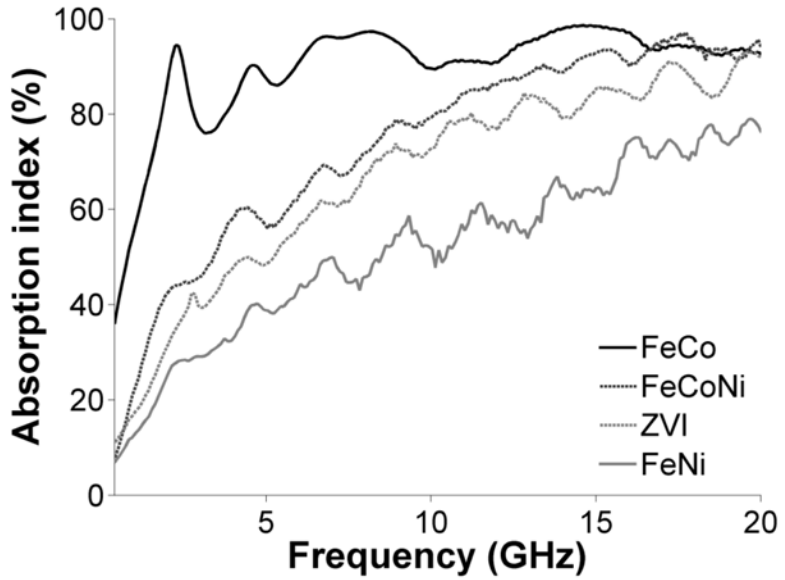

Figure 13 - Percentage absorption rate of the incoming microwave at H_z=0 for the different Pechini nanocomposites. A loading rate of 50 wt.% was aimed at in all cases.

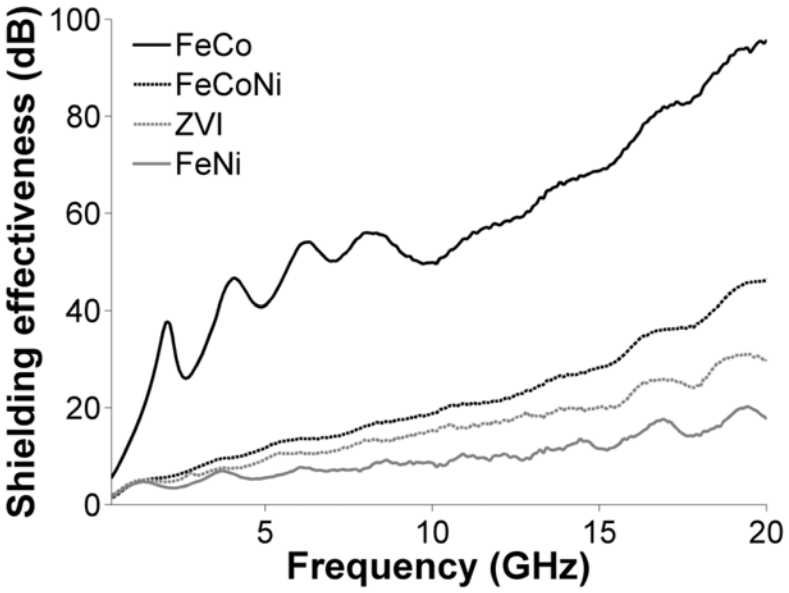

Figure 14 – Shielding effectiveness of the incoming microwave at H_z=0 by the different Pechini nanocomposites. A loading rate of 50 wt.% was aimed at in all cases.

To illustrate the effect of relative permittivity (ε_r) and conductivity (σ) on the microwave absorbing efficiency of these materials, two nanocomposites in which MaNPs were grafted on GO, at 10% or 50% Fe/NcS LR, were compared. As discussed earlier (see Section 7.2), the ε_r and σ values for the lower Fe/NcS LR MaNPs@GO nanocomposite are significantly higher than for its 50% Fe/NcS LR counterpart. This effect, attributed to the insulating character of the deposited magnetite phase, has a clear impact on both, the microwave absorbing efficiency (see Figure 15) and the shielding effectiveness (see Figure 16) of these materials. The obtained results thus indicate that a MNPs@NcS with higher ε_r and σ values is able to absorb an incoming microwave more efficiently and thus provide better EM shielding.

Another interesting feature of these materials is that the reflection rate of the incoming microwave is low, roughly below -10 dB throughout the analyzed frequency range (see Figure 17 and Figure 18). This low reflectivity means that the incoming wave can penetrate the material throughout the frequency range. Thus, the observed A rates are mostly due to signal attenuation, within the nanocomposite, produced by magnetic and electrical losses. At these frequencies, the former are mainly due to the FMR phenomenon induced by the MNPs (see Section 1.3.2.2), while the latter is produced by dielectric losses related to the conductive nature of the NcS (see Section 1.3.1).

These results prove that our materials are suitable to produce EMI shielding solutions based on the effective absorption of the incoming microwaves, achieved in a much wider frequency range than with similar microwave absorbing nanocomposites [11, 12] published in the scientific literature. Indeed these MAMs show a low reflection in a very

narrow frequency range so that the incoming wave can only penetrate and be absorbed in a narrow band.

The reflectivity issue and its dependence on the nanocomposite's conductivity is a delicate balance that should be considered when designing MAMs using the MNPs and NcS as building blocks. Indeed, the NcS should be conductive enough as to promote dielectric losses. However, if its conductivity is too high, its reflectivity will increase and the incoming microwave will not be able to penetrate the material, decreasing the material's efficiency as a microwave absorber. For instance, Figure 19 shows the reflectivity of the different pristine NcS for which the ε_r and σ values were determined, as described in Section 7.2. It stands out that highly conductive NcS, such as GNPs, have higher reflectivity rates and thus could yield inefficient MNPs@NcS MAMs [10, 13], especially if they are decorated with conductive MNPs (such as metallic Fe, Co or Ni NPs) which further increase the NcS' conductivity (see Figure 12 in Section 7.2).

However, it should be kept in mind that these nanopowders will rarely be used as self-standing MAMs. Indeed, operative prototypes require these nanopowders to be further processed, for instance by dispersing them in either a polycarbonate matrix to form thin films (see Chapter 8) or in water, to create an inkjet printing material (see Chapter 9). These operations will thus change the end-material's ε and μ values. However, as it will be shown in the next two chapters, they also offer a new range of possibilities that can be exploited to create novel and versatile microwave absorbing materials.

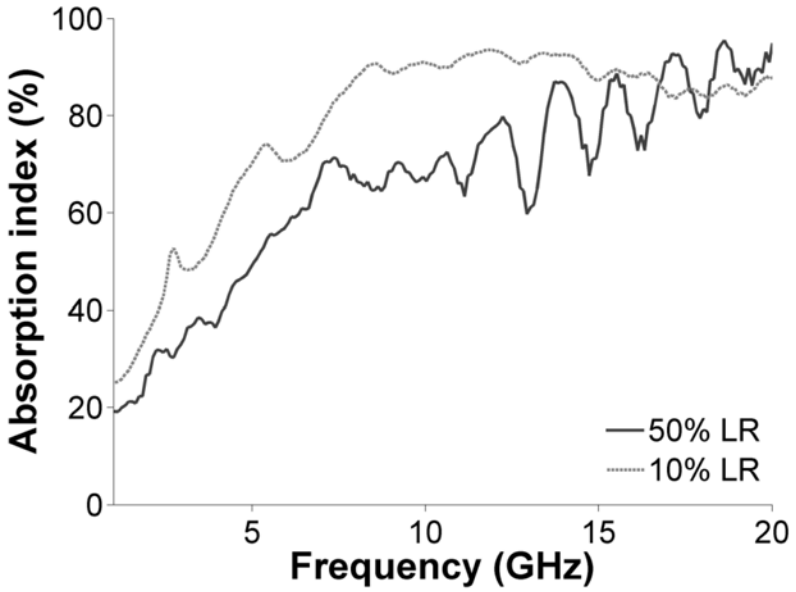

Figure 15 - Percentage absorption rate of the incoming microwave at H_Z=0 by the 10% and 50% intended Fe/NcS LR MaNPs@GO nanocomposites produced with the SOLV-A method.

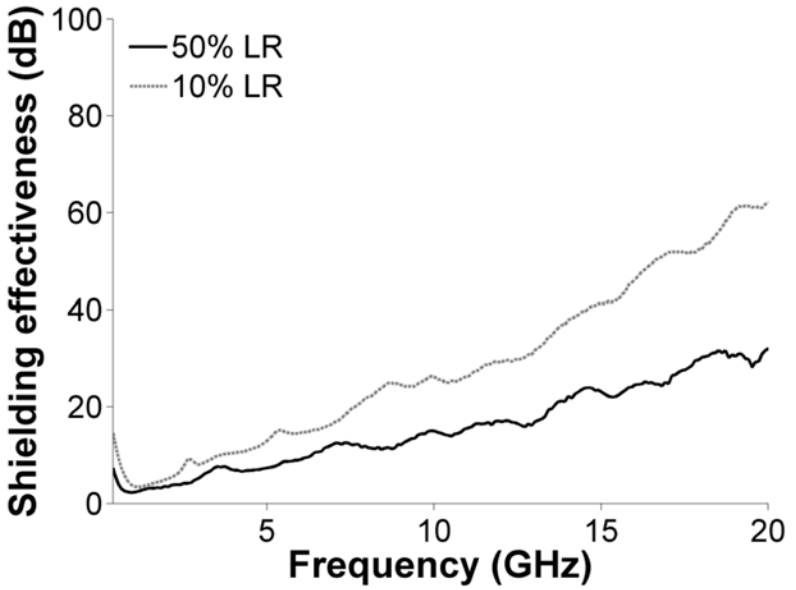

Figure 16 - Shielding effectiveness of the incoming microwave at H_Z=0 by the 10% and 50% intended Fe/NcS LR MaNPs@GO nanocomposites produced with the SOLV-A method.

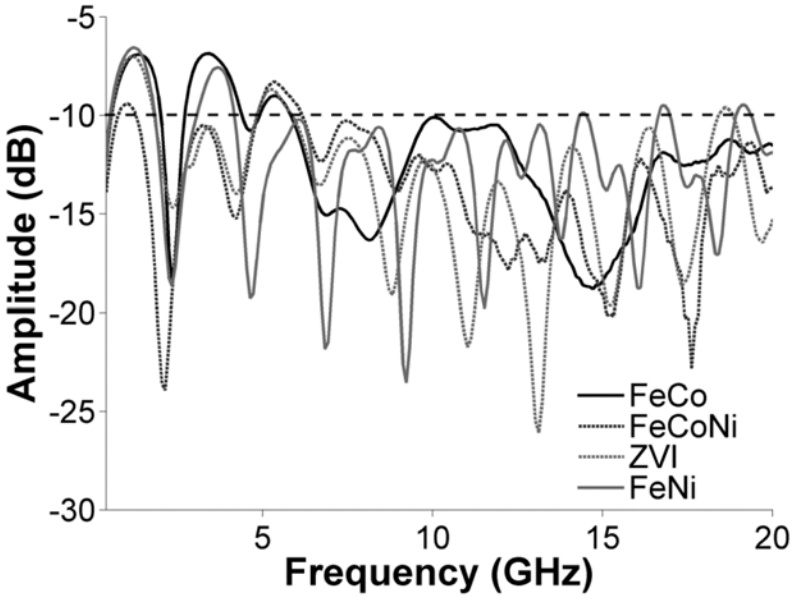

Figure 17 - Reflection (S_{11}) measurements for the different Pechini nanocomposites at null magnetic field. A loading rate of 50 wt.% was aimed at in all cases. The horizontal dashed line indicates the -10 dB limit.

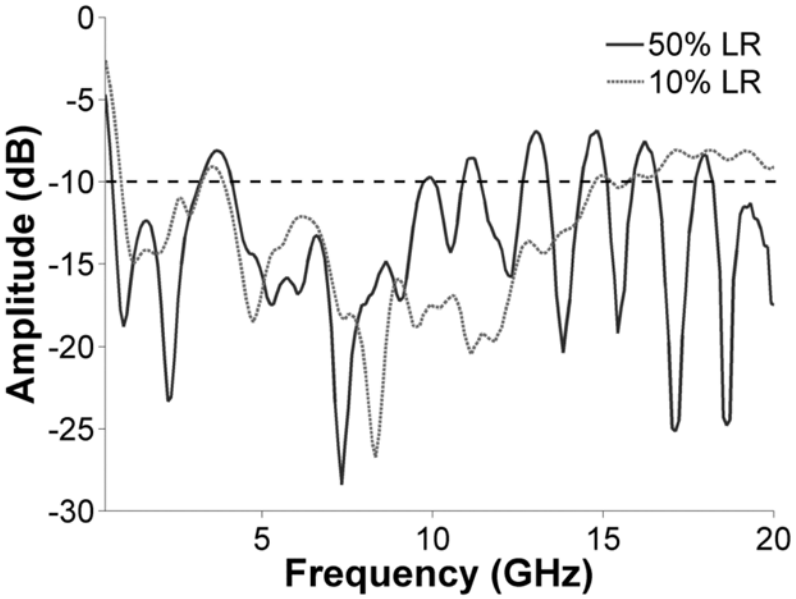

Figure 18 - Reflection (S_{11}) measurements for the 10% and 50% intended Fe/NcS LR MaNPs@GO nanocomposites produced with the SOLV-A method. The horizontal dashed line indicates the -10 dB limit.

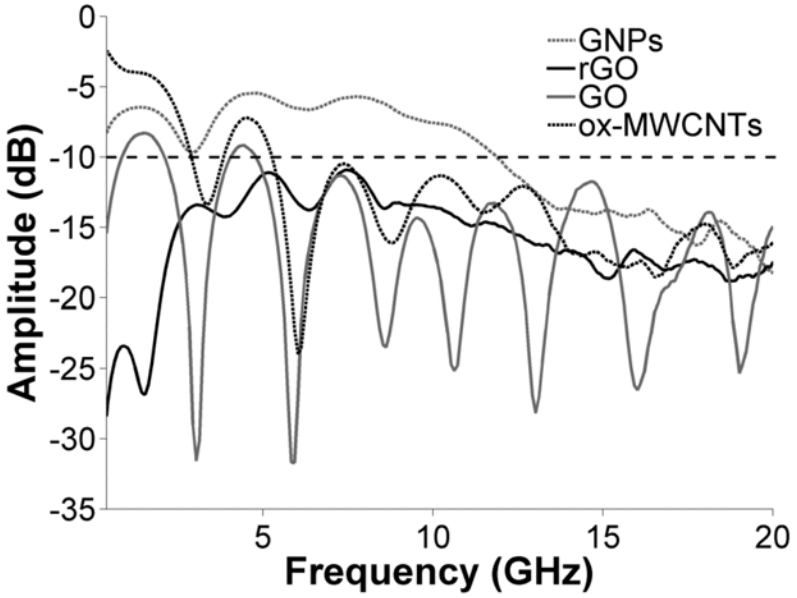

Figure 19 - Reflection (S_{11}) measurements for the pristine NcS presented in Section 7.2. The horizontal dashed line indicates the -10 dB limit.

7.4 Conclusions

The novel VNA-based characterization tool presented in Chapter 6 allowed screening the microwave-range EM properties of some of the MNPs@NcS nanocomposites reported in the first part of this manuscript.

The obtained results clearly demonstrate that the deposited magnetic nanoparticles induce a ferromagnetic resonance (FMR) absorption in the microwave range, which constitutes the main magnetic loss mechanism in these materials. They also prove that the FMR absorption induces a change in the MNPs@NcS' relative complex permeability value, μ_r, around the resonant frequency.

Interestingly, it was possible to identify that certain MNP physicochemical characteristics, easily fine-tuned by the synthetic routes described in the first part of this manuscript, have an influence on the FMR phenomena. For instance, a shift in the zero-field FMR absorption of the nanocomposites can be induced by changing the chemical nature of the deposited MNPs or their size. Also, the intensity of the FMR phenomenon clearly depends on the deposited MNPs purity as well as on their loading rate onto the NcS.

As for the nanocarbon supports, we were able to demonstrate that it is possible to produce different conductivity, σ, and relative electrical permittivity, ε_r, values by choosing different NcS types (*e.g.* graphenic sheets *vs.* nanotubes) or by chemically modifying their surface (*e.g.* through oxidation). Interestingly, we also found that the deposited MNPs also had an impact on the nanocomposite's electrical properties. Indeed, isolating MNPs (such as magnetite) seem to reduce the material's conductivity over the whole frequency range while conductive MNPs (such as metallic NiNPs) tend to increase it.

Finally, we determined that the microwave absorption efficiency of these novel materials is directly proportional to the value of the magnetic permeability, which greatly depends on the grafted MNPs' saturation magnetization (M_s) values. Thus, to produce more efficient MAMs, synthetic efforts should aim at loading a high rate of MNPs with high M_s (as is the case for metallic NPs) and which size is the largest possible, remaining below the

multidomain threshold. As for the NcS, a delicate balance of the electric permittivity, *via* the NcS conductivity, should be kept. Indeed, the nanocarbon support should be conductive enough as to promote the dissipation of the microwave *via* dielectric losses. However, it should not be too conductive; otherwise, the incoming microwave signal will be reflected and will not enter the nanocomposite, reducing its microwave absorption efficiency.

These results are a first exploration of the intricate relationship linking the nanocomposites' MNP and NcS components characteristics to their microwave absorption behavior. They also prove that these materials are suitable to produce low reflectivity, efficient EMI shielding solutions based on the wideband absorption of the incoming microwaves.

7.5 Bibliography

1. C. Kittel, *Phys. Rev.*, 1948, **73** (2), 155-161.
2. J.V.I. Timonen, R.H.A. Ras, O. Ikkala, M. Oksanen, E. Seppälä, K. Chalapat, J. Li and G. S. Paraoanu. "Magnetic nanocomposites at microwave frequencies" in Trends in nanophysics: theory, experiment and, technology. Eds. A. Aldea and V. Bârsan. Springer Science: London, United Kingdom. 2010, pp. 257-285.
3. A. Saib, I. Huynen, D. Vanhoenacker-Janvier, *Proceedings of the 33th European Microwave Conference*, Munich, Germany, October 6-10, 2003; 809-812.
4. W. Yager and R. Bozorth, *Phys. Rev.*, 1947, **72**(1), 80-81.
5. H. Kura, M. Takahashi and T. Ogawa, J. Phys. Chem. C, 2010, 114(13), 5835–5838.
6. A. Saib and I. Huynen, *J. Opt. A- Pure Appl. Op.*, 2005, **7**(2), S124-S132.
7. Q. Le, T. Wang, Y. Zhang and L. Zhang. "Introduction to chemically derived graphene" in Chemically Derived Graphene: Functionalization, Properties and Applications. Ed. J. Zhang. The Royal Society of Chemistry: London, United Kingdom. 2018, pp. 1-29.
8. P. S. Teo, H. N. Lim, N. M. Huang, C. H. Chia, and I. Harrison, *Ceram. Int.*, 2012, **38** (8), 6411–6416.
9. B. Marinho, M. Ghislandi, E. Tkalya, C.E. Koning and G. de With, *Pow. Tech.*, 2012, **221**, 351-358.
10. J-M. Thomassin, C. Jérôme, T. Pardoen, C. Bailly, I. Huynen and C. Detrembleur, *Mater. Sci. Eng. R.*, 2013, **74**, 211-232.
11. B. Quan, X. Liang, G. Ji, Y. Zhang, G. Xu and Y. Du, *ACS Appl. Mater. Inter.*, 2017, **9**(44), 38814-38823.
12. B. Quan, X. Liang, G. Ji, J. Ma, P. Ouyang, H. Gong, G. Xu and Y. Du, *ACS Appl. Mater. Inter.*, 2017, **9**(11), 9964-9974.
13. A.A. Barba, G. Lamberti, M. d'Amore and D. Acierno, *Pol. Bull.*, 2006, **57**, 587-593.

part II

summary
conclusions

As shown in Chapter 6, a completely new EM characterization technique had to be developed in order to exclusively extract the nanopowders EM parameters, ε and μ, and characterize their microwave response. Thanks to an intensive interdisciplinary collaboration, the design and development of the resulting VNA-based characterization method, its test cells and data extraction methodologies were successfully implemented.

Indeed, results obtained with this methodology, shown in Chapter 7, allowed to elucidate how a particular set of physicochemical characteristics of our materials (*e.g.* MNPs composition, size or loading rate, NcS type and oxidation), produced by chemical assembly, influences the MNP@NcS nanocomposite ε-μ values and response in the microwave range.

To the best of our knowledge, it is the first time that a direct relationship is clearly established between these three aspects. By doing so, we prove that a microwave metamaterial design approach, based on the skillful assembly of MNMPs and NcS, is possible. These results also support the claims that certain well-known physical phenomena, such as the ferromagnetic resonance (FMR) of ferr(o/i)magnetic NPs and the conductivity of nanocarbons, can be exploited to induce losses in the microwave range to produce efficient MAMs. Likewise, it is also the first time that synergistic effects between these building blocks are demonstrated, as showcased by the variations in conductivity produced by changing the composition of the MNPs deposited onto MWCNTs.

Consequently, we can now offer a new sort of "material design guidelines" allowing to independently fine-tune ε and μ. Once translated into precise MNP and NcS specifications, these guidelines can be used to purposefully fine-tune the microwave absorption behavior of the resulting MAMs.

part

III

designing new types of microwave absorber materials (MAMs)

chapter 8

Thin microwave absorber films based on multi-walled carbon nanotubes decorated with magnetic nanoparticles

In this chapter, the microwave absorption properties of micrometric films composed of MWCNTs decorated with different types of ferromagnetic nanoparticles (Fe, Co or Ni NPs) and dispersed in polycarbonate are presented. Obtained results illustrate the influence of the NPs composition and size on the films microwave absorption properties, particularly on their zero-field FMR frequency.

Collaborators

Sébastien Depaifve (IMCN/MOST), Julien Mahin (IMCN/MOST), Arnaud Wolf (IMCN/MOST) and Sergey Basov (IMCN/BSMA).

As described in section 1.4, one of the objectives of this research project was to develop a new generation of highly efficient MAMs based on three main building blocks: (1) a nanocarbon support (NcS) such as multi-walled carbon nanotubes (MWCNTs), (2) decorated with different types of magnetic nanoparticles (MNPs), such as Fe, Co or Ni NPs, and (3) dispersed in a polymeric matrix, such as polycarbonate (PC).

The final composite material should possess distinctive EM properties in the microwave range while retaining certain properties of polymer materials such as flexibility, conformability or moldability. Our approach therefore wishes to offer a flexible assembly framework that can be adapted to a wide diversity of functions and shapes in microwave absorption contexts.

Previous researchers participating in the Nano4Waves project have already reported on microwave absorbers based solely on conductive NcS dispersed in a polycarbonate (PC) matrix [1-5]. Consequently, in the current research project, the microwave absorption properties of micrometric films composed of MWCNTs decorated with different types of ferromagnetic nanoparticles (Fe, Co or Ni NPs) dispersed in PC are explored for the first time.

In this chapter, we will demonstrate the correlation between the physicochemical characteristics of the dispersed nanocomposites and the resulting films' microwave absorption properties. Particularly, by using the Fe, Co and Ni@MWCNTs nanocomposites presented in Chapters 3 and 5, we will analyze how changes in the composition and size distribution of the deposited MNPs influence the films' zero-field or natural FMR frequency. To the best of our knowledge, these effects have not been reported previously in the scientific literature, constituting a concrete advance in the field of thin and flexible MAMs.

8.1 Materials and methods

8.1.1 Materials

Makrolon® OD2015 polycarbonate was obtained from Bayer Material Science. The Fe and Co@MWCNTs nanocomposites employed for the creation of the

thin films were obtained following the synthetic procedures described in Chapter 5, sections 5.1.2.1 and 5.1.2.2, respectively. Two Ni@MWCNTs products (AP and AC-S), with different NiNPs size distributions, were also used. These were synthesized following the methodologies described in Chapter 3, sections 3.1.2.1 and 3.1.2.2.1.

8.1.2 MNPs@MWCNTs nanocomposites dispersion in a polycarbonate (PC) matrix (MNPs@MWCNTs_PC)

Four different MNPs@MWCNTs nanocomposites were dispersed in polycarbonate (PC) using melt-mixing as described in [4]. A fixed PC amount (11.8 g) was used to produce each film. However, the engaged quantities of each MNPs@MWCNTs powder were calculated to produce a composite containing 2% (%w/w) of MWCNTs (see Table 1). Given that each synthetic technique produced different M/C %LRs, MNPs@MWCNTs quantities were slightly different in each case (see Table 1). It is important to mention that this particular MWCNTs %w/w loading rate was chosen because of the results obtained by Mesfin *et al.* [3]. Indeed, these researchers proved that a MWCNTs mass loading rate between 2 and 3% ensures the optimum microwave absorption performance and that increased signal reflection is produced above the 3% threshold.

In a typical procedure, PC was first dried under vacuum at 70ºC, for 24 hours. Afterwards, the MNPs@MWCNTs and dried PC powders were introduced in a co-rotating twin-screw DSM-15 micro-extruder preheated at 250 °C. The mixture was melt-mixed at that temperature for 10 minutes and 250 rpm. It was then extruded through a 0.5 mm-diameter die, resulting in an output filament of the same average diameter. The filament was left to cool down to ambient temperature. It was then immediately cut into <1 cm-long pellets.

8.1.3 MNPs@MWCNTs_PC film formation by compression molding

MNPs@MWCNTs_PC films were produced by compression molding as described in [6].

In a typical procedure, 2.5 g of MNPs@MWCNTs_PC were evenly distributed at the center of a mold placed on top of a Teflon sheet. The mold was a square frame cut in a 0.5 mm-thick steel plate. A second Teflon sheet was then placed atop, so that the material was squeezed between two antiadhesive layers. Two steel plates where then placed beneath and above the sandwiched structure.

The whole set-up was transferred into a Fontijne hot press (Fontijne Grotnes Group, Netherlands), preheated at 250 ºC. Starting at t_o (see Figure 1) the sample was left to melt for 30 seconds (up to t_1). After t_1, the pressure was increased to 2.5 T and immediately released. This action was repeated for 15 seconds (t_1 to t_2), increasing the applied pressure in each cycle, to remove trapped air bubbles. The pressure was then raised and kept at 10 T for 1 minute and 45 seconds (t_2 to t_3), summing up to a total compression molding time of about 2 minutes.

The samples were next transferred to a cold Fontijne press and compressed at 7.5 T for 2 additional minutes (t_4 to t_5). The sandwiched structure was then removed, carefully peeling the Teflon sheets to recover the different MNPs@MWCNTs_PC films.

8.1.4 EM characterization of the MNPs@MWCNTs_PC films

Scattering matrix (S-parameters) measurements of the Ni@MWCNTs_PC films were performed using a microstrip method as described in [7]. Typical microstrip sample preparation consisted in cutting an elongated piece of approximately 1.0 cm x 2.5 cm from the polymer film samples. Afterwards, a 1 mm-broad copper strip and an aluminum film were tapped onto the film piece as line and ground, respectively (see Figure 2).

Measurements were performed with an Agilent N5245A PNA-X 70 GHz vector network analyzer (VNA). A DC magnetic field was applied perpendicularly using a NTM 10400M-260 electromagnet. The data acquisition and extraction procedures are identical to those described for the nanopowders in Chapter 6.

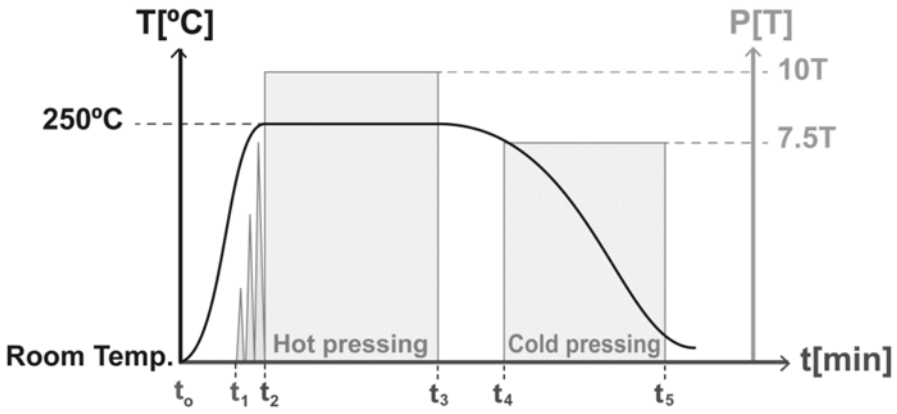

Figure 1 - Schematic representation of the compression molding procedure.

Table 1 – Size distributions, loading rates (% LR) and engaged quantities of the MNPs@MWCNTs and PC

MNPs		MNPs@MWCNTs nanocomposite		Polycarbonate
Type	Size (nm)	Weight (mg)	% LR	Weight (g)
Fe	14.9 ± 4.9	355	29	11.8
Co	24.1 ± 10.0	400	39	11.8
Ni_{AP}	13.6 ± 4.4	303	22	11.8
Ni_{AC-S}	130 ± 47.0	375	31	11.7

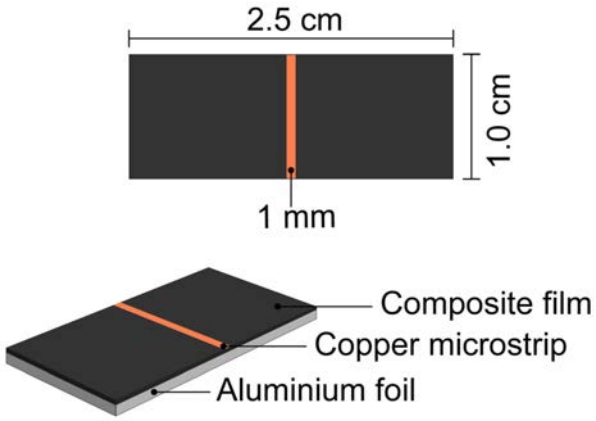

Figure 2 - Microstrip sample dimensions (top) and components (bottom).

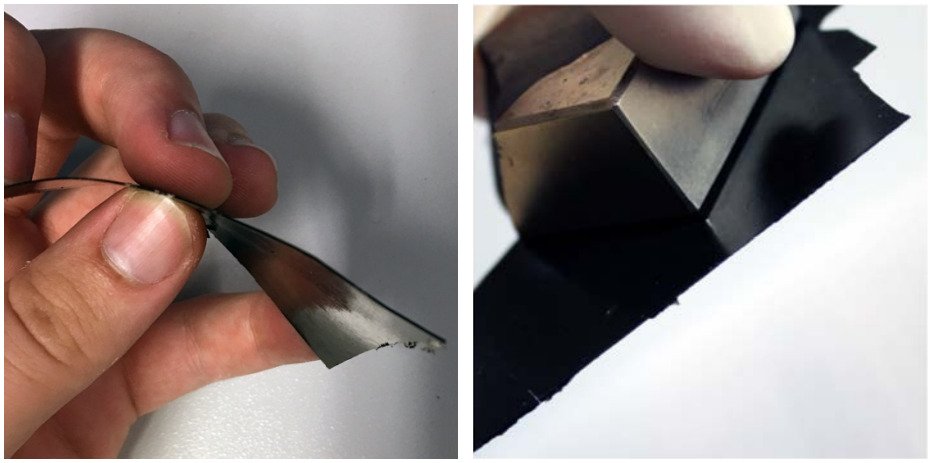

Figure 3 - Typical appearance of MNPs@MWCNTs_PC thin and flexible films (left). Due to their magnetic MNPs@MWCNTs content, they are able to respond and be lifted by a magnet (right).

8.2 Results and discussion

The Fe, Co, Ni_{AP} and $Ni_{AC\text{-}S}$@MWCNTs nanocomposites, synthetized as described in Part II, were dispersed in polycarbonate to produce four different thin films. As shown in Figure 3, the obtained films are thin (~ < 0.5 mm), flexible and, due to the included magnetic nanocomposites, they respond to a magnet.

The different films' magnetic and microwave absorption properties were characterized using a vibrating sample magnetometer (VSM) and a microstrip-based vector network analyzer (VNA) methodology, respectively.

8.2.1 Influence of the MNPs composition and size on the magnetic properties of the MNPs@MWCNTs_PC films

Figure 4, top, shows the magnetization hysteresis loops obtained for the four MNPs@MWCNTs_PC films. As it can be observed, the films saturation magnetization (M_s) values decrease in the order Fe>Co>$Ni_{AC\text{-}S}$>Ni_{AP}. The obtained trend matches the one observed for bulk metallic Fe (218 emu/g)>Co (161 emu/g)>>Ni (54 emu/g) M_s values [8]. Nonetheless, the measured values are considerably inferior.

This difference can be explained by the reduced sizes of the deposited NPs, as explained in the Introduction, section 1.3.2.1.2. Indeed, it is considered that NPs possess a disordered magnetic spin layer at their surfaces [9]. Therefore, as the NP size decreases, the disordered layer to NPs radius ratio becomes significant. Such surface spin disorder reduces the M_s value for smaller nanoparticles [10]. This effect is clearly illustrated when comparing the M_s values of the AP and AC-S nickel products, as previously discussed in section 3.2.3. However, the measured film M_s values are significantly lower than those expected considering the size of the different deposited MNPs (see Table 1) and the values reported in the scientific literature for similarly-sized Fe, Co or NiNPs [11].

This difference must then be due to the concurrence of additional factors. For instance, XPS characterization of the four MNPs@MWCNTs nanocomposites has revealed the presence of ferrimagnetic (FiM) or antiferromagnetic (AF) oxides alongside the ferromagnetic (FM) metallic MNPs (see sections 3.2.2, 5.2.1 and 5.2.2), indicating a core-shell structure. Such metal oxide phases possess lower or null

M_s values when compared to the FM metallic species they derive from. Therefore, by lowering the effective amount of FM phase in the deposited NPs, the oxide phases tend to lower the recorded M_s.

Also, it was observed that the Ni_{AP} and $Ni_{AC\text{-}S}$ films M_s values halved as compared to the untreated nanocomposite powders (see Figure 12 in section 3.2.3). This result suggests that the NPs undergo thermal oxidation in the polycarbonate matrix during melt mixing and compression molding. As discussed above, this oxidation induces size reduction of the magnetic content (metallic nickel core) of the NPs, hence reduction of their magnetization.

Figure 4, bottom, shows a detail of the hysteresis loop highlighting the differences in coercive field (H_c) and remanence magnetization (M_r) for the different films. The fact that both H_c and M_r are close to zero only for the Ni_{AP} film is due to the fact that the deposited NiNPs are superparamagnetic (see section 3.2.3) while the Fe, Co and $Ni_{AC\text{-}S}$ NPs are ferromagnetic. Indeed, according to the averaged superparamagnetic limit (SPL) values reported by Mazaleyrat *et al.* [12] and Guimarães [13] , the deposited Ni_{AP} NPs are well below the SPL size (~28 nm), while the Fe, Co and $Ni_{AC\text{-}S}$ NPs are above it (~14 and ~7 nm for Fe and Co respectively).

As explained in section 1.3.2.1.2, superparamagnetic NPs have null or close-to-zero M_r and H_c values at room temperature because the magnetic anisotropy energy is lowered as the NP size is reduced. Below the SPL size, the magnetic anisotropy energy, which holds the magnetic moment along the easy magnetization axis, becomes comparable to the thermal energy [14]. Consequently, thermal excitation produces a rapid and random magnetic spin reversal or flipping [15] so that the relaxation time of such NPs magnetic moments becomes very small (~10^{-9} s) [16]. In such conditions, the NPs lose their magnetic order.

However, in the case of the ferromagnetic Fe and Co NPs, the magnetic anisotropy and/or exchange coupling energies are sufficiently important to oblige all spins within a single domain to be collinear and rotate in unison. These short-range interactions minimize the NPs magnetic energy [17]. Thus, in the absence of a magnetic field, a non-zero M_r value is observed. Also, the stronger magnetic ordering implies that higher external field strengths are needed to reverse the direction of the collinear spins found in a single domain of the ferromagnetic NPs, producing higher H_c values.

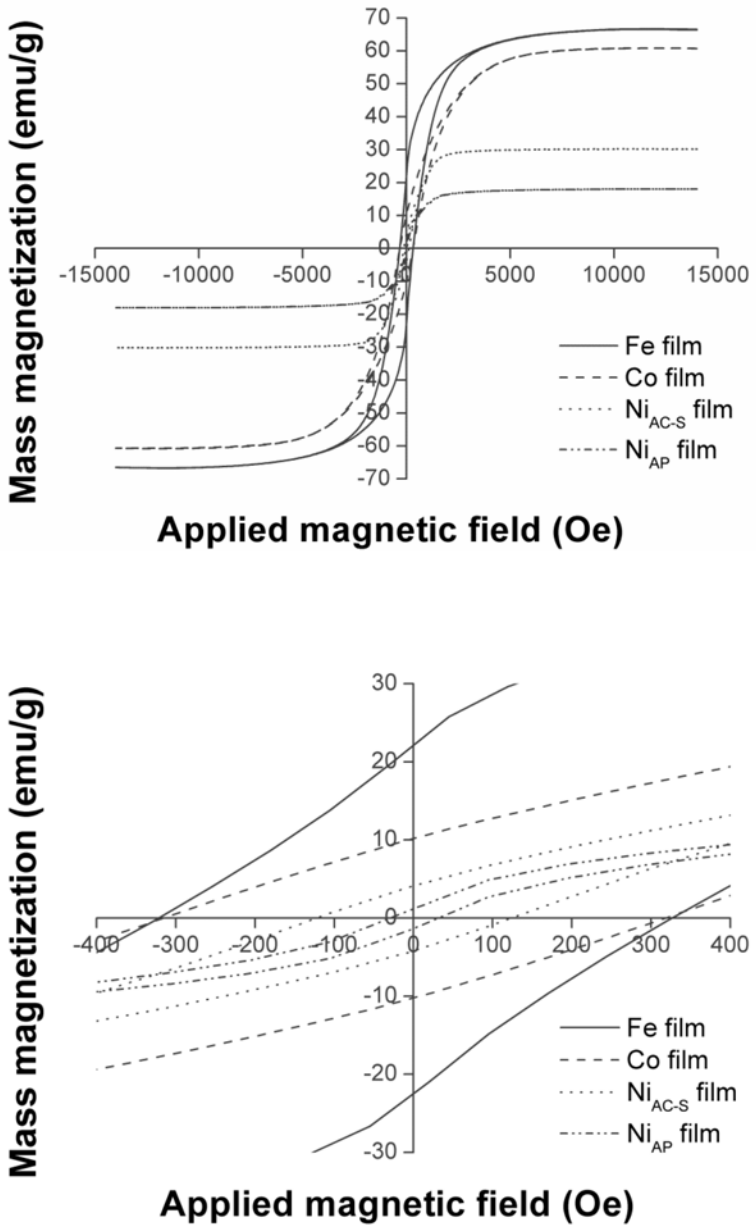

Figure 4 - Magnetization curves recorded against magnetic field at 295K for the MNPs@MWCNTs_PC (top). A detail of the hysteresis loop (bottom) highlights the difference in the H_c and M_r found for these materials.

8.2.2 Influence of the MNPs composition and size on the microwave absorption properties of the MNPs@MWCNTs_PC films

Figure 5 shows a typical result for the S_{21} transmission parameter of a MNPs@MWCNTs_PC composite film. As can be observed, a series of absorption processes were recorded, occurring even in the absence of an external applied magnetic field. Also, their frequency shifted towards higher values as the external magnetic field was increased. As discussed before (see section 7.1), these experimental observations indicate that a ferromagnetic resonance (FMR) is occurring in these films in the range of the microwave frequencies under study (40 MHz to 20 GHz).

As also shown in Figure 5, the absorption frequency, f, at each value of applied magnetic field, H_z, was determined by identifying the absorption minima in the S_{21} curves. Figure 6 shows the extracted minima f values for the nanocomposite films plotted as a function of H_z and the linear regressions derived therefrom. Finally, Figure 7 shows the different MNPs@MWCNTs_PC films natural or zero-field FMR frequency plotted as a function of their saturation magnetization, M_s.

The obtained results clearly evidence that natural FMR frequency is different for each thin film and that it increases as the films' M_s increases. As discussed in previous chapters, the M_s of the nanocomposites depends either on the NPs composition (*e.g.* the Pechini nanopowders described in Chapter 4) and/or size (*e.g.* the NiAP and AC products shown in Chapter 3). Therefore, results shown in Figure 6 and Figure 7 illustrate that these physicochemical parameters, derived from the MNPs grafted onto the NcS, are also provoking striking differences in the FMR absorption properties of these films. To the best of our knowledge, this is the first time that such a correlation is shown for this type of materials.

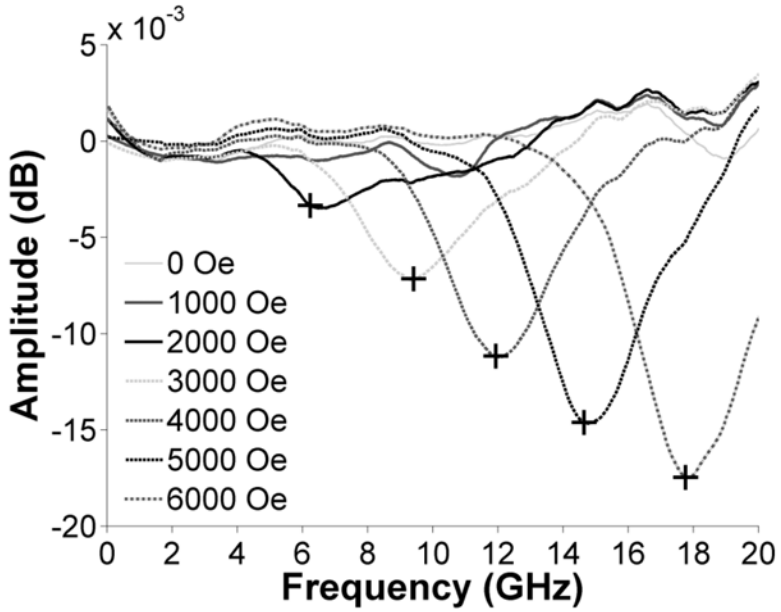

Figure 5 - Typical FMR behavior observed in S_{21} transmission for the Ni@MWCNTs_PC AP composite film. Black crosses indicate absorption frequency minima.

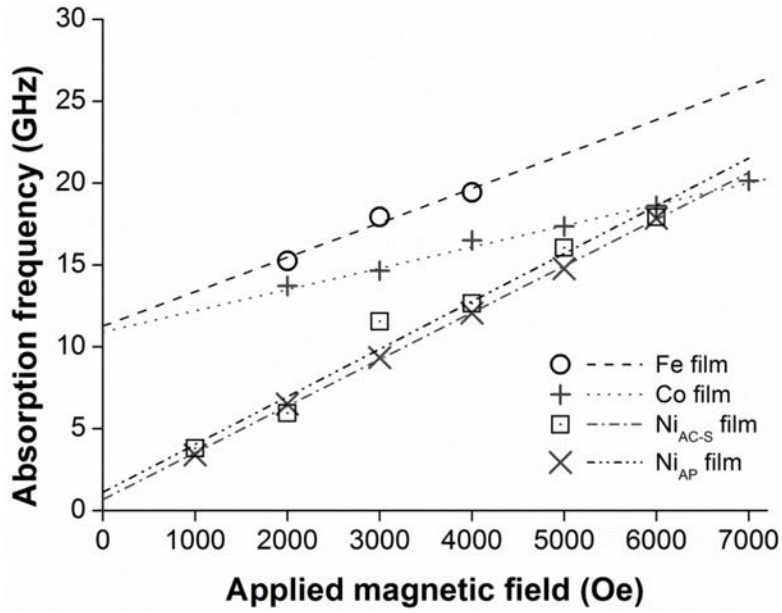

Figure 6 - Dispersion relation between the FMR absorption frequency and the applied magnetic field for the MNPs@MWCNTs_PC films. Symbols represent the experimental data. The dashed lines are the linear regressions of such data.

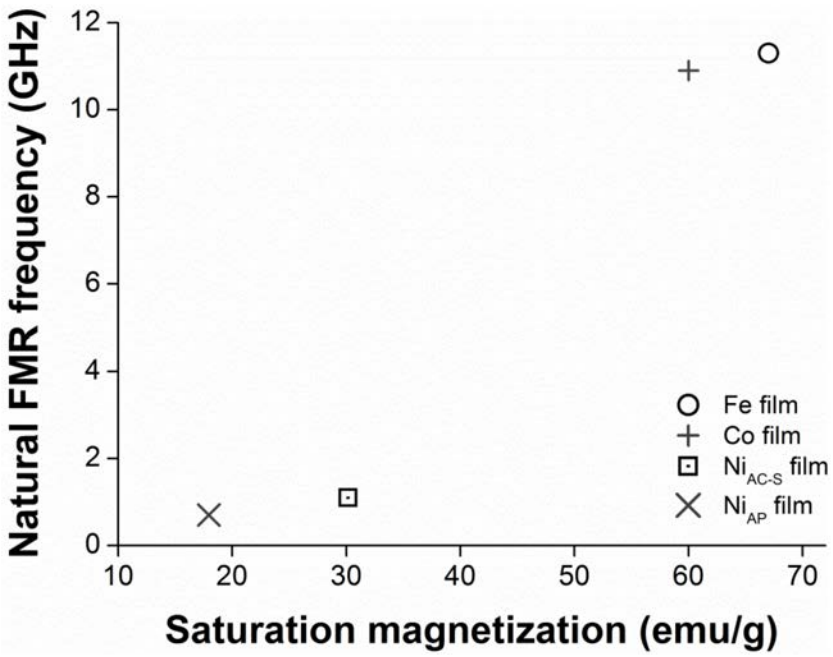

	Fe film	Co film	Ni_{AC-S} film	Ni_{AP} film
Natural FMR *f* (GHz)	11.3	10.9	1.1	0.7
M_s (emu/g)	67	61	30	18

Figure 7 – Dispersion relation between the natural (zero-field) FMR frequency and the saturation magnetization (M_s) of the different MNPs@MWCNTs_PC films.

8.2.3 Microwave absorption and shielding efficiency of the MNPs@NcS_PC films

Figure 8 and Figure 9, respectively, show the microwave (0.4 to 20 GHz) absorption index, *A*, and shielding effectiveness, *SE*, of the four different films.

The Co, Ni_{AC-S} and Ni_{AP} films shows similar absorption efficiencies, absorbing as much as 90% of the incoming microwave at the highest frequencies. Regarding the *SE*, these three films also show a very similar behavior, shielding as much as 40 dB at higher frequencies. Comparatively, the Fe film underperforms by almost 50% in both, *A* and *SE*, throughout the whole frequency range.

Results obtained for the MNPs@NcS nanocomposite powders (see section 7.3) clearly show that both *A* and *SE* tend to increase as the magnetic content of these materials, expressed by their M_s, increased. However, this is not the case for these films, given that the observed order for both *A* and *SE* is Co ≈ Ni_{AC-S}≈Ni_{AP}>>Fe while their M_s decreases in the order Fe > Co > Ni_{AC-S} > Ni_{AP}.

This discrepancy seems to indicate that the loss mechanisms responsible for *A* and *SE* in these films are electrical, due to their similar MWCNTs content (~ 2% w/w), rather than magnetic. This could be due to the low magnetic content of these films (< 1.3% w/w), which might not be enough as to produce detectable magnetic-dependent losses, contrary to what was observed for the pure nanocomposite powders (see Section 7.3). This hypothesis seems comforted by the fact that, at equivalent microwave frequencies, similar *A* and *SE* results were found in the scientific literature for non-decorated MWCNTs_PC films [18-20].

In any case, the observed behavior for the Fe film remains abnormal as compared to its Co and Ni counterparts. The analysis of the different films S_{11} scattering parameters (see Figure 10) shows that all films present a similar low reflection rate (<10 dB) of the incoming microwave. However, the Fe-film transmits the incoming microwave at a higher rate than the other three films, as shown in the S_{21} measurements (see Figure 11), thus reducing its absorption. A possible explanation for such irregularity might be found in factors related to the nanocomposite's dispersion in the PC matrix. Indeed, Thomassin *et al.* [7], Barrau *et al.* [21] or Abbasi *et al.* [22], to cite just a few, have shown that the dispersion of a NcS in a polymeric matrix can significantly affect the resulting composite film's microwave absorbing behavior. A TEM study on thin sections of these films would be required to corroborate this hypothesis.

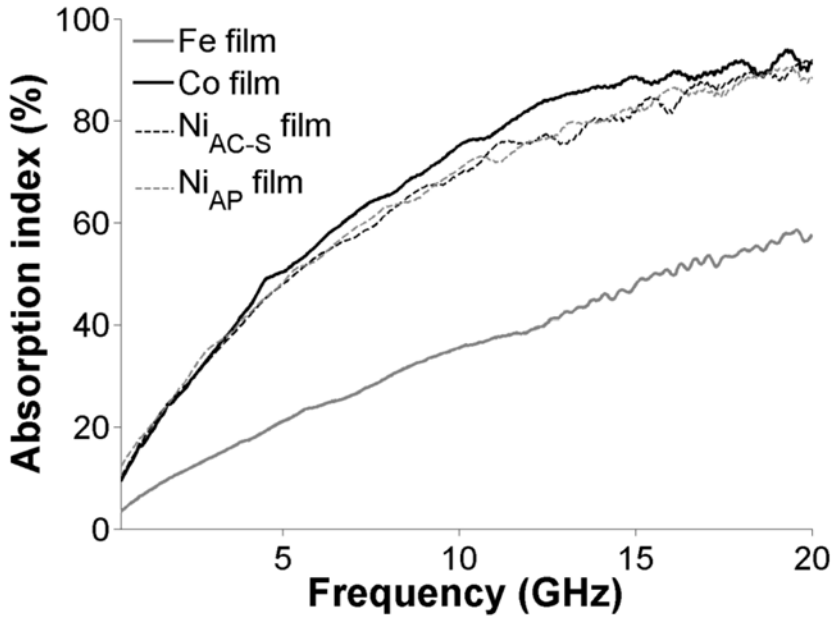

Figure 8 - Percentage absorption rate of the incoming microwave at $H_z=0$ by the different MNPs@NcS_PC films.

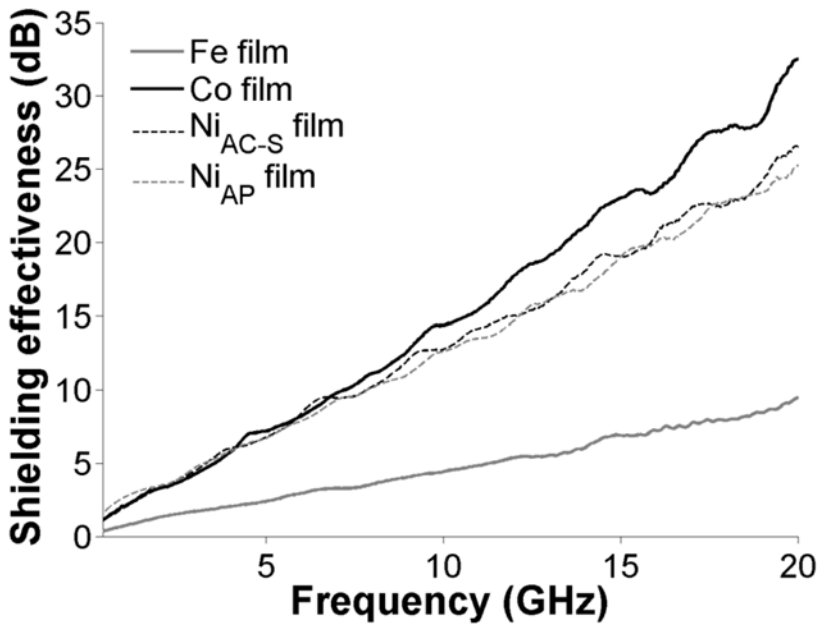

Figure 9 - Shielding effectiveness of the incoming microwave at H_z=0 by the different MNPs@NcS_PC films.

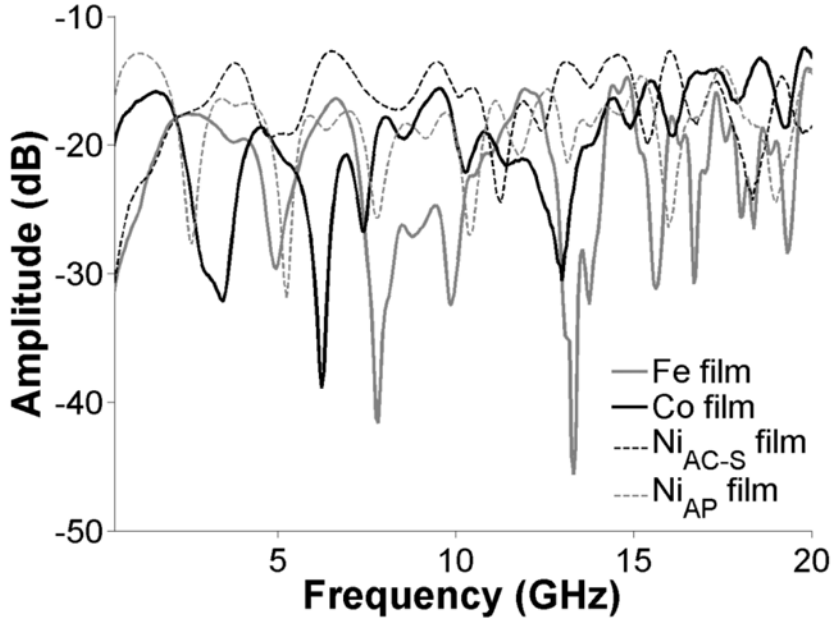

Figure 10 - Reflection (S_{11}) measurements for the different MNPs@NcS_PC films.

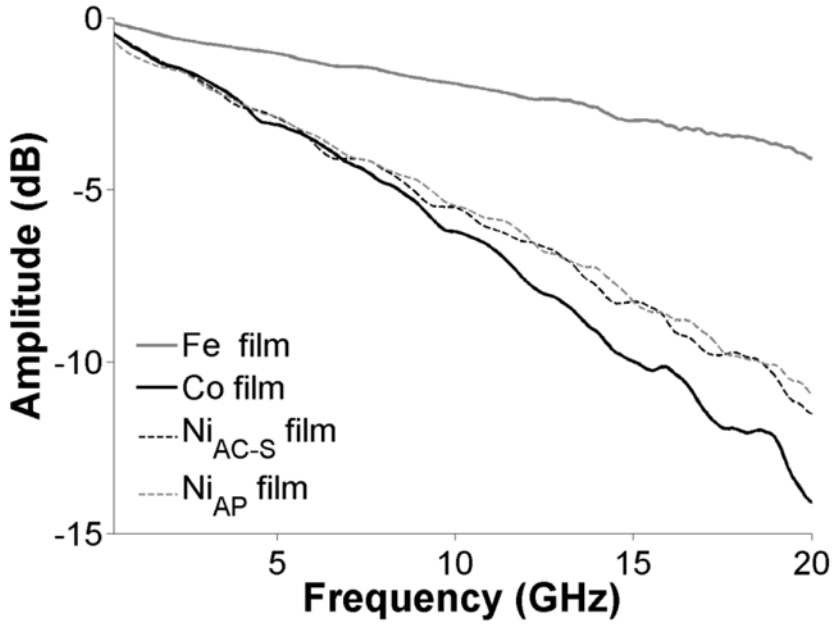

Figure 11 - Transmission (S_{21}) measurements for the different MNPs@NcS_PC films.

8.3 Conclusions

Four different MNPs@MWCNTs_PC thin films were created by dispersing in polycarbonate the Fe/Co/Ni@MWCNTs nanopowders synthetized in Chapters 3 and 5. The dispersed nanocomposites allowed to investigate the impact of the MNPs composition or size on the films EM properties in the microwave range.

Interestingly, we clearly observed an FMR process taking place in all four thin films. Furthermore, we also observed that the natural FMR frequency, f, was directly correlated to the M_s measured for the different films. Given that neither the MWCNTs nor the PC are magnetic, the FMR phenomena and the M_s-f correlation can only be attributed to the MNPs found in the dispersed MNPs@MWCNTs nanocomposites. Nonetheless, the films M_s values halved as compared to those obtained for the nanocomposites prior to their dispersion in the PC matrix. This result suggests that the high temperatures used for the extrusion of the films might be inducing a thermal oxidation of the MNPs, thus reducing the films' effective magnetic content.

However, when analyzing the microwave absorption rate, A, and shielding effectiveness, SE, the effect of the MNPs was not detectable. Indeed, in Chapter 7 we demonstrated that both A and SE tend to increase as the MNPs@NcS M_s increases. However, in the case of these films, the A and SE rates were very similar for the Co, Ni_{AP} and Ni_{AC} films, notwithstanding that their different MNPs composition or sizes produced very different M_s values. Thus, it seems that the observed A and SE behaviors are exclusively related to the MWCNTs, loaded at similar rates in all films and thus producing similar electric losses in them. As for the Fe film, it shows an anomalous transmission rate of the incoming microwave and thus shows reduced A and SE rates, as compared to the other three films. This difference might be due to a reduced quality of the dispersion of the MNPs@MWCNTs in the PC matrix.

In any case, the microwave absorption capacity presented by these films could be exploited to produce thin MAMs for the telecommunications

industry. Also, thanks to the polymeric matrix in which the microwave active nanocomposites are dispersed, different shapes could be easily created, widening the range of potential applications for these materials.

8.4 Bibliography

1. Y. Danlée, I. Huynen and C. Bailly, *Appl. Phys. Lett.*, 2012, **100**, 213105.
2. Y. Danlée, I. Huynen and C. Bailly, *Comp. Sci. Tech.*, 2014, **100**, 182-188.
3. H. M. Mesfin, S. Hermans, I. Huynen, A. Delcorte, C. Bailly, *Mater. Today Proc.*, 2016, **3**(2), 491-496.
4. H. M. Mesfin, A.C. Baudoin, S. Hermans, A. Delcorte, I. Huynen, C. Bailly, *Appl. Phys. Lett.*, 2014, **105**, 103105.
5. R. Jaiswar, Y. Danlée, H. Mesfin, A. Delcorte, C. Bailly, J-P. Raskin and I. Huynen, *Appl. Phys. A.*, 2017, **123**(3), 164.
6. D. Kettels, 2015. The combined use of graphene nanoplatelets and magnetite nanoparticles in polymer host matrices to design novel multilayer EMI shielding structures in the microwave range (MSc dissertation). Université Catholique de Louvain, Louvain-la-Neuve, Belgium.
7. J-M. Thomassin, C. Jérôme, T. Pardoen, C. Bailly, I. Huynen and C. Detrembleur, *Mater. Sci. Eng. R.*, 2013, **74**, 211-232.
8. B.D. Culity and C.D. Graham Introduction to magnetic materials, IEEE Press: Piscataway, NJ, USA, 2009. p.531.
9. R.H. Kodama, *J. Magn. Magn. Mater.*, 1999, **200**, 359-372.
10. A.G. Kolhatkar, A.C. Jamison, D. Litvinov, R.C. Willson and T. R. Lee, *Int. J. Mol. Sci.*, 2013, **14**, 15977-16009.
11. H.M. Lu, W.T. Zheng and Q. Jiang, *J. Phys. D: Appl. Phys*, 2007, **40**, 320–325.
12. F. Mazaleyrat, M. Ammar, M. LoBue, J.P. Bonnet, P. Audebert, G.Y. Wang, Y. Champion, M. Hÿtch and E. Snoeck. J. Alloy Compd., 2009, **483**, 473-478.
13. A.P. Guimarães. Principles of nanomagnetism, Springer-Verlag: Berlin, Germany, 2009.
14. V. Skumryev, S. Stoyanov, Y. Zhang, G. Hadjipanayis, D. Givord, J. Nogués, *Nature*, 2003, **423**, 850–853
15. H.M. Lu, W.T. Zheng and Q. Jiang, Appl. Phys., 2007, **40**, 320-325.
16. C. Caizer "Nanoparticle size effect on some magnetic properties" in Handbook of nanoparticles. Ed. M. Aliofkhazraei. Springer International Publishing: Cham, Switzerland. 2016, pp. 475-519.
17. G.C. Papaefthymiou, *Nano Today,* 2009, **4**, 438-447.
18. S. Biswas, S. S. Panja and S. Bose, *J. Phys. Chem. C.,* 2018, **122**, 19425-19437.
19. S. Pande, A. Chaudhary, D. Patel, B.P. Singh and R.B. Mathur, *RSC Adv.,* 2014, **4**, 13839-13849.
20. N. Bagotia, V. Choudhary and D.K. Sharma, *Compos. Part B –Eng.,* 2017, **124**, 101-110.
21. S. Barrau, P. Demont, A. Peigney, C. Laurent and C. Lacabanne, *Macromolecules,* 2003, **36**, 5187-5194.
22. H. Abbasi, M. Antunes and J.I. Velasco, *Prog. Mater. Sci.,* 2019, **103**, 319-373.

chapter 9

Thin and flexible ultra‐wideband MAMs printed with multi‐walled carbon nanotubes‐based inks

In this chapter, ultra‐wideband MAMs created by inkjet printing resistive frequency‐selective‐surfaces (FSS) on a flexible substrate are presented. Two different MAMs were obtained by using aqueous inks based on either pristine or magnetite NPs‐decorated MWCNTs. In both cases, the obtained MAMs show excellent absorption efficiency with very low reflectivity over a 31 GHz bandwidth, between 9 and 40 GHz. Strikingly, the MaNPs@MWCNTs MAM is half as thin as its pristine MWCNTs counterpart

Related PhD dissertations

Results presented in this chapter are also included in Mr. Rajkumar Jaiswar's PhD dissertation entitled "**Wideband microwave absorber structures based on carbonaceous nanomaterials: from modelling to experimental characterization**" (Université Catholique de Louvain, Louvain-la-Neuve, Belgium, 2019) given they were obtained in close collaboration .

Related publications

R. Jaiswar, F. Mederos-Henry, V. Dupont, S. Hermans, A. Delcorte, C. Bailly, C. Delmotte, V. Lardot, J.P. Raskin, I. Huynen. **A thin ultra-wideband microwave absorbing structure printed on flexible substrate with resistive-ink made of multsiwalled carbon-nanotubes.** Proceedings of the *11th International Congress on Engineered Materials Platforms for Novel Wave Phenomena (Metamaterials),* France, 2017. Marseille, France: IEEE.

R. Jaiswar, F. Mederos-Henry, V. Dupont, S. Hermans, A. Delcorte, C. Bailly, C. Delmotte, V. Lardot, J.P. Raskin, I. Huynen. **An ultra-wideband thin microwave absorber using inkjet-printed Frequency Selective Surfaces combining carbon nanotubes and magnetic nanoparticles.** *Appl. Phys. A.,* 2019, 125(7), 473.

Collaborators

Sébastien Depaifve (IMCN/MOST), Védi Dupont (BCRC/EMRA) and Cathy Delmotte (BCRC/EMRA).

Using a different approach than in the previous chapter, microwave absorbing materials (MAMs) can also be produced by combining planar frequency-selective-surfaces (FSS) with grounded dielectrics to achieve a high-impedance surface. Frequency selective surfaces (FSS) are a subclass of electromagnetic bandgap (EBG) materials that are able to reflect or absorb incident microwaves at some frequencies while remaining transparent to them at other wavelengths [1]. Thus, FSS exhibit bandgap and passband behaviors simultaneously by virtue of their periodic surface geometric pattern. Their microwave absorption efficiency is based on the tuning of the unit cell dimensions and shape such that its effective impedance matches that of free space, thereby minimizing the reflection of electromagnetic wave at the interface [2]. Lumped elements can also be used to increase the absorption bandwidth and intensity. Nonetheless, this increases the complexity of the FSS-based MAM design and manufacture. Traditionally, FSS are patterned on metal screens or sheets, either as self-standing units or included in printed circuit boards. They are manufactured by conventional machining, laser etching or lithography techniques [3].

An alternative approach consists in printing the FSS with a low conductivity or resistive ink onto a dielectric substrate. This variant offers two main competitive advantages. On the one hand, it permits to easily fine-tune and reconfigure the final MAM structure depending on the desired applications and absorption efficiencies. Indeed, the input impedance of the absorber can be modified not only by the geometry of the FSS but also through the surface resistance of the printed layer [4-7]. Their efficiency can be further improved by stacking multiple printed FSS using spacers of optimal thickness. On the other hand, printed electronics can be mass-produced at low cost, are easily fabricated and reduce material waste [7, 8].

Given these considerable advantages, it was decided to explore how to produce MAMs by inkjet-printing resistive FSS patterns on a flexible substrate separated by low-dielectric spacers. The printed layers were obtained by using two different water-based MWCNTs-inks, formulated in collaboration with the Belgian Ceramic Research Centre (BCRC) [1]. One ink employed pristine MWCNTs while the other was based on MWCNTs decorated with magnetite nanoparticles (MaNPs). The latter nanocomposite was obtained with the synthetic routes developed in this research work (see Chapter 2). The design, simulation and experimental results obtained for both MAM structures are detailed below.

9.1 Materials and methods

9.1.1 Materials

Nanocyl (Belgium) supplied the NC3100 multi-walled carbon nanotubes (MWCNTs, 95%C purity). Lexan 8B35E polycarbonate (PC) sheets were offered by Sabic Innovative Plastics (Saudi Arabia). All other reactants were supplied by Sigma Aldrich or BYK, and engaged as received. More details on each reactant are provided in Appendix I while the different physicochemical characterization techniques employed are described in Appendix II.

9.1.2 Synthesis of the MaNPs@MWCNTs nanocomposites

As mentioned above, one of the water-based inks used MWCNTs decorated with magnetite nanoparticles (MaNPs). The SOLV-B synthetic methodology employed to produce this nanocomposite is described in Chapter 2, section 2.1.2.4.2.

[1] Belgian Ceramic Research Centre, Av. du Gouverneur E. Cornez 4, 7000 Mons, Belgium. www.bcrc.be

9.1.3 MWCNTs-ink formulation

Two different inks were formulated by Dr. Védi Dupont at the Belgian Ceramic Research Centre (BCRC). The first one (iCNT-1) was composed of pristine MWCNTs while the second (iCNT-2) employed a MaNPs@MWCNTs nanocomposite.

In a typical procedure, 1 g of pristine or MaNPs-decorated MWCNTs were dispersed in a mixture of 100 mL of distilled water and 1 g of Triton X-100 (Sigma Aldrich). The latter additive reduced the water's surface tension, promoting the wettability of the MWCNTs and their stable dispersion in the aqueous medium.

The mixture was placed in an ice bath and sonicated using a Bioblock Scientific Vibracell 75041 ultrasonic processor (Sonics & Materials Inc., U.S.A.) at 80% of its maximum power. The total sonication time was 6 minutes using alternating on and off periods of 10 seconds each.

After sonication, the dispersion gelled. Thus, 1 g of Disperbyk 190 (BYK) was added to the solution and the sonication procedure described above was repeated.

The dispersion was then centrifuged at 2500 rpm for 30 minutes using a Heraeus Sepatech 2520 centrifuge (Thermo Fisher Scientific, U.S.A.) to remove impurities or possible remaining powder aggregates which could clog the print heads nozzles. The supernatant was recovered and the sediment discarded. Afterwards, the resultant suspension was filtered over a 5 μm pore size polypropylene disk filter (ACRO LCF HDC II filter).

The filtered suspensions viscosity ranged between 5 and 6 mPa·s while its surface tension and density were 30 mN/m and ~1 g/cm^3 respectively.

9.1.4 Inkjet printing

Inkjet printing was also carried out at the Belgian Ceramic Research Center (BCRC) by Dr. Védi Dupont. A DMP-2800 Materials Printer (Fujifilm Dimatix Inc., U.S.A.) equipped with a 10 pL drop cartridge (DMC-11610) and a 21 μm diameter piezoelectric nozzle was used. An optimized waveform for the piezoelectric printhead was designed. It consisted of alternating 8.192 μs on and off pulses. The jetting (printing) pulses were performed at 28 V. Also, in order to ensure the printed film homogeneity, drop spacing and diameter were set to 25 μm and 35 μm, respectively.

Using these parameters, two types of samples were inkjet printed with both types of ink: a) 5-by-5 cm square patches with 2, 3, 5, 8 and 10 printed layers; and b) the 10-by-10 cm FSS patterns (see section 9.1.4 below) with 5 or 10 printed layers. In all cases, samples were printed at room temperature on polycarbonate (PC) Lexan-8B35E (Sabic Europe) sheets. All samples were subsequently annealed in a drying oven at 85 °C for one hour.

9.1.5 MAM design and simulation

The ultrawide-band MAMs design and their numerical simulation were carried out by Rajkumar Jaiswar (ICTEAM/ELEN).

Figure 1 shows the MAM's cross-section (top) and unit cell (bottom) printed with both types of inks. It consists of two resistive-FSS layers printed on 125 μm-thick Lexan 8B35E (Sabic) polycarbonate (PC) sheets. Each FSS is laminated between pristine Lexan 8B35E PC sheets. Each set of laminated FSSs is separated by low-dielectric Roger 5880 (ε=2.2) spacers having different d_1, d_2 and d_3 thicknesses optimized to achieve low reflection between 9 and 40 GHz (see Table 1). The top resistive FSS laminate pattern consists of a wire-mesh enclosing a Jerusalem-cross (JC) while its bottom counterpart is composed of a wire-mesh enclosing a closed-ring and one JC (see Figure 1, bottom). A ground plane was added in both MAM structures, at the bottom of the entire unit cell. In the case of the iCNT-1 MAM, it consisted of a resistive MWCNTs-ink printed to match its input impedance with free

space impedance [6, 10]. A copper ground plane was used for the iCNT-2 MAM.

Simulation of the microwave absorption performance of the designed unit cell was performed in the 5-to-50 GHz frequency range using CST-Microwave Studio (Dassault Systèmes, France). Absorption properties were determined by the reflection parameter, S_{11}, and input impedance (Z_{in}) from the full-wave simulation frequency-solver where a *y*-polarized electric-field is incident normally on the periodic structure of MAMs.

The simulation also optimized the FSS patterns' surface resistances (R_s) in order to obtain the maximum-bandwidth absorption in the simulated range.

9.1.6 Direct current (DC) surface resistance (R_s) and microwave-absorption characterization

The square patches printed using different layers of MWCNTs-ink were cut into five individual bands of equivalent dimensions. A conductive silver paste (G3790, Agar Scientific Ltd) was deposited at regular intervals to ensure good electrical contact with the meter probes (see Figure 2). Each zone delimited by two silver paste electrodes was measured using a B2902A Agilent IV meter (Agilent Technologies, U.S.A.) equipped with two probes. 25 resistance, *R*, measurements were performed in different points of each zone and the surface resistance, R_s (Ω/sq), was calculated for each point using the following relationship:

$$\mathrm{R}_s = \frac{R}{wl} = \frac{1}{\sigma t} \qquad \textbf{Equation 9.1}$$

where *R, w, l* are measured resistance, width and length of the printed patches and σ and t are the conductivity and thickness of the printed layers, respectively. The average R_s value was considered representative of the entire printed surface. The MAM absorption efficiency was characterized using the Agilent PNA-X vector network analyzer described in section 6.1 and the waveguide methodology described in [11].

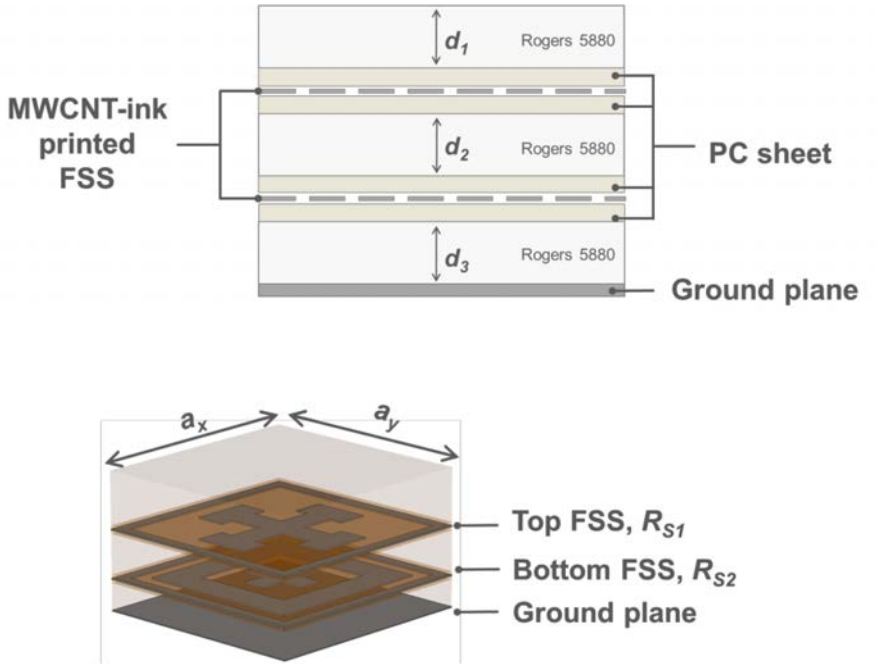

Figure 1 – MAM's cross-section (top) and unit cell (bottom) where a_x=a_y= 9 mm. Adapted from [12].

Table 1 –Thickness (mm) of the different components of both MAM structures

Substrate	Component	iCNT-1 MAM	iCNT-2 MAM
Rogers 5880	d_1	2	0.25
	d_2	1.5	1.5
	d_3	1	0.75
Lexan-8B35E PC (0.125 mm)	FSS (2x)	0.25	0.25
	Sandwich films (4x)	0.5	0.5
	Total	**5.25**	**3.25**

9.2 Results and discussion

9.2.1 DC surface resistance (R_s) characterization.

As described in section 9.1.2, the CST-Microwave Studio simulation was used to determine specific surface resistance (R_s) values for each FSS pattern in order to ensure optimal MAM performance. For the iCNT-1 MAM, the calculated R_s for the top and bottom FSS patterns (R_{S1} and R_{S2} in Figure 1) were 160 Ω/sq and 60 Ω/sq, respectively. While the calculated R_{S1} and R_{S2} for iCNT-2 MAM were 600 Ω/sq and 270 Ω/sq, respectively. It was thus necessary to determine how R_s changed for each ink as the number of printed layers increased.

Figure 3 shows the results of measuring the R_s of 2, 3, 5, 8 and 10 printed layers using the two types of ink. As can be observed, average R_s exponentially decreases as the number of printed layers are increased. This result suggests that as the number of printed layers increases, so does the number of conductive paths available for electron transport throughout the printed film, resulting in improved conductivity. Indeed, MWCNTs can form an entangled interconnected network to support the current transport thanks to their flexible, tubular shape.

In the case of the MaNPs@MWCNTs-based ink, the R_s values are superior to those obtained for an equal number of layers printed with the pristine MWCNTs ink. This is mainly due to the insulating character of the magnetite phase that hinders electron transport throughout the nanocomposite film, as shown in section 7.2, thus increasing its R_s.

Using these results, we were able to determine the number of printed layers that are needed to obtain the calculated R_s in both MAM's FSS. For both types of inks, the top FSS pattern required to be printed in 5 layers while the bottom FSS was printed in 10 layers.

SEM investigation of the printed surfaces showed that the printing configuration and ink-preparation method allowed to obtain extremely regular and smooth surfaces (see Figure 4, inset a). Nonetheless, it also showed that the printed layers have a low scratch resistance. Indeed, punctual micrometric scratches were observed throughout the surface (see Figure 4, inset b).

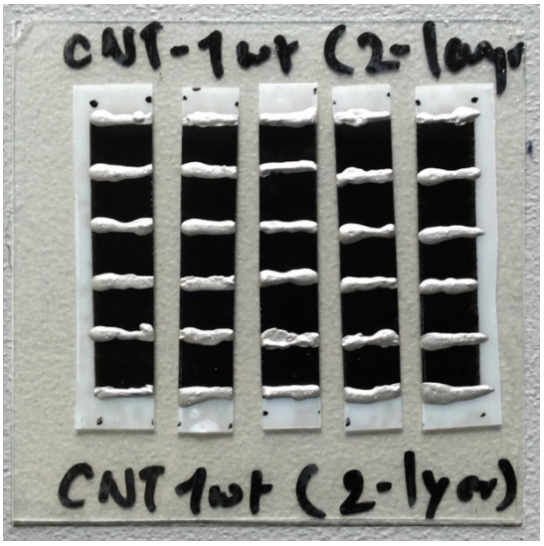

Figure 2 - Typical sample preparation for the DC R_s characterization of the patches printed with different number of MWCNTs-ink layers. Image by Rajkumar Jaiswar.

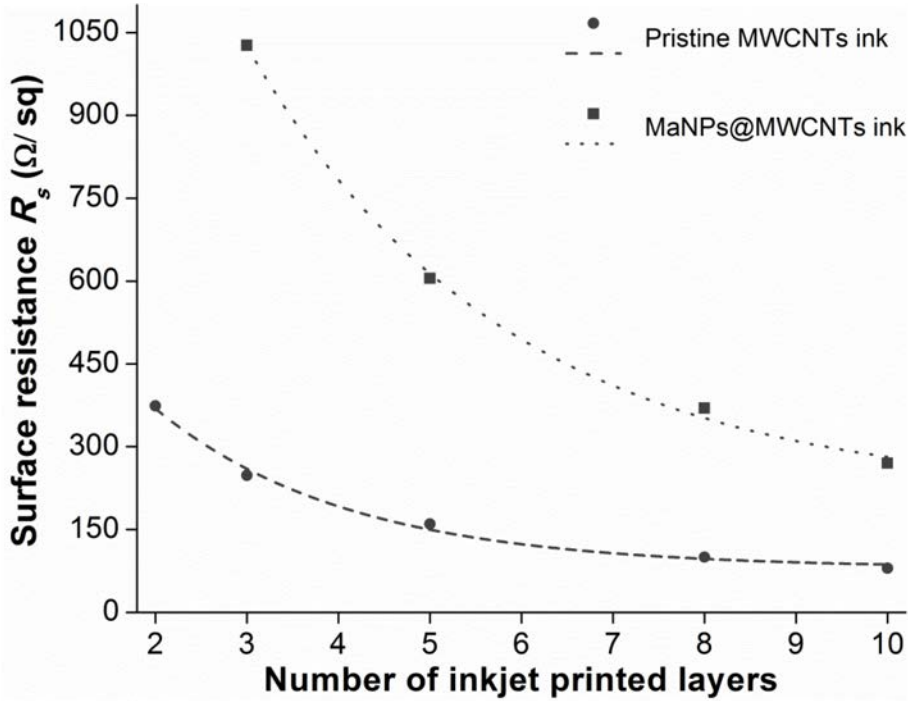

Figure 3 - Average surface resistance (R_s) as a function of the number of inkjet-printed layers with both types of inks. Solid symbols represent the experimental data. Symbols represent the experimental data. The dashed or dotted lines are the exponential regressions of such data. Adapted from [12, 13].

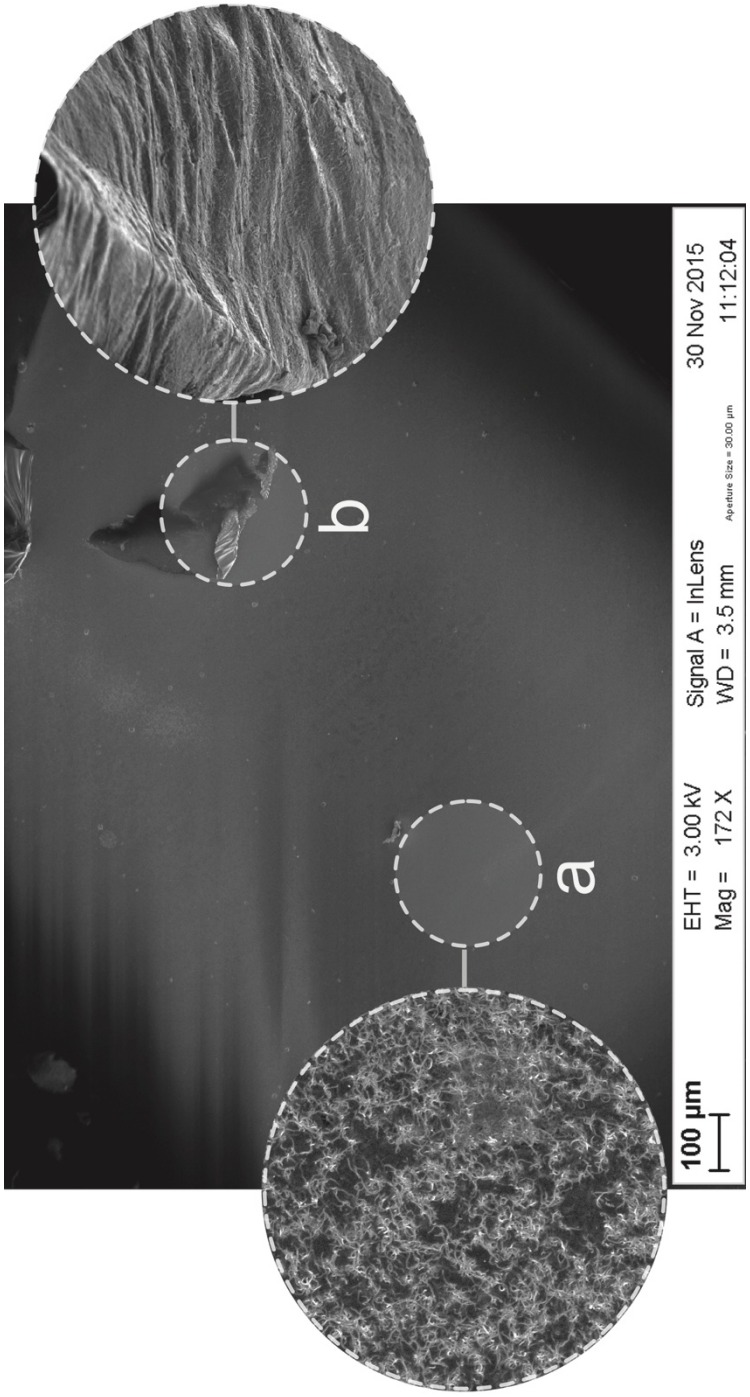

Figure 4 –SEM images of the 10-layer MWCNTs-ink printed surface. A 16 kX magnification (a) clearly shows the MWCNTs. Minute scratches were likewise observed (b, 4 kX).

9.2.2 MWCNTs-inkjet printed FSS patterns and MAM absorption performance

Figure 5 shows the top and bottom printed FSS patterns as well as a perspective view of a MAM obtained by inkjet printing and subsequent assembly.

Figure 6 presents the reflectivity (S_{11} parameter) in the 5-50 GHz frequency range obtained for the iCNT-1 MAM, printed with a pristine MWCNTs-ink. There is an excellent agreement between the measured and simulated MAM's reflection throughout the frequency range. Interestingly, reflection is neglectable (<-10 dB) between 9 and 40 GHz, corresponding to a 31 GHz bandwidth.

Remarkably, as shown in Figure 7, the MAM achieves a high absorption efficiency (~98%) between 9 and 40 GHz, despite its reduced thickness (5.5 mm).

Likewise, Figure 8 and Figure 9 present the reflectivity and associated absorption in the 5-50 GHz frequency range for the iCNT-2 MAM, printed with the MaNPs@MWCNTs-based ink. Given this MAM is backed with a conductive copper ground, reflectivity, R, and absorption, A, are calculated using the following expressions:

$$R = \left| S_{11} - \frac{{S_{21}}^2}{1 + S_{22}} \right| \qquad \textbf{Equation 9.2}$$

$$A = 1 - \mathrm{R}^2 \qquad \textbf{Equation 9.3}$$

Simulated and measured results are also in good agreement, showing negligible reflection (<-10 dB) and a 90% absorption rate in the 7-45 GHz band. Such an absorption performance thus represents a 36 GHz bandwidth for an absorber thickness of 3.25 mm.

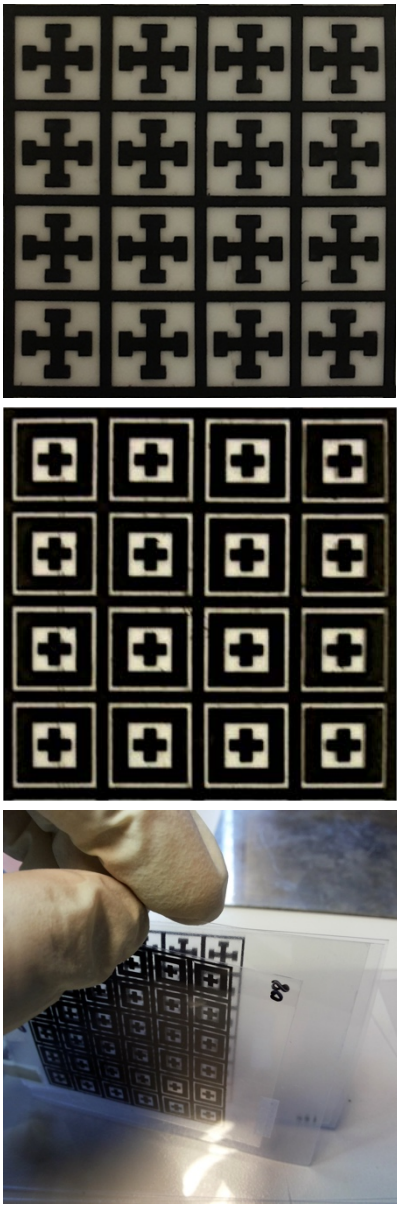

Figure 5 – General view of the top (top) and bottom (middle) resistive-ink FSS patterns printed on Lexan-8B35E PC sheets with the iCNT-1 ink; and perspective view (bottom) of the ungrounded MAM structure. Images by Rajkumar Jaiswar.

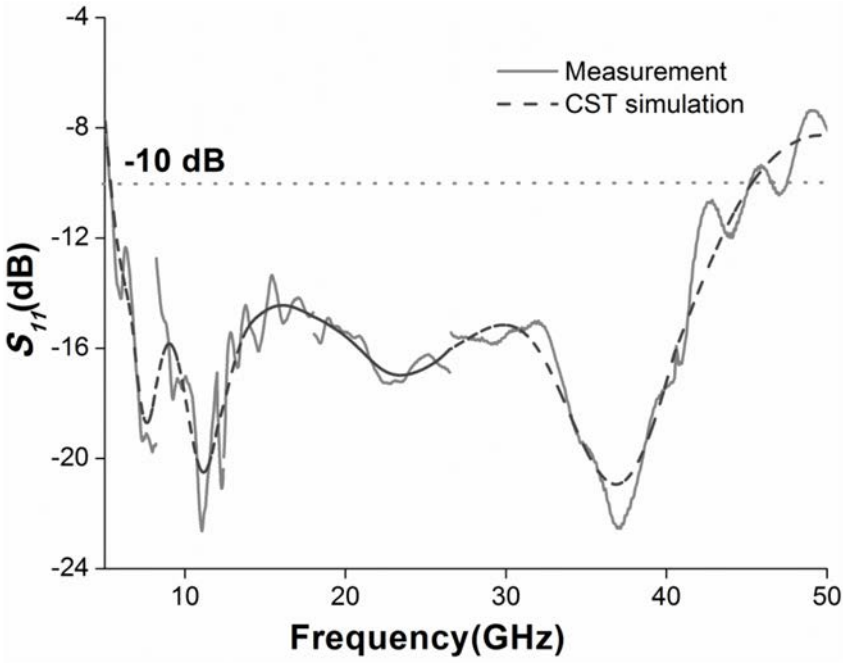

Figure 6 - Measured and CST-simulated reflection coefficient (S_{11}) of the iCNT-1 MAM structure. Adapted from [12].

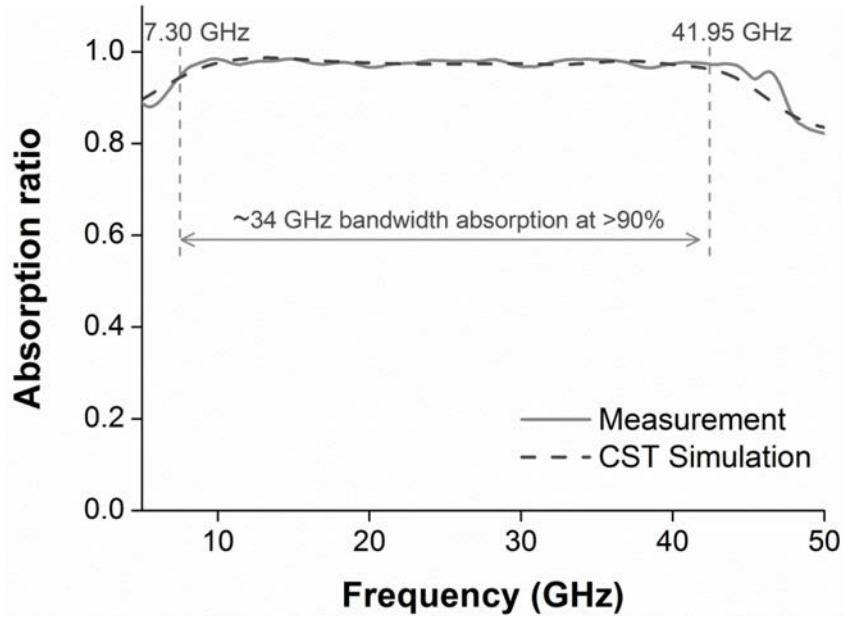

Figure 7 – Measured and CST-simulated absorption ratio of the iCNTs-1 MAM structure. Adapted from [12].

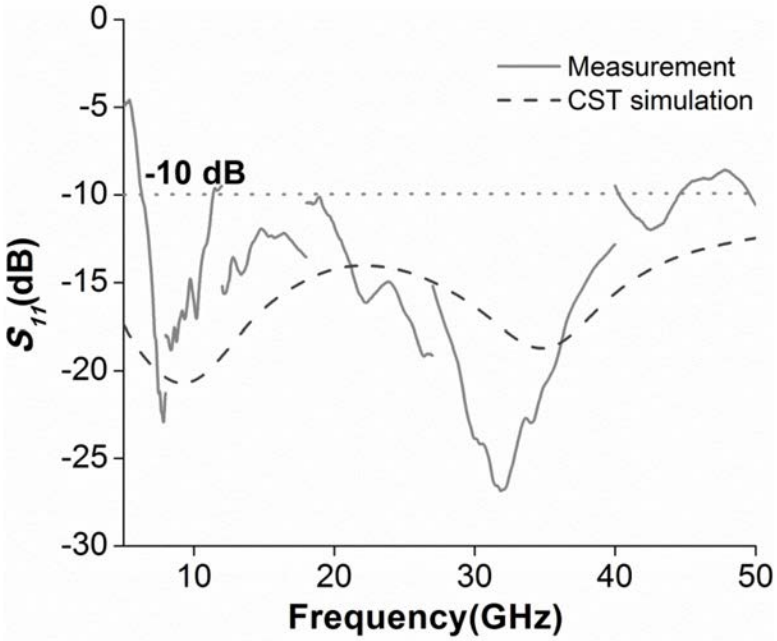

Figure 8 - Measured and simulated reflection coefficient (S_{11}) of the iCNT-2 MAM structure. Adapted from [13].

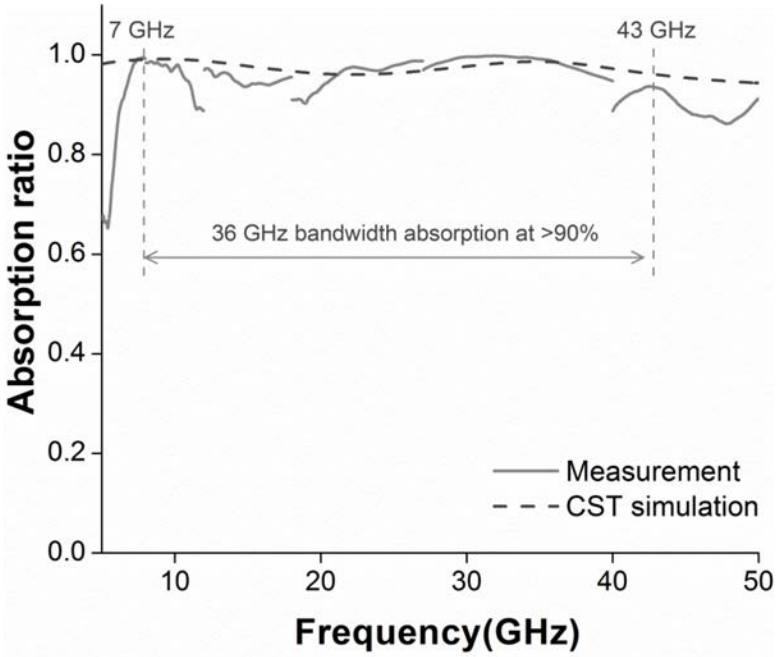

Figure 9 - Measured and CST-simulated absorption ratio of the iCNTs-2 MAM structure. Adapted from [13].

These results prove that both MAMs are suitable as effective EMI shielding materials. Reflection of the incoming microwave is minimal in both cases, even though the iCNT-1 MAM shows a slightly higher absorption rate than its iCNT-2 counterpart. However, the latter is able to absorb the incoming microwave over a larger bandwidth.

Nonetheless, in order to compare these MAM structures to others reported in the scientific literature, it is necessary to calculate two operational parameters. The first one is the fractional bandwidth (FBW), an indication of how wideband a microwave device is.

If such a device operates at a center frequency f_c, between lower frequency f_1 and upper frequency f_2 so that $f_c=(f_1+ f_2)/2$, then it is possible to calculate its FBW by using:

$$FBW = \frac{f_2 - f_1}{fc} \qquad \textbf{Equation 9.4}$$

The FBW values varies between 0 and 2. However, it is more commonly expressed as a percentage between 0% and 200%. Higher percentile values indicate that the device covers a wider bandwidth. In this case, the iCNT-1 MAM has a FBW of 126% while its iCNT2 counterpart shows a FBW value of 146%. These very high FBW values allow classifying these structures as ultra-wideband absorbers (UWBs) [13].

The second comparative parameter is a MAM's relative thickness, *RT*. This parameter allows comparing a device's thickness, *t*, in terms of the wavelength of the incoming microwave, usually at the lower frequency of operation (λ_L), so that:

$$RT = \frac{t}{\lambda_L} \qquad \textbf{Equation 9.5}$$

Considering each MAMs' thickness and their respective lower frequencies of absorption, *RT* values of $0.165\lambda_L$ and $0.075\lambda_L$ are obtained for the iCNT-1 and iCNT-2 absorbers, respectively.

Table 2 compares the *FBW* and *RT* values reported in the scientific literature for other MAM designs, including Jaumann screens [14], circuit analogous (CA) absorbers loaded with either high impedance surfaces [6] or lumped elements [15], multi-layered metamaterial absorbers [16] and a meta-surface Salisbury screen [17]. As can be observed, the iCNT-1 MAM has similar *FBW* values than other absorbers possessing similar *RTs,* even though its operational bandwidth is much larger. More interestingly, the iCNT-2 MAM produced in this research possesses the lowest *RT* and highest FBW over the largest bandwidth. This outstanding performance proves that using MNPs@NcS nanocomposites to create inkjet-printed MAM designs can be an extremely competitive approach to design novel, highly-efficient EMI shielding solutions.

Table 2 – Fractional bandwidth (*FBW*) and relative thickness (*RT*) comparison of different MAM designs

MAM	Bandwidth (GHz)	FBW (%)	RT (λ_L)
iCNT-1	9-40	126	0.165
iCNT-2	7-45	136	0.075
[14]	3-16	132	0.169
[6]	7-23	110	0.112
[15]	2-9	129	0.087
[16]	8-15	63	0.128
[17]	4-19	133	0.112

9.3 Conclusions

New prototypes of thin, highly efficient, ultra-wideband MAMs have been designed, produced and tested. They are based on a layered arrangement of frequency selective surfaces (FSS), inkjet-printed on thin polycarbonate sheets and spaced by dielectric layers. Two types of inks were developed to print the FSS: one in which pristine MWCNTs were used and the second in which the MWCNTs were decorated with magnetite nanoparticles (MaNPs), following a procedure described in Chapter 2.

As demonstrated throughout the present chapter, our design approach to inkjet-printed MAMs depended on a numerical simulation to determine the ideal physical characteristics for each component of the MAM unit cell, such as its thickness and surface resistance (R_S). It also allowed predicting its microwave absorption efficiency and reflectivity over an operational bandwidth. We also proved that by varying the number of printed layers or changing the type of printing ink, it was possible to easily control the FSS' R_s values, so as to adjust them to the simulation results. Indeed, for both types of inks, we determined that the R_s of the printed surface is inversely proportional to the number of printed layers. Nonetheless, for identical number of printed layers, the MaNPs@MWCNTs-based ink gave higher R_s values than its pristine MWCNTs-based counterpart.

The high fractional bandwidth (FWB) values obtained for both prototypes (126% and 146% for the iCNT-1 and iCNT-2 MAMs, respectively) show that the as-obtained MAMs are highly-efficient EMI-shielding alternatives, in which heightened absorption constitutes the main shielding mechanism. Furthermore, the outstanding performance of the MAM printed with decorated MWCNTs, achieved at an extremely low relative thicknesses (0.075 λL), reveals an unimagined new field of application for the different MNPs@NcS nanocomposites synthetized in this research project.

9.4 Bibliography

1. T. K. Wu. Frequency Selective Surface and Grid Array. John Wiley & Sons: New York, USA. 1995.
2. A. Kazemzadeh, *IEEE Antennas Propag.*, 2010, **59**(1), 135-140.
3. D. Ferreira, R. F. S. Caldeirinha, I. Cuiñas, and T. R. Fernandes, *IEEE Antennas Propag. Mag.*, 2018, **60**(6), 110-119.
4. M. Olszewska-Placha, B. Salski, D. Janczak, P.R. Bajurko, W. Gwarek and M. Jakubowska, *IEEE Antennas Propag.*, 2015, **63**(2), 565-572, 2015.
5. E. Yildimy and O. Aydin Civi, Proceedings of the *5th European Conference on Antenna and Propagation* (EUCAP), Italy, 2011. Rome, Italy: EurAAP.
6. F. Costa, A. Monorchio and G. Manara, *IEEE Antennas Propag.*, 2010, **58**(5), 1551-1158.
7. X. Huang, K. Pan and Z. Hu, *Sci. Reports,* 2016, **6**, 38197.
8. Y. Gao, W. Shi, W. Wang, Y. Leng and Y. Zhaom *Ind. Eng. Chem. Res.,* 2014, **53**(43), 16777 - 16784.
9. O-S Kwon, H. Kim, H. Ko, J. Lee, B. Lee, C-H Jung, J-H Choi and K. Shin, *Carbon*, 2013, **58**, 116 – 127.
10. F. Costa, A. Monorchio and G. Manara, *IEEE Antennas Propag. Mag.*, 2012, **54**(4), 35-48.
11. Y. Danlée, 2015. Hierarchically organised materials based on polymers and conductive one-dimensional nanostructures for the control of electromagnetic propagation (Doctoral dissertation). Retrieved from: http://hdl.handle.net/2078.1/157886.
12. R. Jaiswar, F. Mederos-Henry, V. Dupont, S. Hermans, A. Delcorte, C. Bailly, C. Delmotte, V. Lardot, J.P. Raskin, I. Huynen. A thin ultra-wideband microwave absorbing structure printed on flexible substrate with resistive-ink made of multi-walled carbon-nanotubes. Proceedings of the 11th International Congress on Engineered Materials Platforms for Novel Wave Phenomena (Metamaterials), France, 2017. Marseille, France: IEEE.
13. R. Jaiswar, F. Mederos-Henry, V. Dupont, S. Hermans, J.P. Raskin, I. Huynen, *Article submited to the Journal of Applied Physics for publication.*
14. A. Kazemzadeh asnd A. Karlsson, *IEEE Trans. Antennas Propag.*, 2010, **58**(11), 3637-3646.
15. Y. Shang, Z. Shen, and S. Xiao, *IEEE Trans. Antennas Propag.*, 2013, **61**(12), 6022-6029.
16. F. Ding, Y. Cui, X. Ge, Y. Jin, and S. He, *Appl. Phys. Lett.,* 2012, **100**(10), 103504-103506.
17. Z. Zhou, K. Chen, B. Zhu, J. Zhao, Y. Feng and Y. Li, *IEEE Access,* 2018, **6**, 26843-26853.

part III

summary
conclusions

The first designed type of MAM consisted of a series of thin films, obtained by dispersing Fe, Co or Ni@MWCNTs nanocomposites into a polycarbonate matrix. Results presented in Chapter 8 prove that the dispersed nanocomposites impart their microwave behavior onto the obtained films. For instance, an FMR process was clearly detected in these composite materials. Furthermore, certain FMR-related characteristics of the films, such as their natural or zero-field absorption frequency, could be directly related to certain characteristics of the deposited MNPs, such as their composition or size distributions.

Unfortunately, the full potentiality offered by the MNPs@NcS could not be completely unveiled. Two main issues were identified. On the one hand, the low amounts of nanocomposites loaded into the polycarbonate films, which produced very low MNPs loadings. On the other hand, the extrusion temperatures used to prepare these films, which induced the oxidation of the different metallic MNPs. The combination of these factors lowered the effective magnetic content of these films and consequently, the influence of the MNPs on the microwave absorption behavior of these composite materials was almost unperceivable. Indeed, their MAM efficiency was quite mediocre and seemed dominated by the electrical loss mechanisms induced by the MWCNTs.

As shown in Chapter 9, a second type of MAM was obtained by stacking dielectrics and inkjet-printed frequency selective surfaces (FSS) produced using either pristine MWCNTs or one of our MaNPs@MWCNTs nanocomposite. The efficient ultra-wideband absorption achieved by both novel inkjet-printed FSS-MAM structures are remarkable, exceeding the performance of similar solutions published in the scientific literature. More interestingly, the potential benefits of the MNP-NcS synergies described above are here fully revealed by comparing the operative performance of the MAM printed with pristine MWCNTs and its MaNPs@MWCNTs counterpart. Thus, these results are only a first glimpse of what could be achieved if our different MNPs@NcS nanocomposites were systematically employed with this approach to a MAM design.

consi

+ perspectives for

future research

Achieving highly efficient MAMs using MNPs@NcS nanocomposites: concluding remarks

This project's different research endeavors were united by one main objective: developing a new generation of microwave absorbing metamaterials based on the controlled chemical assembly of magnetic nanoparticles and nanocarbon supports.

In order to achieve this goal, we first developed a series of nanochemical synthetic methods to obtain different types of MNPs@NcS nanocomposites. Throughout Part I of this manuscript, we showed how to chemically combine as many as seven different types of MNPs and five different NcS. We also identified which synthetic parameters allow to control the deposited MNPs chemical identity, size or spatial distribution over the NcS, as well as the oxidation state of the latter.

In parallel, as was shown in Part II, a novel EM characterization method was invented and applied to the obtained nanocomposite powders in order to retrieve the electrical permittivity and magnetic permeability without sample preparation. It revealed how the constitutive MNPs and NcS allow controlling the electric permittivity, magnetic permeability and microwave absorption behavior of these materials. These results have brought to light a clear relationship between the physicochemical characteristics of the nanocomposite assemblies and their ability to effectively absorb microwaves. Thus, we can now offer the scientific community a series of precise guidelines (see Figure 1) allowing to obtain novel MAM materials which efficiently dissipate the magnetic and electric energies conveyed by a microwave.

For instance, the pathway towards efficient MAMs demands the creation of high magnetic permeability (μ) materials so that they effectively channel the external magnetic field by providing low resistance paths (see section 1.3.2).

Given that the magnetic permeability is directly dependent on a material's saturation magnetization (M_S), the latter parameter should be maximized in potential MAM nanocomposites. Interestingly, we have shown that higher M_S values can be achieved if pure or alloyed Fe, Co or Ni metallic MNPs, with sizes just below the mono- to multidomain threshold, are deposited onto a NcS.

The as-guided magnetic energy can then be dissipated by ferromagnetic resonance (FMR) absorption, the main magnetic loss mechanism operating at microwave frequencies. Consequently, the intensity of such an absorption should also be maximized in order to increase the materials' overall EM absorption rate. Accordingly, we have found that higher MNPs loading rates produce more intense FMR absorptions and should thus be favored when looking for higher MAM efficiencies. Furthermore, we have proved that the composition and size of the deposited MNPs also impacts the FMR absorption properties of the nanocomposites. Indeed, as for the magnetic permeability, we demonstrated that the FMR natural absorption frequency, f, increases as the system's M_S values increased, paving the way towards frequency-selective MAM functionalities.

The nanocarbon supports' role in the dissipation of electrical energy conveyed by a microwave was also elucidated. As mentioned in section 1.3.1, the main loss mechanism operating in the microwave range is the Ohmic conduction of electrical currents formed on the nanocomposites' surface. Thus, more conductive, non-oxidized NcS such as pristine GNPs or MWCNTs should be favored over rGO, ox-MWCNTs or GO in order to increase microwave absorption rates. We also revealed a remarkable synergistic effect between the chemical nature of the deposited MNPs and the nanocomposite's overall conductivity. Indeed, we demonstrated that for a given NcS, conductive metallic nanoparticles increase the conductivity and thus the microwave absorption rate of the resulting nanocomposites, while insulating MNPs lower it.

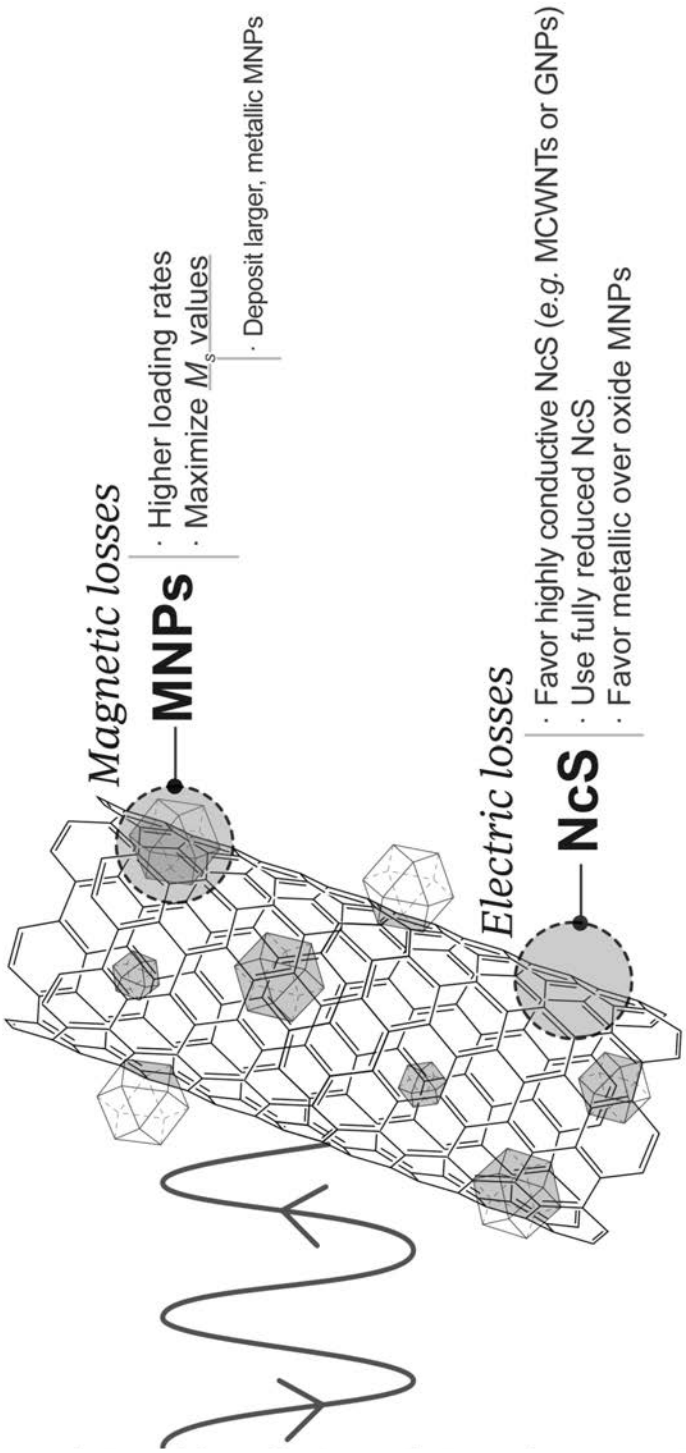

Figure 1 – Synthetic guidelines allowing to obtain novel MAM materials which efficiently dissipate the magnetic and electric energies conveyed by a microwave.

Even so, the as-obtained MNPs@NcS nanopowders will rarely be used as self-standing MAMs in real-life applications. Nonetheless, the above-given guidelines can be used as a basis for the design of novel MAM functional materials, as shown in Part III. This is particularly straightforward for the thin films produced by the dispersion of the nanocomposites in a polycarbonate matrix. Indeed, we demonstrated that in this case, the microwave absorption properties of the nanocomposites are transposed onto the films, following the same principles as outlined above.

Nonetheless, the inkjet printed FSS prototypes design might not replicate these guidelines as much as exploiting the flexibility of the MNP and NcS chemical assemblies developed in this research project and the potential ε and μ permutations it can produce. Indeed, we clearly proved that extremely promising MAM solutions can be found by using a magnetite-based nanocomposite. However, in the above-stated guidelines we affirmed that non-metallic MNPs should produce less efficient magnetic and electric losses and thus reduce the MAM's overall efficiency. This apparent paradox strikingly exemplifies the adjustable nature of the FSS design approach and thus clearly outlines its enormous potential. Indeed, the FSS patterns can be purposely designed and cleverly assembled to exploit the particular EM characteristics of a given MNPs@NcS nanocomposite in order to produce given MAM functionalities. For instance, promising frequency-selective absorption behaviors, tunable with an external applied magnetic or electric field, could be thus created.

Perspectives for future research

In some cases, obtained results met the project's predefined objectives and requirements. In others, encountered problems or challenges remained unsolved. Thus, echoing the structure used for the conclusive remarks given above, a series of ideas for future experimental undertakings will be presented in the following three sections.

Further explorations on the chemical assembly of magnetic nanoparticles and nanocarbon supports

Obtaining more than seven different MNPs compositions would be thrilling in terms of the resulting metamaterial design possibilities. An exploratory decoration of GO with Ni and Co ferrites (mixed oxides XFe_2O_4, where X=Ni or Co) was initiated, using the experience acquired by developing the SOLV-A strategy (Section 2.1.2.4.1). Preliminary but encouraging results were obtained. Indeed, pure Ni or Co ferrite MNPs were deposited onto GO but their size and spatial distribution have yet to be optimized. It would thus be interesting to continue developing these syntheses to offer new types of ferrite NPs, besides MaNPs. Also, by using the Pechini method, it should be possible to produce different binary and ternary Fe/Co/Ni alloys of varying molar ratios by changing the proportions of the Fe/Co/Ni precursors.

As for the deposited NPs size, our results show that the optimal size range, allowing to maximize both M_s and H_c, is situated just below the single to multi-domain transition limit. Therefore, finding other strategies allowing to control the deposited MNPs sizes would be highly appreciated. In the first place, a parametric study involving different capping agents, concentrations, reaction times and temperatures could be applied to the solvothermal synthesis of MaNPs, NiNPs and CoNPs. This study would complement was has been done for polyvinylpyrrolidone, when developing the AC-S synthesis of the Ni@MWCNTs nanocomposite and thus, should show which size ranges can be achieved under certain given experimental conditions.

Another clue that could be further investigated is the combination offered by: a) controlling the speed at which the NPs precursor is added to the reaction mixture; and b) the post-synthetic thermal treatment that simultaneously induces particle growth and creates a protective graphitic shell around the NPs. This combination was used for the decoration of MWCNTs with Ni and Co NPs. Thus, an experimental design testing the impact of adding the NPs precursor at different speeds and the temperature, time or atmosphere of the thermal treatment would be greatly helpful to obtain other NP sizes.

The experimental parameters governing the thermal decomposition reaction used to produce the Fe@MWCNTs could also be explored in detail. Particular efforts should be devoted to controlling the ZVI NPs size distribution to avoid the acid etching procedure. However, if the latter remains a mandatory step in the preparation of these nanocomposites, then a way of removing the empty graphitic shells should be found.

Likewise, different σ and ε_r values could be obtained and their effects on the microwave behavior of the MNPs@NcS nanocomposites monitored if chemically functionalized NcS were used. Commercial sources of chemically functionalized NcS are nowadays available. Otherwise, the nanocarbon functionalization expertise of Prof. Hermans research group could be used to produce functionalized NcS with tailored electrical properties.

Finally, all permutations of MNPs and NcS should be tested, as done in Chapter 2 for MaNPs decoration. Besides obtaining the full set of nanocomposites, useful for MAM design purposes, these investigations would allow understanding how the different NcS impact the obtained MNPs@NcS characteristics, given each method's particular synthetic conditions. The need for this type of experimental investigation was evidenced when preliminary explorations were performed to decorate MWCNTs and GNPs with Fe/Co/Ni Pechini alloys. In both cases, results were partially satisfactory, particularly in terms of the graphitic shell quality and the NPs size distributions.

Further explorations regarding the EM characterization of the MNPs@NcS nanocomposites

Regarding the novel VNA-based EM characterization method, particular attention should be given to making the test cells more robust. Indeed, both the CPW and MS prototypes were fragile, especially the later. Even with a highly cautious manipulation, they broke down after a few cycles of sample filling, measurement and cleaning.

Eventually, more robust and standardized CPW test cells were produced by Multi CB, a printed circuit boards industrial manufacturer. This was unfortunately not the case for the project's latecomer, the MS test cell. Nonetheless, it should definitely be done in order to complete the EM screening of all the nanocomposite powders produced in this research project. Indeed, full screening of the entire range of MNPs@NcS nanocomposites should contribute to unravel, in a more precise way, the complex relationship between the NcS, the MNPs and the nanocomposite's EM response in the microwave range.

Also, new ways of compacting the powders into the test cells etched cavities should be found. As mentioned in Section 7.2, as long as the phenomenological model's filling factor, f, is the same for all samples, direct comparisons can be established between them. Fortunately, such was the case for the measurements performed in this research project. Nonetheless, the ε_r and σ values obtained for our nanomaterials are well below those reported in the scientific literature, an effect that can be attributed to the degree of compacity of the nanopowders. Thus, a detailed study linking the mass of the introduced nanopowders, the compacting method, the obtained filling factor and the variations in ε_r and σ values is necessary.

Further explorations regarding EMI shielding functionalities

Concerning the Fe, Co, Ni@MWCNTs films, different experimental undertakings should be performed to fully unveil the potentialities offered by this MAM design. Firstly, the films should be loaded with a higher rate of

MNPs in order to observe the impact of the magnetic materials on the microwave absorption rates. The solution must come from the MNPs loading rate and not the amount of nanocomposite powder loaded into this films. Indeed, as stated in Section 8.1.2, the latter is restricted to a maximum of 3% (%w/w), in order to avoid excessive reflection of the incoming microwave and film brittleness. Thus, MNPs@MWCNTs nanocomposites with much higher MNPs loading rates (~100%) should be produced for these experiments. Furthermore, the deposited MNPs should possess a size distribution situated just below the mono-to-multidomain transition threshold, to simultaneously optimize both M_s and H_c.

Secondly, a different dispersion method should be found. Indeed, as shown in Chapter 8, the temperature (250°C) used during the extrusion process induces the thermal oxidation of the deposited MNPs, thus reducing the film's magnetic content. Preliminary undertakings were performed to develop an ambient-temperature, solvent-based dispersion method. However, obtained results were unsatisfactory as the nanocomposites were heterogeneously distributed in the polymeric matrix. An alternative would be to use a different polymeric matrix with a lower fusion temperature. Nonetheless, this would firstly demand to study the dispersion behavior of the nanocomposite in the tested polymer matrixes.

Finally, a TEM study on thin sections obtained from the films should be performed. Indeed, this would allow understanding the microstructure formed by the dispersed MNPs@NcS inside the polycarbonate matrix. It would also allow to determine if the MNPs detach from the NcS during the dispersion process.

For the inkjet-printed prototype of MAM presented in Chapter 9, it is perhaps the most exciting venue to thoroughly explore in the near future. Both the ink composition and the FSS structure could be varied in order to expand its range of possible applications, especially as electromagnetic bandgap materials. For instance, magnetic losses, determined by NP composition-dependent FMR, could be exploited to induce highly efficient frequency-selective absorption. In order to achieve this, inks using MWCNTs decorated

with higher loadings of MNPs should be developed. Also, as mentioned above for the polymeric films, the deposited MNPs should possess the appropriate size distributions in terms of M_s and H_c optimization. Furthermore, a metallic MNPs@MWCNTs nanocomposite (Fe, Ni or Co) should be transformed into an inkjet-printable dispersion. FSS specifically designed for its higher ε_r and μ_r values could allow achieving frequency-selective reflections or absorptions. Finally, it should be determined if tunable, frequency-selective absorption behaviors could be achieved under variable magnetic or electric fields.


app
di

en

xes

appendix I

materials + reactants

I.1 Nanocarbon supports

Name	Specification	Company	Country
Multi-walled carbon nanotubes (MWCNTs)	NC3100, 95%C purity	Nanocyl	Belgium
Graphene oxide (GO)	-	Nanoinnova Technologies SL	Spain
Reduced graphene oxide (rGO)	-		
Graphene nanoplatelets (GNPs)	TIMREX BNB90	TIMCAL	Switzerland

I.2 Other reactants

Across, Belgium

Name	Specification
Iron (III) nitrate nonahydrate	99+%
Cobalt (II) nitrate hexahydrate	For analysis

Alfa Aesar, Germany

Name	Specification
Ethylene glycol	Spectrophotometric grade, 99+%
Hydrazine monohydrate	99+%
Iron (II) chloride tetrahydrate	Reagent grade, 99%
Polyethylene glycol 2000	-
Polyvinylpyrrolidone 10,000 (PVP-10,000)	Powder (M.W 10,000)
Tetraethoxysilane	99.9%
Tetramethylammonium hydroxide	25% w/w aq. soln., 99.9999%

BYK, Germany

Name	Specification
Disperbyk-190	-

Bayer Material Science, Germany

Name	Specification
Polycarbonate	Makrolon®OD2015

Merck, Germany

Name	Specification
Polyethylene glycol 400	Synthesis grade
Citric acid monohydrate	For analysis

Sabic Innovative Plastics, Saudi Arabia

Name	Specification
Lexan 8B35E sheets	0.125 mm-thick

Sigma Aldrich, Germany

Name	Specification
(3-aminopropyl)trimethoxysilane	97%
Iron (III) acetylacetonate	97%
Iron (III) chloride hexahydrate	puriss. p.a., Reag. Ph. Eur., ≥99%
Nickel (II) nitrate hexahydrate	97+%
Thionyl chloride	ReagentPlus®, ≥99%
Triethylene glycol	ReagentPlus®, ≥99%
Triton X-100	For molecular biology

VWR, Belgium

Name	Specification
Ethanol	96% v/v, Technisolv
Hydrochloric acid	37% w/w, AnalaR NORMAPUR
Nitric acid	65% w/w, AnalaR NORMAPUR
Sodium Hydroxide	AnalaR NORMAPUR
Toluene	AnalaR NORMAPUR

appendix II

physicochemical characterization techniques

Support scientists and technicians

Sergey Basov (IMCN/BSMA), Arnaud Delcorte (IMCN/BSMA), Pierre Eloy (IMCN/BSMA), Anne Iserentant (ELI/ELIE), Pascale Lipnik (IMCN/BSMA), Benoit P. Pichon (UNISTRA/IPCMS), Claude Polenius (IMCN/BSMA), Koen Robeyns (IMCN/MOST), Laurence Ryelandt (IMMC/IMAP), Jean-François Statsyns (IMCN/MOST), Pascal Van Velthem (IMCN/BSMA), Frederic Van Wonterghem (IMMC/IMAP).

A wide range of analytical techniques were employed to extensively characterize the obtained nanocomposite products. Indeed, revealing the influence of certain synthetic parameters on the nanocomposites most relevant physicochemical characteristics was of foremost importance. Regarding the different types of synthetized nanoparticles (NPs), we systematically evaluated their chemical identity, size, loading rate and spatial distribution over a particular nanocarbon support (NcS). As for the different NcS employed, we studied their characteristic morphologies and sizes, as well as their elemental and molecular compositions. Finally, the magnetic properties of the end nanocomposite powders and their corresponding thin films were also determined.

Accordingly, the crystalline phases constituting the NPs were identified using X-Ray diffraction (XRPD). For certain Fe-containing NPs, ^{57}Fe Mössbauer spectroscopy was also used to complement the XRPD results. Furthermore, energy dispersive X-ray analysis (EDX) coupled to a scanning electron microscope (SEM) or inductively coupled plasma atomic emission spectroscopy (ICP-AES) were used to determine punctual or global elemental profiles, respectively, in the as-synthetized NPs. X-ray photoelectron spectroscopy (XPS) was likewise used to determine the elemental composition and the chemical states of such elements at the surface of the different NPs and NcS. Time-of-Flight Secondary Ion Mass Spectrometry (ToF-SIMs) was also employed in the specific case of the Fe/Co/Ni alloy NPs to address complex issues regarding their surface composition.

Thermogravimetric analysis (TGA) was used to determine the amount of NPs loaded onto a particular NcS. However, in the specific case of the Fe/Co/Ni alloy NPs, ICP-AES was chosen instead to determine the loading of each metal.

Electron microscopy techniques such as SEM or transmission electron microscopy (TEM) were also regularly used to observe the shapes and measure the sizes of the different NPs and NcS composing the synthetized

nanomaterials. They also allowed visualizing the NPs spatial distribution over a particular NcS surface.

Lastly, the magnetic properties of the different nanocomposite powders and their films were evaluated using two types of magnetometers. The former products were studied using a Superconducting Quantum Interference Device (SQUID) while a Vibrating Sample magnetometer (VSM) was used for the latter.

II.1 Characterization techniques and sample preparation methods

A brief overview of each characterization technique experimental procedure and its corresponding sample preparation method is given below. The techniques are listed in alphabetical order.

II.1.1 Inductively coupled plasma atomic emission spectroscopy (ICP-AES)

Samples (~25 mg) were carbonized at 550°C. The leftover ashes were dissolved in 0.05 mL of *aqua regia* and then diluted 1000x. The resulting solutions were measured with an iCAP 6500 Thermo Scientific spectrophotometer (Thermo Fisher Scientific, U.S.A).

II.1.2 ^{57}Fe Mössbauer spectroscopy

Samples were sealed in aluminum foil and mounted on a nitrogen Oxford bath cryostat. ^{57}Fe Mössbauer spectra were recorded at 77 K and room temperature (R.T.) in transmission geometry using a conventional Mössbauer spectrometer equipped with a ^{57}Co(Rh) radioactive source operating at room temperature. The spectra were fitted to the sum of Lorentzians by a least-squares refinement using Recoil 1.05 Mössbauer Analysis Software [1]. All isomer shifts refer to α-Fe at room temperature.

II.1.3 X-Ray powder diffraction (XRPD)

Samples were introduced into 0.5 mm thin-walled glass capillaries (Hilgenberg GmbH, Germany), mounted on a goniometer head and kept at 200 mm distance from the detector. Diffractograms were then collected at room temperature using a MAR345 diffractometer (MarResearch GmbH, Germany), a Mo-Kα (0.71073 Å) anode and a XENOCS focusing mirror. The obtained 2D diffractograms were azimuthally integrated using the Fit2D software, calibrated with a LaB6 standard (NIST 660b Standard).

II.1.4 Scanning electron microscopy with coupled energy-dispersive X-ray spectroscopy (SEM-EDX)

Samples prepared for TEM analysis were also used for SEM imaging. The TEM grids were mounted on double-face adhesive carbon tape adhered to an aluminum sample holder. These were analyzed without further preparation in a FEG-SEM Ultra55 instrument (Carl Zeiss, Germany) equipped with an Oxford Inca EDX system (Oxford Instruments, U.K.). Images were acquired with the SmartSEM software (Carl Zeiss, Germany) at different acceleration voltages ranging between 3 keV and 15 keV, using InLens and SE2 detectors. X-ray fluorescence spectra were collected at 15 keV using the ESPRIT software (Bruker, U.S.A.).

II.1.5 Superconducting Quantum Interference Device (SQUID) magnetometer

Magnetization measurements were performed using a MPMS-XL5 SQUID magnetometer (Quantum Design, U.S.A.) without further sample preparation. Magnetization curves as a function of an applied magnetic field (M(H) curve) were measured at 300 K after applying a degaussing procedure. The magnetization was then measured at constant temperature by sweeping back and forth the magnetic field between +7 T and -7 T.

II.1.6 Time of flight secondary ion mass spectrometry (ToF-SIMS)

Sample powders were manually pressed with a spatula onto adhesive part of Post-it® papers and analyzed without further preparation using a IONTOF TOF.SIMS instrument (IONTOF GmbH, Münster, Germany). A pulsed

Bi^+ metal ion source produced a primary beam using an acceleration voltage of 30 kV. An AC target current of 2 pA with a bunched pulse width lower than 1 ns was used. Both positive and negative secondary ion species were analyzed. For spectra acquisition, a raster of 128 x 128 data points over an area of 200 x 200 μm^2 was employed. The total primary ion beam dose for each analyzed area was always kept below $2x10^{12}$ ions.cm^{-2}. Lateral resolution of ~3 μm and mass resolution $m/\Delta m$ > 5500 at 29 m/z were maintained for positive and negative spectra acquisition. Charge compensation was done with an interlaced electron flood gun (E_k = 20 eV). All data analyses were carried out using the software supplied by the instrument manufacturer, SurfaceLab (v.6.5).

II.1.7 Transmission electron microscopy (TEM)

Samples were dispersed in hexane or ethanol by sonication. Three drops of the supernatant were then deposited onto a holey carbon film supported on a copper grid (C-flat, Protochips, USA), and left to dry, overnight, at room temperature under vacuum. TEM images were obtained on a LEO 922 OMEGA Energy Filter Transmission Electron Microscope (Carl Zeiss, Germany) operating at 120 kV. Particle sizes were analyzed with the AnalySIS Auto 5.0 software (Olympus Soft Imaging Solutions GmbH, Germany) on at least 100 particles per sample as recorded on the TEM images. High resolution TEM (HRTEM), EDX, and electron diffraction (ED) were performed with a JEOL ARM200F microscope (JEOL Ltd., Japan) operating at 200 kV.

II.1.8 Thermogravimetric analysis (TGA)

Samples (5-10 mg) were placed in alumina crucibles and introduced in a TGA/SDTA 851e instrument (Mettler Toledo, U.S.A). Thermograms were recorded up to 900 °C using a 10 °C/min heating rate under an air flux. The samples were recovered after heating and analyzed by XRPD as described above, to identify the chemical nature of the remaining powder. Indeed, TGA data treatment required for the calculation of the NPs loading rates was based on the formula weight of the identified compound. Corrections for residual non-carbonaceous impurities present in the different NcS used were also included in these calculations.

II.1.9 Vibrating sample magnetometer (VSM)

The magnetization measurements of the MNPs@MWCNTs_PC films were performed with a VSM apparatus (Oxford Instruments) at room temperature using typical sweep rates between 0.06 and 0.12 T/min. The magnetic field was applied perpendicularly to the sample at all times. The obtained results were normalized with respect to the amount of MNPs contained in each film. To do so, the corresponding M/C (metal-to-carbon) loading rate (LR) values determined by TGA analysis were used.

II.1.10 X-Ray photoelectron spectroscopy (XPS)

A few milligrams of each sample were deposited on a double-sided adhesive tape clung onto a brass cup, and then introduced onto a Macor® carousel. The analyses were performed on a SSX 100/206 photoelectron spectrometer from Surface Science Instruments (U.S.A) equipped with a monochromatized micro focused Al X-ray source (powered at 20 mA and 10 kV). The pressure in the analysis chamber was around 10^{-6} Pa. A flood gun set at 8 eV and a Ni grid placed 3 mm above the sample surface were used for charge stabilization. The C-(C,H) component of the carbon C1s peak was fixed to 284.8 eV to set the binding energy scale. Data treatment was performed with the CasaXPS program (Casa Software Ltd, UK). Spectra were decomposed with the least squares fitting routine provided by the software with a Gaussian/Lorentzian (85/15) product function and after subtraction of a Shirley-type baseline [2]. Molar fractions were calculated using peak areas normalized on the basis of acquisition parameters and sensitivity factors provided by the manufacturer. Depending on the MNP@NcS combination, the analytical peaks used were C_{1s}, Na_{1s}, Cl_{2p}, O_{1s}, N_{1s}, Ni_{2p}, Fe_{2p}, Co_{2p} and Ni_{2p}.

II.2 Bibliography

1. K. Lagarec and D. G. Rancourt. Mössbauer Spectral Analysis Software for Windows 1.0. Department of Physics, University of Ottawa, Canada, 1998.
2. D.A. Shirley, *Phys. Rev.*, 1972, **B5**, 4709.

appendix III

a short review on the chemistry of iron oxides, hydroxides and oxyhydroxides

The chemical family constituted by iron, its oxides, hydroxides and oxyhydroxides have been of utmost importance to very diverse areas of human activity since the dawn of ages [1]. Accordingly, the scientific community has devoted extensive attention to their transformations and synthesis. Indeed, the different compounds that compose this family are complexly interrelated by a series of physicochemical transformations that are sensibly dependent on a system's particular reaction conditions such as pH, temperature or pressure [2, 3], among other variables.

The later was experimentally observed during the synthesis of a magnetite@graphene nanocomposite by a direct co-precipitation method, in which a lepidocrocite phase was obtained as a synthetic by-product (see Section 2.2.1). In the context of this research project, the presence of iron oxyhydroxide impurities is considered doubly problematic. Firstly, because they are non-magnetic, and secondly because they can readily transform into other, thermodynamically more stable, iron-containing oxyhydroxides, such as goethite, or oxides, such as maghemite or even hematite.

These findings made it clear that it was important to overview the different interrelations existing between the iron-containing species in order to clarify which experimental conditions allowed the obtention of a particular iron-containing compound as a pure phase. The present review thus wishes to give a brief overview on these matters.

III.1 Existing iron oxides, hydroxides and oxyhydroxides

Altogether, there are sixteen known iron oxides, hydroxides and oxyhydroxides [4] whose common names and formulas can be found in Table 1.

Generally speaking, these species consist of closed packed arrays of oxygen atoms or hydroxyl anions (usually in hexagonal (hcp) or cubic close packing (ccp)) in which the interstices are partly filled with divalent or trivalent iron predominately in octahedral coordination, though in certain cases tetrahedral coordination is also observed. The various species differ in the way in which the basic structural units are arranged in space. In some cases, water molecules and small amounts of anions (mainly Cl^-, SO_4^{-2}, CO_3^{-2}) may also participate in the structure.

III.2 Formation and transformations of the different iron oxides, hydroxides and oxyhydroxides: general considerations and mechanisms

Being able to predict which iron oxide will form under a particular set of conditions and whether a single compound or a mixture can be expected is of uttermost importance. Different predictive approaches have been reviewed in the scientific literature.

For instance, a clear guide as to which compound is thermodynamically possible under any set of conditions can be obtained from the change in free energy, ΔG^{o}, for a particular reaction under consideration. A comprehensive list of values required for this calculation applied to the different iron oxides and the soluble Fe species can be found in Cornell and Schwertmann [4].

Whatsoever, it must not be forgotten that a particular transformation considered feasible from the thermodynamic point of view can sometimes not be observed under laboratory conditions. These might be a result of sluggish kinetics, involving other variables not considered by the thermodynamic calculations. This is the case of the transformation of lepidocrocite into goethite, a more stable Fe oxyhydroxide, which has never been observed under ambient conditions in the laboratory [4]. Furthermore, the lepidocrocite to hematite or maghemite transformation has been observed only at high temperatures [4]. Another situation in which thermodynamic predictions might also be insufficient is when dealing with metastable phases that exist for certain periods of time. For example, $Fe(OH)_2$ is thermodynamically unstable with respect to magnetite and other Fe^{3+} compounds. It can, however, exist as a metastable phase for limited periods [4].

A second predictive approach involving redox reaction conditions could be considered more appropriate given the different transformations occurring between the Fe-containing species usually involve changes between the two common Fe valence states, 2^{+} and 3^{+}. In this case, a series of plots traditionally named Pourbaix or "Eh vs pH" diagrams relate the system's redox potential (Eh) variation against its pH, allowing to identify the stability zones of the different possible iron-species.

Table 1 - List of iron oxides, hydroxides and oxyhydroxides. Adapted from [4]

Species	Common name	Chemical formula
Iron oxides		
iron(II) oxide	Wüstite	FeO
iron(II,III) oxide	Magnetite	Fe_3O_4
iron(III) oxide		
alpha phase	Hematite	α-Fe_2O_3
beta phase	-	β-Fe_2O_3
gamma phase	Maghemite	γ-Fe_2O_3
epsilon phase	-	ε-Fe_2O_3
Iron hydroxides		
iron(II) hydroxide	White rust	$Fe(OH)_2$
iron(III) hydroxide	Bernalite	$Fe(OH)_3$
Iron oxyhydroxides		
	Goethite	α-FeOOH
	Akaganéite	β-FeOOH[1]
	Lepidocrocite	γ-FeOOH
	Feroxyhyte	δ-FeOOH
	Ferrihydrite	$FeOOH{\cdot}4H_2O$, $Fe_5HO_8{\cdot}4H_2O$, $Fe_5(OH)O_7{\cdot}4H_2O$
	High-pressure FeOOH	-
Iron (III) oxyhydroxysulfate	Schwertmannite	*ideally* $Fe_{16}O_{16}(OH)_y(SO_4)_z{\cdot}nH_2O$
Iron (II, III) oxyhydroxychloride, sulfate or carbonate	Green rusts I (planar anions, *e.g.*, Cl^- and CO_3^{-2}) and green rusts II (three-dimensional anions SO_4^{-2})	$(Fe^{2+}_{(1-x)}Fe^{3+}_x(OH)_2]^{+x}{\cdot}[x/nA^{-n}{\cdot}m/nH_2O]^{-x}$ *where A is* Cl^-, CO_3^{-2} *or* SO_4^{-2}

[1] Cudennec and Lecerf [5] mention that akaganéite is not strictly an iron oxyhydroxide but rather an oxyhydroxichloride. Indeed, in this compound's structure, oxygen is occasionally replaced by a hydroxide and a chloride ion. The presence of the chloride ion is essential to the stability of the crystal structure, characterized by the presence of large channels in which these ions are positioned. Cornell and Schwertmann [4] point out that fluoride-containing akaganéite minerals have also been found, in which F^- replaces the Cl^- anion.

As for the mechanisms governing not only the obtention of a particular iron-containing species but also the transformations occurring between them, they are still a matter of academic debate [1, 2, 4, 5, 6, 7].

Cornell and Schwertmann [4] consider that the formation of all the Fe-containing hydroxides, oxyhydroxides and oxides follow one of the following four basic mechanisms:

i) Direct precipitation from Fe^{2+} and/or Fe^{3+}-containing solutions by means of either hydrolysis reactions of Fe^{3+} ions or oxidation followed by hydrolysis of Fe^{2+} ions, at various temperatures and pHs.

ii) By the thermal decomposition of metal chelates.

iii) Transformation of an Fe oxide precursor, either by a dissolution/reprecipitation process or,

iv) *Via* a solid state thermal transformation involving internal rearrangements within the structure of the solid precursor.

A different perspective on the same matter has been offered by Cuddenec [9]. Considering that metallic iron is the initial departure point, the author proposes four main oxidation mechanisms that end up in the obtention of hematite, the iron oxide with the highest thermodynamic stability. These mechanisms are:

i) Oxidation under humid air (in the absence of CO_2).

ii) Oxidation in acid aqueous environments.

iii) Oxidation in neutral aqueous environments, in the presence of anions, particularly chloride.

iv) Oxidation in basic environments.

In Cudennec's approach, the other iron oxides, hydroxides and oxyhydroxides are to be considered as intermediary phases that are more or less metastable. The extremely poor solubility of all these solid phases doesn't exclude the possibility that they transform into each other by dissolution and recrystallization mechanisms, as Cornell and Schwertmann have documented [4]. Whatsoever, the structural filiations existing between some of these phases tend to point towards the fact that a topotactic transformation is, sometimes, the only valid mechanism explaining why a particular phase transforms exclusively into another.

The different transformation pathways as summarized by Cuddenec [9] and by Cornell and Schwertmann [4] are shown in Figure 1 and Figure 2 respectively.

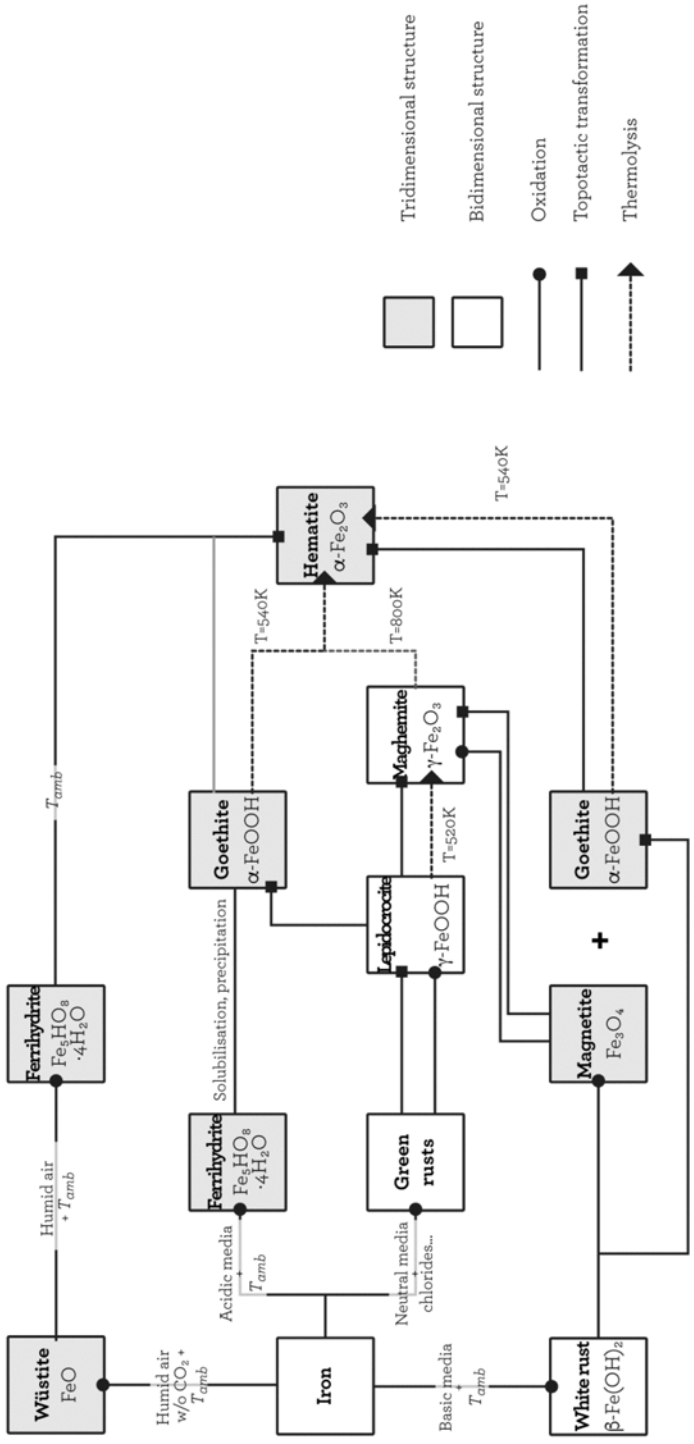

Figure 1- Transformation pathways of the iron-containing oxides, hydroxides and oxyhydroxides. Adapted from Cuddenec [9].

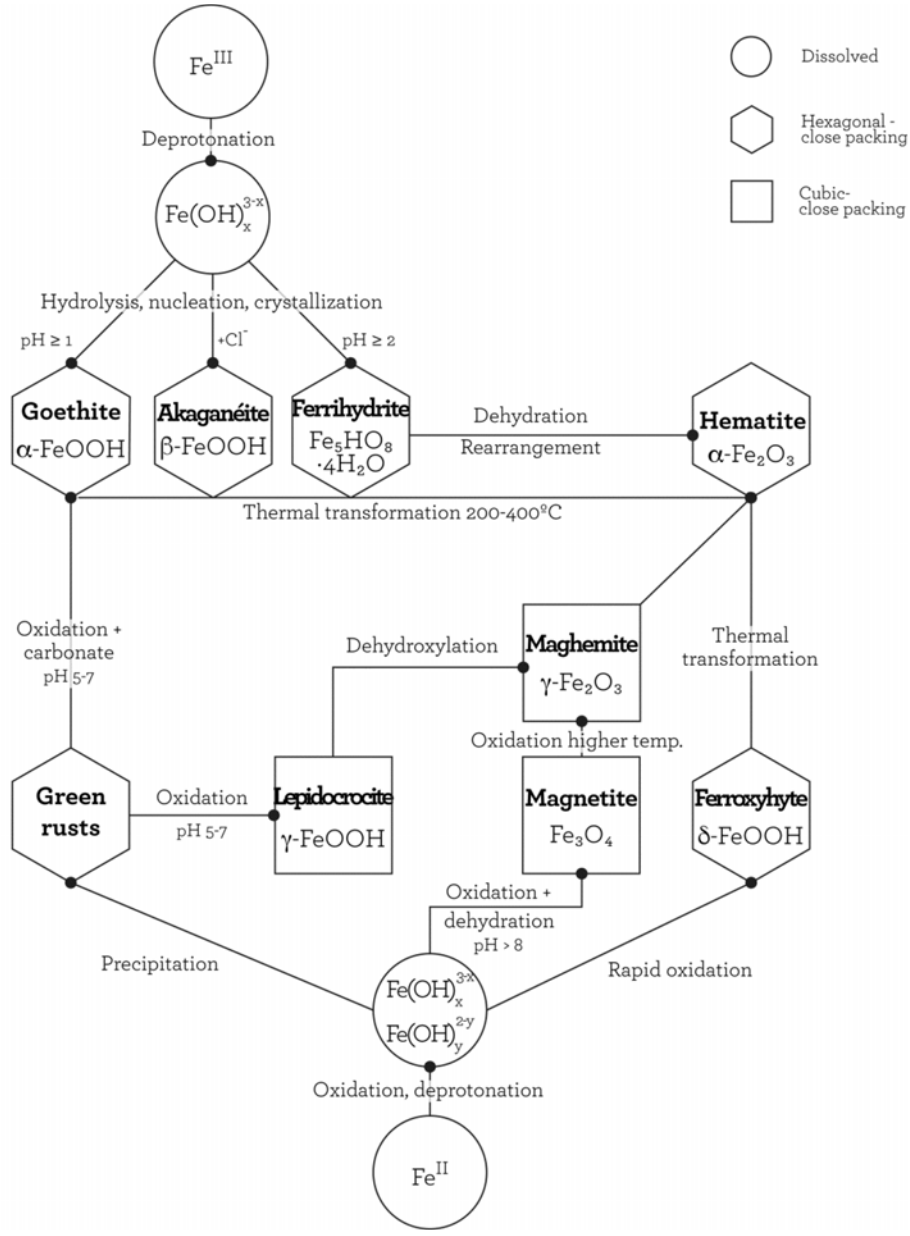

Figure 2- Transformation pathways of the iron-containing oxides, hydroxydes and oxyhydroxides. Adapted from Cornell and Schwertmann [4].

III.3 Experimental conditions leading to particular Fe-containing hydroxides, oxyhydroxides or oxides

The following sections will present a brief review of the mechanisms and reaction conditions that can lead to the formation of a particular iron-containing phase or a mixture of them either from a) a solution of Fe^{3+} ions or b) a solution of Fe^{2+} ions; c) the thermal decomposition of a metal chelate; d) thermally driven transformations in the solid state; and e) dissolution/recrystallization processes.

Green rusts (GR), goethite, lepidocrocite and maghemite have been given special attention, being these species the most possible reaction by-products that can be obtained under the experimental conditions we have used for magnetite synthesis.

III.3.1 Formation of Fe hydroxides, oxyhydroxides and oxides from Fe(III) systems

Most of the reactions departing from Fe ions in an aqueous solution and leading to the obtention of one particular Fe-containing hydroxide, oxyhydroxide or oxide involves a hydrolysis reaction. These reactions spontaneously occur when, in the presence of water, an Fe^{3+} salt dissociates, forms an hexa-aquo ion (see Equation III.1) and then, due to the influence of the electropositive cation, the ligands are deprotonated (see Equation III.2).

$$FeCl_3+6H_2O \rightarrow Fe(H_2O)_6^{3+}+3Cl^- \quad \textbf{Equation III.1}$$

$$Fe(H_2O)_6^{3+} \rightarrow FeOH(H_2O)_5^{2+}+H^+ \ldots \quad \textbf{Equation III.2}$$

This process happens stepwise with ultimately all six ligands being deprotonated. Complete hydrolysis corresponds to the formation of an Fe^{3+} oxyhydroxide or oxide (Equation III.3 and Equation III.4).

$$Fe(H_2O)_6^{3+} \rightarrow FeOOH+3H^+ + 4H_2O \quad \textbf{Equation III.3}$$

$$2Fe(H_2O)_6^{3+} \rightarrow Fe_2O_3 +6H^+ + 9H_2O \quad \textbf{Equation III.4}$$

Initially, low molecular weight species are formed, as shown in Equation III.5 (the Fe^{3+} ion is not shown fully hydrated as in Equation III.2):

$$Fe^{3+}+H_2O \rightarrow Fe(OH)^{2+}+H^+ \qquad \textbf{Equation III.5}$$

However, when the OH/Fe ratio reaches a threshold value of *circa* 1 [4], the low molecular weight species interact to produce dimers (Equation III.6). Trimers or tetramers have not been identified directly.

$$2Fe(OH)^{2+} \underset{k_{21}}{\overset{k_{12}}{\rightleftarrows}} Fe_2(OH)_2^{4+} \qquad \textbf{Equation III.6}$$

The formation of the dimer is rapid, around three orders of magnitude faster than its breakdown (k_{12}=360 $M^{-1}s^{-1}$ while k_{21}=0.4 s^{-1} @25ºC, 3M $NaClO_4$), and thus further polymerization of the dimer may be very swift [4]. Usually, when hydrolysis has reached an advanced state, a red brown solid, suspended or precipitated, is obtained. It contains a mixture of monomers, dimers and polymers of different molecular weights, being these last species more abundant when the OH/Fe ratio reaches higher values [4].

From what was described above, a Fe^{3+} salt solution may lead directly to goethite, lepidocrocite, akaganéite and hematite- or mixtures of these compounds- depending on the experimental conditions.

The key factor governing which oxyhydroxide or oxide forms, as well as its crystallinity, is the rate at which the above-described monomers and dimers are supplied to the growing crystal. The governing factors in this polymerization/crystallization process are thus pH and the Fe^{3+} concentration (and thus, the OH/Fe ratio) as well as temperature. Indeed, the supply rate of growth units has to be such that the solubility products of these oxides are exceeded, but not the much higher one of ferrihydrite. Such a situation arises at low pH (OH/Fe < 1) or, at higher OH/Fe, if the growth units are supplied so slowly that the spatial ordering leading to the more crystalline Fe oxyhydroxides or oxydes can be achieved.

In other terms, the slower the hydrolyzed species are supplied, the better ordered are the phases that result and thus the highly crystalline oxides, such as lepidocrocite, goethite or hematite, can be formed. On the other

hand, when the rate of supply of growth units is relatively rapid, the ferrihydrite is favored. However, the more crystalline Fe species can also form over a wide pH range by transformation of ferrihydrite following a series of dissolution/reprecipitation mechanisms.

The nature of the anion has also been shown to have a significant effect. For example, goethite has been found to be formed exclusively from $Fe(NO_3)_3$ solutions whereas both goethite and lepidocrocite were obtained from $Fe(ClO_4)_3$ solutions. In addition, akaganéite formation seems to require the presence of chloride and fluoride ions [4].

The obtention of magnetite from a Fe^{3+} solution must involve the partial reduction of some of the Fe^{3+} species into Fe^{2+} ions. In the following section, the basic set of chemical reactions involving Fe^{2+} ions will be reviewed, making a special emphasis on those reactions that can take place when Fe^{2+} and Fe^{3+} ions are present.

III.3.2 Formation of Fe hydroxides, oxyhydroxides and oxides from Fe(II) systems

Goethite, lepidocrocite, akagénite, magnetite, maghemite, ferrihydrite, feroxyhyte and hematite can all be produced from Fe^{2+} solutions by oxidation to Fe^{3+} followed by hydrolysis. This process can happen either directly or *via* green rust complexes or $Fe(OH)_2$. The latter species can convert to the oxides either by a solid state reaction or by means of a solution (reconstructive) transformation [4]. Generally, when there is a difference between the structure of the precursor and that of the final oxide, a *via* solution process seems more likely, but an internal rearrangement during oxidation may also take place.

Which oxide forms is governed by the pH, the rate of oxidation and concentration of Fe^{2+}, the temperature and also by foreign compounds in the system.

Given the oxidation reaction of Fe^{2+} with oxygen can be written as:

$$2Fe^{2+} + 3H_2O + \frac{1}{2}O_2 \rightarrow 2FeOOH + 4H^+ \qquad \textbf{Equation III.7}$$

The rate of Fe^{2+} oxidation can then be described by the following equation:

$$\frac{-d[Fe^{2+}]}{dt} = k[Fe^{2+}] \cdot P_{O_2} \cdot [OH^-]^2 \qquad \textbf{Equation III.8}$$

It can be thus clearly observed that the rate of oxidation increases one hundredfold per pH unit. In addition, besides increasing with increasing temperature, this rate has also been shown to be inversely dependent on the ionic strength of the system, directly dependent on the stirrer speed and also influenced by the nature of the counterion. Indeed oxidation of Fe^{2+} is accelerated by ions such as F^-, H_2PO_4 and HPO_4^{-2}, and lowered by others in the order, ClO_4^- > NO_3^- > Cl^- > $H_3SiO_4^-$ > Br^- > I^- > SO_4^{-2} [4]. Likewise, the presence of other iron oxides can promote oxidation in the order ferrihydrite < goethite < lepidocrocite < akaganéite.

Unless the reaction conditions are carefully controlled, mixtures, rather than a monophase product result. Characteristically, Fe^{2+} systems lead to the formation of pairs of products, e.g. goethite/lepidocrocite. Table 2 exemplifies certain experimental conditions favoring the formation of one compound in various pairs of oxides typically formed via the oxidation of Fe^{2+} salts.

Table 2 - Experimental conditions that favor the obtention of a particular Fe-containing compound when departing from Fe^{2+} salts

Goethite	Lepidocrocite
CO_2 present	CO_2 absent
Sulphate	Chloride
Fast oxidation	Slow oxidation
Lower pH	Higher pH
Al, Mn, Co	
Lepidocrocite	**Ferrihydrite**
Slow oxidation	Fast oxidation
pH>5	pH<5
Lepidocrocite	**Magnetite**
Fast oxidation	Slow oxidation
Low temperature	High temperature
Lower pH	Higher pH
Chloride	-
Low $[Fe^{2+}]$	High $[Fe^{2+}]$

The chemical system formed by all the possible Fe-containing species that can be formed from a Fe^{2+} solution is extremely complex. Whatsoever, given the aims of both, our research project and this Appendix, only the chemical system surrounding magnetite and its obtention will be explored, clearly outlining the role played by pH, the oxidation rate of Fe^{2+} and reaction temperature as the most relevant experimental variables to be controlled.

III.3.2.1 Effect of pH, oxidation rate of Fe(II), and temperature: the $Fe(OH)_2$, green rusts type I or II, Fe_5HO_8, α,γ-FeOOH and Fe_3O_4 system

In strongly alkaline solutions (pH > 10) oxidation of Fe^{2+} solutions proceeds via the formation of $Fe(OH)_2$ and usually yields magnetite given that, under these conditions, the solubility product of magnetite is exceeded so that it is more stable than the other Fe^{3+} oxides.

The exact mechanism through which $Fe(OH)_2$ transforms into magnetite is still a subject of debate [4]. Kiyama [8] has indicated that at a pH value above 10, abundant $Fe(OH)_2$ crystals precipitate and, *via* air oxidation, form magnetite. Considering that the involved species have different particle shapes and that the oxidation rate is independent of the concentration of magnetite in the system, this author assumed that the formation of the oxide does not occur by the surface oxidation of the hydroxide (solid phase reaction) but instead occurs in the liquid phase. Other authors [4] observed, however, that magnetite indeed nucleated on the surface of platy $Fe(OH)_2$ crystals but that this growth involved soluble species [4].

Nonetheless, different authors have observed [4, 5, 8] that, alongside magnetite, FeOOH (either lepidocrocite or goethite) is formed in the suspension. Cornell and Schwertmann [4] indicate that the formation of these oxyhydroxides ceases at an early stage of the reaction and that the Fe^{2+} ions in solution interact with them to form magnetite. Indeed, Cudennec [5] has shown that under the oxidative action of oxygen, it dissolves yielding goethite, and then, forms magnetite. One of the hypothesis that have been proposed [5] to explain this reaction pathway is that the goethite formed

from $Fe(OH)_2$ reacts with the residual hydroxide, yielding the more stable magnetite oxide:

$$2\alpha\text{-}FeO(OH) + Fe(OH)_2 \rightarrow Fe_3O_4 + 2H_2O \qquad \textbf{Equation III.9}$$

Different authors [4-8] have also observed that when the amount of base added creates only slightly basic conditions ($7 < pH < 10$), a whitish but relatively amorphous precipitate of $Fe(OH)_2$ and/or ferrihydrite is formed, this later species being favorably produced at lower pH values. The oxidation of this precipitate forms firstly a dark green precipitate whose XRPD analysis proved to be a green rust of type I or II [8], depending on the intercalating anion found in the precursor Fe^{2+} salt.

The obtention of a green rust from the oxidation of $Fe(OH)_2$ has been described by Génin *et al.* [6]. The hydroxide consists of hexagonal close-packed OH^- ions with alternating Fe^{2+} layers and empty spaces forming a sequence AcB□A... In this sequence A and B represent the OH^- planes, c the Fe^{2+} cations and □ the empty spaces. When oxidation of the $Fe(OH)_2$ occurs and some Fe^{2+} are transformed into Fe^{2+}, a hydroxide sheet AcB which was originally electrically neutral, gains an "excess" positive charge. In order to restore electrical neutrality, negative charges provided by anions (such as Cl^-, $SO4^{2-}$ or $CO3^{2-}$) are intercalated into the AcB sheets and thus a green rust (of a type dependent on the nature of the anion) is formed.

Cornell and Schwertmann [4] point out that green rusts are also formed during the oxidation of Fe^{2+} species under weakly acid to weakly alkaline conditions. In this case, the solubility product of $Fe(OH)_2$ is no longer exceeded and its precipitate is not formed. Whatsoever, these authors have established that there are two other possible reaction pathways for green rust formation: either by direct precipitation from a Fe^{2+} salt solution upon oxidation, once their solubility product is exceeded (Equation III.10); or by interaction between the highly reactive 2-line ferrihydrite, Fe_5HO_8, precipitated initially, and Fe^{2+} in solution (Equation III.11). In the presence of a sufficiently high concentration of Fe^{2+}, the green rust is more stable than 2-line ferrihydrite.

$$3FeSO_4 + 0.25O_2 + 4.5H_2O \rightarrow Fe_2^{2+}Fe^{3+}(OH)_5SO_4 + 2H_2SO_4$$ **Equation III.10**

$$Fe_5^{3+}HO_8 + 10FeSO_4 + 17H_2O \rightarrow 5Fe_2^{2+}Fe^{3+}(OH)_5SO_4 + 5H_2SO_4$$ **Equation III.11**

From these equations, it is clear that the formation of the green rust phases depends on the concentration of Fe^{2+} in solution. Indeed, it has been found that once the $[Fe^{2+}]$ falls below a critical level and the pH of the solution becomes slightly acidic (pH < 5), further oxidation leads to the decomposition of the green rust and to the formation of goethite and/or lepidocrocite (see Equation III.12).

$$5Fe_2^{2+}Fe^{3+}(OH)_5SO_4 + O_2 \rightarrow 6FeOOH + 4H_2SO_4$$ **Equation III.12**

Seemingly, which type of allotropic form of FeOOH is obtained depends on which type of green rust is oxidized [5, 6]. γ-lepidocrocite is obtained, mostly as a pure phase, for green rusts containing chloride while α-goethite is obtained exclusively when oxidizing green rusts whose counteranion is carbonate [6]; a mixture of both allotropes can be obtained, depending on the reaction conditions, from sulfate-containing green rusts [5].

Cudennec and Lecerf [5] have postulated that these particularities might be attributed to the effect of the counteranion on the oxidation rate of Fe^{2+}, following the same principles described in section III.3.2 for the formation of these two FeOOH allotropes from a Fe^{2+} solution. Indeed, if the oxidation rate of the ferrous ion is slow, the most thermodynamically stable trivalent iron oxyhydroxide, goethite, is to be produced. Thus, while chlorides seem to accelerate the oxidation of Fe^{2+} ions and thus induce the production of lepidocrocite, carbonates retard this oxidation and orient the reaction towards the obtention of goethite.

However, these authors have also advanced the idea that a complex topotactic transformation takes place and thus the crystalline structure found in a particular green rust, which is basically induced by the counteranion, also plays a fundamental role in the obtention of one or the other iron (III) oxyhydroxide allotrope. Whatsoever, here again, there is no consensus on how this transformation actually takes place given the

structural differences between the green rust and the oxidation products (sheets vs. double bands of octahedra) has been considered by some authors [4, 6] as an evidence that a *via* solution transformation takes place. Nonetheless, the crystallographic evidence produced by Cudennec and Lecerf is, up to this date, the most comprehensive mechanistic explanation of these transformation processes.

At slightly lower pH values, goethite and lepidocrocite form directly from soluble green rust complexes, possibly because the solubility product of the correspondent solid green rust is no longer exceeded. At even more acidic pHs (pH < 4), the $[OH^-]$ is too low to form a green rust and thus ferrihydrite, a compound with a low OH^- content, is formed exclusively [5].

However, at higher pHs (pH > 7) further oxidation of the green rusts yields magnetite once the required Fe^{2+}/Fe^{3+} molar ratio (0.5) is achieved [7, 8]. Indeed, green rusts have a higher molar ratio of Fe^{2+}/Fe^{3+} than magnetite (2.5 to 3.0) [7]. The results produced by Schwertmann and Fechter [7] indicate that the formation of green rust requires a minimum of Fe^{3+} that most probably lies close to 25% of total iron for the chloride form and close to 33% for the sulphate form (no information for the carbonate-based green rust is given). However, once formed, the structures tolerate much higher Fe^{3+} proportions, possibly up to more than 50%. Further oxidation of Fe^{3+} and thus an increase in the Fe^{3+} content causes the green rust to break down and, if the pH and temperature conditions are met, magnetite is produced. However, the oxidation rate of Fe^{2+} ions has to be relatively low. Indeed magnetite formation requires slow oxidation because complete dehydroxylation of the precursor (the green rust) prior to complete oxidation is only possible if sufficient time is available. If, on the other hand, complete oxidation is fast and precedes dehydroxylation, lepidocrocite forms in preference to magnetite. Indeed, dehydroxylation and oxidation appear to be competing reactions steps [4].

From the information exposed above, it seems clear that $Fe(OH)_2$, the two FeOOH allotropes, green rusts and Fe_3O_4 are chemical species interrelated by complex transformation processes. Even though pH and the oxidation rate

of Fe^{2+} ions seem to be crucial experimental variables for the obtention of a particular product, Kiyama [8] has also shown that temperature is an extremely important variable. Indeed, this author proved that independently of the precursor that is oxidized (e.g. $Fe(OH)_2$ or green rusts) higher reaction temperatures favor the formation of a pure magnetite phase while lowering the temperature produces a mixture of magnetite and α or γ-FeOOH and, eventually, the obtention of either one of the non-magnetic allotropic FeOOH species (see Figure 3).

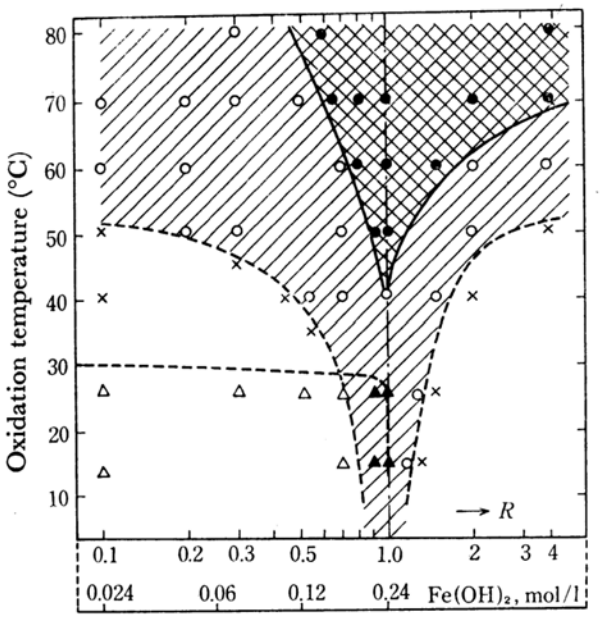

Figure 3- Oxidation conditions for the formation of Fe_3O_4. (Adapted from Kiyama [8])
Legend: ●: Fe_3O_4, ×: α-FeOOH, ○: A mixture of Fe_3O_4 and α-FeOOH, ▲: A mixture of Fe_3O_4, α-FeOOH and γ-FeOOH, △: A mixture of Fe_3O_4 and γ-FeOOH. R=2NaOH/$FeSO_4$ molar ratio.

III.3.3 Formation of Fe oxides from the decomposition of Fe complexes via thermolysis

This process is used to produce iron oxides of well-defined morphology and a narrow size distribution. It usually involves the solvo or hydrothermal decomposition of Fe^{2+} or Fe^{3+} complexes to produce either hematite (under oxidizing conditions, as those produced by the presence of NO_3^- ions) or magnetite (in reducing conditions generally obtained by the addition of amines or polyols) [4]

but has also been performed in the solid state in order to obtain maghemite [10] or a magnetite-hematite mixtures [11].

The exact mechanisms through which the oxides are formed are not very well understood. In alkaline conditions, it is believed the complexes are decomposed forming soluble Fe-hydroxo species that are slowly released [2]. According to what was presented in section III.3.1, the presence of Fe-hydroxo species implies that a hydrolysis reaction has to take place if the oxides are to be formed. Depending on the oxidation state of the complex precursor and thus on the redox nature of the reaction environment, when supersaturation with respect to a particular Fe oxide (magnetite or hematite) is exceeded, nucleation occurs, followed by an equilibrium growth stage. Given that the ligand is destroyed as the complex breaks down, it does not interact with the growing iron oxide.

III.3.4 Formation of Fe oxides from transformation processes

As mentioned before, a particular characteristic of the iron oxide system is the variety of possible interconversions between the different phases. This means that, once obtained, if the appropriate conditions are met, almost every iron oxide can be converted into at least two others [4]. As mentioned before and as can be observed in Figure 1, goethite and hematite are the most common end members of the different transformation processes due to their high thermodynamic stability.

The different transformation processes can be classified in terms of either the chemical changes that occur or the modifications observed in the compounds' structural features. Transformations that involve a chemical modification are dehydration (loss of H_2O molecules), dehydroxylation (loss of OH moieties) and oxidation/reduction (transfer of electrons and change in Fe oxidation state). On the other hand, the structural transformation processes are either topotactic or reconstructive.

Topotactic transformations take place in the solid phase, usually at high temperatures given they involve atomic rearrangements within the crystal lattice. In this type of transformations, there must be an agreement in three dimensions between the reactant and the product's structures. In reconstructive transformations, however, there is no structural relationship between the reactant and the product given the former is dissolved and the later precipitates afterwards from solution. Table 3 below summarizes the interconversions that, accordingly to Cornell and Schwertmann [4], can take place between the different iron oxides.

Table 3 - Transformations that can take place between the different iron oxides. Adapted from [4]

Precursor	Product	Type of transformation	Preferred medium
Goethite	Hematite	Thermal or mechanical dehydroxylation	Gas/vacuum
		Hydrothermal dehydroxylation	Solution
	Maghemite	Thermal dehydroxylation	Air + organic
Lepidocrocite	Maghemite, hematite	Thermal dehydroxylation	Gas/vacuum
	Goethite	Dissolution/reprecipitation	Alkaline solution
	Magnetite	Reduction	Alkaline solution with Fe^{2+}
Akaganéite	Hematite	Thermal dehydroxylation	Gas/vacuum
	Goethite	Dissolution/reprecipitation	Alkaline solution
	Hematite	Dissolution/reprecipitation	Acid solution
	Magnetite	Dissolution/reduction	Alkaline solution with N_2H_4
δ-FeOOH	Hematite	Thermal dehydroxylation	Gas/vacuum
Feroxyhyte	Goethite	Dissolution/reprecipitation	Alkaline solution
Ferrihydrite	Hematite, Maghemite	Thermal dehydroxylation/dehydration	Gas/vacuum
	Goethite	Dissolution/reprecipitation	Aqueous solution pH 3-14
	Akaganéite	Dissolution/reprecipitation	Acidic media; presence of Cl
	Lepidocrocite	Dissolution/reprecipitation	pH 6, presence of cysteine
	Hematite	Aggregation, short-range crystallization within ferrihydrite aggregate	Aqueous solution at pH 6-8
	Substituted magnetite	Dissolution/reprecipitation	Alkaline solution with M^{II}
Hematite	Magnetite	Reduction	Reducing gas
		Reduction-dissolution reprecipitation	Alkaline solution with N_2H_4
Magnetite	Maghemite, hematite	Oxidation	Air
Maghemite	Hematite	Thermal conversion	Air
$Fe(OH)_2$	Magnetite	Oxidation	N2; Alkaline solution
	Goethite Lepidocrocite Magnetite Maghemite	Oxidation	Alkaline solution
FeO	Magnetite (+Fe)	Disproportionation	Air

III.3.4.1 Formation of Fe(III) oxyhydroxides and oxides from thermally-driven transformations

As mentioned in the introduction to this manuscript, in the context of this research project, the most interesting thermal transformations are those that relate hematite to maghemite, magnetite or one of the FeOOH polymorphs that can be formed while trying to obtain magnetite (*e.g.* lepidocrocite or goethite). Indeed, the fact that all the above-mentioned species can eventually transform into the most thermodynamically stable hematite implies that our nanocomposites could eventually lose their magnetic properties.

Generally speaking, all the polymorphs of FeOOH, as well as ferrihydrite, can be dehydroxylated and dehydrated to those of Fe_2O_3 under the influence of either heat or mechanical stress. Most of the times, the end product of these reactions is hematite; only in the case of lepidocrocite, maghemite is obtained as an intermediate phase.

Even though these transformations have been extensively investigated in the dry state, they can also take place in solution, under hydrothermal conditions. Whatsoever, no consensus has been reached on the different processes' onset temperature. This is partly due to the fact that this temperature mainly depends on the nature of the compound, its crystallinity, the presence of chemical impurities or if the process occurs under air or under vacuum. For example, it has been observed that as the crystallinity of goethite improved, the endothermic (DTA) peak temperature shifted from 260 to 320 ºC [4]. Furthermore, the dynamic nature of the used thermoanalysis methods (*e.g.* DTA), in which the temperature of the endothermic peak is usually higher than the equilibrium temperature of the conversion, also plays a role. Nonetheless, the temperature range values reported by Cornell and Schwertmann [4] are presented in Table 4 and can be used as a reference.

Table 4 - Temperature ranges for thermally-driven transformations amongst certain Fe-containing species

Precursor	Product	Transformation temperature (ºC)
Goethite	Hematite	260-320 ºC
Lepidocrocite	Maghemite	200-280 ºC (air) 120 ºC (vacuum)
Maghemite	Hematite	370 – 600 ºC

III.3.4.1.1 The transformation of magnetite to maghemite or hematite

In the specific case of the magnetite to maghemite or hematite transformation, the thermally-induced topotactic change of magnetite into maghemite or hematite must be accompanied by an oxidation process.

Different authors indicate that the oxidation from Fe_3O_4 to γ-Fe_2O_3 can be fully accomplished at approximately 220 ºC [12]. Nonetheless, the results obtained previously in our research group [3] clearly indicate that this process takes place gradually, and that, contrary to what certain authors recently claim [3], there is not a clearly-defined onset temperature at which the oxidation process begins nor there is a definite reaction time at which it is completed.

For instance, it was found that after heating a magnetite sample under air, at 220ºC for 6 hours, the finer grains changed color from black to a reddish-brown, an indication of the magnetite to maghemite transformation which was confirmed by μ-Raman spectroscopy and X-ray diffraction [3]. However, the larger grains remained black, their surface covered with minute maghemite particles. This was explained by the fact that magnetite-to-maghemite oxidation is a diffusion-governed process, in which particle size are of outmost importance to the oxidation rate. Indeed, Siddhu *et al.* [12] have proposed that the oxidation process of magnetite occurs via the outward diffusion of iron cations towards the particle's surface. Whatsoever, the oxidation state of the migrating iron cations remains unclear and no conclusive evidence has yet been provided to solve this issue. For instance, the investigations conducted by Haneda and Morrish [13] indicate that the magnetite to maghemite conversion occurs most easily in ultrafine micrometric magnetite particles. Furthermore, contrary to what

was reported by Sidhu *et al.* [12], they demonstrated that the activation temperature for the oxidation process decreases as magnetite particles' size decrease, thus making it possible for this transformation to occur even at room temperature. This is in agreement with has been observed in our laboratory: our synthetized nanocomposites, whose magnetite nanoparticles are three orders of magnitude smaller than those investigated by Haneda and Morrish, also turn reddish-brown when left exposed to air, at room temperature.

Also, a second process, involving the transformation of magnetite or maghemite into hematite is also possible. This oxidation process is particularly crucial to the applications that depend on the ferrimagnetic iron oxides' magnetic properties given that hematite is antiferromagnetic. As with the magnetite to maghemite transformation, the conversion of any of the two-ferrimagnetic iron oxides into hematite is a diffusion-driven process dependent on temperature and particle size [14].

Furthermore, the inversion of the cubic spinel structure into hematite's hexagonal form is also a thermally activated process. However, the reported temperature at which this transformation occurs is highly variable and may range from ≈ 250 ºC to ≈ 900 ºC [14]. For example, David and Welch [15] found that precipitated magnetite of undetermined particle size presented equal amounts of magnetite and hematite after heating a sample at 400 ºC for 4 hours. Sidhu [16] established that maghemite powders with an average crystal size of 500 Å oxidized to form hematite at a very slow rate (about 10% reaction completed in one week) when heated at temperatures above 320 ºC, having to reach temperatures above 450 ºC in order to obtain increasingly higher rates of oxidation. Our own results [3] have shown that no hematite is observed while heating under air, at 410 ºC, a sample of agglomerated magnetite nanoparticles whose average size is 10.9 ± 3.5 nm. Accordingly, Cornell and Schwertmann [4] have reported that in the temperature range comprised between 200 and 250 ºC, magnetite crystals transformed solely into maghemite while hematite was obtained at

temperatures above 500 ºC. They have also stated that at even higher temperatures (*T*>500 ºC) magnetite would directly change into hematite.

III.3.4.2 Formation of Fe(III) oxyhydroxides and oxides from dissolution/reprecipitation processes

Of all the dissolution/reprecipitation reactions reviewed by Cornell and Schwertmann [4], only three seem to be of direct relevance to the development of this research project.

The first of them is the lepidocrocite to goethite/hematite transformation given the former has been obtained as a non-desired product in several of our magnetite synthesis and could thus be transformed into the non-magnetic goethite or hematite species. In alkaline conditions, such as the ones used in some of our synthesis, goethite can nucleate from soluble $Fe(OH)_4^-$ species released by the dissolution of lepidocrocite. Using a poorly crystalline lepidocrocite and higher temperatures (above 80 ºC according to the experimental data shown by Cornell and Schwertmann [4]), hematite can be obtained, possibly via a dehydroxylation process.

The second reaction of interest is the maghemite and goethite to hematite transformation. In this case, under hydrothermal conditions maghemite (150 ºC – 180 ºC) and goethite (180 ºC) can transform into hematite by means of a dissolution/reprecipitation mechanism. A change in the habit of the reactant and product's crystals tend to support the existence of such a mechanism. For the maghemite to hematite transformation, reaction kinetics seem to depend on the nature of both the reaction medium and the base, while in the case of goethite they are mostly dependent on the crystallinity and crystal size of the goethite precursor.

The last reaction to be considered is the reduction of lepidocrocite into magnetite in alkaline media, following the reaction shown in Equation III.13:

$$2FeOOH + Fe^{2+} \rightarrow Fe_3O_4 + 2H^+ \qquad \textbf{Equation III.13}$$

Neutralization of the protons promotes the reaction and allows for the system to become supersaturated with respect to magnetite. The transformation is believed to occur *via* solution. However, it is also thought

that the actual mechanism could involve the adsorption of Fe^{2+} species on lepidocrocite's surface groups in order to form magnetite directly.

This reaction could theoretically be a solution for the lepidocrocite contaminations obtained during the synthesis of some of our nanocomposites. Indeed, if these are replaced in an alkaline media with an excess of Fe^{2+} ions (using $FeCl_2{\cdot}4H_2O$ or $FeSO_4$ as precursors, for example), one should actually expect the contaminant to transform into magnetite.

III.4 Bibliography

1. Y. Cudennec, and A. Lecerf, *Solid State Sci.*, 2005, **7**, 520-529.
2. G. Navarro, R. Acevedo, A. Soto and M. Herane, *J. Phys. Conf. Ser.*, 2008, **134**, 012023.
3. F. Mederos-Henry, 2013, Magnetite nanoparticles supported on graphene: nanocomposites for the production of microwave-responsive metamaterials. Master thesis. UCLouvain, Louvain-la-Neuve, Belgium. 71 pp.
4. R.M. Cornell and U. Schwertmann, *The iron oxides. Structure, properties, reactions, occurrences and uses (2nd ed).*, 2003, Wiley-VCH; Darmstadt, Germany. 664 pp.
5. Y. Cudennec and A. Lecerf, *C.R. Chimie*, 2003, **6**, 437-444.
6. J.M. Génin, G. Bourrié, F. Trolard, M. Abdelmoula, A. Jaffrezic, P. Refait, V. Maitre, B. Humbert and A. Herbillon, *Environmental Science Technology*, 1998, **32,** 1058-1068.
7. U. Schwertmann and H. Fechter, *Clay miner.*, 1994, **29**, 87-92.
8. M. Kiyama, *B. Chem. Soc. Jpn.*, 1974, **47**(7), 1646-1650.
9. Y. Cudennec, Y (n.d.). Structures cristallines des oxydes, oxy-hydroxydes et oxydes de fer. In *Academic*. Retrieved January 9, 2014. http://fr.academic.ru/dic.nsf/frwiki/1576800
10. Y.C. Zhang, J.Y. Tang and X.Y. Hu, *J. Alloy. Compd.*, 2008, **462**(1-2), 24-28.
11. M.E. Mendoza, F. Donado, R. Silva, M.A. Pérez, and J.L. Carrillo, *J. Phys. Chem. Solids*, 2005, **66**, 927-931.
12. P.S. Sidhu, R.J. Gilkes, and A.M. Posner, *J. Inorg. Nucl. Chem.*, 1977, **39**, 1953-1958.
13. K. Haneda, and A.H. Morrish, *Journal de Physique- Colloque C1, supplément au n°4*, 1977, **38**, C1 321-323.
14. C. B. De Boer and M.J. Dekkers, *Geophysics Journal International*, 2001, **144**, 481-491.
15. I. David and J.E. Welch, *T. Faraday Soc.*, 1956, **52,** 1642-1650.
16. P.S. Sidhu, (1988) *Clay. Clay Miner.*, 1988, **36**(1), 31-38.
3. Fajaroh, F.; Setyawan, H.; Nur, A. and Lenggoro, I.W. *Adv. Powd. Technol.*, 2013, **24**, 507-511.

appendix IV

supplementary
information

IV.1 Oxygenated functions abundance in the different nanocarbon supports as determined by XPS.

XPS analyses were performed on the different nanocarbon supports. The C_{1s} peak was fitted using aromatic (C-arom), alkyl (C-(C,H)), alcohol (C-O), carbonyl/ether (C=O, O-C-O) and acyl ((C=O)-OH) components. The quantification of the different components' contribution to the C_{1s} peak area indicate that the total amount of oxygenated functions decreases in the order GO>>rGO>GNPs for the graphenic supports and ox-MWCNTs>MWCNTs. Table 1 below summarizes the % atomic concentrations of each component and the C/O ratio calculated for each NcS. The XPS spectra for the C1s peak of the different NcS are presented in Figures 1-3.

Table 1 – C/O ratio calculated from the atomic concentration (%) of O_{1s}, N_{1s} and C_{1s} XPS peaks of the different NcS. C_{1s} peak components detailing the abundance of the oxygenated functions are included.

Peak	O_{1s}	N_{1s}	C_{1s}						C/O ratio
			C=O, O-C-O	(C=O)-OH	C-O	C-(C,H)	C_{arom}	C_{total}	
Position (eV)	532.6	401.1	288.8	286.9	286.3	284.8	284.4		
MWCNTs	2.2	0.1	0.0	0.0	0.0	0.0	97.7	97.7	**44.2**
ox-MWCNTs	5.5	0.0	1.1	1.9	0.0	0.0	91.5	94.5	**17.3**
GNPs	2.2	0.1	0.1	0.0	0.0	13.2	84.3	97.7	**44.2**
rGO	9.0	2.2	0.2	2.9	5.4	2.7	77.6	88.7	**9.8**
GO	30.3	0.6	5.3	28.9	3.9	22.7	8.2	69.1	**2.3**

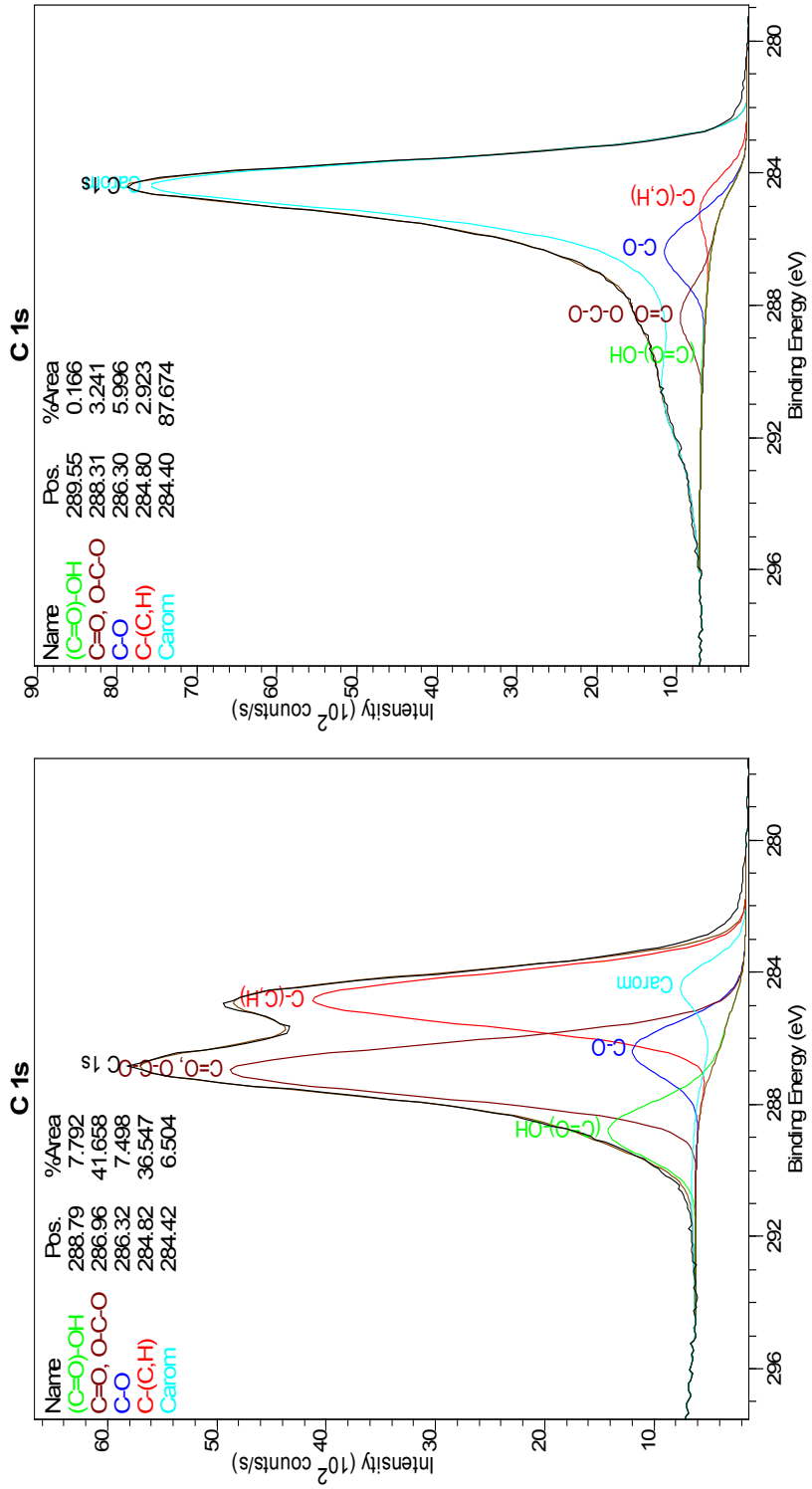

Figure 1 – XPS spectra for the C1s peak of GO (left) and rGO (right).

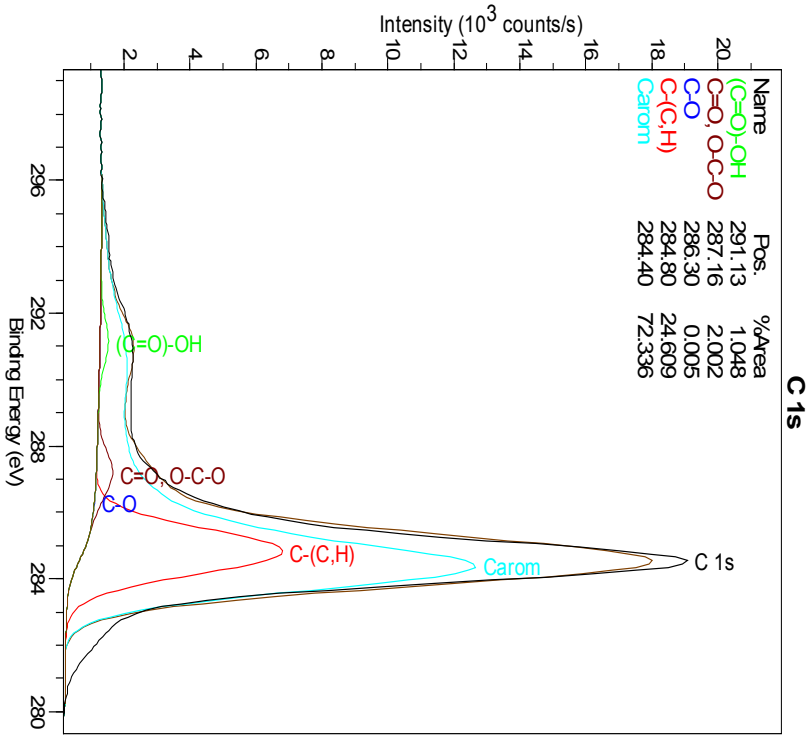

Figure 2 – XPS spectrum for the C1s peak of GNPs.

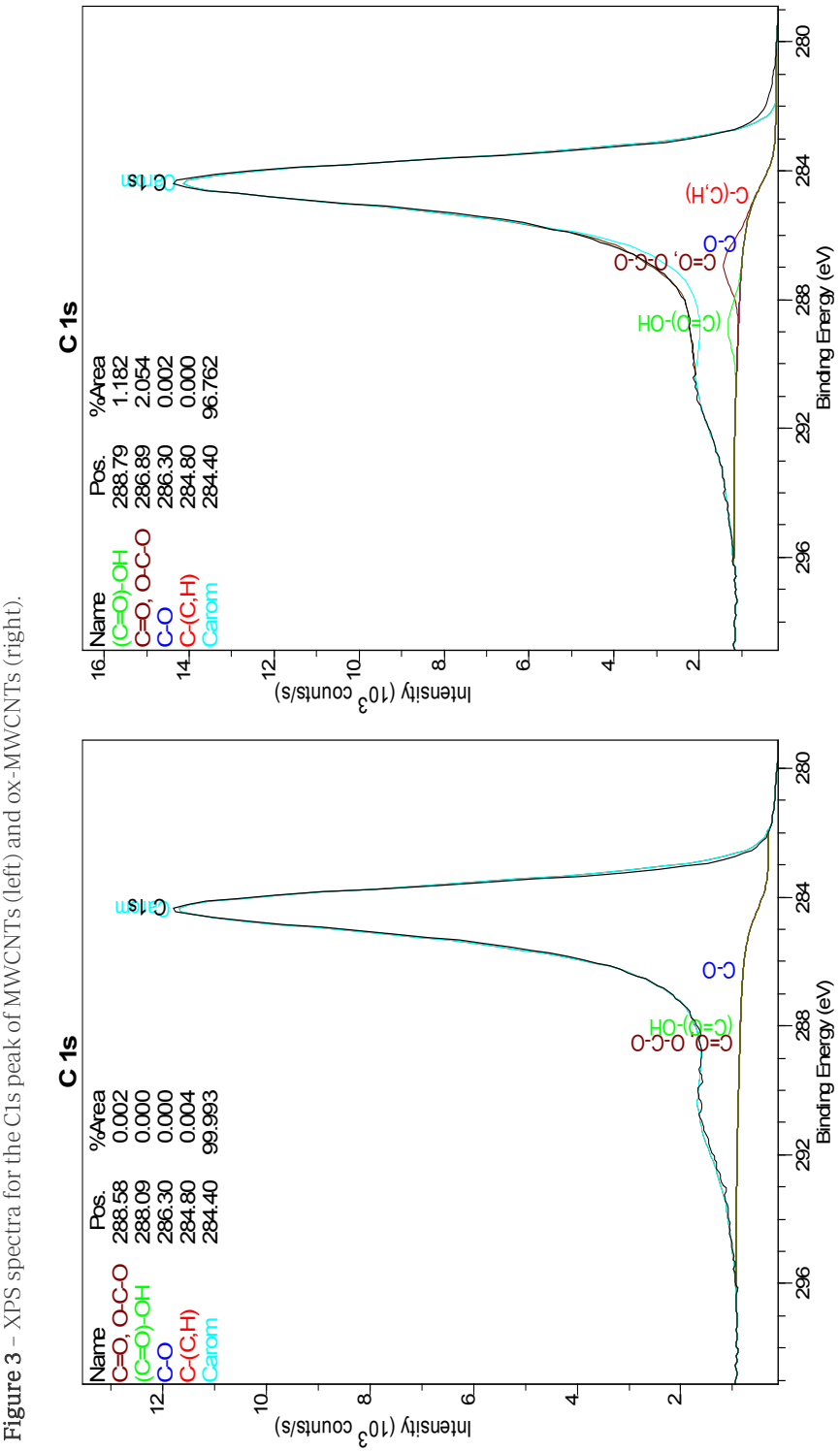

Figure 3 – XPS spectra for the C1s peak of MWCNTs (left) and ox-MWCNTs (right).

IV.2 Pourbaix diagram for cobalt

Edited from the Materials Project Database. Available online at: https://materialsproject.org

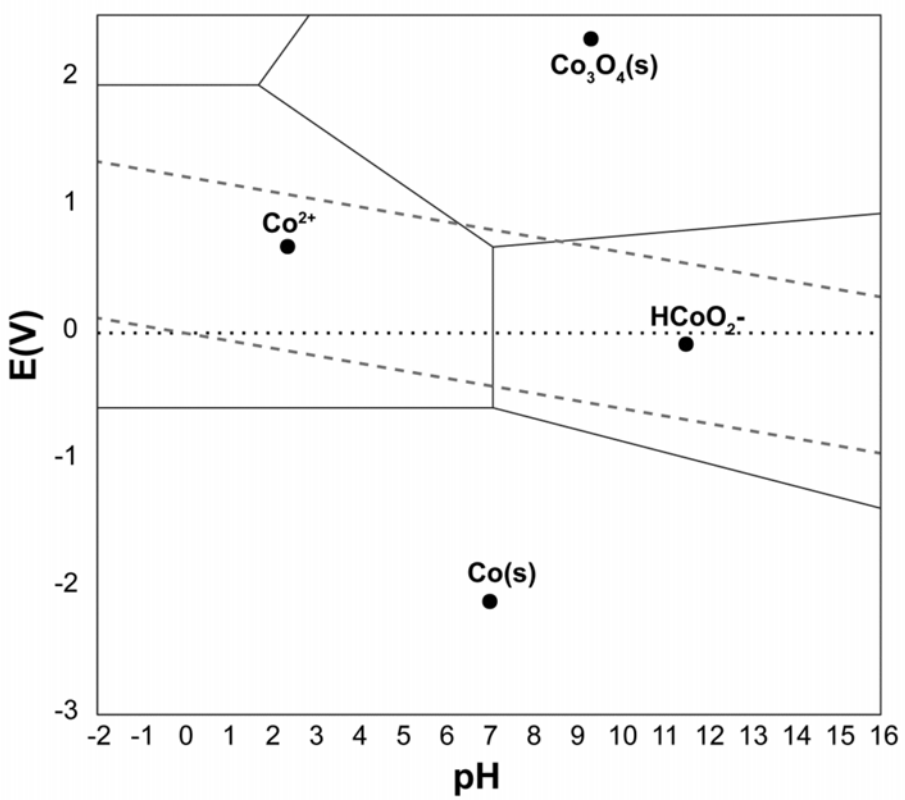

IV.3 Supplementary XPS results for Fe/Co/Ni alloys

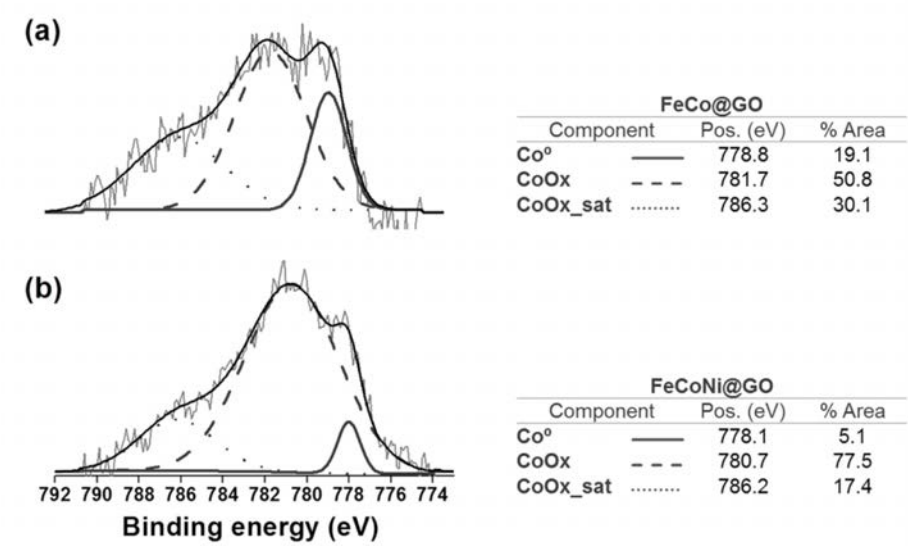

Figure 4 - XPS $Co2p_{3/2}$ peak region showing metallic (Co^0) and oxidized (Coox+Coox sat) components in (a) FeCo and (d) FeCoNi alloy NPs deposited on GO.

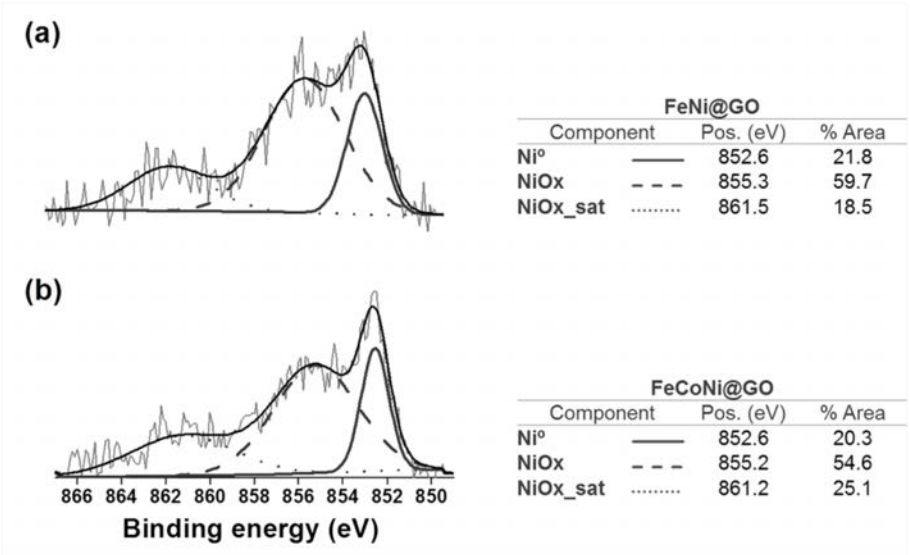

Figure 5 - XPS $Ni2p_{3/2}$ peak region showing metallic (Ni^0) and oxidized (Niox+Niox sat) components in (a) FeNi and (d) FeCoNi alloy NPs deposited on GO.